UNIVERSITY OF CALIFORNIA
SANTA CRUZ

PLANAR TUNNELING SPECTROSCOPY OF GRAPHENE AND BILAYER GRAPHENE

A dissertation submitted in partial satisfaction
of the requirements for the degree of

DOCTOR OF PHILOSOPHY

in

PHYSICS

by

John Lloyd Davenport II

June 2020

The Dissertation of John Davenport is approved:

Professor Jairo Velasco, Jr., Chair

Professor David Lederman

Professor Zack Schlesinger

Quentin Williams
Acting Vice Provost and Dean of Graduate Studies

Table of Contents

List of Figures

Abstract

Planar Tunneling Spectroscopy of Graphene and Bilayer Graphene

John Lloyd Davenport II

Graphene is our viewing window into two-dimensions. Just a single atom thick, this sheet of carbon confines electron in the x-y plane, drastically transforming their properties from those in free space. In order to access the intriguing, surprising and applicable physics that results from 2D confinement, it is necessary to develop tools to accurately probe graphene. In the fifteen years since electrical current was first run through graphene, transport measurements of two-dimensional materials have reached new heights of cleanliness and sophistication—showing novel states of matter by pushing current through graphene near equilibrium at ultra-high magnetic fields. Additionally, spectroscopy techniques involving tunneling have also developed to provide fundamental insight on graphene's electronic structure far from equilibrium. While both of these techniques, device-based transport and tip-based tunneling, have revolutionized the study of graphene and its relatives, neither technique is capable of directly probing these 2D materials in ultra-high magnetic fields *and* away from equilibrium. In my thesis I will present a third technique that hybridizes transport and tunneling. The method is called planar tunneling spectroscopy (PTS) and it has three attributes that enable the access of new information on graphene: (1) PTS can spectroscopically probe occupied and unoccupied states; (2) PTS is fully compatible with the world's highest sustained magnetic fields; and (3) PTS has full control over

the external electric field and the amount of charge within the graphene sheet. Each of these three attributes have enabled other techniques to reveal novel physics in graphene. Here, I will show all three attributes work together for the first time.

With the unconventional power of PTS, we will tour through many of the properties that make graphene interesting: its linear dispersion, anomalous quantum Hall states, and unique screening behavior, to name a few. Afterward, we will take one step towards three dimensions by adding another sheet of carbon. Bilayer graphene is more than the sum of its parts. We will see that the coupling between its component layers bends and warps its band structure in ways that are compelling for a material-by-design applications. Finally, we will explore how to probe the inherent electronic structure of BLG without changing it, as is often unintentionally done. To make these subtle but substantial corrections, we will harness the true power of PTS—its simplicity and its control. The new techniques developed in this thesis for building devices, conducting tunneling spectroscopy, rendering data and thinking about tunneling physics will hopefully inform upcoming spectroscopic studies of 2D materials as this young field reaches maturity.

List of Abbr.

1D	One-dimensional
2D	Two-dimensional
DOS/$g(\varepsilon)$	Density of states
μ	Chemical potential
E_F	Fermi energy
V_b	Sample-probe bias
V_G	Back-gate Voltage
n	Charge density (10^{12}cm^{-2})
hBN	hexagonal Boron Nitride
BLG	Bernal-stacked bilayer graphene
STS/STM	Scanning tunneling spectroscopy/microscopy
PTS	Planar tunneling spectroscopy
PTC	Point tunneling contact
AFM	Atomic force microscopy
LL	Landau level
VHS	van Hove Singularity
BE	Band edge
HEB/HEB*	High energy bands (occupied/unoccupied)

To My BIG Family

Acknowledgements

Firstly, I would like to thank my advisor, Professor Jairo Velasco, Jr. for the opportunity to work on cutting edge physics and for his continuous guidance. Jairo is a talented and driven scientist and I am humbled to have been in his first batch of students. I am also grateful to have had mentorship from the other two members of my thesis committee, Professor David Lederman and Professor Zack Schlesinger. Dr. Lederman, thank you for teaching me to be a thorough experimentalist. Your diligent use of scientific method is inspiring and refreshing. Also, thank you for teaching me to install, operate, fix and maintain the equipment in your lab. Dr. Schlesinger, your intuitive approach to the counterintuitive subject of quantum mechanics will always resonate with me. I hope that you can find hints of it in this thesis. Thank you for so many compelling discussions.

Next, I would like to thank all of the Velasco Group members, past and present. We started together in an empty room with scotch tape and dreams, and over the past 4 years our collective efforts and enthusiasm have brought the Velasco Group to the cutting edge. Specifically, I would like to thank Eberth Arturo Quezada-Lopez, Zhehao Ge and Fred Joucken. Were it not for my partner in crime, Arturo, I would certainly not be writing this acknowledgement section. Arturo is a kind, humorous and clever lab partner who has encouraged me to do good work since we met. Zhehao Ge, I am deeply thankful to you for the pivotal insight you provided on my project during our overlap in the Velasco Group. I hold your passion for objective truth in high esteem.

Fred, thank you for the numerous enlightening discussions on tunneling into bilayer graphene.

I have had the pleasure of mentoring several undergraduate and high school students, who I would like to mention here. Junyan Liu, Hechin (Albert) Chen, Carlos Nuñez-Lobato, Bruce Ji, Jonah Baughman, Salma Lira, Kian Jansepar, Armando Cardeñas, Alex Mordaunt and Alan Chen. I would like to give a special thanks to Alexander Stram, for his sustained contribution to fabricating novel tunneling devices.

In my 25 years as a student, there have been many professors and teachers that have cultivated my love for physical science. In particular, I would like to thank Professors Randolph Peterson, Ron Pongdee, Doug Drinen and Matthew Rudd for inspiring me to have fun and think unconventionally about science and math. Along those lines, I am very grateful to my dear friends, Dr. David Mordaunt and Dr. Sophie Morley for their professional guidance and stimulating discussions. Thank you, Dave and Sophie for helping me across the finish line!

I am so grateful to my loving family, to whom I dedicate this work. To my unbelievably supportive, free-thinking parents: mom and dad, words cannot express how fortunate I feel to be your son. To my amazing siblings: Marguerite, Sophie, and Stuart, thank you for inspiring me to do what I love and to share my passion with others.

Last but not least, I would like to thank Jane, the love of my life. Your support has made all the difference in pursuing this degree.

~~Outside of the lab, thank you to my friends and surfing companions in Santa Cruz. You know who you are!~~

Chapter 1:

Introduction and Motivation

"How can we directly observe electron behavior and symmetry in two dimensions?"

–John Davenport, PhD Candidate

"By symmetry we mean the existence of different viewpoints from which the system appears the same. It is only slightly overstating the case to say that physics is the study of symmetry."

–Philip W. Anderson, Nobel Laureate[1]

Physical systems behave according to their symmetries. Governing forces can vary over 60 orders of magnitude between relativistic and quantum regimes, necessitating drastically different measurement and theory techniques between the two.[1] Nevertheless, symmetry remains a key tool for determining conservation laws and dynamics in *all* physical systems. Solid state physics uses the symmetry of crystals—dictated by the arrangement of their constituent atoms—to explain and predict a wide variety of phenomena. Compare, for example, graphene, a two-dimensional (2D) sheet of carbon just one atom thick, to hexagonal boron nitride (hBN), another 2D material with an atomic arrangement nearly identical to that of

[1]The observable universe is 10^{26} m across, while the Planck length is 10^{-34} m

graphene. Graphene's honeycomb pattern is entirely carbon and thus has inversion symmetry, while hBN consists of alternating boron and nitrogen atoms and lacks inversion symmetry. The implication of their differing symmetries is dramatic: graphene has an exceedingly high electrical conductivity, while hBN on the other hand is an excellent insulator. A third 2D material, bilayer graphene, has symmetry that can be continuously tuned with an electric field, between a conducting state (similar to graphene) and an insulating state (like hBN). These three complementary materials are an ideal platform for investigating how fundamental symmetry dictates material properties—a connection that is at the core of condensed matter physics. This thesis harnesses the contrasting properties of graphene, hBN and bilayer graphene to probe electronic states and reveal symmetry breaking in 2D.

Material properties dictate the nature and magnitude of a material's response to a given stimulus. Electrical conductivity, for instance, determines the amount of current that will flow with a specific potential applied. Measuring condensed matter phenomenology *via* materials properties typically involves providing a *stimulus* (e.g. applying a voltage or shining light) and measuring a *response* (such as detecting current flow or collecting reflected light). Specific stimuli and responses vary widely between experiments, just as a given material has a library of different properties. However, in special cases the majority of entries in this library can be traced back to a few more fundamental attributes: density of states (DOS) and chemical potential (μ) are among them. Notice, for instance, that metals typically reflect light, conduct electricity and heat, and can be deformed without breaking. Most metals, as it turns out, have a similar

relationship between their DOS and μ, namely, there is a high DOS at energy μ. Together DOS and μ, which are deeply connected to the metallic atoms' bonding symmetry, endow the metal with a "sea" of charges that reflect light, conduct electricity and enable elastic deformations. The DOS is a count of the possible states at a given energy, and μ is the amount of energy gained with the addition of charge. These two quantities constitute the electronic structure. Knowledge about a material's electronic structure is an invaluable key for tying theoretical predictions to experimental observations.

Bulk crystals have long been a testbed for relating symmetry to observed phenomenology *via* materials properties. While there are a host of established methods for dictating bulk material properties (compressibility, heat capacity, etc), the underlying quantities, DOS and μ, are experimentally challenging to measure. Their elusiveness can be traced back to the crystal's symmetry. A cartoon bulk crystal is shown in Fig. 1.1 as an orange block. In the center of the block, atoms are regularly spaced with respect to each other in a repeating arrangement that seems to extend to infinity. At the surface of the crystal, however, the situation is strikingly different. An abrupt termination of the uniformly spaced atoms at the surface can gives rise to emergent surface states that can have completely different properties than the bulk. The main two direct probes of DOS, photoemission and tunneling spectroscopy, apply a stimulus to a crystal (light in one case, voltage in the other), and collect ejected charges. However, the ejected charges must first breach the surface, then travel to a detector. Along their transit, charges may interact and are liable to alter their measured state. As

a result, the measured DOS does not necessarily reflect the bulk DOS, but rather, the DOS of the surface.

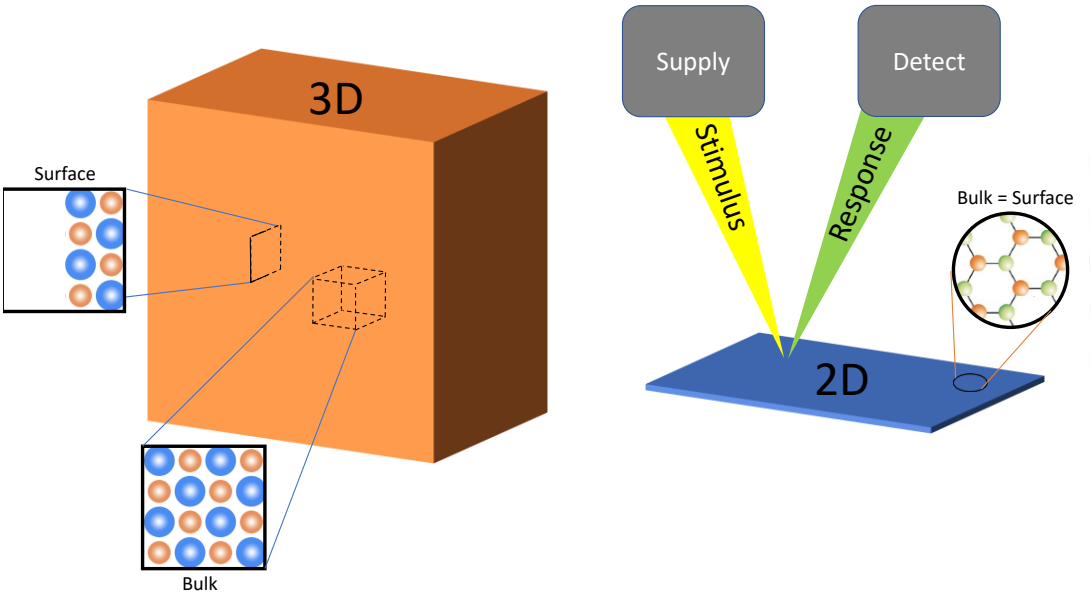

Figure 1.1: Two-dimensional materials vs bulk crystals. In bulk crystals like the one represented by an orange block on the left, the electronic behavior is dictated by lattice symmetry, which is broken at the surface. In a two-dimensional material (shown as a blue sheet on the right) lattice symmetry is not changed at the surface, allowing novel physics to exist and be probed with conventional stimulus-response methods (represented by yellow and green beams, respectively)

In 2D materials the surface and bulk are one in the same. Fundamental properties like DOS and μ are thus accessible to direct probing with photoemission and

tunneling spectroscopy. A cartoon 2D material is shown as a blue sheet in Fig. 1.1. Indeed, since the first tunneling spectroscopy study of graphene was reported in 2008, spectroscopy has played an integral role in exploring exotic phenomena in 2D. One such phenomenon is the integer quantum Hall effect (IQHE), which was discovered in silicon MOSFETs in 1980.[2] The electrical conductivity of quantum Hall systems assumes discretized values in the presence of a magnetic field. This quantized Hall conductivity is attributed to an organization of the 2D DOS into cyclotron orbits called Landau levels. In the original quantum Hall systems, Landau levels were measured indirectly with transport and capacitance techniques because they were below the sample surface, out of reach of direct probing from photoemission and tunneling spectroscopy.[3] With the discovery of graphene came a new, more accessible platform for exploring the IQHE.[4] Graphene's Landau levels are fully exposed and ideal for probing with tunneling spectroscopy, which directly measures the DOS.[5,6] Additionally, graphene can be isolated on a dielectric substrate and made into a capacitor. By applying a potential across the capacitor, charges are induced in graphene, changing its μ.[7] Tunability of μ and access to the DOS are two unique characteristics of 2D materials like graphene that differentiate them from their bulk predecessors.

New, unconventional states of matter can provide insight on fundamental physics. The IQHE, for instance, significantly altered the way solids are described with topology.[8] At high magnetic fields (B) and low temperatures (T), kinetic energy is quenched, and thermal energy is limited. As a result, electrostatic repulsion between

charges breaks the symmetry of Landau levels, opening a gap in the DOS at μ.[9] In 2D materials these symmetry broken Landau levels can have a variety of competing electronic orders—from valley ferromagnets to skyrmion solids—and they connect underlying symmetries with quantities like DOS and μ.[10] However, symmetry broken Landau levels have the propensity to exist at high B (>10T) and low T (<100mK). Therefore, they are inaccessible to conventional tunneling spectroscopy, which requires extremely low mechanical noise that is incompatible with high B or low T. As a result, there remains a gap in direct information about 2D materials' DOS and μ in extreme B and T.

One conventional characterization technique used for probing symmetry broken Landau levels in 2D materials is electron transport. Transport measurements involve injecting current and measuring the resulting potential difference across different parts of 2D material nanodevices. Transport measurements are mechanically stable, so they are fully compatible with high B and low T. However, they *do not* yield the sample's DOS and μ directly, but instead probe related quantities such as conductivity and charge density. In order to expand fundamental knowledge about symmetry-broken Landau levels in 2D materials, there is a need for measurement techniques that directly probe DOS and μ, yet are as mechanically stable as device-based transport measurements. This thesis focuses on one such technique.

Because two dimensional materials are fully exposed to direct probes, their crystal symmetries are sensitive to the local electrostatic environment. For example, different magnitudes of electrostatic potential applied between the layers of bilayer

graphene can break the inversion symmetry between neighboring carbon atoms, resulting in major changes to the DOS and μ.[11] The same tunable symmetry that makes bilayer graphene a compelling playground for exploring electrons in 2D also makes its inherent DOS and μ difficult to measure and understand. For instance, conventional tunneling spectroscopy is known to change the electronic structure of bilayer graphene as it is measured.[12] This elusive electronic structure begs a fundamental measurement question: how can we directly measure the DOS and μ in 2D materials without unintentionally altering them? In my thesis I introduce and employ a technique that addresses this question. The technique utilizes the properties of graphene, hBN, and bilayer graphene in parallel.

Since Geim and Novoselov first isolated graphene in 2004,[7] the family of 2D materials has steadily grown with members that now span a broad spectrum of physical properties. Different 2D materials can be magnetic, semiconducting, insulating, metallic, or superconducting they can host skyrmions, charge density waves, Mott insulators and valley ferromagnets, to name a few.[13] Figure 1.2 shows a small sample of unique 2D materials: graphene, a semimetal shown in gray, chromium (III) iodide, a ferromagnet shown in purple, $NbSe_2$, a superconductor shown in orange and hBN, an insulator shown in blue are all shuffled together. Two dimensional materials are appealing from a device physics perspective because they can be layered atop one another with atomically sharp interfaces. The right panel of Fig. 1.2 shows a cartoon example of a heterostructure composed of 2D materials with colors matching the sheets shown to the left. Such heterostructures are more than the sum of their parts—they have

shown new, emergent properties unique from the properties inherent to the layers. Drawing on the emergent properties of 2D heterostructures brings new device functionalities into reach. One such function is the ability to perform tunneling spectroscopy in high magnetic fields with full control of the electrostatic environment. My thesis employs a new type of device made possible by heterostructures to realize this functionality.

The main experimental focus of my thesis is the planar tunneling spectroscopy (PTS) device, which can spectroscopically probe at high B and with full control of the electrostatic environment. The devices use several-atom-thick hBN as an insulating tunneling barrier that separates either graphene or bilayer graphene from a printed metallic probe.[14] Measuring the electrical conductance across the ultrathin hBN in different conditions provides direct access to the DOS and μ of graphene and bilayer graphene. Because the devices are as mechanically stable as transport devices, they are fully compatible with the highest continuous B fields and lowest cryostat temperatures available. Additionally, the geometry of the device is akin to a planar capacitor, making its electrostatics straightforward to simulate. Therefore, tunneling devices based on 2D materials nicely fill the need for a direct probe compatible with the extreme experimental conditions where symmetry broken Landau levels manifest.

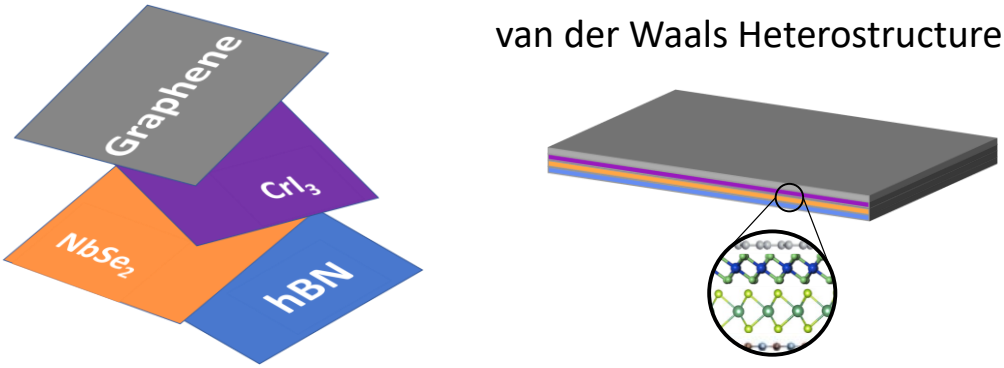

Figure 1.2: Assembling heterostructures out of 2D materials. Two-dimensional materials, shown as colored sheets on the left, can be mechanically assembled into heterostructures with atomically sharp interfaces, depicted on the right. These heterostructures can exploit the variety of properties in their individual components. Heterostructures can also show emergent phenomena, implying the total is greater (or different) than the sum of its parts.

During my doctoral work I have harnessed PTS devices to measure the fundamental properties of electrons and symmetries in 2D. My thesis details the background, methods, results and interpretation that constitute my discoveries. Beginning in Chapter 2, I outline the established theory behind graphene and bilayer graphene's unique electronic structure. In Chapter 3, I introduce the fundamentals of tip-based and planar tunneling measurements. Chapter 4 is a detailed description of the fabrication methods employed to produce high quality graphene tunneling devices as well as a novel scheme for fabricating point tunneling contacts. Then, the results of

tunneling into monolayer and bilayer graphene at low T and high B are given in Chapters 5, 6 and 7, including interpretation of the data. Chapter 8 contains the outlook for exciting new PTS directions as well as some closing remarks.

References

(1) Anderson, P. W. More Is Different. *Science (80-.).* **1972**, *177* (4047), 393–396. https://doi.org/10.1126/science.177.4047.393.

(2) Klitzing, K. v.; Dorda, G.; Pepper, M. New Method for High-Accuracy Determination of the Fine-Structure Constant Based on Quantized Hall Resistance. *Phys. Rev. Lett.* **1980**, *45* (6), 494–497. https://doi.org/10.1103/PhysRevLett.45.494.

(3) Richard E. Prange, S. M. G. *The Quantum Hall Effect*; Springer-Verlag, 1987.

(4) Zhang, Y.; Tan, Y.-W.; Stormer, H. L.; Kim, P. Experimental Observation of the Quantum Hall Effect and Berry's Phase in Graphene. *Nature* **2005**, *438* (7065), 201–204. https://doi.org/10.1038/nature04235.

(5) Tersoff, J.; Hamann, D. R. Theory of the Scanning Tunneling Microscope. *Phys. Rev. B* **1985**, *31* (2), 805–813. https://doi.org/10.1103/PhysRevB.31.805.

(6) Miller, D. L.; Kubista, K. D.; Rutter, G. M.; Ruan, M.; de Heer, W. A.; First, P. N.; Stroscio, J. A. Observing the Quantization of Zero Mass Carriers in Graphene. *Science (80-.).* **2009**, *324* (5929), 924–927. https://doi.org/10.1126/science.1171810.

(7) Novoselov, K. S.; Geim, A. K.; Morozov, S. V; Jiang, D.; Zhang, Y.; Dubonos, S. V; Grigorieva, I. V; Firsov, A. A. Electric Field Effect in Atomically Thin Carbon Films. *Science (80-.).* **2004**, *306* (5696), 666–669. https://doi.org/10.1126/science.1102896.

(8) Haldane, F. D. M. Model for a Quantum Hall Effect without Landau Levels:

Condensed-Matter Realization of the “Parity Anomaly.” *Phys. Rev. Lett.* **1988**, *61* (18), 2015–2018. https://doi.org/10.1103/PhysRevLett.61.2015.

(9) Stormer, H. L.; Tsui, D. C.; Gossard, A. C. The Fractional Quantum Hall Effect. *Rev. Mod. Phys.* **1999**, *71* (2), S298--S305. https://doi.org/10.1103/RevModPhys.71.S298.

(10) Barlas, Y.; Yang, K.; MacDonald, A. H. Quantum Hall Effects in Graphene-Based Two-Dimensional Electron Systems. *Nanotechnology* **2012**, *23* (5), 52001. https://doi.org/10.1088/0957-4484/23/5/052001.

(11) Zhang, Y.; Tang, T.-T.; Girit, C.; Hao, Z.; Martin, M. C.; Zettl, A.; Crommie, M. F.; Shen, Y. R.; Wang, F. Direct Observation of a Widely Tunable Bandgap in Bilayer Graphene. *Nature* **2009**, *459*, 820.

(12) Holdman, G. R.; Krebs, Z. J.; Behn, W. A.; Smith, K. J.; Watanabe, K.; Taniguchi, T.; Brar, V. W. Dynamic Band Structure and Capacitance Effects in Scanning Tunneling Spectroscopy of Bilayer Graphene. *Appl. Phys. Lett.* **2019**, *115* (18), 181601. https://doi.org/10.1063/1.5127078.

(13) Novoselov, K. S.; Mishchenko, A.; Carvalho, A.; Castro Neto, A. H. 2D Materials and van Der Waals Heterostructures. *Science (80-.).* **2016**, *353* (6298). https://doi.org/10.1126/science.aac9439.

(14) Chandni, U.; Watanabe, K.; Taniguchi, T.; Eisenstein, J. P. Signatures of Phonon and Defect-Assisted Tunneling in Planar Metal–Hexagonal Boron Nitride–Graphene Junctions. *Nano Lett.* **2016**, *16* (12), 7982–7987. https://doi.org/10.1021/acs.nanolett.6b04369.

Chapter 2:

Fundamentals of Graphene and Bilayer Graphene

Symmetry plays an important role in the unique properties of graphene systems. This chapter treats the bonding, band structure, Landau quantization and electron correlations in graphene and bilayer graphene (BLG) from a symmetry perspective. The treatment begins with a review of the underlying bonding symmetries and degeneracies that enable delocalized electronic states in graphene and BLG. Next, we examine a covalent bonding model that introduces the "linear combination of atomic orbitals" technique. In Section 2.3, a closer look is taken at the off-diagonal hopping parameters in real space. Section 2.4 introduces the tight binding approximation, and the technical principles that enable derivation of graphene's band structure. The tight binding calculation for graphene is presented in Section 2.5. Sections 2.6 examines the high symmetry points K and K' in reciprocal and real space. Graphene's extraordinary band structure exhibits relativistic effects at low energies. To explore these effects, we approximate the Hamiltonian in Section 2.7, calculate the density of states (DOS) in Section 2.8, and explore the resulting massless Dirac fermions in a perpendicular magnetic field in Section 2.9.

Bilayer graphene (BLG) is more than the sum of its parts. In Section 2.10 we show the tight binding calculation for BLG, then in Section 2.11 we explore the shape of the BLG band structure and calculate its DOS. Bilayer graphene has a band gap that is sensitive to the symmetry of the system. This symmetry can be tuned by a

perpendicular electric field, a treatment of which is provided in Section 2.13. For a more detailed look at BLG's band structure, Sections 2.12 and 2.13 include additional hopping parameters and asymmetries into the BLG band structure. At low energies, BLG's band structure hosts relativistic effect distinct from those in a single graphene sheet. A derivation of the low energy Hamiltonian and comments on the mass-inducing effects of interlayer coupling are presented in Section 2.14.

This introduction concludes with an examination of electron-electron interactions in thin carbon films. As two examples, electron-electron repulsion can lift degeneracies and renormalize the band structure. These two phenomena are discussed in Sections 2.16 and 2.17, respectively.

2.1 Symmetry and Hybridization in Electron Orbitals

There is a direct correspondence between conserved quantities and symmetries of a system. For example, in a single electron atom with nucleus charge Zq, angular momentum is conserved $dJ/dt = 0$. Hamiltonian of the single electron atom is spherically symmetric $\mathcal{D}H\mathcal{D}^{\dagger} = H$, where $\mathcal{D}$ is the unitary rotation operator.[1] The connection between conserved quantities and underlying symmetries can be traced back to Noether's theorem,[2] and in quantum mechanics is related to the degeneracy of a quantum state. In addition to angular momentum and energy, there is another—albeit subtler—constant of motion that is connected to orbiting bodies. This quantity is known as the Laplace-Runge-Lenz vector $\vec{A}_{LRL} = \vec{L}x\vec{p} - mk\hat{r}$, where $\vec{L}$ is the angular momentum and $\vec{p}$ is the linear momentum. The Laplace-Runge-Lenz vector is

conserved for the centrosymmetric potential $V(\vec{r}) = -k/r^2$. This conserved quantity is tied to a symmetry that endows the hydrogen atom with an additional set of quantum numbers $m_l = 0, \pm 1, \ldots, \pm l$. The quantum number m_l represents the orbital angular momentum in the z direction as well as the orbital shape. Together, conservation of angular momentum and the Laplace-Runge-Lenz vector result in $2n^2$ degenerate states at principal quantum number n (where we include spin degeneracy).

The underlying symmetries of the single electron atom dictate the carbon bonding geometry within graphene sheets. Assuming that the electron's energy is compliant with the atomic spectrum ($-\frac{13.6\text{ eV}}{n^2}$ to first order), the electron will reside in a stationary state with a set of three quantum numbers (neglecting electron spin): n—the principle quantum number that depends on energy and determines distance from the nucleus $< r >$; l—the orbital angular momentum that dictates the angular shape of the orbital (which spherical harmonics, for example); and m_l—the z-component of orbital angular momentum which provides additional $2l + 1$ degeneracy to a given state. Four of the six electrons in a neutral carbon atom reside in the state $n = 2$, the remaining two occupy the 1s orbital due to the 2-fold spin degeneracy. If the carbon atom is isolated, electron screening from the core electrons raises the energy of the $l = 1$ "2p" states, and the resulting electron configuration is $1s^2 2s^2 2p^2$. In the presence of neighboring carbon atoms, the situation changes dramatically.

In the absence of screening, the carbon $n = 2$ state is 8-fold degenerate (2s, $2p_x$, $2p_y$, and $2p_z$ orbitals can each carry spin up or spin down electrons) and any linear combination of these degenerate orbitals is itself a solution to the Schrodinger equation.

Cartoons of each $n = 2$ orbital is shown in Fig. 2.1(a), where a red circle and three blue shapes depict the 2s, $2p_x$, $2p_y$ and $2p_z$ orbitals. Note that the bottom blue circle represents a side view of the same dumbbell shape shown in its neighbors. In the presence of other atoms, these orbitals may form linear combinations or "hybridize" to minimize interatomic energy with neighboring atoms. The components of one such hybrid state, the sp^2 state, is shown in Fig. 2.1(b) as a set of purple asymmetric dumbbells that each lay along a midsection of the same equilateral triangle (shown in black). In this configuration, the in-plane $2p_x$ and $2p_y$ orbitals hybridize with the 2s orbital, leaving the $2p_z$ orbital intact and sticking out of the plane. A cartoon of the full hybrid state is shown in Fig. 2.1(c), where each orbital retains one of the 4 electrons in the valence shell.

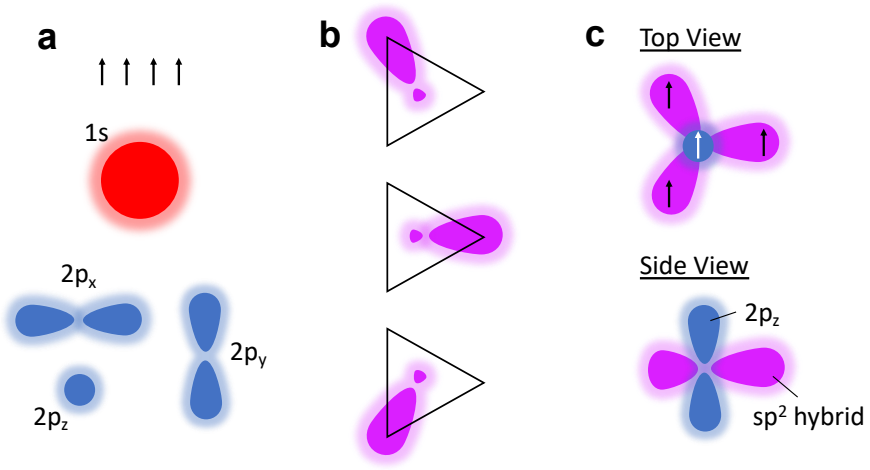

Figure 2.1: Cartoon of sp^2 hybridization. (a) Orthonormal orbitals in the $n = 2$ state. There are four degenerate states (neglecting spin) given by $l = 0, , m_l = 0$ (2s state shown as a red circle) and $l = 1, m_l = \pm 1, 0$ (2p$_x$,2p$_y$ and 2p$_z$ states, shown as blue orbitals). Notably the smaller blue circle depicts a top-down view of a dumbbell-shaped 2p$_z$ orbital. (b) Hybridized sp^2 state showing the combination of the 2s, 2p$_x$ and 2p$_y$ states in purple. (c) Resulting hybridized $n = 2$ state where three hybridized orbitals are in a single plane, with a 2p$_z$ orbital normal to the plane. Arrows represent electrons, which are evenly distributed about the four orbitals.

While hybridization is possible in all atoms, carbon is especially versatile in its bonding configurations due to its 4 valence electrons. Two species that are adjacent to carbon on the periodic table—boron and nitrogen—cannot easily bond in the sp^2 or sp^3 orbitals without having a lone pair of electrons that is not energetically favorable.

Carbon, however, can form sp^2 bonds and have a single valence electron remaining that is delocalized and free to roam from its $2p_z$ state. Indeed, carbon's hybridization and associated bonding versatility underpins the miracle of organic chemistry. In the context of this thesis it also endows graphene with peculiar properties. In order to understand these properties from a fundamental level, we next dive into the energetics of bonding.

2.2 Covalent Bonding

The hydrogen atom's spherical symmetry is conducive to analytically finding its discrete energy level spectrum $\{E_n\}$ and corresponding orbitals $|\phi_n\rangle$. *Two* hydrogen atoms that are in proximity, however, lack this spherical symmetry, and cannot be solved using the exact form of the real space Hamiltonian. An alternative, top-down approach to solving for the energy spectrum and orbitals of diatomic hydrogen begins by constructing a trial wave function in the orthonormal $\{|\phi_n\rangle\}$ basis.

A schematic of this technique, known as Linear Combination of Atomic Orbitals (LCAO), is shown in Fig. 2.2. The trial wave function $|\Psi\rangle$ can be written $|\Psi\rangle = c_1|\phi_1\rangle + c_2|\phi_2\rangle$ where $|\phi_1\rangle$ is the 1s orbital in atom 1.[3] Noting that the Hamiltonian for the system consists of the Hamiltonian H_1 of a single hydrogen plus a potential energy contribution V_2 from the neighboring hydrogen, the Schrödinger equation in the $\{|\phi_1\rangle, |\phi_2\rangle\}$ basis can be written

$$\langle\phi_1|H_1|\Psi\rangle + \langle\phi_1|V_2|\Psi\rangle = \langle\phi_1|E|\Psi\rangle \tag{2.1}$$

$$\langle\phi_2|H_2|\Psi\rangle + \langle\phi_2|V_1|\Psi\rangle = \langle\phi_2|E|\Psi\rangle \tag{2.2}$$

Exploiting the orthogonality of $\{|\phi_n\rangle\}$, namely $\langle\phi_j|\phi_i\rangle = \delta_{ij}$ and defining a "hopping parameter" $\gamma = -\langle\phi_2|V_1|\phi_1\rangle = -\langle\phi_1|V_2|\phi_2\rangle$ which is discussed in the next section,

$$\begin{bmatrix} \varepsilon_{1s} & -\gamma \\ -\gamma & \varepsilon_{1s} \end{bmatrix} \begin{bmatrix} c_1 \\ c_2 \end{bmatrix} = E \begin{bmatrix} c_1 \\ c_2 \end{bmatrix} \tag{2.3}$$

The 2 x 2 Hamiltonian matrix has energy eigenvalues that are readily found as the roots of the characteristic equation $\det(H - EI) = 0$. The spectrum and corresponding orbitals are

$$E_{\pm} = \varepsilon_{1s} \pm \gamma \tag{2.4}$$

$$|\Psi\rangle_{\mp} = \frac{1}{\sqrt{2}} \begin{bmatrix} 1 \\ \pm 1 \end{bmatrix} \tag{2.5}$$

Notably, there are two linear combinations of atomic orbitals that are themselves mutually orthogonal. The first of which, $|\Psi\rangle_{-} = 1/\sqrt{2}(|\phi_1\rangle + |\phi_2\rangle)$ is a bonding orbital with energy $\varepsilon_1 - \gamma$. The bonding orbital has probability density $|\Psi|^2 d\tau$ concentrated directly between the two atomic sites. The higher energy, antibonding orbital $|\Psi\rangle_{+} = 1/\sqrt{2}(|\phi_1\rangle - |\phi_2\rangle)$ has a node in between the two hydrogen atoms. Using the superficial analogy to the infinite quantum well, a higher concentration of nodes corresponds to a higher quantum kinetic energy. Interestingly, the perturbation of a neighboring nucleus can lower the ground state energy, leading to energetically favorable bonding, as Hund's rules permit.

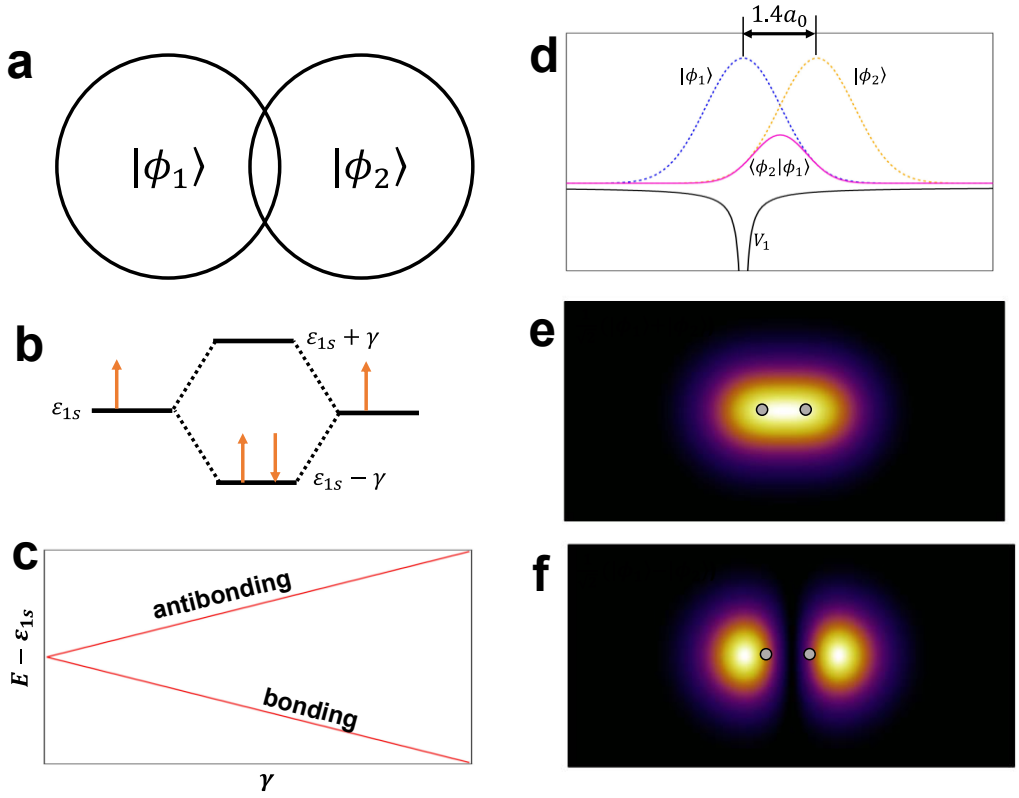

Figure 2.2: Linear Combination of Atomic Orbitals. (a) Schematic of the system where two H atoms, each with electron configuration $1s^1$ are brought in proximity. (b) Molecular orbital diagram showing the high energy and low energy solutions to the Schrödinger equation for the H_2 molecule. The ground state configuration consists of paired electrons in the low energy "bonding" orbital depicted as up and down orange arrows on the bottom horizontal line. (c) Eigenvalue solutions to the matrix in Eq. 2.3. Off diagonal overlap γ term determines the energy splitting between bonding and antibonding orbitals. When $\gamma = 0$, the bonding and antibonding energies are degenerate. (d) One dimensional projection of individual H 1s orbitals shown as blue and orange lines that are overlaid with the Coulomb potential of the left H atom, shown

as a black line. The separation of orbital peaks is the H_2 bond length $1.4a_0$. (e,f) Two-dimensional slices of the bonding (e) and antibonding (f) orbitals at z = 0. Light and dark regions correspond to high and low values of $|\psi|^2$ Gray circles mark the positions of H nuclei.

The simple picture of diatomic hydrogen will help us understand graphene. Consider the case where the distance between hydrogen atoms is infinite. As a result, $\gamma = 0$ and the bonding and antibonding orbitals are degenerate. Under certain conditions, the two carbon atoms in graphene's unit cell are decoupled, leading to a 2-fold degeneracy of the conduction and valence (π bonding and π^* antibonding) electronic bands. Although the spatial arrangement of carbon atoms in graphene does not change, coupling between sites changes due to modulation in electron waves that overlay the lattice.

As a final note, briefly consider the case where γ is nonnegligible but the two atoms are of different species (hydrogen and sodium, for instance). In this case, the symmetry of the system has been broken, and the diagonal elements ε_1 and ε_2 of the Hamiltonian are not equal. As a result, the energy eigenvalues show different behavior:

$$E_{\pm} = \frac{\varepsilon_1 + \varepsilon_2}{2} \pm \frac{\sqrt{(\varepsilon_1 + \varepsilon_2)^2 - 4\gamma^2}}{2} \tag{2.6}$$

There is a resulting gap between the bonding and anti-bonding orbitals even as $\gamma \to 0$. Moreover, in the case that each atom has one valence electron, the lower energy configuration is a pairing of electrons on the lower energy atom. Thus, changing the symmetry of even the simplest system can have drastic implications on the energy

spectrum and observed physics. This is evident in bilayer graphene, a system with readily tunable symmetry.

2.3 Hopping between Orbitals

Atomic orbitals are stationary states. In an isolated carbon atom, an electron residing in a $2p_z$ orbital will remain there unless perturbed by external means. Figures 2.3(a) and 2.3(c) show isolated, offset carbon $2p_z$ orbitals sliced with the XY plane one Bohr radius away $z = a_0$. In graphene, neighboring carbon atoms perturb the electron causing it to hop between $2p_z$ orbitals. A cross section of the perturbative Coulomb potential $V(\vec{\rho}, z = a_0)$ due to one carbon atom is shown as a contour plot in Fig. 2.3(b). The probability of hopping between neighboring $2p_z$ orbitals is given by the overlap between $V|\phi_B\rangle$ and $|\phi_A\rangle$. Figure 2.3(d) is a schematic of the hopping probability density. Each slice is taken at a separate height above a carbon atom. Notably, the $2p_z$ orbital is symmetric about the $z = a_0$ nodal mirror plane, so slices shown in Fig. 2.3(d) depict $\phi_A V \phi_B(\rho, \pm z)$. The area of highest probability density lies directly above and below on the axis shared the two carbon atoms. The hopping probability γ_0 is the sum of each density plot shown, multiplied by the overlaid function V. Because each individual $2p_z$ orbital has cylindrical symmetry, γ_0 can be used to completely characterize hopping between a given carbon site and its three neighboring carbon sites.

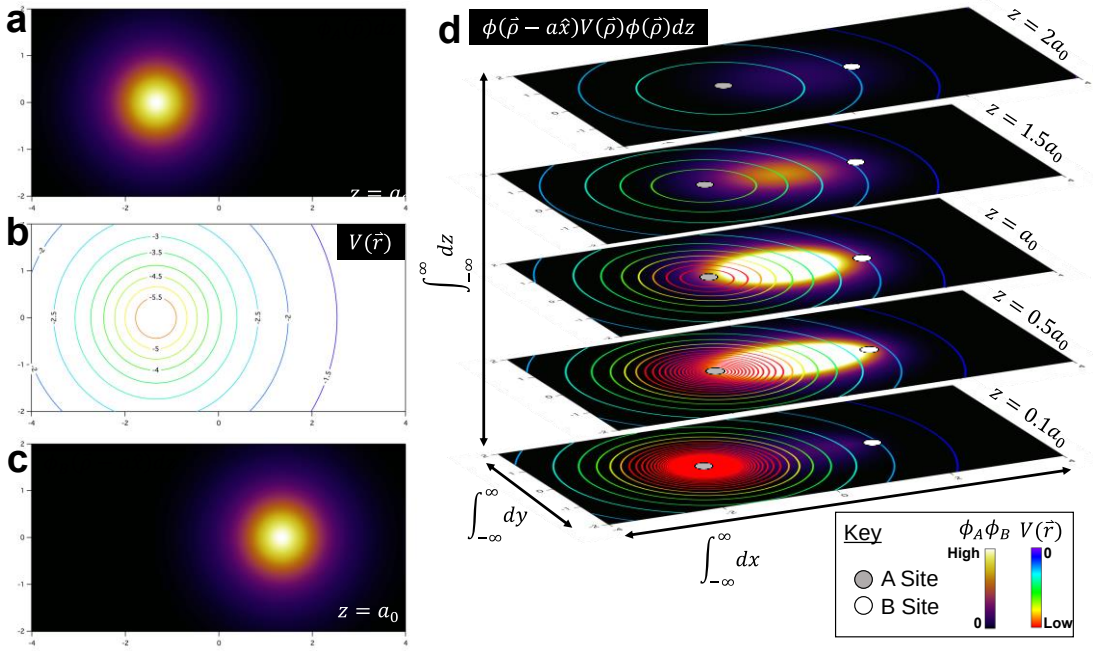

Figure 2.3: Visualizing the carbon in-plane hopping parameter γ_0. (a, c) Calculated probability density slice of left (a) and right (c) carbon $2p_z$ orbitals taken one Bohr radius above the nucleus of neighboring intrinsic carbon atoms. (b) Potential energy slice taken in the same plane as (a) and (c). (d) Three-dimensional visualization of the hopping parameter calculation. Each of the 5 stacked slices shows the product of neighboring carbon $2p_z$ orbitals overlaid with the perturbing potential due to one of the carbon nuclei. The slices are all above the nuclei and indicate a node at z = 0. The system is symmetric about the plane z = 0.

2.4 Tight Binding Calculation Overview

The translational symmetry of crystalline solids determines many of their material properties. Due to this symmetry solutions to the Schrödinger equation on a repeating crystal lattice are plane waves indexed by a crystal momentum $k = p/\hbar$, and modulated by a repeating function that shares the periodicity of the unit cell. These solutions, known as Bloch Waves, can assume a continuous spectrum of eigenvalues E_k which determines the dispersion of wave packets composed of Ψ_k. Specifically, a crystal's unit cell potential $V(\vec{r})$ is invariant under lattice vector translation operator $\tau(\vec{R}_l)$ where $\{\vec{R}_l\}$ are suitable lattice vectors. The kinetic energy operator $\hat{T}$ is translationally invariant, so in the case that $\tau(\vec{R}_l)V(\vec{r}) = V(\vec{r} + \vec{R}_l) = V(\vec{r})$, there is an eigenbasis shared by H and $\tau(\vec{R}_l)$. As result, solving the Schrödinger equation $(\hat{T} + \hat{V})\Psi_k = E_k\Psi_k$ on a lattice where $V(\vec{r} + \vec{R}_l) = V(\vec{r})$ requires that

$$\Psi_k = \sum_{\vec{R}_l} e^{-i\vec{k}\cdot\vec{R}_l}\, \psi(\vec{r} - \vec{R}_l) \tag{2.7}$$

where ψ is a function that shares the periodicity of the unit cell. The eigenvalue and eigenfunction solutions Ψ_k and E_k depend strongly on the arrangement of atoms in the unit cell, and the underlying lattice structure. In many cases, the dispersion relation or "band structure" of a crystal provides insight on the crystal's physical properties such as conductivity, heat capacity, permittivity and capacitance.[4]

One approach to determine E_k and Ψ_k is the tight binding method. As its name implies, the tight binding method assumes that electrons sit in local orbitals bound to their respective atoms and are only weakly perturbed by the potential of their nearest

neighbors. As discussed above, this perturbation enables electron hopping between neighboring orbitals. The full Hamiltonian of the crystal with lattice vectors $\vec{R}_l$ can be written as a kinetic energy operator $\hat{T}$ and a superposition of atomic potentials:

$$H = \hat{T} + \sum_{\vec{R}_l} V(\vec{r} - \vec{R}_l) \tag{2.8}$$

Assuming that a given atomic orbital has minimal overlap with the potential of neighboring nuclei, $\psi(\vec{r} - \vec{R}_m) \sum_{\vec{R}_l \neq \vec{R}_m} V(\vec{r} - \vec{R}_l)$ is small, and it is then convenient to express ψ as a weighted sum of the m atomic orbitals $\{\phi_m\}$ in the unit cell with weights $\{c_n\}$. For example, ϕ_A and ϕ_B form a basis of inequivalent carbon $2p_z$ orbitals in graphene's two atom unit cell.

With Ψ_k expressed in the $\{\phi_m\}$ basis, the task then becomes to determine weights $\{c_m\}$ such that Ψ_k is a solution to the Schrödinger equation $H\Psi_k = E_k\Psi_k$. This is done using a variational approach, where the trial Bloch wave function $\Psi_k{}' = \sum_{R_l} \psi'(r - R_l) e^{i\vec{k}\cdot\vec{R}_l}$ is acted upon with $\langle\phi_m|H$, and then minimized by setting $\frac{d}{dc_m}\langle\phi_m|H|\Psi_k\rangle = 0$. Notably, in the nearest neighbor approximation employed in the next section, all but the nearest neighbor hopping terms and onsite energies disappear from the product of infinite sum.

This final step of the tight binding approach varies slightly when applied to graphene. With a two-atom unit cell, graphene's Hamiltonian can be expressed as a 2 x 2 matrix in the $\{\phi_m\}$ basis. It is uniquely straightforward to solve for graphene's tight binding energy spectrum Ψ_k simply by diagonalizing a 2 x 2 matrix.

2.5 Graphene Tight Binding Calculation

Carbon atoms in graphene are sp^2 hybridized and thus have three nearest neighbors. The resulting crystal structure, depicted in Fig. 2.4(a), resembles a honeycomb. Although the carbon honeycomb is a repeating structure, it is not a Bravais lattice. Specifically, two vectors cannot be chosen such that repeatedly translating *a single* carbon atom by integral combinations of the vectors yields a honeycomb. However, two vectors *can* be used to build a carbon honeycomb if the unit cell (shown with a yellow outline in Fig. 2.4(b)) consists of *two inequivalent* carbon sites. These two carbons are shown as shaded and open circles in Fig. 2.4(a) and are referred to as A and B sites, respectively. The Bravais lattice that underlies a two-carbon unit cell is hexagonal and has lattice vectors $R_1 = (3a/2, \sqrt{3}a/2)$ and $R_2 = (3a/2, -\sqrt{3}a/2)$ shown in red. Graphene's lattice can be assembled from infinite copies of the unit cell that are each translated by a unique linear combination $\vec{R}_{mn} = m\vec{R}_1 + n\vec{R}_2$, where $m, n \in \mathbb{Z}$.

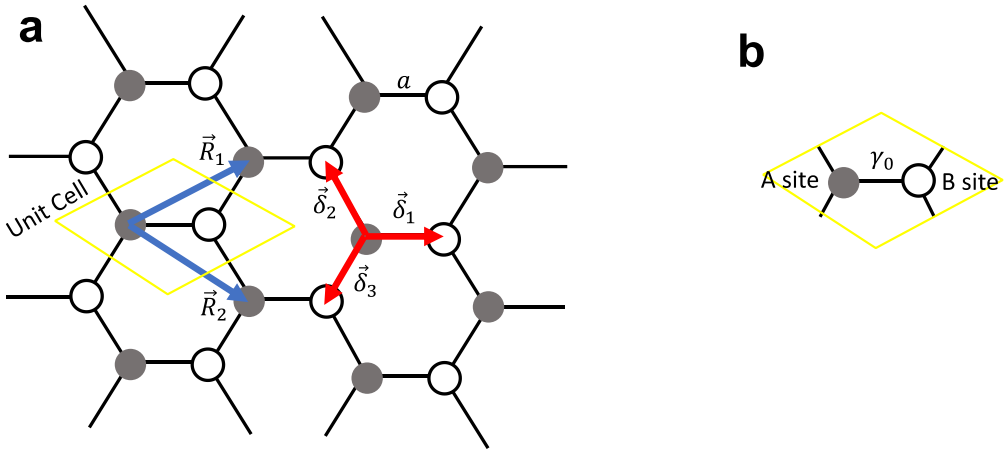

Figure 2.4 Graphene's lattice and nearest neighbor vectors. (a) Graphene's unit cell, outlined in yellow, consists of two carbon atoms: site A and site B, shown as gray and white circles, respectively. Blue arrows define the hexagonal lattice vectors $\vec{R}_1$ and $\vec{R}_2$. Repeated translations of the unit cell by integral combinations of $\vec{R}_1$ and $\vec{R}_2$ build graphene's honeycomb structure. Red arrows denote the position $\{\vec{\delta}_i\}$ of neighboring B sites around a given A site, for example. (b) Individual 2-component unit cell with carbon hopping energy γ_0.

Alternatively, graphene's lattice can be produced by first establishing a hexagonal lattice with A sites, then placing 1/3 of a B site in three positions around each A site. The displacements of these three nearest neighbor B sites with respect to an A site is given by the vectors $\delta_1 = (1,0)$, $\delta_2 = (-a/2, \sqrt{3}a/2)$ and $\delta_3 = (-a/2, -\sqrt{3}a/2)$, which are shown as blue arrows in Fig. 2.4(a). This alternate set of

basis vectors proves useful when dealing with nearest neighbor hopping, discussed below.

Graphene has a periodic crystal structure and so its energy eigenfunctions are Bloch waves. Each Bloch wave Ψ_k can be expressed

$$\Psi_k = \frac{1}{N}\sum_{m,n} \psi_{u.c.}(\vec{r}) e^{i\vec{k}\cdot\vec{R}_{mn}} \tag{2.9}$$

where $\psi_{u.c.}(\vec{r})$ repeats with the unit cell. Notably, the momentum dependent phase factor $\exp(i\vec{k}\cdot\vec{R}_{mn})$ is constant within each unit cell and differs between unit cells.

Similar to the case for diatomic hydrogen discussed in Section 2.2, $\psi_{u.c.}(\vec{r})$ is assumed to be a linear combination of atomic orbitals,

$$\psi_{u.c.}(\vec{r}) = c_A\phi_A(\vec{r}) + c_B\phi_B(\vec{r} - a\hat{x}) \tag{2.10}$$

where $\phi_A = \phi_B$ is the $2p_z$ orbital of an isolated atomic carbon atom (indices are for labelling convenience) and a is the carbon-carbon bond length. Certain values of weights c_A and c_B make Ψ_k an eigenfunction of the Hamiltonian. Our goal will be to determine these specific values, and their matching eigenvalue spectrum E_k, also known as the band structure or dispersion relation.

Graphene's Hamiltonian can be expressed as a kinetic energy operator together with the superposition of potential wells due to each carbon nucleus. Pulling out the energy operators $H_0 + V(\vec{r} - a\hat{x})$ for a single unit cell (at $\vec{R}_{mn} = 0$, for instance):

$$H = H_0 + V(\vec{r} - a\hat{x}) + \sum_{m,n\neq 0} [V(\vec{r} - \vec{R}_{mn}) + V(\vec{r} - \vec{R}_{mn} - a\hat{x})] \tag{2.11}$$

In order to achieve our goal of determining c_A and c_B, we must express the Schrödinger equation $H\Psi_k = E_k\Psi_k$ in the atomic orbital $\{\phi\}$ basis. Using Bra-Ket notation we act on both sides of the time independent Schrödinger equation with $\langle\phi|$,

$$\begin{aligned}\langle\phi_A|H_0|\Psi_k\rangle + \langle\phi_A|V(\vec{r}-a\hat{x})|\Psi_k\rangle \\ + \left\langle\phi_A\right|\textstyle\sum_{mn\neq 0}[V(\vec{r}-\vec{R}_{mn}) + V(\vec{r}-\vec{R}_{mn}-a\hat{x})]\left|\Psi_k\right\rangle \\ = E_k\langle\phi_A|\Psi_k\rangle\end{aligned} \tag{2.12}$$

In the nearest neighbor approximation, there is no overlap between A sites in different unit cells. Noting that the basis functions $|\phi\rangle$ chosen for $\psi_{u.c.}$ are eigenfunctions of H_0, namely $H_0\phi = \varepsilon_{2p_z}\phi$, the first term in Eq. 2.12 becomes

$$\langle\phi_A|H_0|\Psi_k\rangle = \left\langle\phi_A\middle|H_0\middle|\textstyle\sum_{m,n}(c_A\phi_A + c_B\phi_B)e^{i\vec{k}\cdot\vec{R}_{mn}}\right\rangle = c_A\varepsilon_{2p_z} \tag{2.13}$$

Additionally, with the help of the perturbative potential $V(\vec{r}-a\hat{x})$, electrons can hop from the B site orbital $\phi_B(\vec{r}-a\hat{x})$ into $\phi_A(\vec{r})$.

$$\begin{aligned}\left\langle\phi_A\middle|V(\vec{r}-a\hat{x})\middle|\textstyle\sum_{m,n}(c_A\phi_A + c_B\phi_B)e^{i\vec{k}\cdot\vec{R}_{mn}}\right\rangle = \left\langle\phi_A\middle|V(\vec{r}-a\hat{x})\middle|\textstyle\sum_{m,n}c_B\phi_B e^{i\vec{k}\cdot\vec{R}_{mn}}\right\rangle \\ = \gamma_0\end{aligned} \tag{2.14}$$

The third term in H accounts for V and Ψ_k evaluated at all other unit cells besides the central unit cell at $\vec{R}_{mn} = 0$. Notably, electrons cannot hop into $\phi_A(\vec{r})$ from any orbitals $\phi_B(\vec{r}-\vec{R}_{mn}-a\hat{x})$ in unit cells beyond those directly bordering the central unit cell. That is to say, electrons at unit cell (0,0) can stay within that unit cell, or hop to neighboring unit cells at positions $-\vec{R}_1$ or $-\vec{R}_2$ (each directly to the lift of the region outlined by a yellow diamond in Fig. 2.4(a)). Using the convention introduced above,

from the origin electrons can hop by lattice vectors $\vec{R}_{00}$ $\vec{R}_{-10}$ and $\vec{R}_{0-1}$. The resulting overlap can be expressed as

$$\begin{aligned}&\left\langle \phi_A \middle| \sum_{mn\neq 0}[V(\vec{r}-\vec{R}_{mn})+V(\vec{r}-\vec{R}_{mn}-a\hat{x})] \middle| \sum_{m,n}(c_A\phi_A+c_B\phi_B)e^{i\vec{k}\cdot\vec{R}}\right. \\ &= c_B\langle\phi_A|V(\vec{r}-\vec{R}_{-10}-a\hat{x})|\phi_B\rangle e^{i\vec{k}\cdot\vec{R}_{-10}} \\ &+ c_B\langle\phi_A|V(\vec{r}-\vec{R}_{0-1}-a\hat{x})|\phi_B\rangle e^{i\vec{k}\cdot\vec{R}_{0-1}}\end{aligned} \tag{2.15}$$

Considering onsite energy and nearest neighbor hopping, the coefficient $H|\Psi_k\rangle$ in the $|\phi_A\rangle$ basis is

$$\langle\phi_A|H|\Psi_k\rangle = c_A\varepsilon_{2p_z} - c_B\gamma_0(1+e^{i\vec{k}\cdot\vec{R}_{0-1}}+e^{i\vec{k}\cdot\vec{R}_{-10}}) \tag{2.16}$$

Taking the same approach, we next determine the the coefficient $H|\Psi_k\rangle$ in the $|\phi_B\rangle$ basis:

$$\langle\phi_B|H|\Psi_k\rangle = c_B\varepsilon_{2p_z} - c_A\gamma_0(1+e^{i\vec{k}\cdot\vec{R}_{01}}+e^{i\vec{k}\cdot\vec{R}_{10}}) \tag{2.17}$$

Noting that $\vec{R}_{-10} = -\vec{R}_{10}$, the Schrödinger equation can then be expressed in matrix form

$$\begin{bmatrix} \varepsilon_{2p_z} & \gamma_0 f(\vec{k}) \\ \gamma_0 f^*(\vec{k}) & \varepsilon_{2p_z} \end{bmatrix} \begin{bmatrix} c_A \\ c_B \end{bmatrix} = E_k \begin{bmatrix} c_A \\ c_B \end{bmatrix} \tag{2.18}$$

Where $f(\vec{k}) = 1 + 2e^{i3k_x a/2}\cos(\sqrt{3}k_y a/2)$. The energy eigenvalues $\{E_k\}$ of the 2 x 2 H matrix are found using the characteristic equation. The resulting energy spectrum and associated eigenfunctions are

$$E_k = \varepsilon_{2p_z} \pm \gamma_0|f(\vec{k})| \tag{2.19}$$

$$\Psi_k = \frac{1}{\sqrt{2}}\begin{bmatrix} 1 \\ e^{i\theta} \end{bmatrix} \tag{2.20}$$

The Bloch wave phase dependence $\exp(i\vec{k}\cdot\vec{R}_{mn})$ modulates Ψ_k between unit cells but not within each unit cell. However, it is convenient to recognize that the above result can be acquired by framing the phase-dependent hopping in terms of nearest neighbor vectors $\vec{\delta}_1 = (a, 0), \vec{\delta}_1 = \frac{a}{2}(-1, \sqrt{3})$ and $\vec{\delta}_1 = -\frac{a}{2}(-1, -\sqrt{3})$, shown as red arrows in Fig. 2.4(a). The phase-dependent hopping function $f(\vec{k})$ can then be expressed $f(\vec{k}) = \sum_{\vec{\delta}} e^{i\vec{k}\cdot\vec{\delta}}$.[2]

It should therefore come as no surprise that weights $\langle\phi_A|H\Psi\rangle$ between neighboring atoms at different lattice cites have their own phase dependence. Phase dependent hopping underpins the ubiquitous tight binding dispersion relation. In the case of graphene, there are unique momenta K and K' at the edges of the Brillioun zone that lead to peculiar phase factors. At these momenta, there is no hopping between A and B sites. As a result, the dimerized anti-bonding orbital and its bonding counterpart exist at the same energy. Thus, graphene's valence and conduction bands are degenerate at two infinitesimally small points in reciprocal space.

The reciprocal lattice can be reconstructed by first determining reciprocal lattice vectors $\vec{L}_1$ and $\vec{L}_2$ such that $\vec{L}_i \cdot \vec{R}_j = 2\pi\delta_{ij}$. The resulting reciprocal lattice vectors are $\vec{L}_1 = \frac{2\pi}{a}\left(\frac{1}{3}, \frac{1}{\sqrt{3}}\right)$ and $\vec{L}_2 = \left(\frac{1}{3}, \frac{-1}{\sqrt{3}}\right)$ which overlay the band structure in in Fig. 2.5(a).

[2]Note that this convention does not follow from the Bloch wave phase factor $e^{i\vec{k}\cdot\vec{R}_{mn}}$ because $\vec{R}_{mn}$ are vectors connecting unit cells, *not* neighboring carbon atoms. Nevertheless, I adopt this widespread convention for ease of connection to existing literature.[14,15]

These vectors $\vec{L}_1$ and $\vec{L}_2$ build a hexagonal Bravais reciprocal lattice with hexagonal Brillouin zones that have inequivalent equivalent sites K and K' along the vertices. Although inequivalent points K and K' are not connected by a reciprocal lattice vector, they can be found by rotating and scaling $\vec{L}_1$ and $\vec{L}_2$. Rotating $\vec{L}_1$ by $\frac{\pi}{6}$ and scaling its length by ½, the point (defined to be) K is at $\frac{2\pi}{a}\left(0, \frac{2}{3\sqrt{3}}\right)$. Rotating the K vector clockwise by $\frac{\pi}{3}$ yields the K' vector $\frac{2\pi}{a}\left(\frac{1}{3}, \frac{1}{3\sqrt{3}}\right)$. Reciprocal lattice vectors $\vec{L}_1$ and $\vec{L}_2$ can then be used to recreate the high symmetry points of the first BZ, denoted by black dots in Fig. 2.5(a).

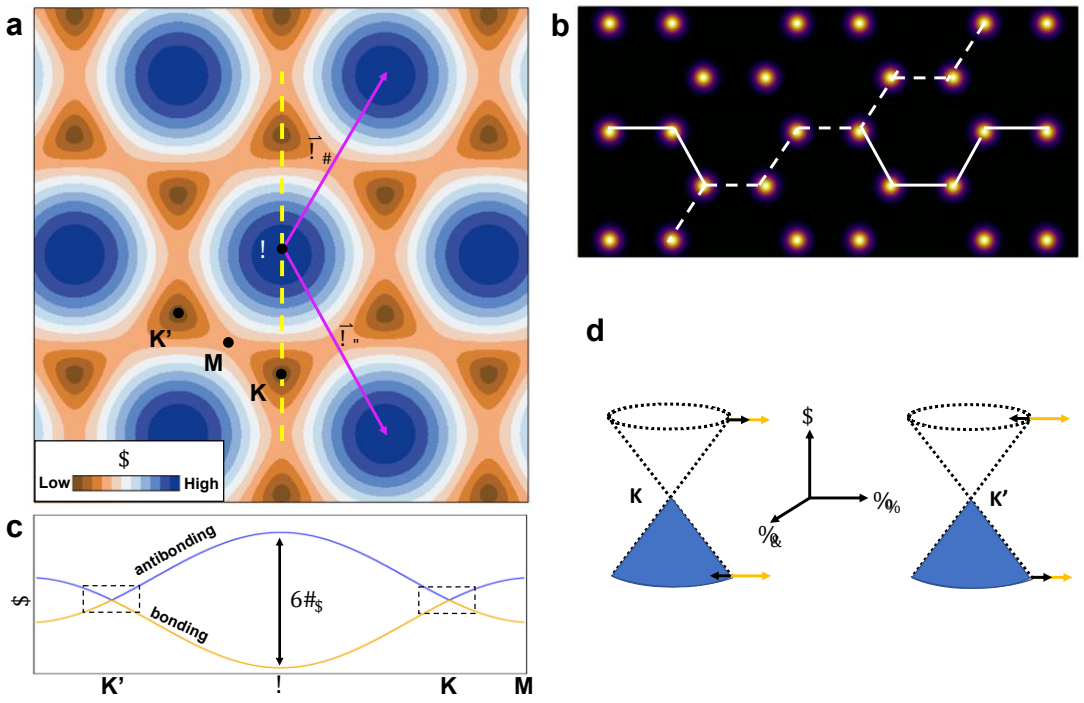

Figure 2.5: Reciprocal space representation of graphene. (a) Top view of graphene's conduction band E_k^+ where blue and orange regions are high and low

energy, respectively. Magenta arrows are vectors $\vec{L}_1$ and $\vec{L}_2$ that connect identical points in reciprocal space. High symmetry points K, K', M and Γ are denoted with black dots. (b) High symmetry directions along the honeycomb lattice. Zigzag and armchair edges are followed by white dashed and dotted lines, respectively. (c) Line profile of the valence (orange) and conduction (blue) bands taken along the M-K'-Γ-K path marked with a yellow dashed line in (a). Notably, the valence and conduction bands touch at two inequivalent points K and K', outlined with black dashed boxes. (c) Linear approximation of the graphene bands near K and K'. Orange arrows represent the direction of momentum and black arrows represent the direction of pseudospin.

2.6 Real-Space Representation of High Symmetry Momenta

We now turn to the real space representation of the eigenfunctions $\Psi(\vec{r})$ to investigate some of the unique characteristics of graphene's band structure. At each high symmetry point in reciprocal space, $\Psi(\vec{r})$ is modulated by a distinctive $\vec{k}$ vector. At K', for instance, $\vec{k}$ points along the zigzag direction of graphene's honeycomb as shown in Fig. 2.5(b). The left panel of Fig. 2.6(a-d) shows the envelope function $e^{i\vec{k}\cdot\vec{r}}$ where blue, green and red regions mark low, zero and high values, respectively. In graphene's valence band, shown in the middle panel of Fig. 2.6(a-d), $|\vec{k}|$ modulates Ψ such that the real part of Ψ repeating pattern -1,+1/2,+1/2 at atomic sites along the zigzag direction. Adopting the convention from Section 2.5, we can easily observe that the off-diagonal term in H is $-\gamma_0 \sum_{\vec{\delta}} e^{i\vec{k}\cdot\vec{\delta}} = (-1)(-1) + (-1)(+1/2) + (-1)(+1/$

$2) = 0$. Therefore, at K', the valence band or bonding orbital between A and B sites in the unit cell has energy ε_{2p_z}.

Graphene's conduction band evaluated at K' is shown in the right panel of Fig. 2.6(c). Here, $\Psi(\vec{r})$ has a less straightforward repeating sequence than the valence band. Atoms along the zigzag direction appear to follow the pattern -1,-1/2,+1/2,+1. To decipher the implications of the pattern, we focus on a representative B site where $\Psi = 1$ (shown as a red circle). Neighboring atoms have amplitudes +1/2,+1/2 and -1. Therefore, H evaluated at this particular site has off diagonal elements $\sum_{\vec{\delta}} e^{i\vec{k}\cdot\vec{\delta}} = (+1)(-1) + (+1)(+1/2) + (+1)(+1/2) = 0$. A similar real-space investigation of the K point is presented in Fig 2.6(d). Notably, at the K point, the envelope function modulates $\Psi(\vec{r})$ along a vertical zigzag direction, rotated 60 degrees from K'. Although K and K' are inequivalent in reciprocal space, they produce the same alternating patterns at atomic sites along the zigzag direction. The implications are intriguing: $\vec{k}$ evaluated at high symmetry points K or K' modulates $\Psi(\vec{r})$ along the zigzag direction such that next nearest neighbor hopping vanishes for both bonding and anti-bonding arrangements. A profound result of this is that valence and conduction bands touch at two degenerate points K and K'.

The real space representation $\Psi(\vec{r})$ can also provide insight on gap energies and dimerization. Figure 2.6(a) shows the $\Psi(\vec{r})$ modulated by envelope function $e^{i\vec{k}\cdot\vec{r}}$ where $\vec{k} = 0$ is at the Γ point. Without a modulating function, the difference between the bonding orbital (shown in the middle panel) and the antibonding orbital (shown in

the right panel) is readily apparent. Following the procedure outlined above, we directly evaluate the net hopping between nearest neighbors at a given atomic site. In the middle panel, it is clear that the net hopping is $-\gamma_0 \sum_{\vec{\delta}} 1 = -3\gamma_0$. In the antibonding orbital, the net hopping is $-\gamma_0 \sum_{\vec{\delta}}(-1) = 3\gamma_0$. The energy gap at Γ is thus $6\gamma_0$ (assuming no electron-hole asymmetry—or equivalently—that neighboring orbitals are orthogonal). This visualization lends itself well to the treatment of diatomic hydrogen, discussed in Section 2.2. For completeness, we turn to the M point, at which $\vec{k}$ aligns with the armchair direction, shown in Fig. 2.6(d). The envelope function $e^{i\vec{k}\cdot\vec{r}}$ that modulates $\Psi(\vec{r})$ is shown in the left panel and $\Psi(\vec{r})$ evaluated at atomic sites is shown in the middle and right panels. At this point in reciprocal space, each atomic site has a net coupling to nearest neighbors of $\pm\gamma_0$, with the valence band corresponding to lower energy. Superficially, this can be interpreted electrons feeling an effective energy gap when traveling along the armchair direction and no gap when travelling in the zigzag direction. In reality, semiclassical electrons are dispersive wave packets composed of energy eigenstates, and thus they will neither be perfectly conducting nor insulating as the real space picture suggests.

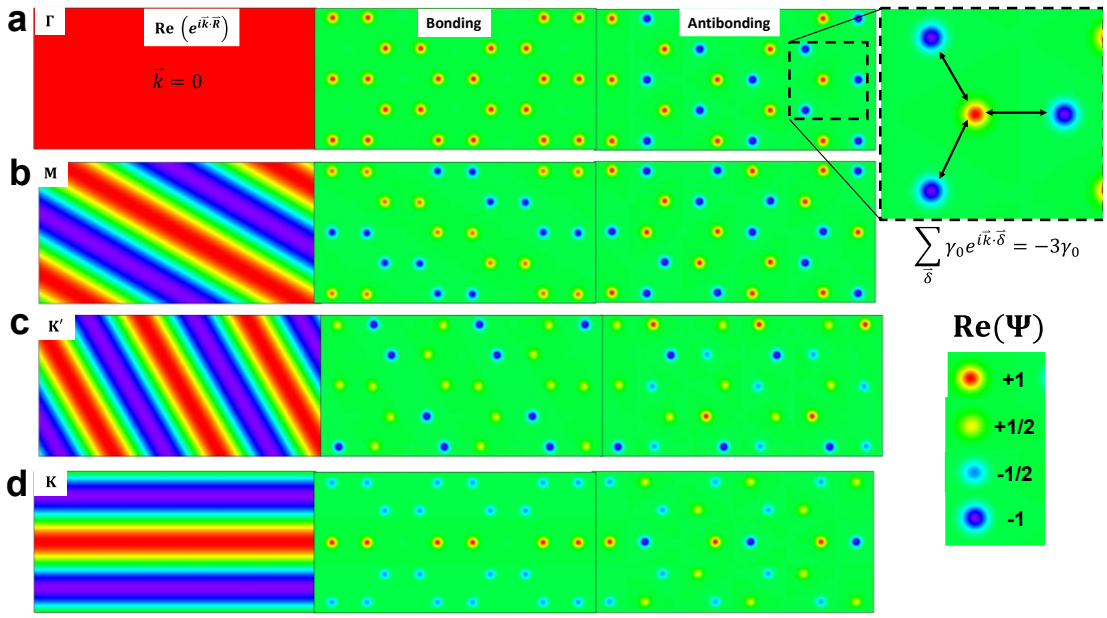

Figure 2.6 High symmetry momenta in real space: Panels in each row, the left panel shows the Bloch wave phase factor $e^{i\vec{k}\cdot\vec{r}}$, the middle panel shows the bonding solution to H (valence band discussed in the main text), and the right panel shows the anti-bonding solution to H (conduction band). In all panels, red, green and blue regions correspond to high, zero and low values. Each row is evaluated at a different high symmetry point in the first BZ with (a), (b), (c), (d) are at the, Γ, M, K' and K points, respectively. The zoom in panel on the right expands an A site and its nearest neighbor B sites when $\vec{k}$ is evaluated at the Γ point. The overlap between A site and neighboring B sites is observed to be $-3\gamma_0$ which corresponds to the conduction band energy at Γ.

There connection between the real space representation of the high symmetry momenta provides several insights about graphene and bilayer graphene. Specifically, graphene has only one fitting parameter, namely its Fermi velocity v_F or "band slope"

at low energies. In this section we have seen explicitly that this parameter incorporates the carbon-carbon distance as well as the orbital overlap between neighboring carbons. Notably, v_F causes the bands to change in energy as $\vec{k}$ is modulated, because neighboring carbons have different coordinates in the x-y plane. In the case of bilayer graphene, discussed in Section 2.10, there are also neighboring carbons that share the same coordinates in the x-y plane. As a result, the coupling between stacked carbons in bilayer graphene causes a $\vec{k}$-independent splitting in the bands. Additionally, this real space picture will be extended to the curvature of bilayer graphene's bands in the context of real-space hopping in section 2.11.

2.7 Approximating the Hamiltonian of Graphene

The off diagonal term in H are derived in Section 2.5 to be $-\gamma_0 f(\vec{k})$ where $f(\vec{k}) = 1 + 2e^{i\frac{3}{2}k_x a}\cos\left(\frac{\sqrt{3}}{2}k_y a\right)$, which can expanded around the K point $\frac{2\pi}{a}\left(\frac{2}{3\sqrt{3}}\right)$ to yield

$$f(\vec{k}) \approx 1 + 2\left(1 + i\frac{3}{2}k_x a\right)\left(-\frac{1}{2} - \frac{\sqrt{3}a}{2}\sin\left(\frac{2\pi}{3}\right)\right) \tag{2.21}$$

Simplifying the above expression,

$$f(\vec{k}) \approx \tilde{z}(k_x a + ik_y a) \tag{2.22}$$

where $\tilde{z} = 3i/4$ is a phase factor. Therefore, the Hamiltonian matrix at low energies can be approximated as

$$H = \hbar v_F \begin{bmatrix} 0 & k_x - ik_y \\ k_x + ik_y & 0 \end{bmatrix} \tag{2.23}$$

Introducing a new parameter $v_F = \left(\frac{3}{2}\right)\frac{\gamma_0 a}{\hbar}$ with units (m/s) that is deemed the "Fermi velocity." The Hamiltonian now has the form $H = v_F\vec{\sigma}\cdot\vec{p}$ where $\vec{\sigma}$ is a 2-component vector of 2 x 2 Pauli spin matrices and $\vec{p} = \hbar\vec{k}$ is the crystal momentum. A similar approximation around the K' point, yielding a Hamiltonian with the same form.

The associated eigenvalue spectrum is $E_k = \hbar v_F|k|$, indicating graphene's low energy bands follow a linear dispersion. In typical semiconductor systems, the electron mobility can be attributed to how easily electrons move throughout a sample. In the absence of disorder, the mobility is limited by the charge carrier's effective mass, given by $m^* = \left(\frac{d^2E_k}{dk^2}\right)^{-1}$. In graphene, $\left(\frac{d^2E_k}{dk^2}\right) = 0$, so the charge carriers in graphene mimic relativistic particles with zero rest mass that travel at an effective "speed of light" $v_F \approx c/300$.

2.8 Calculating the Density of States

As discussed in Chapter 1, the density of electronic states DOS is a directly calculable quantity that underpins material properties and physical phenomena. Formally, the thermodynamic DOS at energy E describes how many electronic states exist between energies E and $E + dE$. Just as mass density can be integrated over a space interval to find a total mass, the DOS is integrated over an energy range to find the total number of states in that energy range. Specifically,

$$N = \int_{-\infty}^{\infty} g(E)dE \tag{2.24}$$

From the dispersion relation,

$$N = \int_{0}^{\infty} dN \tag{2.25}$$

In a 1-D box of length L, the nth mode can be calculated by $n = Lk/\pi$, where $k = 2\pi/\lambda$. In a d- dimensional (hypercubic) box, the relation changes to $n = \left(\frac{Lk}{\pi}\right)^d$. The above integral can be changed into

$$N = \left(\frac{L}{\pi}\right)^d \int_{0}^{k_{max}} d^d k \tag{2.26}$$

$$N = \left(\frac{L}{\pi}\right)^d A_d \int_{0}^{k_{max}} k^{d-1} dk \tag{2.27}$$

Where A_d is the solid angle in d dimensions. The dispersion relation E_k can be substituted into the above relation to yield an integral over energy. Assuming a generic dispersion relation $E_k = \alpha k^\beta$, the integral becomes

$$N = \left(\frac{L}{\pi}\right)^d A_d \int_{0}^{E_F} \left(\frac{E}{\alpha}\right)^{\frac{d-\beta}{\beta}} dE \tag{2.28}$$

Where E_F is the Fermi level or chemical potential (the two are equivalent at T = 0 K). The integrand of the above expression is the DOS. Graphene is a 2D system ($d = 2$) with a linear dispersion relation ($\beta = 1$) at low energies. Therefore, graphene's density of states can be approximated as linear. Due to the linear density of states, the number of charges in graphene increases as the square of the energy. Typically, in experiment,

the charge density is an independent parameter and the chemical potential is either measured or inferred. The relevant expression is then $E_F = \hbar v_F \sqrt{\pi n}$.

A simple analogy relates the density of states to a peculiarly shaped container of water. As water is poured into the container, the total volume water increases, as does its level. While the water volume is independent of the shape of container, the height certainly depends on the shape. In the analogy, volume is the total charge density n and the water level is the chemical potential μ. As conventional 2DEG DOS is much like a conventional cylindrical juice glass, while graphene's linear DOS is more akin to a martini glass—much more exciting. Analogies aside, two important ingredients gave rise to graphene's anomalous DOS expression reflect: charges in graphene travel in two dimensions, and the travel with a linear dispersion. In Section 2.17, we will see how this unique behavior effects electric field screening in graphene.

2.9 Massless Dirac Fermions in the Quantum Hall Regime

Interestingly, graphene's low energy Hamiltonian $H = v_F \vec{\sigma} \cdot \vec{p}$ is a specific instance of the Dirac Hamiltonian in two dimensions.[5] The Dirac equation $(v_F \vec{\sigma} \cdot \vec{p} - i\hbar\partial_t)\Psi = 0$ is used in high energy physics to describe the behavior of ultra-relativistic particles.[6] The eigenfunctions in the massless 2D case are two-component spinors with a momentum-dependent phase factor that can be expressed $\Psi = e^{i\vec{k}\cdot\vec{r}} \begin{bmatrix} 1 \\ \pm e^{i\theta} \end{bmatrix}$ and eigenvalues $E_p^{\pm} = \pm \hbar v_F |\vec{k}|$. In the Dirac equation, the chirality operator $\vec{\sigma} \cdot \vec{p}$

commutes with H and is thus conserved. In quantum field theory, $\vec{\sigma} \cdot \vec{p}$ projects spin onto momentum. Recognizing that the low energy eigenfunctions in graphene are in the unit cell orbital basis $\{\phi\}$ necessitates an analog of real spin called "pseudospin"—a 2 component spinor that encodes electron occupation in the unit cell. The pseudo spin degree of freedom has two major implications: (1) particles are prohibited from backscattering when incident on a barrier that preserves the structure of H (a phenomenon known as Klein tunneling); and (2) particles gain a phase of π (known as a Berry's phase) following a closed, adiabatic traverse of phase space. Effect (1) contributes to the exceptionally high conductivity observed in graphene, while effect (2), discussed below, has implications in the quantum Hall regime.

Upon completion of an adiabatic closed path in reciprocal space, charges in conventional two-dimensional electron gases (2DEG) gain an undetectable 2π Berry's phase. Along a similar closed loop, however, iso-relativistic Fermions in graphene accumulate a π Berry's phase that causes observable interference phenomena. The difference in winding number can be attributed to the pseudospin degree of freedom arising from graphene's Dirac nature.[7] Closed loops in momentum space can be associated with cyclotron orbits about a perpendicular magnetic field.

At low B, room temperature or in samples with high electron density or disorder, semiclassical electrons lose their quantum phase information to scattering events before an orbit is completed. In ultra clean samples or at high B, however, unimpeded orbits coalesce to form quantum states known as Landau levels (LLs). These LLs have been extensively studied in semiconductor-based two-dimensional

electron gases (2DEGs). Graphene systems also show Landau quantization at accessible magnetic fields ($B \approx 1\,T$) with the intriguing twist of a nontrivial Berry's phase. In each cyclotron orbit, semiclassical electrons travel adiabatically around a closed loop in momentum space. In the case of graphene, the completion of this loop tacks a Berry's phase onto the wave function, causing it to deviate from the ordinary LL spectrum of the 2DEG.

In order to explore the behavior of massless chiral particles in a perpendicular B, we derive the LL spectrum for graphene. In the presence of an external magnetic field $\vec{B} = B\hat{z}$, classical charged particles confined to travel in the x-y plane undergo cyclotron orbits. The Hamiltonian $H = \frac{\pi^2}{2m}$, where $\pi = \vec{p} - q\vec{A}$ is the canonical momentum and the vector potential $\vec{A} = (0, -Bx, 0)^T$ is taken in the Landau gauge. When expanded out, $H = \frac{1}{2m}\left(p_x^2 + p_y^2 - 2qBp_y x + q^2B^2x^2\right)$ is similar to the Hamiltonian for a harmonic oscillator, with a kinetic term and a potential term that goes as the square of the position. In fact, with the introduction of coordinate $X = x - p_y/m\omega_c$, where $\omega_c = qB/m$ is recognized as the cyclotron frequency, $H = \frac{p_x^2}{2m} + \frac{1}{2}m\omega_c^2X^2$ is *identical* to the Hamiltonian of the 1D harmonic oscillator. Indeed, solving Hamilton's relations yields the expected periodic motion where oscillations in the x and y direction have a phase difference of $\pi/2$. The resulting trajectories are cyclotron orbits in the x-y plane.

The quantum mechanical picture of 2D cyclotron motion is easily adapted from the classical Hamiltonian. First, position and momenta are replaced with Hermitian

operators $\hat{p}$ and $\hat{X}$ that have the canonical commutation relation $\left[\hat{X}_i, \hat{p}_j\right] = i\hbar\delta_{ij}$. Rather than solve for the equations of motion, our goal becomes to solve the Schrödinger equation, yielding the energy eigenfunctions (orbitals) and eigenvalues (spectrum). Recognizing the similarities to the classical harmonic oscillator enables us to solve for the energy spectrum by "factorization" of the H into a product of ladder operators—a direct result of the symmetry of the Hamiltonian. The final result, $H = \hbar\omega_c(a^\dagger a + \frac{1}{2})$ yields eigenvalues that are evenly spaced by a cyclotron gap energy $\hbar\omega_c$. The corresponding wave functions are written:

$$\psi_n = A_n \mathcal{H}_n\left(\hat{X}\right) \exp\left(-\frac{\hat{X}^2}{2} + \frac{ip_y y}{\hbar}\right) \tag{2.29}$$

where $\hat{X} = \frac{x}{\lambda_B} - \frac{p_y \lambda_B}{\hbar}$ is the x-coordinate of the cyclotron center, normalized by the magnetic length $\lambda = \sqrt{\hbar/eB}$, and shifted constant of motion $\frac{p_y \lambda_B}{\hbar}$. [8–11] As determined by the symmetry of H, the eigenfunctions ψ_n are each products of a harmonic oscillator eigenfunction (which is a gaussian scaled by a Hermite polynomial $\mathcal{H}_n$) in the x direction and a plane wave in the y direction.

A similar treatment can be applied to Landau quantization in graphene.[12] When a perpendicular B is applied, the low-energy Hamiltonian remains a 2x2 matrix of the form $H = v_F \vec{\sigma} \cdot \vec{\pi}$, with off diagonal terms $p_x \pm ip_y$ shifted to canonical momentum $\pi = \vec{p} - e\vec{A}$ by the vector potential $\vec{A}$:

$$H = v_F \begin{bmatrix} 0 & \pi^\dagger \\ \pi & 0 \end{bmatrix} \tag{2.30}$$

Adopting the Landau gauge introduced above, $\pi = p_x + ip_y - eBxp_y$. As discussed above, translations in the x direction $\tau(x)$ leave H unchanged $[H, \tau(x)] = 0$. It is then convenient to express the eigenfunctions Ψ in terms of the (orthonormal, complete) basis $\{\psi_n\}$. The resulting wave function will generally have separate amplitudes on the A and B carbon sites. Therefore, $\Psi = (\alpha\psi_n, \beta\psi_m)^T$ in the atomic site basis.

Recognizing another connection to the quantum harmonic oscillator (albeit, in a massless case), we again adopt a ladder operator method to determine the Landau level (eigenvalue) energies. The operators π and $\pi^\dagger$ are linear combinations of momentum and position operators, as are a and $a^\dagger$. As a result, $\pi\psi_n = -\frac{\sqrt{2}i\hbar}{\lambda_B}\sqrt{n}\psi_{n-1}$, and $\pi^\dagger\psi_n = \frac{\sqrt{2}i\hbar}{\lambda_B}\sqrt{n+1}\psi_{n+1}$. Clearly, canonical momenta π and $\pi^\dagger$ are proportional to ladder operators a and $a^\dagger$. Therefore, the Schrödinger equation for cyclotron orbits in graphene can be rephrased as[13]

$$\pi\alpha\psi_n = E\beta\psi_m \qquad \pi^\dagger\beta\psi_m = E\alpha\psi_n$$

$$\alpha\frac{\sqrt{2}i\hbar}{\lambda_B}\sqrt{n}\,\psi_{n-1} = E\beta\psi_m \qquad -\beta\frac{\sqrt{2}i\hbar}{\lambda_B}\sqrt{m+1}\,\psi_{m+1} = E\alpha\psi_m$$

$$E = \mathrm{sgn}(n)\hbar v_F\sqrt{2eB|n|}, \quad n \in \mathbb{Z} \tag{2.31}$$

$$\Psi_{n\neq 0} = \frac{1}{\sqrt{2}}\begin{bmatrix}\psi_n \\ \psi_{n-1}\end{bmatrix} \tag{2.32}$$

$$\Psi_{n=0} = \begin{bmatrix} \psi_0 \\ 0 \end{bmatrix} \tag{2.33}$$

Note that the quantum harmonic oscillator in the massive case had a Hamiltonian proportional to $a^\dagger a + 1/2$, and thus had an eigenvalue spectrum with equally spaced levels separated by the proportionality constant $\hbar\omega$, in the case of 2D massless Dirac fermions the "ladder operators" act individually on components on the wave function. As a result, the eigenvalues are not proportional to index n, but proportional to $\sqrt{n}$. Additionally, there is an intriguing zero-point energy that arises from the structure of the Hamiltonian. Specifically, there is a nontrivial cyclotron orbital ($\psi_0, 0$) that is carbon-site specific in a given valley. When this polarized ground state is acted on with H, an eigenvalue of zero is returned.

2.10 Bilayer Graphene Tight Binding Calculation

Bernal stacked bilayer graphene (BLG) is composed of two layered graphene sheets arranged so that the B site of the top layer lies directly above the A site of the bottom layer. Figure 2.7 depicts bilayer graphene, where pink and orange circles are sites A_1 and B_1 in the top layer, white and gray circles are A_2 and B_2 sites in the bottom layer. Note that B_1 sites rest directly above A_2 sites, blocking them from view in the schematic. With the same honeycomb structure and in-plane carbon-carbon bond length a as graphene, BLG can similarly be expressed with a hexagonal Bravais lattice (with lattice vectors $\vec{R}_1$ and $\vec{R}_2$) that underpins a repeating unit cell. In BLG, however, the unit cell is composed of 4 distinct carbon $2p_z$ orbitals, each residing on a different

site. Therefore, BLG's Hamiltonian H can be expressed in the $|\phi_{2p_z}\rangle$ basis as a 4 x 4 matrix with diagonal entries that correspond to onsite energies, and off diagonal entries overlap $2p_z$ orbitals on neighboring sites.

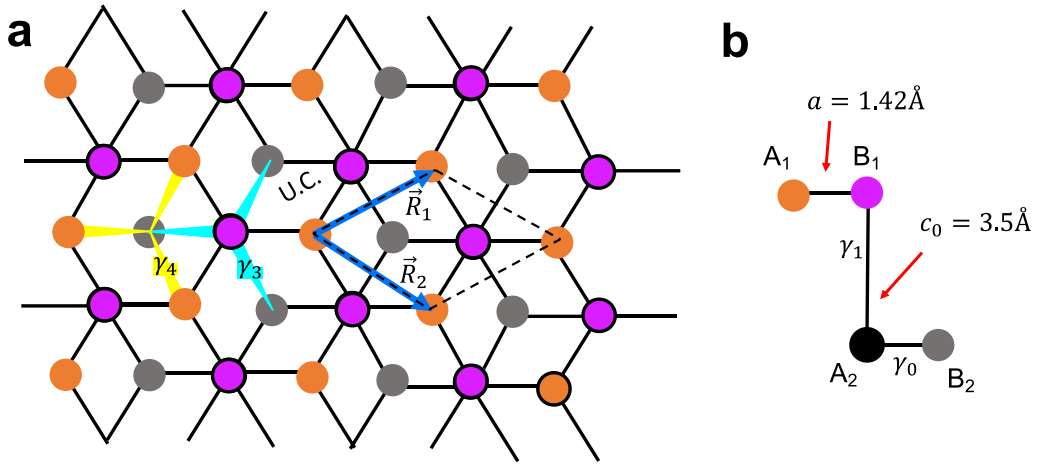

Figure 2.7: The BLG lattice and hopping parameters. (a) Bilayer graphene's unit cell, outlined with a black, dashed line, consists of four carbon atoms: sites A_1 and B_1 in the top layer, shown as orange and magenta circles, respectively and sites A_2 and B_2 in the bottom layer, shown as black and gray circles, respectively. Note that the black A_2 sites are eclipsed by the pink B_1 sites. Blue arrows define the hexagonal lattice vectors $\vec{R}_1$ and $\vec{R}_2$ which are identical to those in graphene. Repeated translations of the unit cell (outlined with a black, dashed perimeter) by integral combinations of $\vec{R}_1$ and $\vec{R}_2$ build the BLG lattice. (b) An alternate sideview schematic of atomic sites in the BLG unit cell with intralayer hopping γ_0 and dimer site hopping γ_1 depicted as black lines. Additional skew hopping terms γ_3 and γ_4 are depicted in (a) as cyan and yellow

wedges, respectively. For example, the narrow side of yellow wedges attach to the top of the bottom-layer site B_2 and fat side of yellow wedges attaches to the underside of top layer sites A_1.

As a first approximation, coupling between BLG's top and bottom sheets occurs only at the B_1-A_2 dimer. The Hamiltonian can then be built from two identical 2 x 2 matrix blocks that encode electron hopping in each individual sheet (intralayer hopping). These two blocks are coupled with a single off diagonal element γ_1 that expresses the coupling at the dimer sites. Setting all identical onsite energies to zero the approximated Hamiltonian is expressed[14,15]

$$H = \begin{bmatrix} 0 & -\gamma_0 f(\vec{k}) & 0 & 0 \\ -\gamma_0 f^*(\vec{k}) & 0 & \gamma_1 & 0 \\ 0 & \gamma_1 & 0 & -\gamma_0 f(\vec{k}) \\ 0 & 0 & -\gamma_0 f^*(\vec{k}) & 0 \end{bmatrix} \tag{2.34}$$

The corresponding eigenvalues are

$$E_k = \pm\sqrt{\frac{\gamma_1^2}{4} + \gamma_0^2\left|f(\vec{k})\right|^2} + \alpha\frac{\gamma_1}{2} \tag{2.35}$$

where $f(\vec{k})$ retains its form discussed in Section 2.5, and $\alpha = \pm 1$. As in the case of graphene, the phase dependence of intralayer hopping $f(\vec{k})$ vanishes at the K and K' points in reciprocal space. At these points, $E_k = \pm\frac{\gamma_1}{2} + \alpha\frac{\gamma_1}{2}$. Two of the bands become degenerate at zero energy, and the remaining two bands, termed the "high energy bands (HEB)" are shifted in opposite directions by the dimer site coupling γ_1. This splitting

of HEB and HEB* follows from the covalent bonding discussion in Section 2.2; the A_2 and B_1 sites form bonding and antibonding orbitals that are split by twice their coupling γ_1.

Figure 2.8(b) demonstrates the modulation of γ_1, which is schematized by a pink unit cell line in in the inset. The four BLG bands near the K point are shown when $\gamma_1 = 0.25$ and $\gamma_1 = 0.5$ eV (and all other hopping parameters are specified in the "default values" key) as orange solid lines and blue dashed lines, respectively. As expected from the above discussion, the blue dashed HEB and HEB* bands are each closer to zero than their orange counterparts, showing that γ_1 controls the magnitude of splitting between HEB and HEB*.

2.11 Bilayer Graphene Band Shape and the Density of States

At low energies, BLG's bands are nearly parabolic. This can be seen by first replacing $\gamma_0|f(\vec{k})|$ with $\hbar v_F|\vec{k}|$, an approximation that is outlined in Section 2.7. Assuming that $\hbar v_F\left|\vec{k}\right| \ll \gamma_1$, a truncated Taylor series expansion of Eq. 2.35 yields $E_k \approx \pm\frac{(\hbar v_F)^2}{\gamma_1}\left|\vec{k}\right|^2$. In the case of graphene, linear bands near K and K' are equated with massless charges traveling at speed v_F. Remembering that the effective mass determines band curvature: $m^* = \left(\frac{d^2E_k}{dk^2}\right)^{-1}$, BLG's charges have an effective mass determined by the dimerization of A_2 and B_1 sites. Specifically, $m^* = \frac{2(\hbar v_F)^2}{\gamma_1}$. Inserting

the original expression for v_F, the effective mass can be written as a ratio of intra and interlayer hopping parameters: $m^* = \frac{\gamma_1}{2v_F^2} = \left(\frac{2\hbar^2}{9a^2}\right)\frac{\gamma_1}{\gamma_0^2}$.

It is instructive to take a pause and compare the differences in band shape between monolayer and bilayer graphene. In a single graphene sheet, the low energy bands are approximated as conical, and thus the concept of an effective mass does not apply. In BLG, the bands are curved, with a conventional effective mass. Reverting to our real space representation of the high symmetry momenta in graphene introduced in Section 2.6, we must note that there is carbon-carbon coupling in BLG that is independent of $\vec{k}$. Naively, we can then imagine semiclassical charges emanating through BLG's lattice by first hopping between adjacent carbon atoms in each plane, acquiring energy $-v_F\pi$, but also hopping between layers, with energy cost γ_1. The resulting "and" statement for all energy changing possibilities results in energy change $v_F^2\pi^2/\gamma_1$. This energy dispersion maps readily onto classical particle, where the mass is given as $\frac{\gamma_1}{2v_F^2}$. One interpretation that follows attributes the emergence of a mass from the nearly planar symmetry of bilayer graphene being broken by the dimer-site coupling term [ref?].

In deriving the above expression for band shape, we made several large assumptions: firstly, we assumed that the diagonal elements of *H* are all identical; and secondly, we assumed that dimer site hopping between A_2 and B_1 sites is the sole coupling between individual graphene layers. These two assumptions are relaxed sequentially over the next two sections. Nonetheless, the effective mass picture in BLG

gives a first approximation at the low energy spectrum. The low energy DOS can be acquired from Eq. 2.28 where $d = 2$ and $\beta = 2$. The resulting expression for the BLG DOS is constant $g(\varepsilon) = m/2\pi\hbar^2$, exactly twice what we calculate for a conventional 2DEG, due to the additional 2-fold valley degeneracy in BLG.

After calculating the DOS, we integrate it to find the Fermi level E_F as a function of charge density n. Reverting to our water analogy in Section 2.8, unlike the Martini glass DOS of monolyer graphene, BLG has a DOS that is roughly constant. Thus we expect that as charge is added linearly to BLG, its Fermi energy will increase linearly. In Chapter 6, we will use this heuristic argument as a jump-off point to extract the BLG DOS parameters in a novel way: by watching the "juice glass" fill and track the "water height." From the shape of the container we will deduce its shape.

2.12 Electron-Hole Asymmetry γ_4 and Trigonal Warping γ_3

In addition to dimer site and intralayer hopping γ_0 and γ_1, there can also be skew hopping between neighboring carbon atoms. Figure 2.7(a) depicts skew hopping terms γ_3 and γ_4 as yellow and cyan wedges, respectively. The wedges represent out of plane hopping between B_2 and B_1 in the case of γ_3 or B_2 and A_1 in the case of γ_4. Because skew hopping occurs between sites with different x-y coordinates, both γ_3 and γ_4 are modulated by phase factor $f(\vec{k})$ as they populate the off diagonals of H. As discussed in Section 2.6, the cause of this phase modulation is the momentum $\hbar\vec{k}$ of electronic states superimposed on 4 offset hexagonal lattices.

Skew hopping between identical sites in different graphene layers, quantified by $\gamma_3 f(\vec{k})$, causes trigonal warping in the BLG band structure.[5] The simple BLG band structure introduced in Section 2.10 has approximately parabolic bands assuming $a|\vec{k}-\vec{K}| \ll 1$ (for example, $a|\vec{k}-\vec{K}| = 0.1$ when $E_k \approx \pm 0.7$ eV). While the isoenergetic lines in this regime are circular, they exhibit C_3 symmetry at higher energies, conforming to the symmetry of $f(\vec{k})$. The trigonal transition is readily visible in Fig. 2.5(a). In addition to the built-in C_3 character of graphene and BLG bands at high energy, there is another source of trigonal warping even at low energies in BLG. This low energy trigonal warping is caused by γ_3. While trigonal warping hosts interesting physics such as a Lifshitz transition and Fermi pockets, the experimental technique employed in this thesis is not sensitive to the ~0.1 meV energy scales on which these effects are relevant, nor are the techniques sensitive to the shape of the band structure in momentum space. For this reason, we include previously reported values of γ_3, but do not attempt to extract its value from our experiments.

The final hopping parameter, γ_4 effects the curvature of BLG's valence and conduction bands. Fig. 2.8(c) demonstrates this effect near the K point, where γ_4 is represented by a magenta line in the inset. The four BLG bands near the K point are shown when $\gamma_4 = 0$ and $\gamma_4 = 0.25$ eV as orange solid lines and blue dashed lines, respectively. Notably, the blue π band is wider than its orange counterpart, whereas the blue π^* band is narrower than its orange counterpart. Following the effective mass discussion in Section 2.11, it can be concluded that increasing γ_4 results in a higher effective mass in the valence band than in the conduction band. Unlike trigonal warping

due to γ_3, asymmetry γ_4 between the masses of electrons and holes can be probed directly by measuring the BLG DOS. Interestingly, the effect seems to be revered for the HEB and HEB*. For example, Fig. 2.8(c) shows that the curvature of the π band *decreases* and the curvature of the HEB *increases* as γ_4 is increased from 0 to 0.25. This may have implications at very low charge densities, for instance, when the Fermi level occupies both π and HEB, which endow charges with different effective masses.

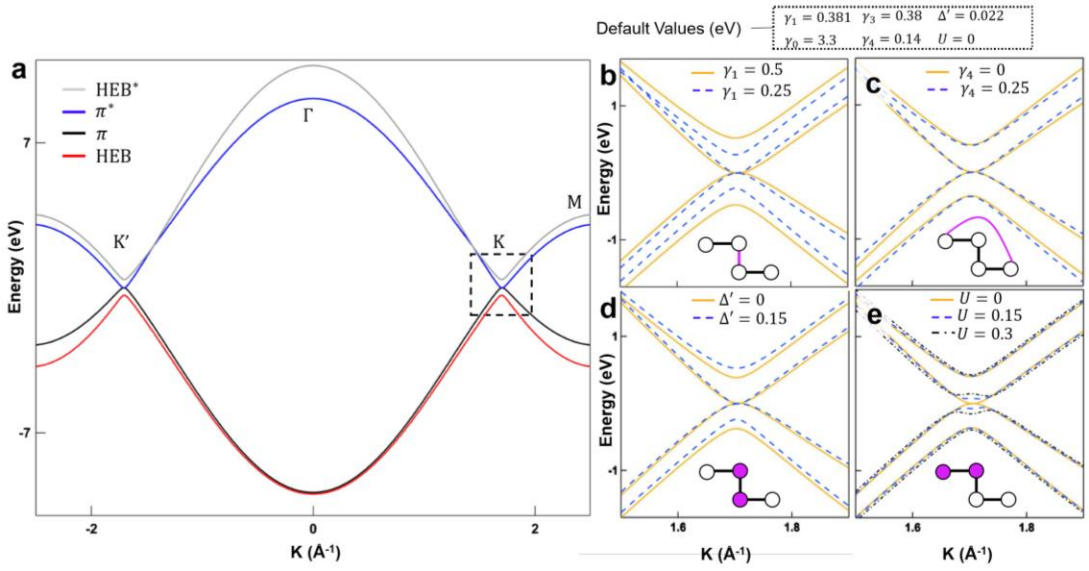

Figure 2.8: Dependence of the BLG band structure on hopping energies. (a) Bilayer graphene's four relevant bands: high energy bands from dimer site coupling (HEB and HEB* shown in red and gray, respectively), and π bonding and antibonding orbitals (π and π^*, shown in black and blue, respectively). (b) Modulation of dimer site hopping parameter γ_1, schematized by a pink vertical line connecting sites B_1 and A_2 in the inset unit cell. The four BLG bands near the K point are shown when $\gamma_1 = 0.5$ and $\gamma_1 = 0.25$ eV as orange solid lines and blue dashed lines, respectively. The blue dashed HEB and HEB* bands are each closer to zero than their orange counterparts.

(c) Modulation of skew hopping parameter γ_4, schematized by a pink unit cell line in in the inset. The four BLG bands near the K point are shown when $\gamma_4 = 0$ and $\gamma_4 = 0.25$ eV as orange solid lines and blue dashed lines, respectively. The blue π band has less curvature than its orange counterpart, whereas the blue π^* band is more curved than its orange counterpart. (d) Modulation of *intrinsic* onsite energy difference Δ', schematized by pink circles at sites B_2 and A_1. The four BLG bands near the K point are shown when $\Delta' = 0$ and $\Delta' = 0.15$ eV as orange solid lines and blue dashed lines, respectively. Blue and orange π and π^* bands are nearly identical. However, the blue HEB and HEB* are uniformly shifted upward from their orange counterparts. (e) Modulation of *extrinsic* onsite energy difference U, schematized by pink circles at sites A_1 and B_1. The four BLG bands near the K point are shown when $U = 0$, $U = 0.15$, and $U = 0.3$ eV as orange solid lines, blue dashed lines, and black dashed-dotted lines, respectively. Blue, orange and black HEB and HEB* are nearly identical. However, while orange π and π^* bands touch at the K point, there is a gap between their blue and black counterparts. Notably, gap in the black lines is in the shape of a "Mexican hat." Unless otherwise stated the parameters used to calculate low energy band structure in Figs. (b)-(e) are listed in the "default values" key.

2.13 Intrinsic and Extrinsic Onsite Energy Differences and the Tunable Band Gap

In the previous two sections, BLG was treated as two coupled graphene sheets. Here, we relax the assumption that onsite energies are not identical within a unit cell. There are two cases where this becomes relevant: (1) intrinsic; and (2) extrinsic asymmetry between sites in the unit cell. In the first case, it is reasonable to assume that BLG's two constituent graphene sheets are identical. Therefore, the unit cell presented in Fig. 2.7(b) has an inversion center and the only onsite energy difference should arise between A and B sites within a given layer. The parameter $\Delta' = \frac{1}{2}(\varepsilon_{B_1} + \varepsilon_{A_2} - \varepsilon_{A_1} - \varepsilon_{B_2})$ quantifies the energy difference between non-dimer and dimer sites. In the case where an inversion center is present, the energies at sites A_1, A_2, B_1, B_2 are $(0, \Delta', \Delta', 0)^T$. Evaluated at the K and K' points, Hamiltonian becomes

$$H = \begin{bmatrix} 0 & 0 & 0 & 0 \\ 0 & \Delta' & \gamma_1 & 0 \\ 0 & \gamma_1 & \Delta' & 0 \\ 0 & 0 & 0 & 0 \end{bmatrix} \tag{2.36}$$

with eigenvalues $E_{K(K')} = \Delta' \pm \gamma_1, 0$, where 0 is 2-fold degenerate. This picture affords a simple interpretation: at both K and K' points, two of the four BLG bands touch and the remaining two (HEB and HEB*) are split by energy $2\gamma_1$. Specifically, the HEB (bonding orbital) and HEB* (antibonding orbital) reside at energies $-(\gamma_1 - \Delta')$ and $\gamma_1 + \Delta'$. In essence, the central 2 x 2 block of H has a bonding and antibonding orbital of its own, that are split by energy $2\gamma_1$ and offset by Δ'. It follows that Δ' induces an electron-hole asymmetry.

Figure 2.8(d) demonstrates the modulation of Δ', which is schematized by magenta circles at sites B_2 and A_1 in the inset. The four BLG bands near the K point are shown as orange solid lines and blue dashed lines when $\Delta' = 0$ and $\Delta' = 0.15$ eV, respectively. While the blue and orange π and π^* bands are nearly identical, the blue HEB and HEB* are uniformly shifted upward from their orange counterparts. This agrees with the above interpretation, including in regions where around the K point.

One compelling attribute of BLG is its tunable layer symmetry. In the above discussion, the BLG unit cell is assumed to have inversion symmetry. In the presence of an external electric field, inversion symmetry is broken and the diagonal terms in H change accordingly. Assuming an layer potential difference $U = \frac{1}{2}(\varepsilon_{A_1} + \varepsilon_{B_1} - \varepsilon_{A_2} - \varepsilon_{B_2})$ between layers, the Hamiltonian at K and K' becomes

$$H = \begin{bmatrix} U/2 & 0 & 0 & 0 \\ 0 & U/2 & \gamma_1 & 0 \\ 0 & \gamma_1 & -U/2 & 0 \\ 0 & 0 & 0 & -U/2 \end{bmatrix} \tag{2.37}$$

with eigenvalues $E_{K(K')} = \pm\frac{U}{2}, \pm\sqrt{\gamma_1^2 + U^2/4}$,

The second set of eigenvalues can be approximated as $\gamma_1\left(1 + \frac{1}{8}\left(\frac{U}{\gamma_1^2}\right)\right)$. Typical experimental ranges of U are < 100 meV, whereas $\gamma_1 \approx 400$ meV. Therefore, at K and K' points, two of BLG's four bands straddle the $2p_z$ orbital energy (set to zero here for

convenience) at energies $\pm U/2$ and the HEB and HEB* lie above and below at energies $\pm\gamma_1$.

Figure 2.8(e) illustrates the modulation of *extrinsic* onsite energy difference U, which is schematized in the inset by magenta circles at unit cell sites A_1 and B_1. The four BLG bands near the K point are shown when $U = 0$, $U = 0.15$, and $U = 0.3$ eV as orange solid lines, blue dashed lines, and black dashed-dotted lines, respectively. The blue, orange and black HEB and HEB* are nearly identical. However, while orange π and π^* bands touch at the K point, there is a gap U between their blue and black counterparts. Notably, the application of an electric field perpendicular to the BLG plane changes U. Therefore, the symmetry of the BLG unit cell can be tuned *in situ*, resulting in drastic changes to the BLG electronic structure.[15] Importantly, an electric field is partially screened by BLG layer asymmetry, resulting in a lower gap than expected.[16] The role of screening in BLG is discussed further in Chapter 7.

The extrinsic onsite energy difference U can be tuned with a perpendicular displacement field. Figure 2.9 shows a schematic of bilayer graphene that is separated from top and back gate electrodes by insulators with thicknesses d_t and d_b and relative permittivities ϵ_t^r and ϵ_b^r (the superscript r reminds us that these parameters are unitless). Potential differences on either one of the gate electrodes V_t or V_b will induce a charge asymmetry in the layers $n_t - n_b \neq 0$ (with more charge on the layer closer to the respective electrode), with the individual sheet densities directly related to the displacement fields from the top and back gates. Following a now standard convention for BLG, we define $D = (D_t + D_b)/2$ Where $D_t = \epsilon_t^r V_t/d_t$, which has units of V/nm

(a factor of ϵ_0 relates D_t to the conventional displacement field in this convention).[17–20]

From Gauss's law, the charge asymmetry induces an associated electric field between the BLG sheets is $E = \frac{e}{2\epsilon_r\epsilon_0}[n_t - n_b]$ where ϵ_r is the relative permittivity of bilayer graphene. The potential energy difference between sheets can then be expressed as

$$U = ec_0E = \frac{e^2c_0}{2\epsilon_r}\left[\frac{\epsilon_b^r}{d_b}V_b - \frac{\epsilon_t^r}{d_t}V_t\right] \tag{2.38}$$

The coefficient that includes the graphene sheet spacing (c_0) and ϵ_r can be grouped together following a more general convention into a screening parameter $\alpha = \frac{ec_0}{2\epsilon_r}$. In general, the amount of total charge on the layers $n_t + n_b$ effects the relation between the charge asymmetry and the interlayer energy difference. Screening between BLG sheets is accounted for by either self-consistently calculating α with tight binding, or using more involved ab-initio calculations.[15,16]

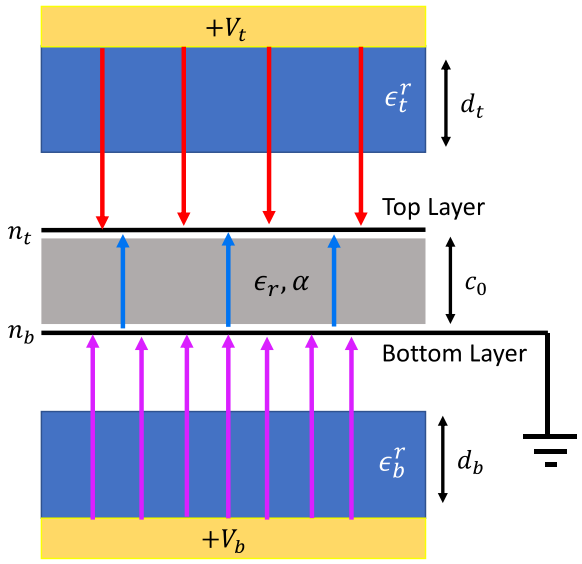

Figure 2.9: Tuning layer symmetry with a displacement field. (a) Top and bottom layers of bilayer graphene (BLG), shown as parallel black lines, are separated by a distance c_0. Each layer has a different charge density, n_t or n_b, induced by the electrode closer to that layer. The electric field between the layers is related to the charge difference between the layers, as well as the relative permittivity of the BLG itself (ϵ_r). To first order, ϵ_r is inversely related to α, a directly calculable quantity.

In Sections 2.12 and 2.13, we introduced additional nearest neighbor hopping parameters and onsite energy differences to the basic Hamiltonian from Section 2.10. Including these extra features, the general form of BLG's tight binding Hamiltonian H is:

$$H = \begin{bmatrix} \varepsilon_{A1} & -\gamma_0 f(\vec{k}) & \gamma_4 f(\vec{k}) & -\gamma_3 f(\vec{k}) \\ -\gamma_0 f^*(\vec{k}) & \varepsilon_{A1} & \gamma_1 & \gamma_4 f(\vec{k}) \\ \gamma_4 f^*(\vec{k}) & \gamma_1 & \varepsilon_{B1} & -\gamma_0 f(\vec{k}) \\ -\gamma_3 f^*(\vec{k}) & \gamma_4 f^*(\vec{k}) & -\gamma_0 f^*(\vec{k}) & \varepsilon_{B2} \end{bmatrix} \tag{2.39}$$

where onsite energies are shifted to $\varepsilon_{A1} = -\frac{U}{2}$, $\varepsilon_{B1} = -\frac{U}{2} + \Delta'$, $\varepsilon_{A2} = \frac{U}{2} + \Delta'$, $\varepsilon_{B2} = \frac{U}{2}$. Figure 2.8(a) shows the corresponding energy eigenvalues. Comparing the full spectrum to that of graphene, shown in Fig. 2.5(a), it is clear that the bands have similar shape, and only deviate appreciably at the K and K' points. Next, we will focus on the BLG band structure at these points, in order to explore emergent massive Dirac fermions.

2.14 Bilayer Graphene Landau Level Spectrum

When a perpendicular magnetic field B is applied to BLG, the low energy Hamiltonian h can be written in terms of the conjugate momenta. Following the procedure outlined in Section 2.9, $\pi = p_x - ip_y - eBp_y$, where the problem is framed in the Landau gauge $(0, -Bx, 0)^T$. Recognizing that the Hamiltonian is invariant under y-translations, it is convenient to express the energy eigenfunctions Ψ in terms of Harmonic oscillator eigenfunctions $e^{-ik_y y}|n\rangle$.[8–10] The Schrodinger equation then becomes a system of two equations that couple the low energy and dimer sites:

$$\frac{c_1}{2m^*}(\pi^\dagger)^2 \sum_m \langle m|\Psi\rangle|m\rangle = c_2 E \sum_m \langle m|\Psi\rangle|m\rangle \tag{2.40}$$

Acting with ladder operator $\pi^\dagger$ and dotting both sides with the ket $\langle n|$,

$$\frac{c_1}{2m^*}\sqrt{(m+1)(m+2)}\sum_n\sum_m\langle m|\Psi\rangle\langle n|m+2\rangle = c_2E\sum_n\sum_m\langle m|\Psi\rangle|m\rangle\langle n|m\rangle \tag{2.41}$$

$$\frac{c_2}{2m^*}\sqrt{(n+1)(n+2)} = c_1E \tag{2.42}$$

Following the same procedure for the other of the two equation yields

$$\frac{c_1}{2m^*}\sqrt{(n)(n-1)} = c_2E \tag{2.43}$$

As a result, we find that the energy spectrum $E_n = \hbar\omega_c\sqrt{n(n-1)}$ and the corresponding eigenfunctions are $\frac{1}{\sqrt{2}}\begin{bmatrix}\psi_n\\ \psi_{n-2}\end{bmatrix}$.

2.15 Symmetry Breaking in the Quantum Hall Regime

Landau levels (LL) are ideal platforms for studying spontaneous symmetry breaking. Here we discuss the physics that underlies symmetry breaking in these quantum cyclotron orbits. At high B the low energy graphene dispersion relation, shown in Fig. 2.5(d), is sliced into isoenergetic contours. These contours are circular near the K and K' points and they are spaced by energy $E_n\hbar v_F\sqrt{2\pi nB}$ (derived in Section 2.9). As a result, kinetic energy is quenched—electrons are confined to travel within a state space contour and cannot disperse from one another. The implications of these discretized, dispersionless slices are profound. In the absence of kinetic energy, the mutual Coulomb repulsion between electrons $V = -\frac{ke}{<r>}$, which usually is

suppressed from screening, becomes the dominant energy scale.[11] With sufficient repulsion and no states to scatter into, electrons form correlated states wherein they spontaneously polarize.

Correlated electron behavior is exotic and complex. At first glance, however, one of its key characteristics—quantum polarization—is straightforwardly demonstrated by Hund's rules.[21] Take, for example, the ionization states of carbon's 6-fold degenerate 2p state. As electrons are added to the $n = 2, l = 1$ orbitals of a carbon atom, they tend to fill orbitals such that they are spin polarized. When the 2p state is half filled, electrons reside in separate m_l states and have aligning spin. Therefore, the electron configuration $1s^2 2s^2 2p^3$ is a *polarized* state. Notably, this polarization is due to two ingredients: (1) the state is antisymmetric with respect to exchange of particles; and (2) there is sufficient electrostatic repulsion between charges. Ingredient (1) is a necessary requirement for all fermions. Notably, the wave function can be antisymmetric under exchange of particles if it forms a Slater-type state that is antisymmetric in any of its degrees of freedom (spin or space in the case of the 2p state). Ingredient (2) then breaks degeneracy of all different occupations. As discussed in Section 2.2, the space-symmetric state will have a probability density that maximizes electrostatic repulsion potential. Conversely, the space-antisymmetric state has a lower energy of repulsion and is thus favorable. In the case of the 2p state, the result is spin polarization—the lower energy state is antisymmetric in space and is therefore symmetric in spin.

Quantum polarization due to exchange splitting is illustrated in Fig. 2.10(a), where the antisymmetric (blue) and symmetric (red) wave functions Ψ and their corresponding probability densities $|\Psi|^2$ are depicted in real space. The red wave function corresponds to spin-antisymmetric two electron state, which has a smaller mean electron-electron distance than the bottom state, leading to higher Coulomb repulsion energy. As a result, this system will spontaneously polarize into a spin-symmetric state (shown as the bottom state), giving rise to observable magnetic effects.

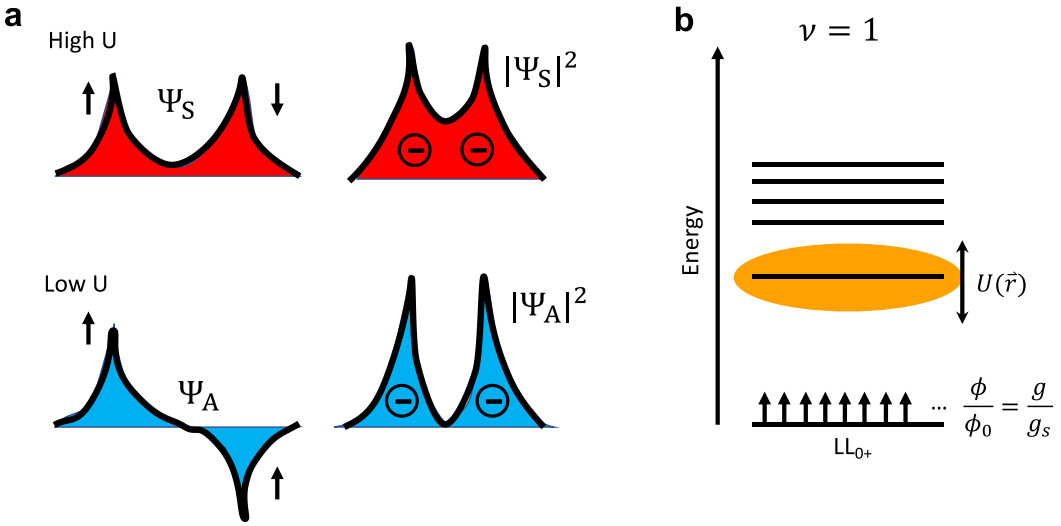

Figure 2.10 Exchange splitting and Landau level (LL) polarization. (a) Symmetric (red) and antisymmetric (blue) wave functions Ψ and their corresponding probability densities $|\Psi|^2$ in real space. The red wave function corresponds to spin-antisymmetric two electron state, which has a smaller mean electron-electron distance than the bottom state, leading to higher Coulomb repulsion energy. (b) Cartoon schematic of graphene's LL spectrum in the absence of disorder or temperature broadening. The orange oval around the N=1 LL depicts the scale of electron-electron Coulomb repulsion energy

$U(\vec{r})$. When filling factor $\nu = 1$, electrons are exchange-polarized: all electrons are in same valley (K, for example) and have the same spin (up, for example).

The above analogy can be generalized to systems with additional degrees of freedom. Low energy electrons in graphene and BLG occupy two possible spin states and two possible pseudospin (valley) states. In the absence of external fields, many-body interactions and disorder, the result is a 4-fold degeneracy. When confined to a specific Landau level, Coulomb repulsion can cause the degeneracy to be lifted, leading to spontaneous quantum polarization at specific filling factors. In the case of graphene, for instance, charges confined to Landau levels will spontaneously polarize into spin or valley antiferromagnets.[22,23] This effect is depicted in Fig. 2.10(b), where black horizontal lines represent LLs, with narrow linewidths indicating the lack of dispersion. An orange oval represents the dominant Coulomb repulsion energy scale, and upward pointing arrows represent spin-polarized electrons. Interestingly, the polarization of LLs does not depend on the external magnetic field, but on dominance of Coulomb repulsion within each quantum cyclotron orbit.

2.16 Electron-Electron Interactions and Fermi Velocity Renormalization

We conclude this chapter by investigating the abnormal nature of electron-electron interactions in graphene and one astounding implication: namely, Fermi velocity renormalization. Within a material, the bare coulomb interaction $V \propto 1/r$ between electrons is screened by the Fermi sea. In the Thomas-Fermi (TF) treatment

of low temperature screening the Coulomb potential due to a point charge inserted into the material is renormalized to be the Yukawa potential $V(\vec{r}) = \frac{q}{|\vec{r}|} e^{k_0|\vec{r}|}$, which diminishes faster than the Coulomb potential.[4] The characteristic screening length is inversely related to the TF wave vector $k_0 = 4\pi e^2 \rho(E_F)$, which is dependent on the density of states at the E_F. According to Fermi Liquid Theory, screening and scattering are determined by electrons near the Fermi level. Electrons at E_F are characterized by Bloch waves with wave vector k_F so it is instructive to determine the 2D Yukawa potential energy in terms of the k_F and k_0,

$$U(\vec{r}) = \frac{2\pi q^2}{\kappa}\left(\frac{1}{k_F + k_0}\right) \tag{2.44}$$

At first glance, it may appear that the screened potential energy decreases as charge is introduced into the system, (which raises k_F). However, k_F and k_0 are intricately tied together by both the dimensionality of the material and its dispersion relation. The denominator of Eq. 2.52 can be factored showing $U(\vec{r}) = k_F^{-1}(1 + k_0/k_F)^{-1}$, which is equivalent to adjusting the in-plane material permittivity by $\epsilon = 1 + k_0/k_F$. Notably k_0, which depends on the density of states is constant and $k_F \propto \sqrt{n}$, so as charge is added to the system, the relative permittivity decreases.[24] This counterintuitive result contrasts what is observed in 3D metals, where increasing charge density increases screening ($n \to \infty$, $\epsilon \to \infty$), as expected. As we would expect increased charge density to lead to metallic behavior ($n \to \infty$, $\epsilon \to \infty$). Clearly, the dimensionality of the system plays a major role in screening dynamics.

In graphene, the picture is even more surprising. Linear dispersion and two-dimensionality ensure that as charges are added to graphene, both k_F and $\rho(E_F)$ scale as $\sqrt{n}$. Therefore, the ratio k_0/k_F is constant, and the coulomb interaction is independent of n, resembling the bare 2D Coulomb repulsion $U(k_F)\sim 1/k_F$ with a renormalized coupling to the effective electromagnetic field. The resemblance between screened interaction in graphene and the bare coulomb repulsion motivates an analog of the fine structure constant with a solid-state context.

The Wigner-Seitz radius r_s in 3D metals characterizes how close electrons are to one another in real space. The generalized notion of an electron radius has close ties with the fine structure constant in QED, and indeed r_s—like the fine structure constant—is a ratio between the Coulomb energy, and the Fermi energy (the energy of a "Dirac sea" in QED, if you will). In graphene, the impact parameter can be calculated by noting that the interparticle distance (a function of n) determines the coulomb repulsion. Specifically, $U = q^2/(\kappa\langle r\rangle)$ where $\langle r\rangle = (n\pi)^{-1/2}$. Graphene's Fermi energy $E_F = v_F\hbar(n\pi)^{1/2}$ as well, so the ratio $r_s = U/E_F$ is a constant! This is quite counterintuitive. Essentially, as charges are added to graphene, there is no change in the screening length, nor is there a change in the coupling between electrons and their mutual repulsion. On an hBN substrate, $r_s = e^2/\kappa\hbar v_F \approx 0.8$, which pales in comparison to $r_s \approx 68.5/\sqrt{\tilde{n}}$ in BLG ($\tilde{n} = n/10^{12}$ cm^{-2}). Nonetheless, the small interaction parameter in graphene is independent of n, and robust against screening from nearby conductors.[24,25]

One implication of graphene's impact parameter r_s is the renormalization of the Fermi velocity v_F. In Section 2.5, tight binding was used to derive the single particle band structure for a single electron traveling through graphene. The resulting bands are conical near K and K' points, with parameter $v_F = 3\gamma_0 a/2\hbar$ defining the slope of the cone depending only on the carbon-carbon spacing a and hopping γ_0. As discussed above, electrons in graphene feel the presence of their counterparts on neighboring sites. A more realistic description of the dispersion relation comes from the Dyson equation, which accounts for scattering events via perturbation theory. The result of a many-body Greens function approach is accessible experimentally via the spectral function

$$A(\varepsilon, k) = \left(\frac{1}{\pi}\right) \frac{\mathrm{Im}\Sigma}{(\varepsilon - E_0(k) - \mathrm{Re}\Sigma)^2 + \mathrm{Im}\Sigma^2} \tag{2.45}$$

where $E(k)$ is the bare band dispersion, calculated in Section 2.5, and Σ is the complex self-energy. In essence, $A(\varepsilon, k)$, which is a Lorentzian centered at $\mathrm{Re}\Sigma$ with width $\mathrm{Im}\Sigma$, sifts and broadens the bare electron dispersion. The shift in energy can be calculated by Dyson series,[26]

$$E(k) = E_0(k) + \mathrm{Re}[\Sigma(E_0(k), k)] \tag{2.46}$$

in both the "on shell" or "off shell" approximation (depending on whether the sum is taken to infinity or truncated after the second term). Motivated by ultraclean transport measurements that showed fluctuations in graphene's cyclotron mass (not its effective mass!), Das Sarma, et. al.[26] predicted that the Fermi velocity $v_F^* = \partial E(k)/\partial k$ is subject to change as graphene is emptied of charge. In their work, Das Sarma, et. al. calculated

Σ series diagrammatically then showed that the Fermi velocity is subject to change at low n:

$$\frac{v_F^*(k)}{v_F} = \frac{1 + \frac{1}{v_0}\frac{\partial}{\partial k}\mathrm{Re}\Sigma(k,\omega)}{1 - \frac{1}{v_0}\frac{\partial}{\partial \omega}\mathrm{Re}\Sigma(k,\omega)} \tag{2.47}$$

where ω is evaluated at $E(k)$. The leading order term in the series evaluated at $k = k_F$ is

$$\frac{v_F^*}{v_F} = 1 - \frac{r_s}{\pi}\left[\frac{5}{3} - \ln(r_s)\right] + \frac{r_s}{4}\ln\left(\frac{k_c}{k_F}\right) \tag{2.48}$$

The ultraviolet cutoff $k_c = 1/a$ is a constant given by the carbon-carbon spacing. As discussed above, $r_s \approx 0.8$ so the first two terms in the above expression are constant. The final term changes as the negative log of k_F. The implications are thus observable only when E_F is near charge neutrality.[27,28] Interestingly, we found that the TF screening length and impact parameter are both n-independent. Why, then, should we expect the spectral function to renormalize at low n? The answer lies in the geometry of the crystal. There is an emergent renormalization that occurs due to the ultraviolet cutoff k_c. In effect, if the de Broglie wavelength at graphene's Fermi level is on the order of the two-carbon unit cell, then the bare band structure is recovered. At longer electron wavelengths, the cone is squeezed to be steeper. Notably, because the valence and conduction bands overlap at K and K', the Fermi level can be continuously tuned from electrons to holes. Charge inhomogeneity from extrinsic disorder often blurs the low-density regime ($|n| < 10^{10}$ cm^{-2}) where renormalization is observable.

Experimental details on directly measuring v_F with full control of n, including a plot of Eq. 2.56 are presented in Chapter 5.

To conclude this chapter, graphene and bilayer graphene have a plethora of intriguing aspects that can be traced back to their underlying symmetries. Here we scratched the surface by exploring symmetries that contribute to bond hybridization, degenerate bands and pseudospin degeneracy in graphene. In BLG, many of these symmetries can be broken by changing the energy difference or hopping parameters in the Hamiltonian—either by external means or internal attributes. We derived the single particle LL spectrum of both graphene and BLG, drawing connections to the ubiquitous harmonic oscillator. Finally, we discussed symmetry is broken by kinetic energy-quenching LLs, leading to correlated electron behavior and spontaneous polarization.

References

(1) Sakurai, J. J.; Napolitano, J. *Modern Quantum Mechanics*, 2nd ed.; Cambridge University Press, 2017. https://doi.org/10.1017/9781108499996.

(2) Noether, E. Invariant Variation Problems. *Transp. Theory Stat. Phys.* **1971**, *1* (3), 186–207. https://doi.org/10.1080/00411457108231446.

(3) Donald A. McQuarie. *Quantum Chemistry*; University Science Books, 2008.

(4) Ashcroft, N. W.; Mermin, N. D. *Solid State Physics*; Cengage Learning, 2011.

(5) Castro Neto, A. H.; Guinea, F.; Peres, N. M. R.; Novoselov, K. S.; Geim, A. K. The Electronic Properties of Graphene. *Rev. Mod. Phys.* **2009**, *81* (1), 109–162. https://doi.org/10.1103/RevModPhys.81.109.

(6) Peskin, M. E.; Schroeder, D. V. *An Introduction to Quantum Field Theory*; Addison-Wesley: Reading, USA, 1995.

(7) McCann, E. *Electronic Properties of Monolayer and Bilayer Graphene*; Springer, 2012.

(8) Richard E. Prange, S. M. G. *The Quantum Hall Effect*; Springer-Verlag, 1987.

(9) Tapash Chakraborty, P. P. *The Quantum Hall Effects: Integral and Fractional*; Springer, 1995.

(10) MacDonald, A. H. *Qauntum Hall Effec: A Perspective*; Springer Netherlands, 1989.

(11) Stormer, H. L.; Tsui, D. C.; Gossard, A. C. The Fractional Quantum Hall Effect. *Rev. Mod. Phys.* **1999**, *71* (2), S298--S305. https://doi.org/10.1103/RevModPhys.71.S298.

(12) McClure, J. W. Diamagnetism of Graphite. *Phys. Rev.* **1956**, *104* (3), 666–671. https://doi.org/10.1103/PhysRev.104.666.

(13) McCann, E.; Fal'ko, V. I. Landau-Level Degeneracy and Quantum Hall Effect in a Graphite Bilayer. *Phys. Rev. Lett.* **2006**, *96* (8), 86805. https://doi.org/10.1103/PhysRevLett.96.086805.

(14) Wallace, P. R. The Band Theory of Graphite. *Phys. Rev.* **1947**, *71* (9), 622–634. https://doi.org/10.1103/PhysRev.71.622.

(15) McCann, E.; Koshino, M. The Electronic Properties of Bilayer Graphene. *Reports Prog. Phys.* **2013**, *76* (5), 56503.

(16) Gava, P.; Lazzeri, M.; Saitta, A. M.; Mauri, F. Ab Initio Study of Gap Opening and Screening Effects in Gated Bilayer Graphene. *Phys. Rev. B* **2009**, *79* (16), 165431. https://doi.org/10.1103/PhysRevB.79.165431.

(17) Zhang, Y.; Tang, T.-T.; Girit, C.; Hao, Z.; Martin, M. C.; Zettl, A.; Crommie, M. F.; Shen, Y. R.; Wang, F. Direct Observation of a Widely Tunable Bandgap in Bilayer Graphene. *Nature* **2009**, *459*, 820.

(18) Taychatanapat, T.; Jarillo-Herrero, P. Electronic Transport in Dual-Gated Bilayer Graphene at Large Displacement Fields. *Phys. Rev. Lett.* **2010**, *105* (16), 166601. https://doi.org/10.1103/PhysRevLett.105.166601.

(19) Hao, Y.; Wang, L.; Liu, Y.; Chen, H.; Wang, X.; Tan, C.; Nie, S.; Suk, J. W.; Jiang, T.; Liang, T.; et al. Oxygen-Activated Growth and Bandgap Tunability of Large Single-Crystal Bilayer Graphene. *Nat. Nanotechnol.* **2016**, *11* (5), 426–431. https://doi.org/10.1038/nnano.2015.322.

(20) Ju, L.; Wang, L.; Cao, T.; Taniguchi, T.; Watanabe, K.; Louie, S. G.; Rana, F.; Park, J.; Hone, J.; Wang, F.; et al. Tunable Excitons in Bilayer Graphene. *Science (80-.).* **2017**, *358* (6365), 907–910. https://doi.org/10.1126/science.aam9175.

(21) Dial, O. E. Single Particle Spectrum of the Two Dimensional Electron Gas, MIT, 2007.

(22) Nomura, K.; MacDonald, A. H. Quantum Hall Ferromagnetism in Graphene. *Phys. Rev. Lett.* **2006**, *96* (25), 256602. https://doi.org/10.1103/PhysRevLett.96.256602.

(23) Young, A. F.; Dean, C. R.; Wang, L.; Ren, H.; Cadden-Zimansky, P.; Watanabe, K.; Taniguchi, T.; Hone, J.; Shepard, K. L.; Kim, P. Spin and Valley Quantum Hall Ferromagnetism in Graphene. *Nat. Phys.* **2012**, *8* (7), 550–556. https://doi.org/10.1038/nphys2307.

(24) Das Sarma, S.; Adam, S.; Hwang, E. H.; Rossi, E. Electronic Transport in Two-Dimensional Graphene. *Rev. Mod. Phys.* **2011**, *83* (2), 407–470. https://doi.org/10.1103/RevModPhys.83.407.

(25) Jang, C.; Adam, S.; Chen, J.-H.; Williams, E. D.; Das Sarma, S.; Fuhrer, M. S. Tuning the Effective Fine Structure Constant in Graphene: Opposing Effects of Dielectric Screening on Short- and Long-Range Potential Scattering. *Phys. Rev. Lett.* **2008**, *101* (14), 146805. https://doi.org/10.1103/PhysRevLett.101.146805.

(26) Das Sarma, S.; Hwang, E. H. Velocity Renormalization and Anomalous

Quasiparticle Dispersion in Extrinsic Graphene. *Phys. Rev. B* **2013**, *87* (4), 45425. https://doi.org/10.1103/PhysRevB.87.045425.

(27) Elias, D. C.; Gorbachev, R. V; Mayorov, A. S.; Morozov, S. V; Zhukov, A. A.; Blake, P.; Ponomarenko, L. A.; Grigorieva, I. V; Novoselov, K. S.; Guinea, F.; et al. Dirac Cones Reshaped by Interaction Effects in Suspended Graphene. *Nat. Phys.* **2011**, *7* (9), 701–704. https://doi.org/10.1038/nphys2049.

(28) Chae, J.; Jung, S.; Young, A. F.; Dean, C. R.; Wang, L.; Gao, Y.; Watanabe, K.; Taniguchi, T.; Hone, J.; Shepard, K. L.; et al. Renormalization of the Graphene Dispersion Velocity Determined from Scanning Tunneling Spectroscopy. *Phys. Rev. Lett.* **2012**, *109* (11), 116802. https://doi.org/10.1103/PhysRevLett.109.116802.

Chapter 3:

Theory of Electron Tunneling Spectroscopy

When two conductors are in proximity, there is a nonzero probability that electrons can tunnel from one to the other. The behavior of tunneling is a direct result of the wavelike nature of matter. In classical optics, for example, an electromagnetic wave incident on an interface will both reflect and transmit through the interface with an attenuation. In quantum mechanics, small objects like electrons incident on a potential energy barrier exhibit a similar characteristic. Disparate from any classical intuition, matter can transmit into and through regions where it has less-than sufficient energy. In correspondence with classical mechanics, the probability of tunneling exceedingly small for macroscopic objects. On the nanoscale, however, tunneling is necessary component of a full description of particle dynamics. Indeed, in the century since it was discovered, the application of quantum tunneling as diagnostic tool has shed light on intricate and complex physical phenomena—from high temperature superconductivity to nuclear decay processes.[1]

In this chapter I provide a mathematical description of tunneling spectroscopy—the primary experimental characterization technique used in this thesis. Besides its power as a spectroscopic tool, quantum tunneling can be well described with elementary perturbation theory. In this chapter, we will calculate the tunneling current expected to flow between two electrodes. We will see that this current is exponentially dependent on the distance between electrodes, and directly proportional

to the electrodes' density of available tunneling states. From the general two conductor problem, we will explore the fundamentals of tunneling spectroscopy, specifically tip-based scanning tunneling spectroscopy (STS) —a system that has revealed a multitude of exotic physics in graphene over the past decade. This will include a brief introduction to inelastic tunneling, which plays an important role in graphene STS. Subsequently, we will describe planar tunneling spectroscopy (PTS), wherein the tunneling probe is a metal plate. Then compare both tip-based and plate-based spectroscopies of graphene in order to build background for the experiments in Chapters 5,6 and 7. Specifically, we will address the issue of momentum conservation. This will include a review of the major developments in STS and PTS on graphene over the past decade.

The second part of the Chapter is a practical introduction to the PTS of graphene systems. We will discuss the origins of several nuanced effects that occur within its rich tunneling spectra. This will begin with a discussion of tuning the Fermi level in graphene with gate electrodes. Then, the case of tunneling into many-body states is described. We conclude this chapter with a review of the measurement setup that discusses the instrumentation and technique used to acquire the data presented in Chapters 5,6 and 7.

3.1 Fermi's Golden Rule

Low energy quantum dynamics are determined by the Schrödinger equation $H\Psi = i\hbar\partial_t\Psi$.[2] As a corollary, the Hamiltonian H in the Schrödinger picture has a complete set of eigenstates $\Psi = e^{-iE_n t/\hbar}|n\rangle$ that have phases proportional to time and energy. Therefore, the relative phase between two stationary states is periodic and depends on their energy difference. This can be interpreted as a beat frequency. Because the states are ordinarily orthogonal, there is no chance of electrons transitioning between the two. In the presence of a perturbative potential, however, their overlap is dictated by the matrix element between them at $t = 0$, weighted by their relative phase factors. The rate of transition is dependent on how the matrix element varies in time—which is dictated entirely by how the perturbing potential varies in time.[3,4]

There are two cases of interest applicable to spectroscopic measurement: (1) the periodic perturbation; and (2) the constant perturbation. The goal in both cases is to determine the projection of the time-evolved wave function on one of its time-evolved basis states. This projection d_n is found by evaluating the integral:[5]

$$d_n(t) = d_n(0) - \frac{i}{\hbar}\int_0^t \langle f|H'(t)|i\rangle e^{-i\omega_{if}t}\,dt \qquad (3.1)$$

Where $|i\rangle$ and $|f\rangle$ are the initial and final state kets. In the case of the time-periodic potential with frequency ω, the above integral is found to be the time-independent matrix overlap modulated with a phase proportional to $\omega - \omega_{if}$. In the Born approximation, the modulus squared of d_n gives the probability of transitioning as a

function of time (conveniently interpreted as a cumulative probability function). Taking the limit as time goes to infinity, then dividing by the oscillation period, the average transition rate is found to be the ubiquitous "Fermi's Golden Rule":

$$\Gamma_{if} = \frac{2\pi}{\hbar}|\langle f|H'(t)|i\rangle|^2\delta(E_i^0 - E_f^0 - \hbar\omega) \tag{3.2}$$

Notably, the transition will only occur if the excitation frequency (incoming photon energy, for example) matches the resonant frequency of the system. In the case of a spectroscopic measurement, the initial state is an attribute of the system, and the excitation frequency couples that state to a continuum of external states with density ρ_c. The average rate can then be expressed

$$\bar{\Gamma}_{if} = \frac{2\pi}{\hbar}|\langle f|H'(t)|i\rangle|^2\delta(E_i^0 - E_f^0 - \hbar\omega)\rho(E_f^0) \tag{3.3}$$

Next, we turn to examine the case where H' is constant. The perturbation, although time independent, couples two time-evolved eigenstates and thus necessitates the machinery of time-dependent perturbation theory. We can adiabatically turn on the constant potential by defining it as $H' = \lim_{\eta\to 0} H'e^{\eta t}$. In this case, from the general result in Eq. 3.1 the probability amplitude weight d_n on the n^{th} eigenstate becomes

$$d_n = d_n(0) - \lim_{\eta\to 0}\frac{i}{\hbar}\int_0^t \langle f|H'|i\rangle e^{-(i\omega_{if}t - i\eta)}\,dt \tag{3.4}$$

Which can be evaluated directly. Following a similar procedure as above, the transition rate is determined to be

$$\Gamma_{if} = \frac{2\pi}{\hbar}|\langle f|H'|i\rangle|^2 \delta(E_i^0 - E_f^0) \tag{3.5}$$

Remarkably, both the time-periodic and constant perturbations arrived at the Golden Rule expression for transition rate. This convenient result is not the case for a general time-dependent perturbation potential and was made possible by the form of the integrals in Eq. 3.52 and Eq. 3.49.

3.2 The Bardeen Method

The Bardeen transfer matrix approach to tunneling is used to calculate the tunneling current that flows between two electrodes, separated by a short distance. In his treatment, Bardeen asserts two assumptions: (1) stationary electronic states (energy eigenfunctions) in both electrodes, although mutually orthogonal, are not solutions to the system's overall Schrödinger equation; and (2) the potential due to one of the electrodes acts as a time-independent perturbation to the Hamiltonian of the other electrode.[6] Figure 3.1(a) is a cartoon schematic adapted from Chen,[7] that depicts Bardeen's approach. The energy diagram in Fig. 3.1(a) shows the potential wells of the sample (U_S, on the left) and probe (U_P, on the right). Blue and orange lines illustrate the stationary states of the sample and probe, respectively.

Assumption (1), above, enables a straightforward mapping of this problem onto intrasystem transitions discussed in the previous section. Let's assume that the "sample" electrode is perturbed by the potential of the "probe" electrode. Using the adiabatic approach discussed in the previous section, we introduce the constant probe

potential $U_P e^{i\eta t}$ then take the $t \to 0$ limiting case. After time t, the probability weight associated with finding the system in the n^{th} energy eigenstate of the sample is

$$|c_n^S(t)|^2 = \frac{2\pi}{\hbar}\left|\langle\psi_n^S|U_p|\psi_m^P\rangle\right|^2 \delta(E = E_m^P - E_n^S)\rho_P(E) \tag{3.6}$$

Where E s the energy of both the sample (S) and probe (P) initial and final states, respectively. This can be interpreted as the average rate at which a population of electrons is depleted from this state.

The matrix element $M_{\mu\nu} = \langle\psi_\mu^S|U_p|\psi_\nu^P\rangle$ is the spatial overlap between sample and probe eigenstates in the tunneling barrier, multiplied by the probe potential energy. By Bardeen's first assumption, the Schrödinger equation in the probe can be substituted in for the perturbing potential

$$M_{\mu\nu} = \langle\psi_\mu^S|E_\mu^S|\psi_\nu^P\rangle + \frac{\hbar^2}{2m}\left\langle\psi_\mu^S\right|\frac{d^2}{dz^2}\left|\psi_\nu^P\right\rangle \tag{3.7}$$

Conservation of energy necessitates that $E_\mu^S = E_\nu^P$. Repeating the above step to substitute in the sample Schrödinger equation (and noting that $U_P = 0$ in the sample),

$$M_{\mu\nu} = \frac{\hbar^2}{2m}\frac{d}{dz}\left[\left\langle\psi_\mu^S\right|\frac{d}{dz}\left|\psi_\nu^P\right\rangle - \left\langle\psi_\mu^S\right|\frac{d}{dz}\left|\psi_\nu^P\right\rangle\right] \tag{3.8}$$

In real space, this general form of the Bardeen matrix element can be expressed as a volume integral. Evaluating the z component of the volume integral which connects the two electrodes yields the overlap in its typical form

$$\frac{\hbar^2}{2m}\int_{z=z_0}[\psi_\nu^S\frac{d}{dz}\psi_\mu^{P*} - \psi_\mu^{P*}\frac{d}{dz}\psi_\nu^S]dxdy \tag{3.9}$$

Reassuringly, the above integrand has the form of a current operator $\vec{J} \propto \Psi^* \nabla \Psi - \Psi \nabla \Psi^*$, which follows from the probability continuity equation $\nabla \cdot \vec{J} + \partial_t |\Psi|^2 = 0$. This resemblance provides the interpretation that the Bardeen matrix overlap is simply the time derivative of probability distribution $|\psi_\nu^{S*} \psi_\mu^P|$. Expanded to the three-dimensional case, the matrix element arrives at its general, applicable form[1,8]

$$M_{\mu\nu} = \frac{\hbar^2}{2m} \int_\Sigma [\psi_\nu^S \vec{\nabla} \psi_\mu^{P*} - \psi_\mu^{P*} \vec{\nabla} \psi_\nu^S] dS \tag{3.10}$$

3.3 Tunneling Out of Equilibrium

When the two systems are in equilibrium, the rate of leaving and returning to a state are equal. When the two electrodes are brought out of equilibrium by a bias eV_b, however, there will be a net current from one electrode to the other. Recognizing that tunneling occurs between occupied states in one electrode and unoccupied states in the other electrode, the forward and reverse rates can then be written

$$\begin{aligned} \bar{\Gamma}_{P \to S} = \frac{4\pi}{\hbar} \sum_n \sum_m |M_{\mu\nu}|^2 f(E_n^P - E_F)[1 \\ - f(E_m^S - E_F)\delta(E_m^P - E_n^S - eV_b)] \end{aligned} \tag{3.11}$$

$$\begin{aligned} \bar{\Gamma}_{S \to P} = \frac{4\pi}{\hbar} \sum_n \sum_m |M_{\mu\nu}|^2 f(E_n^S - E_F)[1 \\ - f(E_m^P - E_F)\delta(E_m^P - E_n^S - eV_b)] \end{aligned} \tag{3.12}$$

Where $f(\epsilon)$ is the Fermi-Dirac distribution and $f(\epsilon)[1 - f(\epsilon - \Delta\epsilon)]$ is a "top hat" function with height 1 and width $\Delta\epsilon$ at $T = 0\ K$. Turning to the case where probe and sample electrodes have some distribution of states as a function of energy $\rho(\epsilon)$, the

discrete sums are converted to integrals $\sum_n = \int \rho(\epsilon) d\epsilon$. Combining the forward and reverse currents, the low temperature net current between tip and sample becomes

$$I = \frac{4\pi e}{\hbar} \int_{E_F}^{E_F + eV_b} |M(\epsilon)|^2 \rho_P(\epsilon + eV_b) \rho_S(\epsilon) d\epsilon \tag{3.13}$$

The tunneling current then has three main components: $\rho(\epsilon)$ for both the sample and probe electrode—materials properties that are independent of the tunneling geometry—and $|M(\epsilon)|^2$, the matrix element that describes overlap between sample and probe wave functions in the barrier.

Out-of-equilibrium tunneling between the density of states of the probe is depicted in Fig. 3.1(b). The probe, shown in orange on the right, and sample, shown in blue on the left, are separated by a potential barrier. The Fermi energies of the sample and probe, E_F^S and E_F^P, are shifted with respect to one another by a sample bias eV_b. As a result, charges tunnel with a directionality between the two.

In conventional tunneling spectroscopy, it is assumed that both $\rho_P(\epsilon)$ and $|M(\epsilon)|^2$ are constant in the experimentally relevant energy ranges. This assumption, which will be validated in the Section 3.5, enables the aforementioned constants to be pulled out of the integral. Neglecting any modulation in E_F during the measurement, the approximated differential tunneling conductance becomes

$$\frac{dI}{dV_b} = \frac{4\pi e}{\hbar} |M|^2 \rho_P \rho_S(\epsilon + eV_b) \tag{3.14}$$

This powerful result underpins the central experimental results in this thesis. Tunneling spectroscopy has the power to determine the sample's electronic structure away from the Fermi level with spectroscopic energy tuned by eV_b.[9,10]

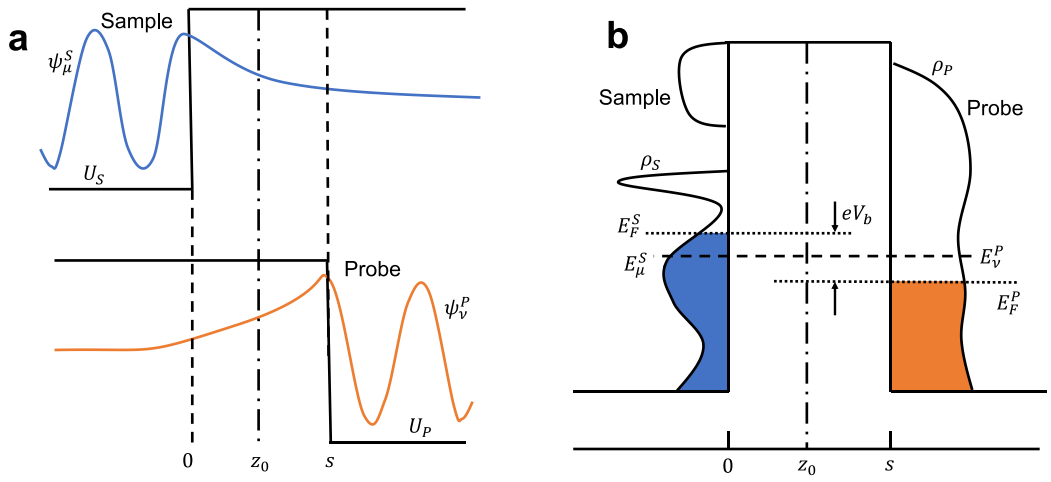

Figure 3.1: Illustration of the Bardeen approach.[7] (a) Energy diagram of the potential wells of the sample (U_S, on the left) and probe (U_P, on the right). Three x-y planes at height 0, z_0, and s to the right of the sample surface are shown as dashed lines. Blue and orange lines illustrate the stationary states of the sample and probe, respectively. Note that $U_S(z > s) = 0$, although $\psi_\mu^S(z > s) \neq 0$, as discussed in the main text. (b) Out-of-equilibrium tunneling between the density of states of the probe (on right) and sample (on left). Occupied electron states in the sample and probe are shown in blue and orange, respectively. The Fermi energies of the sample and probe, E_F^S and E_F^P, are shifted with respect to each other by energy eV_b. Conservation of energy necessitates that $E_\mu^S = E_\nu^P$, though the indices μ and ν need not be equivalent.

The assumption that ρ_P is energy independent is reasonable for metallic probes that have a high DOS near the Fermi level. But how valid is the assumption that $|M(\epsilon)|^2$ is energy-independent? Does the assumption lose validity when the tunneling

geometry changes? How is the matrix element overlap treated in the case where one electrode hosts nearly free electrons and the other hosts solid state Bloch waves? The Bardeen tunneling matrix element $M(\epsilon)$ is an area of intense debate and the next two Sections compute it for an STM tip-sample and planar probe-sample junctions.

3.4 Approximating $M_{\mu\nu}$ for STM—The Tersoff-Hamann Approximation

Shortly after the scanning tunneling microscope (STM) was invented by Binnig and Rohrer in 1981, Tersoff and Hamann (TH) reported a powerful approximation to the Bardeen approach—one which yielded the sample's local electronic structure directly.[11] Their original assumption, which was later expanded by Chen,[12] accounts for tunneling from a spherical S orbital at the apex of the STM tip. This appropriately named S-wave tunneling allows for convenient distillation of the general tunneling matrix element $M_{\mu\nu}$. The time-independent probe S-wave is a Green's function for the 3D Helmholtz operator that satisfies both $(\nabla^2 - k^2)g(\vec{r} - \vec{r}_0) = \delta(\vec{r} - \vec{r}_0)$, and the boundary conditions of normalization and attenuation. Specifically, the tip wave function is a modified spherical Bessel function of the second kind: $g(\vec{r} - \vec{r}_0) = e^{i\vec{\kappa}\cdot(\vec{r}\cdot\vec{r}_0)}/|\vec{r} - \vec{r}_0|$. Plugging the S-wave form for ψ_ν^P into Eq. 3.58 and rewriting the kinetic term as a Helmholtz operator,

$$M_{\mu\nu} = \frac{\hbar^2}{2m}\int_\tau [\psi_\nu^S(\nabla^2 + \kappa^2)\psi_\mu^{P*} - \psi_\nu^S\kappa^2\psi_\mu^{P*} - \psi_\mu^{P*}\nabla^2\psi_\nu^S]dV \qquad (3.15)$$

The implications of Eq. 3.63 are illustrated in Fig. 3.2(a), where an STM tip, represented by an orange triangle, hangs above a sample, shown as a blue standing

wave in a box. Both the tip and sample wave functions attenuate in the vacuum between them. The circular, orange glow emanating from the tip apex represents $\psi_\nu^{P*}(z < s)$ which is approximated as an S-wave, and the blue glow above the box represents $\psi_\mu^S(z > 0)$. Notably, because the decay constant of each surface state is determined by the out-of-plane component of its momentum $\kappa = |\vec{k} \cdot \hat{z}|$, and because momentum is conserved, both $\psi_\nu^{P*}(z < s)$ and $\psi_\mu^S(z > 0)$ share the same κ. Therefore, the first and second terms in the above integrand from Eq. 3.63 cancel and the remaining term is the product $\psi_\mu^S \delta(\vec{r} - \vec{r}_0)$, shown as a blue dot in the xy plane in Fig.3.2(a). Integrating $\psi_\mu^S \delta(\vec{r} - \vec{r}_0)$ yields

$$M_{\mu\nu} \propto \psi_\mu^S(\vec{r}_0) \tag{3.16}$$

Thus, the TH approximation leads to an elegant result: the Bardeen matrix element is simply proportional to the sample wave function, evaluated at the position of the tip (a point in the $z = s$ plane). The power of this result lies in its spatial resolution, as we demonstrate next.

Reintroducing the approximate matrix element into the expression for dI/dV_b, and assuming that the density of states of the probe ρ_P is constant (it is, after all, a single S orbital),

$$\frac{dI}{dV_b}(V_b) \propto |\Psi|^2 \rho_S(\epsilon + eV_b) \tag{3.17}$$

The product $|\Psi|^2 \rho_s(\epsilon)$ is known as the local density of states (LDOS). In essence, the LDOS introduces spatially varying probability density $|\Psi|^2$ to the DOS, which ordinarily counts the amount of states in a certain energy range, weighing all states

equally. By including real space wave function probability density, the LDOS adds appropriate weights to states depending on their intensity at $\vec{r}_0$. The STM $dI/dV_b(V_b)$ measures a quantity that is proportional to the LDOS at energy $E_F^S + eV_b$.[13]

Notably, although the matrix element is evaluated at an intermediate plane between the sample and tip, the LDOS corresponds to the sample wave function directly at the apex of the tip (at height z = s). Increasing s will thus exponentially decrease the Bardeen matrix element, and thus the tunneling dI/dV_b. In this way, STM has high (< 10 pm) sensitivity to sample topography and can map atomic scale images and the LDOS in the same region. In addition to the tip-sample separation s, the matrix element is also exponentially sensitive to the out-of-plane momentum. The interplay between decay length, momentum and energy in the context of graphene tunneling spectroscopy are discussed in the next section.

3.5 Approximating $M_{\mu\nu}$ for Planar Tunnel Junctions

In the previous Section, the Tersoff-Hamann (TH) S-wave approximation showed that a local STM probe directly measures the LDOS—a quantity that spatially weights the density of states ρ_S with the probability density $|\Psi|^2$. In the planar tunneling geometry, where the TH S-wave approximation emphatically *cannot* be applied, we are in need of another approach to calculate the matrix element $M_{\mu\nu}$. Using one such approximation, we will see in this Section that $M_{\mu\nu}$ between a planar, amorphous metallic probe and graphene sample is (1) independent of space; (2) weakly dependent on energy and (3) strongly dependent on in-plane momentum.

We begin by addressing the one-dimensional case, shown in Fig. 3.1(a). Consider a particle with energy E incident on a barrier of height $V(x)$. In the region to the left of the barrier, right traveling solutions to the Schrödinger equation are plane waves $\psi = Ae^{ikx-i\omega t}$, where the momentum $\hbar k$ is simply the difference between kinetic and potential energies, $k = \sqrt{E-U}/\hbar$. Within the barrier, $U > E$ and k is imaginary. Right-propagating solutions are then $Be^{-\kappa x}$, where we defined the decay constant $\kappa = ik = \sqrt{2m(U-E)}/\hbar$. Notably, as E increases or κ decreases, the particle has a larger probability of residing on the other side of the barrier.

Wave function decay between two planar electrodes in the PTS junction is entirely dependent on the out-of-plane component of momentum k_z. Drawing from the 1D tunneling example, we define the decay constant as $\kappa = ik_z$. Notably, in the 1D tunneling picture E and κ are inextricably tied together. In the 3D PTS junction, however, a portion of the total momentum $\vec{k}$ is carried in the plane of the electrodes. Specifically, $k_z^2 = \left|\vec{k}\right|^2 - \left|\vec{k}_{||}\right|^2$, where $\vec{k}_{||}$ is the in-plane component of $\vec{k}$. The decay constant is then

$$\kappa = \sqrt{\frac{2m(\Phi - E_\mu)}{\hbar^2} + |\vec{k}_{||}|^2} \tag{3.18}$$

Each of the components of the Bardeen matrix element $\delta M = \psi^{P*}\partial_z\psi^S - \psi^S\partial_z\psi^{P*}$ can be approximated by the state at the surface weighted by this z-momentum-dependent decay. Dropping the indices μ, ν for clarity,

$$\psi^S = \psi^S(0)e^{-\kappa_S z_0}, \qquad \psi^P = \psi^P(s)e^{\kappa_P(s-z_0)} \tag{3.19}$$

Assuming that momentum and energy are conserved, $\kappa_S = \kappa_P \equiv \kappa$. The Bardeen matrix element in Eq. 3.58 can then be written

$$M = -\frac{\hbar^2}{m}\kappa e^{-\kappa s}\int\int \psi_\nu^S(0)\psi_\mu^{P*}(s)dxdy \tag{3.49}$$

Simply put, the Bardeen matrix element of two parallel plate electrodes is the convolution of their surface states, weighted by an energy, separation, and parallel momentum-dependent decay factor.

While the exponential decay is straightforward to calculate, calculating the surface state overlap without *a priori* knowledge of the wave functions is tricky in all but the simplest cases. Luckily, graphene's surface states are simple Bloch waves (introduced in Chapter 2) that are easily enough plugged into Eq. 3.58. Indeed, treatments of graphene-insulator-graphene (GIG) planar tunnel junctions were reported several years ago.[14,15] In those works, both electrodes were assumed to be nearly-neutral graphene with Fermi surface approximated as infinitesimal and doubly degenerate at the K and K' points. Notably, the small Fermi surface overlap and stringent crystal momentum conservation requirement were responsible for the observed negative differential resistance (NDR). In order to determine the Bardeen matrix element for metal-insulator-graphene (planar tunneling spectroscopy, PTS) junctions, we will follow the methodology of Feenstra, et. al.,[14] but we will replace one of the graphene electrodes with an amorphous metal probe.

The amorphous metal probe is assumed to host a nearly free electron (NFE) surface state that feels a random potential due to the lack of long-range crystallinity. Because of the spatially varying random potential, the probe surface state assumes a

continuous energy range (fat band) at a given momentum $\vec{k}_{||}$. While both energy and momentum are still assumed to be conserved in the PTS system, there are ample states in the probe that coincide with graphene's low energy bands. In essence, the assumption of NFE states in a weak random potential relaxes the momentum conservation imposed by a probe with well-defined bands. As a result, the PTS system is not expected to show the momentum-matching resonant NDR[16,17] previously shown in GIG devices.

The surface states in graphene are Bloch waves that behave according to the low energy dispersion derived in the previous chapter.

$$\psi_k^S(\vec{x}, z = 0) = \frac{1}{N}\sum_{m,n} \psi_{u.c.}(\vec{r}) e^{i\vec{k}_{||}\cdot\vec{R}_{mn}} \tag{3.20}$$

Imposing momentum conservation, the NFE probe surface state can similarly be described as

$$\psi_k^{P*}(\vec{x}, z = s) = \frac{1}{\sqrt{V}} e^{i\vec{k}_{||}\cdot\vec{x}} \tag{3.21}$$

In this case, the tunneling matrix element can be expressed

$$M = -\frac{\hbar^2}{m}\kappa e^{-\kappa s}\int \sum_{m,n} \psi_{u.c.}(\vec{r})\, dxdy \tag{3.22}$$

$$\left|M_{\mu\nu}\right|^2 \propto \kappa^2 e^{-2\kappa s}, \qquad \kappa = \sqrt{\frac{2mE_\mu}{\hbar^2} - |\vec{k}_{||}|^2} \tag{3.23}$$

The current that flows between graphene and an amorphous metallic probe can be expressed

$$I \propto \int_{E_F}^{E_F + eV_b} \kappa(\epsilon)^2 e^{-2\kappa(\epsilon)s} \rho_S(\epsilon) d\epsilon \tag{3.24}$$

Where the sample density of states is assumed to be constant in accordance with the NFE approximation outlined above. Therefore, the differential tunneling conductance can be written

$$\frac{dI}{dV_b} \propto \left(\frac{2m(\Phi - eV_b)}{\hbar^2} + |\vec{k}_{||}|^2\right) e^{-2\kappa s} \rho_S(eV_b) \tag{3.25}$$

In the above expression, $\kappa^2 = \left(\frac{2m(\Phi - eV_b)}{\hbar^2} + |\vec{k}_{||}|^2\right)$ is written explicitly to address the dependence of dI/dV_b on bias voltage V_b and parallel momentum $\vec{k}_{||}$, respectively. Graphene's work function is ~5eV,[18] which is 6 x higher than the range of eV_b discussed in this thesis. Even with the inclusion of a dielectric hBN tunneling barrier, the barrier height between graphene's Fermi level and the hBN conduction band edge is ~1.5 eV.[15] We thus expect κ to vary be < 10 % when $|V_b| < 0.75$ V, which is the maximum experimental range accessed in this thesis.

The dependence of dI/dV_b on $k_{||}$, however, is enormous. Graphene has one of the largest Brilluoin zones known, with fermi surface at the K point > 1.7 Å $^{-1}$. The tunneling conductance between graphene and the planar metal probe (or an STM tip, for that matter), is expected to be vanishingly small. As a back of the envelope calculation for comparison, imagine if graphene's Fermi energy instead were at the Γ point. The total momentum $2meV_b/\hbar^2$ is roughly 0.3 Å $^{-1}$. Therefore, in a 20 Å-thick junction, the dI/dV_b would increase by an expected 10^{68} times! In order to circumvent this low bias suppression of dI/dV_b STM will approach close to the sample. Using the same rough approximation, an STM tip 1 Å above graphene would measure a factor of 5 difference between the Γ and K points. In tunneling junctions where the barrier

thickness is limited by the monolayer limit of the dielectric barrier, elastic tunneling is exceedingly suppressed. In order to measure and appreciable conductance at all, it is therefore necessary to rely on second-order scattering processes, as discussed in Section 3.7.

Figure 3.2(b) illustrates the NFE approximation and its implications. Within the planar probe, shown as an orange rectangle, nearly free electrons have momentum $\hbar\vec{k}$ characterized by in-plane $\vec{k}_{||}$ and normal k_z wave numbers. States with higher k_z diffuse farther into the vacuum below the probe, shown as an orange glow. In the sample, shown as a blue sinusoid confined to a box, states with higher k_z diffuse farther into the vacuum. The sample state diffusion is shown as a blue glow. Assuming that $\vec{k} = \vec{k}_{||} + k_z\hat{z}$ is conserved, blue and orange glows will have identical decay lengths $1/k_z$. The resulting matrix element in Eq. 3.58 includes a convolution of $\psi_\mu^S(0)$ and $e^{i\vec{k}_{||}\cdot\vec{x}}$, where $\vec{x}$ is a coordinate in the $z = s$ plane. The integrand of this convolution is shown in the lower panel of (b). Unsurprisingly, the convolution removes the Bloch wave phase factor, leaving an integral over the lattice orbitals. Since the lattice is normalized by design, the convolution is a constant—namely 1.

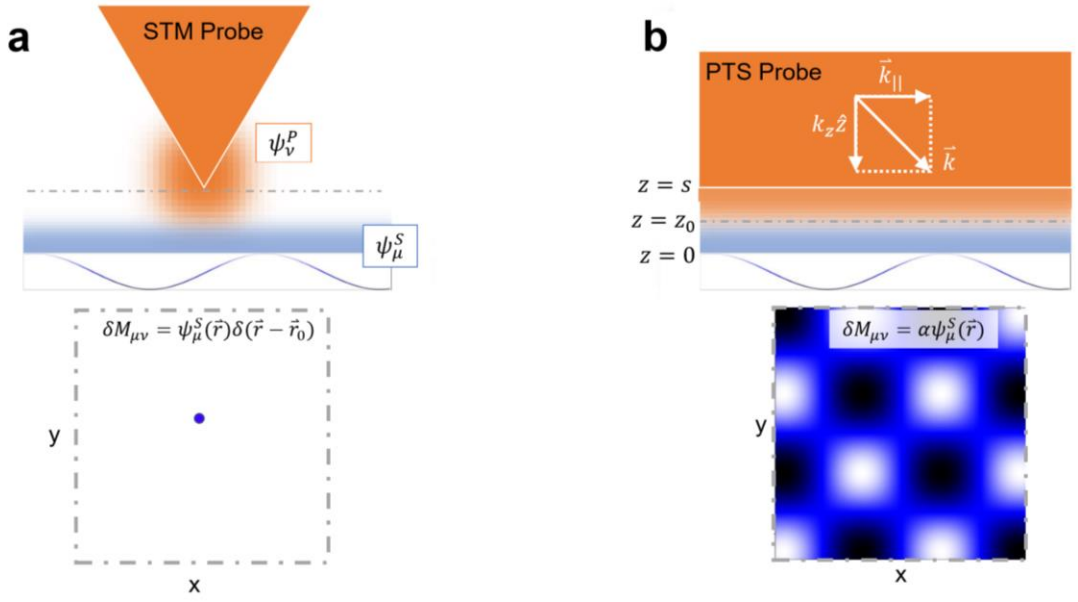

Figure 3.2: Illustration of the Bardeen matrix elements for STM and PTS. (a) An STM tip (orange triangle) is brought near a sample with arbitrary wave function ψ_μ^S. The confined portion of ψ_μ^S is shown as a blue standing wave with amplitude illustrating probability amplitude. The remaining portion of ψ_μ^S emanates outward as a blue haze with decay constant κ, discussed in the main text. The probe wave function ψ_ν^P is assumed to be a spherical Bessel function of the second kind, shown as a radially dimming orange halo around the STM tip. Following the treatment in the main text, the product $\psi_\mu^S \nabla^2 \psi_\nu^{P*}$ is the convolution of the sample wave function and a delta function located at the apex of the tip. This is shown as a blue dot in the x-y plane in (a). (b) A planar tunneling probe filled with nearly free electrons is brought near the same fictitious sample as in (a). Nearly free electron states diffuse out of the probe, shown as an orange haze, with decay constant $\kappa = ik_z$, the z-component of de Broglie wavenumber. At a given energy, states with lower $\vec{k}_{||}$ will diffuse farther into the

vacuum. The product $\psi_\mu^S \nabla^2 \psi_\nu^{P*}$ in this case is simply a $\alpha \psi_\mu^S$ where α is a constant discussed in the main text. In both the STM and PTS cases, $M_{\mu\nu}$ is found by integrating the lower panel in the $(x, y, z = z_0)$ plane.

In summary, while planar tunneling junctions cannot access the LDOS $dI/dV_b \propto |\Psi|^2 \rho_S$ like STM, they can access the global DOS underneath the tunneling junction. Instead of using the Tersoff-Hamann S-wave approximation discussed in the previous section, we approximated the planar probe as a bath of nearly free electrons (that need not have a well-defined dispersion in the material but have some semblance of in-plane and out of plane momentum at the time of tunneling). This approximation, together with momentum and energy conservation, yielded the (weak) energy-dependence and (strong) momentum-dependence of $|M|$. Thus, STM and PTS complement each other—the former accesses the spatially resolved LDOS ($dI/dV_b \propto |\Psi|^2 \rho_S$), while the latter integrates out the spatial wave function, retrieving the global DOS ($dI/dV_b \propto \rho_S$).

As a final note, in this Section we discussed the decay lengths associated with in-plane momentum $\vec{k}_{||}$. In the case of graphene tunneling devices, this topic assumes paramount importance. A detailed treatment of momentum conservation and inelastic tunneling are discussed in Section 3.7.

3.6 The Role of hBN

In the previous section, the tunneling barrier between electrodes was assumed to be a small vacuum separation. While this is applicable to ultrahigh vacuum STM measurements that typically hover the tip ~3 A above the sample, the situation is more variable between PTS junctions. In this thesis, several atomic layers of the van der Waals insulator hexagonal Boron Nitride (hBN) are used as the tunneling barrier. The use of a material as a tunneling gap raises two important questions: (1) why can the hBN-spaced tunnel junction be treated as perturbative tunneling, versus vertical transport through the barrier material? (2) How does the in-plane dispersion of the dielectric material influence the tunneling characteristics of the junction? To answer question (1), we note that the conductance per channel (~1-10 nS) is much lower than the quantum of conductance e^2/h ~ 80000 nS, enabling the safe assumption that the tunneling, rather than vertical transport, is taking place.[15] Furthermore, the potential energy $U(\vec{r})$ in hBN varies smoothly in a neutral "jellium" approximation compared to $\psi(\vec{r})$ —so the WKB treatment of tunneling can safely be applied.[15] Next, we will provide a bit of background on the WKB approximation, then offer a response to question (2) that follows references.[19] Finally, we provide a heuristic discussion on the open-ended question of how to treat atomically thin dielectric tunneling barriers.

In the WKB approximation, the translation operator $\tau(\Delta z) = \exp(ip_\perp \cdot \vec{r}/\hbar)$ is addressed in the classically forbidden regions $(U(z) - E) < 0$, resulting in exponential decay $\exp(-\kappa_\perp \cdot \vec{r})$ where $\kappa_\perp = \sqrt{2m(U(\vec{r}) - E)}/\hbar$. In essence, the WKB approach, which assumes a slowly varying $U(\vec{r})$, uses the kinetic energy–

assumed to be the deficit between total and potential energy—to find the imaginary momentum. In the case of a vacuum barrier, the perpendicular decay constant $\kappa_\perp$ is readily found by assuming that E and $U(\vec{r})$ are constant and m is the free electron mass. In hBN, however, finding $\kappa_\perp$ is more complicated.

In the first reported hBN tunneling device, Britnell, et. al. assumed that the tunneling barrier was isotropic. By noting the simplest approximation for dispersion is simply the sum of in-plane and out-of-plane dispersions:

$$\varepsilon(\vec{k}) = \varepsilon_{||}(k_{||}) + \varepsilon_\perp(k_\perp) \tag{3.26}$$

The in-plane dispersion $\varepsilon_{||}(k_{||})$ is well studied with ARPES and modeling techniques,[20] showing a band gap of ~5.5 eV. The out-of-plane energy component can be modeled as a monotonic chain (hBN's stacking is typically AA')

$$\varepsilon_\perp = 2\gamma\cos(k_\perp h) \tag{3.27}$$

where γ describes the interlayer coupling and l is the distance between layers (~3.4Å). The hBN valence band maximum E_{VBM}, which lies ~3 eV from the Fermi level in graphene Solving the WKB tunneling equation in the limit that $(E - E_{VBM}) \ll 2\gamma$, k_z was then found to be

$$k_\perp \approx \frac{\sqrt{2m^*(E-E_{VBM})}}{\hbar}, \qquad m^* = \frac{\hbar^2}{2\gamma l^2} \tag{3.28}$$

Assuming that the interlayer coupling is 4 eV, and the distance between graphene's Fermi level and hBN's valence band is 1.5 eV[15] the vertical-transport effective mass m^* is found to be ~0.5 times the bare electron mass.[21] A comparison of this effect is plotted as dashed, gray lines in Fig. 3.3(a). The lower effective mass and barrier height

only increases the tunneling overlap. At high $k_{||}$ in panels (b) and (c) the hBN lines show negligible correction to the vacuum lines.

While at first glance the assumption of an isotropic barrier with separable dispersion seems drastic, the recovered tunneling characteristics show good agreement with experimental data in their work, with only slight deviations at low V_b. Furthermore, later work by de la Barrera, et. al [ref]. presented a more detailed calculation that compensates for the imaginary bands in hBN's out-of-plane direction. Notably, the more detailed treatment yielded only a minor correction to the bare-bones approximation of Britnell, et. al. Therefore, the Bardeen approach can be readily applied to our hBN-filled PTS devices with the caveat that tunneling effective mass m^* is renormalized by the hBN barrier.

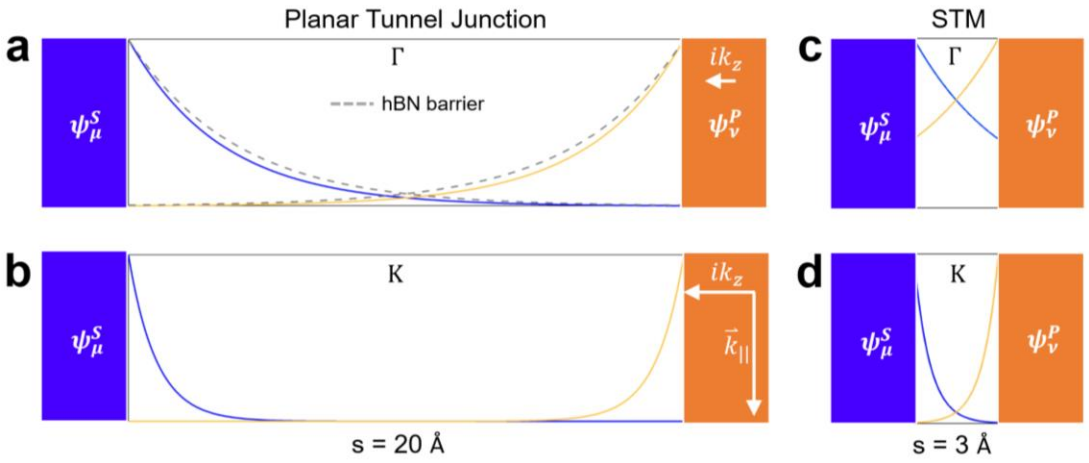

Figure 3.3: Comparison of exponential decay in PTS vs. STM. (a-b) Calculated PTS tunneling between amorphous metal and graphene when $V_b = 1\ V$ at two different in-plane momenta $\vec{k}_{||}$. The graphene ψ_μ^S (blue rectangle) and probe ψ_ν^P (orange rectangle) are separated by 20 Å the barrier height is approximated as 3.5 eV (graphene's work

function - eV_b). Both wave functions exponentially decay into the barrier with decay constant $\kappa = ik_z$ given in the main text. At the Γ point, $\vec{k}_{||} = 0$ and $\kappa = 0.3\ \text{Å}^{-1}$, depicted by a short left-pointing arrow. At the K point, $\vec{k}_{||} = 1.7\ \text{Å}^{-1}$ and $\kappa = 1.8\ \text{Å}^{-1}$, represented by a longer white arrow pointing to the left. Gray, dashed lines illustrate how the decay would be different if the vacuum barrier were replaced with hBN. In the hBN, the barrier height is assumed to be 0.5 eV (energy difference between hBN band and graphene's fermi level – eV_b), and the effective mass is assumed to be $0.5m_0$, discussed in the main text. (c-d) Tunneling with a shorter barrier in the STM. Graphene and the probe are separated by 3 Å, and the wave functions show a larger overlap as a result.

3.7 Inelastic Tunneling into Graphene

In Section 3.5, it was established that the Bardeen matrix element $M_{\mu\nu}$ is strongly dependent on the parallel momentum $\hbar k_{||}$. This dependence is illustrated in Fig. 3.3, where the wave function decay into the barrier from the sample and probe is shown as blue and orange lines, respectively. In Fig. 3.3(a), the in-plane momentum is low, and as a result the imaginary component of k_z is also, leading to moderate overlap between sample and probe wave function in in the barrier. Panel (b) of the same figure shows the case where in-plane momentum is high, which causes a vanishingly small overlap of wave functions in the barrier.

Tunneling into graphene near its Fermi level poses a major problem: The K and K' points are at high momentum values ($|\vec{k}| \sim \frac{4\pi}{3\sqrt{3}a} = 1.7A^{-1}$), and thus $M_{\mu\nu}$ coupling a probe to graphene near E_F is expected to be vanishingly small. Because elastic tunneling is suppressed, inelastic tunneling, in which $E, \vec{k}_{||}$ and as a result κ are subject to change, becomes dominant. The primary matrix element $M_{\mu\nu}$, is greatly enhanced, for instance if tunneling electrons scatter to low momentum near the Γ point (where $|\vec{k}_{||} = 0|$). Phonon modes in graphene, hBN, or both have energies $\{\hbar\omega_0, \hbar\omega_1, \hbar\omega_2, \dots\}$, and corresponding momenta $\{\hbar\vec{k}_0, \hbar\vec{k}_1, \hbar\vec{k}_2, \dots\}$ that may connect graphene's fermi surface to momenta near Γ. In this way, the momentum mismatch is accounted for, enabling tunneling current to flow above a certain threshold $eV_b = \hbar\omega_i$.[22]

Excitation of each additional mode opens another tunneling channel proportional to $g(eV_b - \hbar\omega_i)\Theta(eV_b - \hbar\omega_i)$ if $V_b > 0$, and $g(eV_b - \hbar\omega_i)\Theta(eV_b - \hbar\omega_i)$ if $V_b < 0$, resulting in a series of tunneling conductance enhancements. The overall tunneling conductance has parallel contributions from each available tunneling channel and can be written:

$$\frac{dI}{dV_b}(eV_b) \propto \sum_i [g(eV_b - \hbar\omega_i)\Theta(eV_b - \hbar\omega_i) + g(eV_b + \hbar\omega_i)(1 - \Theta(eV_b + \hbar\omega_i))] \tag{3.29}$$

Where $g(eV_b)$ is the BLG density of states and $\Theta(\epsilon)$ is the Heaviside function. Taking the derivative of Eq. 3.78 with respect to eV_b,

$$\frac{d^2I}{dV_b^2}(eV_b) \propto \sum_i [g(eV_b - \hbar\omega_i)\delta(eV_b - \hbar\omega_i) - g(eV_b + \hbar\omega_i)\delta(eV_b + \hbar\omega_i))] \tag{3.30}$$

$$\frac{d^2I}{dV_b^2}(eV_b) \propto \sum_i [\delta(eV_b - \hbar\omega_i) - \delta(eV_b + \hbar\omega_i)] \tag{3.31}$$

Therefore, phonon-assisted tunneling enhancements are associated with sharp peaks in tunneling $\frac{d^2I}{dV_b^2}$ spectra that are antisymmetric about $eV_b = 0$ and peak energy corresponds to phonon energy $\hbar\omega_i$.[1,23,24] Experimental signatures of inelastic tunneling into graphene are presented in chapters 5 and 6.

3.8 Tunneling into Many-Body States

As discussed in Section 2.16, Landau levels (LL) in graphene quench kinetic energy, resulting in exchange-enhanced spin and valley polarized states. This spontaneous polarization of quantum Hall states has been extensively studied with transport measurements, which can have an energy resolution of several μeV.[25–28] However, transport measurements can only indirectly measure gap energies, and it is thus important to discuss tunneling spectroscopy of exchange-split LLs.[29] While PTS is fully compatible with dilution refrigerator temperatures and high DC magnetic fields, it presents several issues to the measuring correlated electronic states discussed above. Firstly, the tunneling probe is a large metal plate that is ~ 2 nm away from the graphene sample, possibly screening coulomb repulsion between electrons with a mirror potential. Secondly, compared to an STM tip, the PTS probe is far from the graphene

sample. As a result, phonon-enhanced inelastic tunneling channels are the only signal available to PTS devices with few layer hBN barriers. Therefore, direct access to sensitive correlated gaps is blurred by the necessary condition $|eV_b| > \hbar\omega_p$, and further blurred by enhancements in dI/dV_b due to multiple phonon channels.

3.9 Measurement Scheme

The tunneling spectroscopy data presented in chapters 5,6 and 7 were acquired in a Janis 12 T VariTemp cryostat system at liquid helium temperature. The measurement apparatus is shown in Fig. 3.4, where the cryostat is outlined with a red rectangle. The sample is plugged into the end of a probe arm that has cryogenic coaxial cables (LakeShore type SC) running from a sample socket to a hermetic electrical connection.[3] Before being measured, the probe is lowered into the cryostat sample space, where it sits in helium exchange gas. The electrical connection on the top of the probe that sits outside of the cryostat is plugged into the tunneling electrical instrumentation, outlined in blue. All temperature control and magnetic field control is done with the instruments outlined in yellow.

[3] Before samples are wirebonded and cooled in the Janis cryostat, they are first characterized at room temperature, then 80 K, in a LakeShore cryogenic probing station. Details on system cooling and sample exchange in the Janis cryostat are provided in Appendices B and C, respectively.

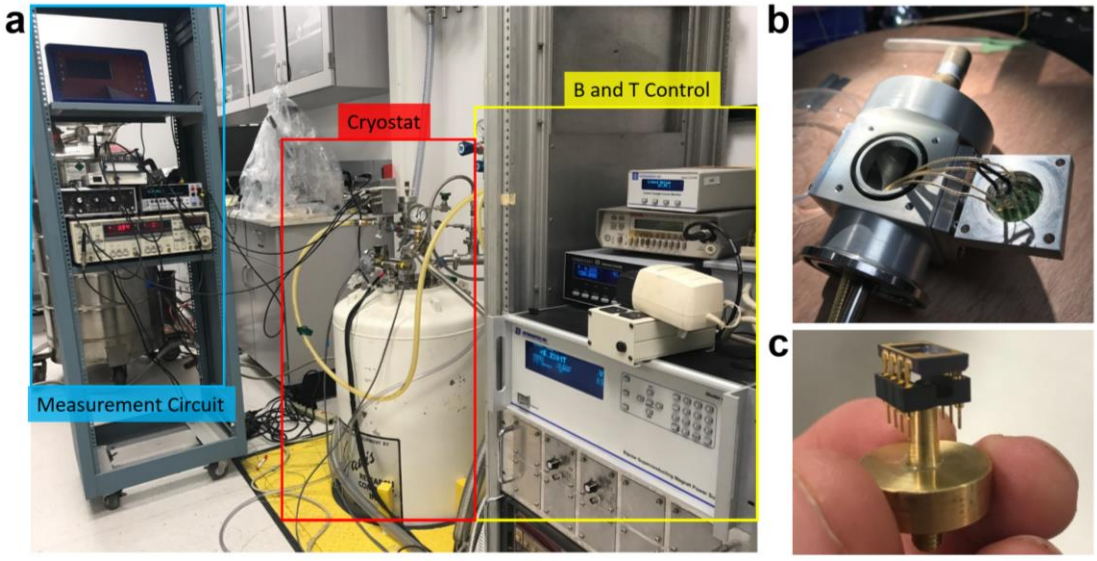

Figure 3.4: Overview of the measurement instrumentation. (a) The Janis cryostat with 12 T superconducting magnet is outlined with a red rectangle. While being measured, devices are plugged into the end of a long probe that is lowered into the cryostat (recessed into the floor). Hardware for controlling the temperature and magnetic field in the cryostat is outlined in yellow. Tunneling electronics are placed on a rack, outlined with a blue rectangle, that is near the Janis cryostat. (b) Cryogenic coaxial cables are used to enhance the signal to noise ratio in the tunneling measurement. They are wired to a hermetically sealed multipin connector at the top of the probe. (c) A chip carrier containing a wire bonded complete devices is plugged into a DIP socket. The legs of the dip socket shown in the figure have not yet been wired to the center conductor of the cryogenic coaxial cables.

A schematic of the tunneling circuit is shown in Fig. 3.5. The tunneling measurement technique uses a voltage divider to add the AC output of a lock-in

amplifier (SRS830 output V_{AC} = 1 mV at 13 Hz) to the DC output from an DAC (National Instruments $|V_{probe}| < 1$ V). The summed signal is applied to the tunneling probe, and the drain current is collected at the graphene contact. The drain signal is then amplified by a current to voltage preamplifier (Ithaco 1211 or Keithley). The amplified signal is connected to a BNC-T, with one end measured by the computer *via* an analog to digital converter (ADC), and the other end connected to the lock-in amplifier. The output of the lock in amplifier, or "dI", is measured by a separate channel in the ADC. The control software, Mezurit2, computes the ratio of the input and output signals from the lock-in to determine $dI/dV_b(V_b)$. Additionally, silver paint is used to connect a gate lead directly to the p-Si that underlies the PTS/SiO_2 heterostructure. The potential on this lead V_G is controlled with a source meter (Keithley 2400). Typical ranges of $|V_G|$ are below 80 V. Figure 3.6(a) shows the tunneling measurement conducted in Mezurit2 under normal operation, with the yellow and blue line traces corresponding to the measured $I(V_b)$ and $dI/dV_b(V_b)$ channels. The measurement electronics are shown in Fig. 3.6(b).

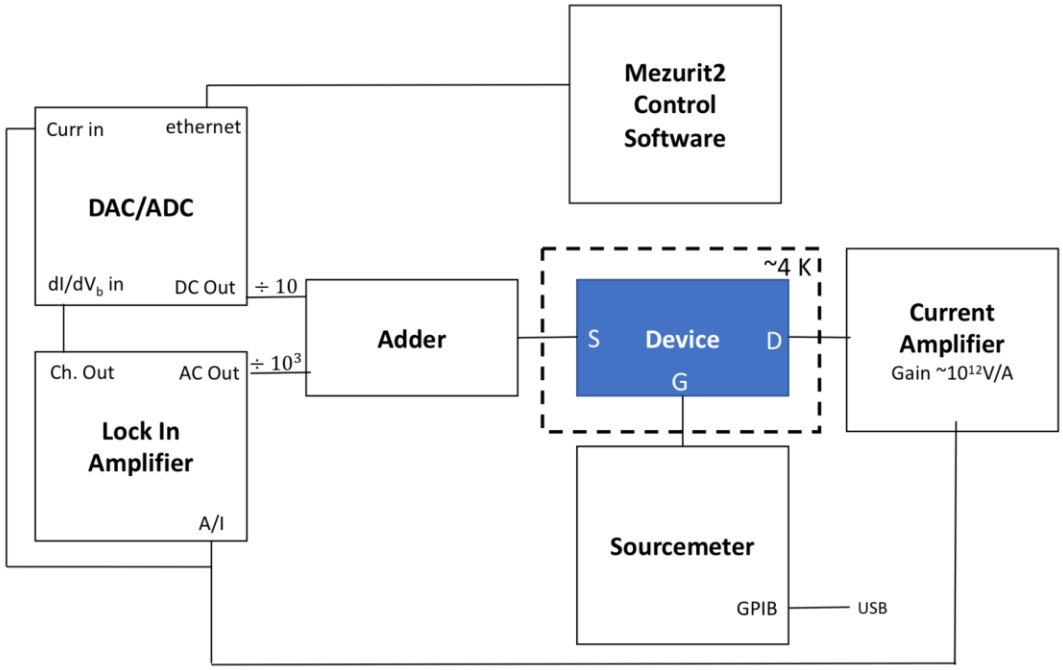

Figure 3.5: Tunneling measurement circuit diagram. An adder box is used to offset the analog output of a lock-in amplifier with a DC voltage set by a digital to analog converter (DAC). The summed signal is fed into the cryostat *via* cryogenic coaxial cables and applied between the tunneling probe and graphene. The resulting signal is collected and amplified with a current to voltage preamplifier. The amplified signal is connected to the analogue input (A/I) of the lock in amplifier. The output of the lock-in amplifier is connected to an analog to digital converter (ADC) to be stored by the control software, Mezurit2. Additionally, a GPIB-controlled source meter is connected to the silicon back gate of the tunneling device to apply a back-gate voltage V_G.

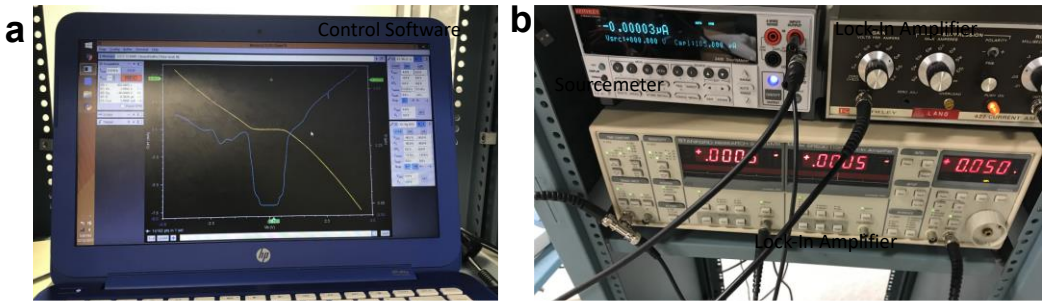

Figure 3.6: Images of the control software and tunneling measurement instruments. (a) The control laptop controls V_b and V_G and measures tunneling current I and differential conductance dI/dV_b. (b) Image of the tunneling electronics during a measurement. Note that in this image a Keithley current preamplifier is used, rather than the Ithaco instrument mentioned in the main text.

In order to create a $dI/dV_b(V_b, V_G)$ map—a main focus of this thesis—line traces of $I(V_b)$ and its (analog) derivative $dI/dV_b(V_b)$ are collected at multiple values of V_G. Figure 3.7(a) shows typical current and conductance characteristics in blue and black, respectively. These traces were collected at 4.2 K with $V_G = -10\ V$. The traces have several prominent features that are analyzed and interpreted in Chapter 6. Figure 3.7(b). The gate dependence $dI/dV_b(V_b)$ is demonstrated by the data in Fig 3.7(b), where spectra taken at three different values of V_G are shown. The traces are vertically offset for clarity, and they show yellow (purple) coloration at high (low) intensity to illustrate how they are converted to a colormap. Figure 3.7(c) shows a $dI/dV_b(V_b, V_G)$ map compiled from 160 different $dI/dV_b(V_b, V_G)$ traces at incremental values of V_G.

High and low intensity of dI/dV_b are represented by yellow and purple regions, respectively.

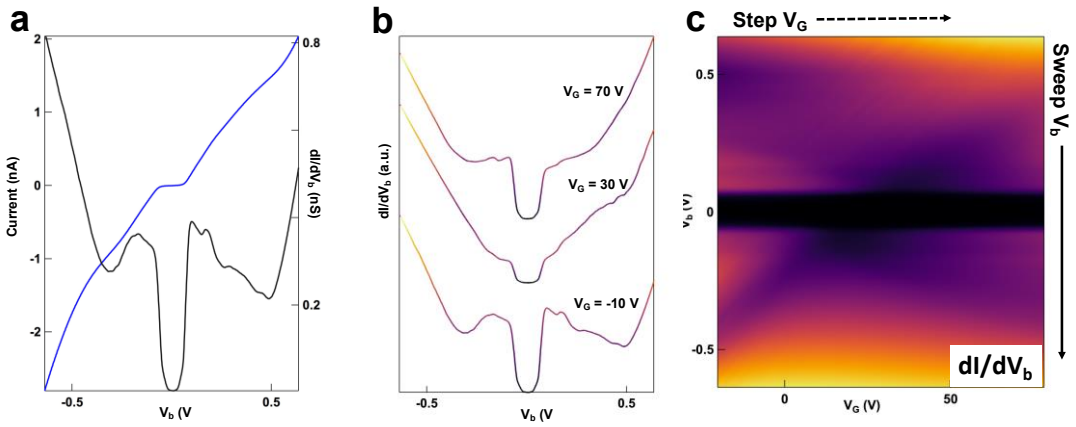

Figure 3.7: Creating tunneling $dI/dV_b(V_b, V_G)$ maps. (a) The tunneling characteristic $I(V_b)$ at a constant $V_G = -10\ V$ is plotted in blue, with its corresponding (analog) derivative dI/dV_b shown in black. (b) Tunneling $dI/dV_b(V_b)$ spectra taken at three different values of V_G. The traces are vertically offset for clarity, and they show yellow (purple) coloration at high (low) intensity to illustrate how they are converted to a colormap. **(c)** 160 different $dI/dV_b(V_b, V_G)$ traces at incremental values of V_G are compiled together to create a $dI/dV_b(V_b, V_G)$ map. High and low intensity of dI/dV_b are represented by yellow and purple regions, respectively. Analysis and interpretation of this data is presented in Chapter 6.

3.10 Summary

To summarize this chapter, I began with a general overview of tunneling between two conductors. Next, I used the TH approximation to derive that the differential tunneling conductance between a sharp conducting probe and a planar sample is given by the LDOS of the sample evaluated at the position of the probe. Afterwards, I continued on to arguably the most relevant section to the experimental results of this thesis, in which I derived that a planar probe hosting nearly free electrons can directly probe the density of states of a nearby sample. Inelastic tunneling, dielectric barriers, and the tunneling measurement were presented afterward. All of these sections will play a vital role in analyzing and interpreting the tunneling measurements presented in Chapters 5, 6 and 7. In the next chapter, however, we will turn to the fabrication employed to realize planar tunneling nanodevices.

References

(1) Wolfe, E. L. *Principles of Electron Tunneling Spectroscopy*; Oxford Science Publications, 1985.

(2) Schrödinger, E. An Undulatory Theory of the Mechanics of Atoms and Molecules. *Phys. Rev.* **1926**.

(3) Sakurai, J. J.; Napolitano, J. *Modern Quantum Mechanics*, 2nd ed.; Cambridge University Press, 2017. https://doi.org/10.1017/9781108499996.

(4) Griffiths, D. J. *Introduction to Quantum Mechanics*; Cambridge University Press, 2004.

(5) Shankar, R. *Principles of Quantum Mechanics*; Springer, 1980.

(6) Bardeen, J. Tunnelling from a Many-Particle Point of View. *Phys. Rev. Lett.* **1961**, *6* (2), 57–59. https://doi.org/10.1103/PhysRevLett.6.57.

(7) Chen, C. J. *Introduction to Scanning Tunneling Microscopy*; Oxford Scholarship Online, 2007.

(8) Lounis, S. Theory of Scanning Tunneling Microscopy. **2014**.

(9) Brar, V. W. Scanning Tunneling Spectroscopy of Graphene and Magnetic Nanostructures, UC Berkeley, 2010.

(10) Wong, D. Tuning Electrostatic Potentials for Imaging the Quantum Properties of Massless Dirac Fermions in Graphene, UC Berkeley, 2017.

(11) Tersoff, J.; Hamann, D. R. Theory of the Scanning Tunneling Microscope. *Phys. Rev. B* **1985**, *31* (2), 805–813. https://doi.org/10.1103/PhysRevB.31.805.

(12) Chen, C. J. Perturbation Approach for Quantum Transmission. *Mod. Phys.*

Lett. B **1991**, *05* (02), 107–115. https://doi.org/10.1142/S0217984991000149.

(13) Datta, S. *Quantum Transport, Atom to Transistor*; Cambridge University Press, 2005.

(14) Feenstra, R. M.; Jena, D.; Gu, G. Single-Particle Tunneling in Doped Graphene-Insulator-Graphene Junctions. *J. Appl. Phys.* **2012**, *111* (4), 43711. https://doi.org/10.1063/1.3686639.

(15) Britnell, L.; Gorbachev, R. V; Jalil, R.; Belle, B. D.; Schedin, F.; Mishchenko, A.; Georgiou, T.; Katsnelson, M. I.; Eaves, L.; Morozov, S. V; et al. Field-Effect Tunneling Transistor Based on Vertical Graphene Heterostructures. *Science (80-.).* **2012**, *335* (6071), 947–950. https://doi.org/10.1126/science.1218461.

(16) Britnell, L.; Gorbachev, R. V; Geim, A. K.; Ponomarenko, L. A.; Mishchenko, A.; Greenaway, M. T.; Fromhold, T. M.; Novoselov, K. S.; Eaves, L. Resonant Tunnelling and Negative Differential Conductance in Graphene Transistors. *Nat. Commun.* **2013**, *4* (1), 1794. https://doi.org/10.1038/ncomms2817.

(17) Kang, S.; Fallahazad, B.; Lee, K.; Movva, H.; Kim, K.; Corbet, C. M.; Taniguchi, T.; Watanabe, K.; Colombo, L.; Register, L. F.; et al. Bilayer Graphene-Hexagonal Boron Nitride Heterostructure Negative Differential Resistance Interlayer Tunnel FET. *IEEE Electron Device Lett.* **2015**, *36* (4), 405–407. https://doi.org/10.1109/LED.2015.2398737.

(18) Song, S. M.; Park, J. K.; Sul, O. J.; Cho, B. J. Determination of Work Function of Graphene under a Metal Electrode and Its Role in Contact Resistance. *Nano*

Lett. **2012**, *12* (8), 3887–3892. https://doi.org/10.1021/nl300266p.

(19) de la Barrera, S. C.; Feenstra, R. M. Theory of Resonant Tunneling in Bilayer-Graphene/Hexagonal-Boron-Nitride Heterostructures. *Appl. Phys. Lett.* **2015**, *106* (9), 93115. https://doi.org/10.1063/1.4914324.

(20) Kharche, N.; Nayak, S. K. Quasiparticle Band Gap Engineering of Graphene and Graphone on Hexagonal Boron Nitride Substrate. *Nano Lett.* **2011**, *11* (12), 5274–5278. https://doi.org/10.1021/nl202725w.

(21) Sachs, B.; Wehling, T. O.; Katsnelson, M. I.; Lichtenstein, A. I. Adhesion and Electronic Structure of Graphene on Hexagonal Boron Nitride Substrates. *Phys. Rev. B* **2011**, *84* (19), 195414. https://doi.org/10.1103/PhysRevB.84.195414.

(22) Zhang, Y.; Brar, V. W.; Wang, F.; Girit, C.; Yayon, Y.; Panlasigui, M.; Zettl, A.; Crommie, M. F. Giant Phonon-Induced Conductance in Scanning Tunnelling Spectroscopy of Gate-Tunable Graphene. *Nat. Phys.* **2008**, *4*, 627.

(23) Chandni, U.; Watanabe, K.; Taniguchi, T.; Eisenstein, J. P. Signatures of Phonon and Defect-Assisted Tunneling in Planar Metal–Hexagonal Boron Nitride–Graphene Junctions. *Nano Lett.* **2016**, *16* (12), 7982–7987. https://doi.org/10.1021/acs.nanolett.6b04369.

(24) Vdovin, E. E.; Mishchenko, A.; Greenaway, M. T.; Zhu, M. J.; Ghazaryan, D.; Misra, A.; Cao, Y.; Morozov, S. V; Makarovsky, O.; Fromhold, T. M.; et al. Phonon-Assisted Resonant Tunneling of Electrons in Graphene--Boron Nitride Transistors. *Phys. Rev. Lett.* **2016**, *116* (18), 186603.

https://doi.org/10.1103/PhysRevLett.116.186603.

(25) Zhang, Y.; Tan, Y.-W.; Stormer, H. L.; Kim, P. Experimental Observation of the Quantum Hall Effect and Berry's Phase in Graphene. *Nature* **2005**, *438* (7065), 201–204. https://doi.org/10.1038/nature04235.

(26) Velasco, J.; Jing, L.; Bao, W.; Lee, Y.; Kratz, P.; Aji, V.; Bockrath, M.; Lau, C. N.; Varma, C.; Stillwell, R.; et al. Transport Spectroscopy of Symmetry-Broken Insulating States in Bilayer Graphene. *Nat. Nanotechnol.* **2012**, *7* (3), 156–160. https://doi.org/10.1038/nnano.2011.251.

(27) Bolotin, K. I.; Ghahari, F.; Shulman, M. D.; Stormer, H. L.; Kim, P. Observation of the Fractional Quantum Hall Effect in Graphene. *Nature* **2009**, *462*, 196.

(28) Young, A. F.; Dean, C. R.; Wang, L.; Ren, H.; Cadden-Zimansky, P.; Watanabe, K.; Taniguchi, T.; Hone, J.; Shepard, K. L.; Kim, P. Spin and Valley Quantum Hall Ferromagnetism in Graphene. *Nat. Phys.* **2012**, *8* (7), 550–556. https://doi.org/10.1038/nphys2307.

(29) Song, Y. J.; Otte, A. F.; Kuk, Y.; Hu, Y.; Torrance, D. B.; First, P. N.; de Heer, W. A.; Min, H.; Adam, S.; Stiles, M. D.; et al. High-Resolution Tunnelling Spectroscopy of a Graphene Quartet. *Nature* **2010**, *467*, 185.

Chapter 4:

Tunneling Device Fabrication

This chapter is a detailed description of how to make two different types of tunneling nano-devices out of 2D materials. The first is the planar tunneling spectroscopy (PTS) device studied in Chapters 5, 6, and 7 which has a large area (~4 μm^2) flat tunneling probe. The second, a point tunneling contact (PTC) device detailed in Chapter 8, achieves much smaller probe areas by utilizing a mask hBN layer. These two devices follow the same general structure: a few-layer hexagonal Boron Nitride (hBN) acts as a tunneling barrier that separates a metallic tunneling probe from either graphene or bilayer graphene (BLG), which rests on a thicker (>20 nm) hBN substrate. Both device types also incorporate a back gate by assembling the heterostructure on an SiO_2/p-Si chip. However, while the two device geometries have similarities, their fabrication is markedly different. The first half of this chapter provides details on fabrication of the PTS device which incorporates a bottom-up assembly technique method adapted from Zomer, et. al.[1] The second half of this chapter focuses on fabrication of the PTC device which combines hBN etching and the pickup method which have both become ubiquitous in 2D materials heterostructure fabrication.[2]

4.1 General Heterostructure Assembly

Two dimensional materials can be assembled into layered heterostructures that have atomically sharp interfaces.[3] There are a variety of assembly procedures that can be divided into two general categories: bottom-up assembly and top-down assembly. Each technique has nuances which change depending on the intended heterostructure, however, the two technique types can be summarized with their respective general schemes, which are depicted in Fig. 4.1.

The transfer stage used to construct all heterostructures in this thesis (both bottom-up and top-down) is shown in Fig. 4.1(a). The stage consists of a diode heating element fastened between an XYϕ translational/tilt stage and a copper block where a target 2D material (e.g. hBN) can be placed. Adjacent to this stage is an XYZ micromanipulator to which an aluminum bracket can be fastened, holding a top 2D material (e.g. graphene) above the target substrate. Additionally, there is an adjustable focus zoom lens with a long (10 cm) working distance for imaging the top and target 2D materials. In this particular transfer stage, the top 2D material is lowered into contact with the target 2D material.

Bottom up transfers typically involve exfoliating the bottom layer directly onto an SiO_2/Si chip, and exfoliating the next layer onto a sticky, clear polymer on glass, then laminating the two together and dissolving away the polymer. Figure 4.1(b) shows one possible layout of the transfer stage in this process, in which the top material (graphene, in this case) is lowered into contact with the substrate flake (hBN, in this case) *via* a transfer bracket. Attached to the transfer bracket is an isolated flake of

graphene on MMA monomer, schematized in Fig. 4.1(c). Graphene rests on an island of MMA/tape which was cut out with a razor blade from the original thin layer of MMA that was spin coated over tape on glass. Figure 4.1(d) [i-iv] are optical images taken at different stages of the transfer process: (i) is a graphene flake exfoliated on clear MMA monomer; (ii) is an ideal hBN substrate on SiO_2; (iii) shows the graphene being lowered into contact with the hBN and (iv) is the complete heterostructure after the MMA has been dissolved away.

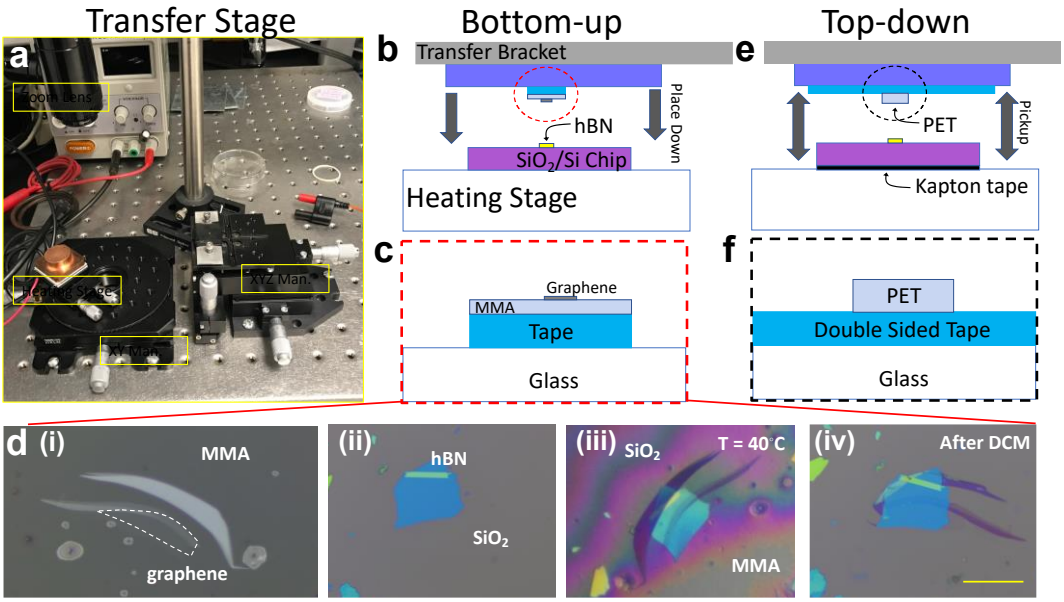

Figure 4.1: Two methods of heterostructure assembly. (a) Image of the transfer stage (b) Side-view schematic of the bottom-up transfer technique in which a transfer bracket (gray) is used to lower graphene in contact with hBN (yellow rectangle) on SiO_2 (lavender), which rests on a heated copper transfer stage (orange). (c) Zoom in of the graphene assembly. Graphene is isolated on a cutout square of MMA/Tape that is supported by a glass slide. (d)[i-iv] optical microscope images taken during the transfer

process. Graphene (outlined in white) on MMA [i] and hBN on SiO_2 [ii]. The graphene on MMA is lowered into contact with hBN on SiO_2 in [iii] and the MMA changes color as it comes in contact with SiO_2, with multicolored lines resulting from thin film interference. Following removal of MMA with dichloromethane (DCM), graphene rests on hBN [iv]. The scale bar is 20 μm. (e) Side-view schematic of the top-down transfer technique, in which PET is used to pick up hBN (yellow) off of SiO_2 (lavender). In this scheme the SiO_2 chip is fixed to the copper stage (orange) with double-sided Kapton tape (black). (f) Zoom in of the PET assembly where a square of PET is fastened to a glass slide with double-sided tape.

Rather than place flakes on top of each other, one by one (as is done with the bottom up method), the top down approach uses a sticky polymer (in this case, PET) to pick up a top flake, then sequentially pick up subsequent layers. Figure 4.1(e) shows one possible layout of the transfer stage in this process, in which PET fixed to a glass slide is lowered into contact with the target flake (hBN, in this case) *via* a transfer bracket. An up-close schematic of the PET/glass assembly is shown in Fig. 4.1(f). A small (1 mm^2) square of PET is fixed to a glass slide with double sided tape. When the PET is brought in heated contact with the hBN, it deforms, promoting adhesion between the two. The PET is then retracted, peeling the hBN off of SiO_2. This process is repeated in order to pick up subsequent 2D materials until the desired heterostructure is assembled. Once the PET has assembled the desired heterostructure, it is then melted

off of the double-sided tape and onto SiO_2. Finally, the PET, which overlays the heterostructure is removed with DCM and the transfer process is complete.

4.2 PTS Heterostructures: Bottom-Up Dry Transfer Method

In order to assemble the PTS heterostructures studied in Chapters 5, 6, and 7 we first exfoliate hBN onto SiO_2 (details on exfoliation technique are provided in Appendix A). Suitable hBN substrates that are flat, ~20 nm thick, and large (>400 μm^2) are then identified using bright field, dark field (DF) and differential interference contrast (DIC) modes in an optical microscope (Zeiss Axioscope A1). A representative, blue substrate hBN is shown in Fig. 4.1 (d)[ii] where the scale bar is 20 μm. Concurrently, a 1:12 solution of methyl methacrylate (MMA) monomer in methyl isobutyl ketone (MIBK) is spin coated on a transparent piece of tape stuck on a 1" square glass at 1200 rpm for 1 minute. Graphite is then exfoliated onto the MMA/Tape/glass substrate as outlined in Appendix A. A droplet of water is used to seal the graphite/MMA/tape/glass square face to a black surface, enhancing the imaging contrast. In this configuration, the green color contrast for thin (<6 layer) flakes of graphene is approximately 1.5% * N_{Layers}. Using this relation, monolayer graphene of suitable size (typically > 300 μm^2 with aspect ratio < 0.25) are identified. Next, a fresh razor blade is used to cut a small (~1 mm^2) square around the chosen graphene flake. All MMA/tape except for the square under and around the graphene is then removed. A diagram and optical image of graphene on MMA ready to be transferred are shown in Figs. 4.1(c) and 4.1(d)[i], respectively.

The substrate hBN/SiO_2/Si chip is placed on top of the level copper transfer stage at room temperature. Next, the substrate hBN is located with the zoom lens. The graphene/MMA/tape/glass square is then fixed via double sided tape to an aluminum bracket, that is then bolted to the transfer stage XYZ manipulator with the graphene facing down. With the Z manipulator fully extended, the graphene is shifted in the XY plane until it is above the substrate hBN in the correct orientation. Next, the hBN is gently rotated with a pair of tweezers until it has the desired orientation with respect to the graphene. This orientation may change depending on the objective geometry` of the final device.

With both flakes in a favorable orientation, the graphene is lowered to within 1 mm of the target hBN, as determined by the difference between their respective focal planes in the zoom lens. After final adjustments to the relative XY alignment of the two flakes is made, the graphene is lowered until the SiO_2/ MMA contact area is ~40 μm from the target flakes, which remain slightly separated. The diode heating element is then ramped at 1 $^{\circ}$C/min until the transfer stack has reached 40 $^{\circ}$C (as indicated by the temperature of the transfer stage). By the time the stack has reached 40~$^{\circ}$C, the MMA polymer has relaxed, bringing the target flakes into contact. Additional lowering of the graphene ensures adequate adhesion between the MMA and chip, which will later be lifted off of the stage by the bracket. Once the transfer has reached 40 $^{\circ}$C, the diode heating element is turned off and the transfer is left to cool to room temperature.

Finally, the bracket is slowly lifted, bringing the entire assembly—chip, hBN, graphene, MMA/tape and glass slide—with it. The glass square is gently removed from

the transfer bracket and placed in a dichloromethane (DCM) bath for 15 minutes at room temperature and 15 minutes at 40°C. After letting the bath cool to room temperature for 15 minutes, the chip is then removed with tweezers from the DCM into a drizzle of acetone for 5 seconds, then a 5 second rinse of isopropanol. Once the chip is gently blown dry with UHP N_2 gas, the first transfer is complete.

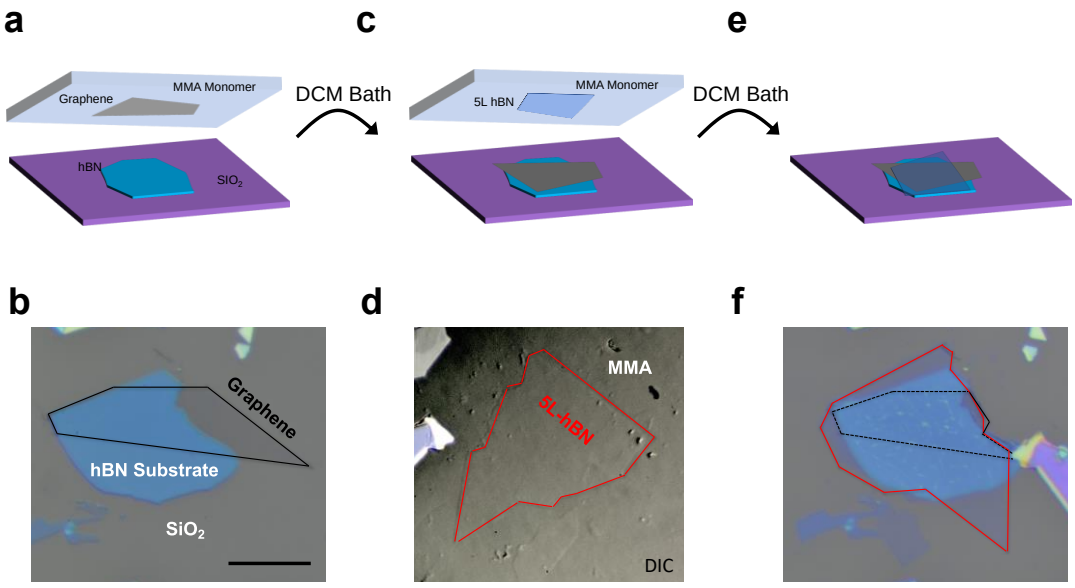

Figure 4.2: Bottom-up assembly of a PTS heterostructure. (a) Cartoon schematic of graphene (gray) resting on methyl-methacrylate (MMA) monomer to be placed on top of substrate hBN (blue) on SiO_2 (b) Graphene / hBN heterostructure prior to being capped by a tunneling barrier. Graphene is outlined with a black line. Scale bar is 20 μm. (c) Schematic of thin hBN on MMA to be placed on top of the graphene / hBN heterostructure (d) Thin (5 layer) hBN exfoliated on MMA and imaged in differential interference contrast (DIC) mode. The thin hBN is outlined with a red line. (e) Cartoon

and (f) optical micrograph of the complete heterostructure after transferring thin hBN on top of the stack in (b).

The transfer process discussed above is repeated to cap the graphene / hBN (or BLG / hBN) heterostructure with a thin hBN tunneling barrier. Notably, thin layers of hBN have a green contrast of < 0.5%, making them undetectable to the human eye in bright field imaging. Additionally, thin hBN does not share graphene's incremental increase in green contrast with number of layers. Therefore, we employ a combination of differential interference contrast (DIC) and tapping mode atomic force microscopy (AFM, discussed in Section 4.5) to locate and characterize thin hBN tunneling barriers before they are transferred.

Figure 4.2(d) shows a representative DIC image of 5-layer (confirmed by AFM) hBN outlined in red on MMA. The flake thickness was determined to be 2 nm by AFM. A cartoon of the hBN on MMA is shown in Fig. 4.2(c) as a blue assembly hovering above a graphene/hBN heterostructure. The located characterized and isolated tunneling hBN is transferred on graphene/hBN, which is assembled beforehand according to Fig. 4.2(a) and Fig. 4.2(b). A cartoon and an optical image of the complete PTS heterostructure are shown in Figs. 4.2(e) and 4.2(f), respectively, where graphene is outlined in black and thin hBN is outlined in red.

4.3 PTC Heterostructures: Top-Down "Pickup" Method

Although the transfer technique outlined above is straightforward and reliable (~80 % success rate) for assembling 2D materials heterostructures, it exposes the transferred layer to MMA, which compromises device quality.[4] In response to this shortcoming, recent assembly techniques incorporate a top-down approach, in which a top layer is picked up by a sticky polymer, then is used to pick up each subsequent layer *via* van der Waals attraction. In this way, interfaces are never exposed to polymer or solvent, leading to higher quality devices with enhanced device mobility, lower charge inhomogeneity and reduced contact resistance.[2,5,6]

In order to assemble the PTC heterostructures studied in Chapter 8, we employ a variation of a top-down transfer technique that incorporates polyethylene terephthalate (PET) polymer. First, a 1 mm^2 section is cut out of a sheet of PET and fastened to a 1" square glass slide with double sided tape. A schematic and optical image PET on glass are shown in Fig. 4.1(f). Concurrently, a sample of prepatterned hBN is attached to the transfer stage with double sided Kapton tape, heated to 40°C, and located in the zoom lens. The glass square with PET attached is then attached to the transfer stage bracket, bolted to the XYZ stage with PET facing down, and lowered within 1 mm of the target prepatterned hBN flake. The cartoon in Fig. 4.3(a) shows the PET approaching a prepatterned hBN (teal) on SiO_2 (lavender). Figure 4.3(c)[i-iii] captures the sequence of the PET pickup method. Initial contact between PET and the SiO_2, appearing as a yellow region left of the multicolored thin film interference stripes in Fig. 4.3(c)[i], is made ~40 μm from the mask hBN, seen as a small bunch of teal

polygons. As the stage heats past 50˚C, the PET is lowered further until it contacts the mask hBN, as depicted in Fig. 4.3(c)[ii]. Once the PET/ SiO_2 contact region extends ~20 μm past the mask hBN, and the stage temperature has reached 65˚C, the PET is slowly retracted, picking up the mask hBN. Flakes that have been picked up typically will change color, as shown in Fig. 4.3(c)[iii]. Whereas the cluster of hBN flakes appeared to be light blue in Fig. 4.3(c)[i], after being picked up they appear gray-white in Fig. 4.3(c)[iii]. Notably, this image was taken directly after the pickup, when hBN (the gray cluster of shapes) hovers ~1mm above its former substrate SiO_2 which is visible as a purple background. The yield for this pickup step is nearly 100 %.

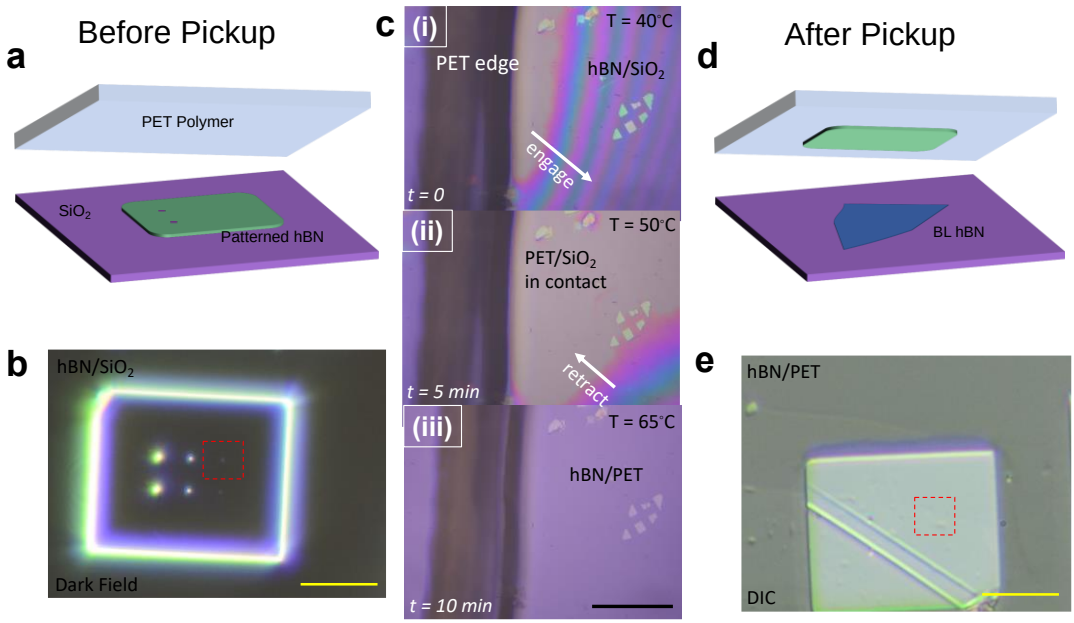

Figure 4.3: Top-down assembly of a PTC heterostructure. (a) Schematic of prepatterned mask hBN (teal) resting on SiO_2 (lavender) with a clean PET polymer square before contact (b) Dark field optical image of mask hBN. Etched holes of various sizes are visible as an array of bright points within the bright rectangular edge of the mask hBN. The scale bar is 10 μm. (c) Sequence of the PET pickup process: (i) before the PET overlays the mask hBN; (ii) when PET is in full contact with mask hBN; and (iii) after the PET has been retracted and the mask hBN has been picked up. (d) Schematic mask hBN (teal) now resting on PET (lavender) with its underside exposed. Below the PET, the SiO_2 has been replaced with a thin layer of hBN that will be picked up next. **(e)** Differential Interference Contrast (DIC) image taken of the underside of the mask hBN shown in (b).

After the top layer mask hBN is picked up, it is then used to lift thin hBN off of SiO_2, as schematized in Fig. 4.3(d). The process is repeated to pick up graphene or BLG next, followed by an hBN substrate and graphite back gate. Once the desired heterostructure has been assembled on PET, it is then placed down on a clean SiO_2/Si chip by heating the stage slowly to 125 ˚C, which laminates the PET to SiO_2. Finally, the sample is placed overnight in a bath of DCM at 50 ˚C, rinsed with a stream of acetone then isopropanol and blown dry with clean N_2 gas.

4.4 Electron Beam Lithography

Electron beam lithography (EBL) is used to define a polymer mask for patterning electrodes on both device types (PTS and PTC) as well as etching the PTC mask hBN (Section 4.6). Figure 4.4 shows a step by step sequence of the EBL process used to define electrodes on a PTS heterostructure. A complete heterostructure is first spin coated with a bilayer of PMMA resist (Microchem 495 70 sec @ 3000 rpm / 950 for 70 sec @ 4000 rpm) then baked at 185 ˚C for 5 min. Figures 4.4(a) and 4.4(b) are a side-view schematic and optical image of the PTS heterostructure overlaid with PMMA (teal) where substrate hBN in Fig. 4.4(b) is yellow and tunneling hBN and graphene are outlined in blue and black, respectively. The chip is scratched with a diamond scribe several millimeters from the heterostructure. The XY coordinates of the heterostructure are recorded with respect to a known spot on the diamond scribe scratch and used to pattern a grid of alignment markers around the heterostructure. All patterning is done with an FEI SEM/FIB DualBeam system with a 30 kV accelerating voltage, 40 μm

aperture, and beam currents of ~40 pA (small features) and ~1 nA (large features). Patterning is controlled with an external beam blanker and Nano Pattern Generating System (NPGS) control software (see appendix for more details on exposure parameters).

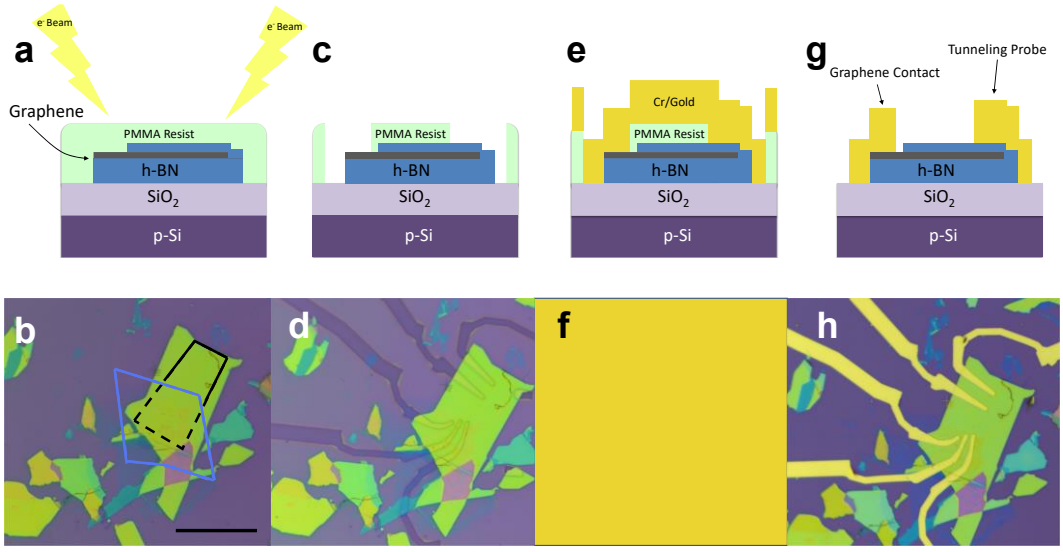

Figure 4.4: Cartoon schematic of electron beam lithography. (a) The tunneling van der Waals heterostructure consisting of graphene (gray) sandwiched between tunneling and substrate hBN layers (blue) which rests on SiO_2/Si (purple/lavender) is spin coated with PMMA resist (teal). Specific areas of the resist are exposed to an electron beam. (b) Optical microscope image of tunneling heterostructure (substrate hBN is yellow, graphene and thin hBN are outlined in black and blue, respectively) under a layer of PMMA. (c) Cartoon and (d) optical image after development, where the exposed regions of PMMA have been removed. **(e,f)** Cartoons and optical images taken after

thermal evaporation of Cr/Au over entire chip. **(g)** Cartoon and **(h)** optical image taken of a complete device after lifting off the remaining PMMA.

After the grid of alignment markers has been patterned in the SEM, the chip is developed (1 min MIBK/IPA 1:2, 1 min IPA, 1 min deionized H_2O) to remove exposed PMMA resist. Images of the developed alignment markers are used in Computer Assisted Design (CAD) program to draw a unique electrode pattern for that heterostructure. The process of patterning and development discussed above is repeated for the electrode pattern, following an alignment step in the SEM. A schematic and representative optical image of developed electrode patterns are shown in Figs. 4.4 (c) and 4.4(d), respectively. Once the electrode pattern has been developed, the sample is mounted in a thermal evaporator for depositing metal. Electrical contacts consisting of 2-5 nm Cr sticking layer and 50-115 nm Au are deposited at rates of 0.1 and 0.8 Å/sec, respectively in a pressure $<10^{-6}$ Torr. Figures 4.4(e) and 4.4(f) are a schematic and cartoon representation of the sample directly after thermally evaporating Cr/Au. To complete the electrode fabrication, the sample is then soaked in acetone overnight at 50 $^{\circ}$C, agitated with a Pasteur pipet until unwanted Au/Cr is lifted off, then rinsed with isopropanol and blown dry. Figures 4.4(g) and 4.4(h) show a schematic and optical image of the completed EBL process.

4.5 Atomic Force Microscopy Characterization

We used tapping mode in an Oxford Instruments CypherS atomic force microscope (AFM) within a glove box to determine the thicknesses of the tunneling and the supporting hBN layers of PTS devices. Figure 4.5(a) shows an AFM scan of a seven-layer hBN flake resting on polymer. This hBN flake acts as tunneling barrier in the completed device. Figure 4.5(b) shows a closeup AFM scan of the step edge between the hBN and underlying polymer. A corresponding line profile from this scan (shown in Fig. 4.5(c)) reveals that this hBN is 2 nm thick. Figure 4.6 is an AFM scan of the supporting hBN, which rests on an SiO_2/Si substrate. An optical micrograph of the completed device is displayed in the inset and contains a red square that outlines the region corresponding to the AFM scan. Figure 4.6(b) shows a line profile taken along the red line in Fig. 4.6(a). The profile indicates that this supporting hBN flake is 15 nm thick. The thicknesses of these two hBN layers are used to calculate the charge density (n) using a planar capacitor model, discussed in Chapter 5.

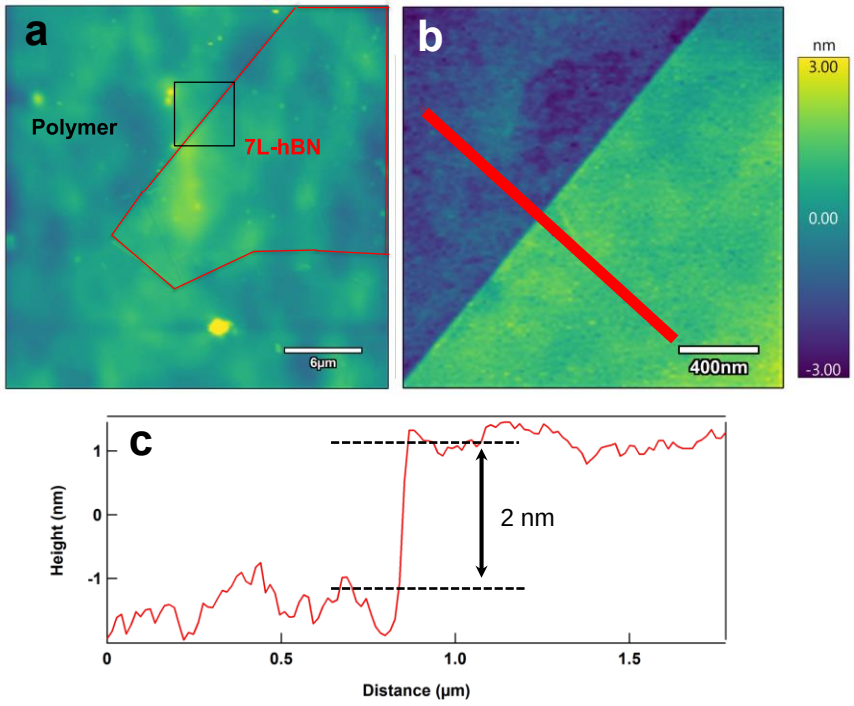

Figure 4.5: Atomic force microscopy (AFM) characterization of tunneling hBN on polymer. (a) Tapping mode AFM scan of a thin hBN flake (outlined in red) on polymer. (b) Zoom in AFM scan of the black outlined square in (a). (c) Line profile taken along the red line in (b).

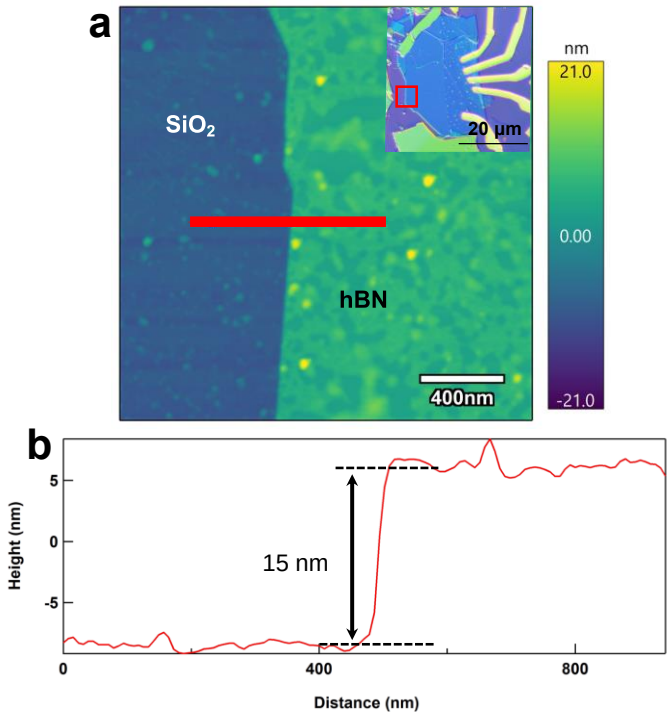

Figure 4.6: AFM characterization of substrate hBN. (a) Tapping mode AFM scan of the substrate hBN that rests on SiO_2. Inset: optical micrograph taken of the completed PTS device from which AFM scans are taken. The red square outlines the AFM-scanned region. (b) Line profile taken along the red line in (a). **(c)** Schematic of the van der Waals heterostructure showing graphene (gray), sandwiched between thin hBN (blue) and substrate hBN (also blue). The heterostructure rests on SiO_2 (lavender) which is grown on doped silicon (purple). Thicknesses of the thin hBN, substrate hBN and SiO_2 are labelled t_{hBN1}, t_{hBN2} and t_{SiO_2}, respectively.

4.6 Pre-patterning Mask hBN

Before creating the PTC heterostructure, a mask hBN is shaped with a combination of EBL and reactive ion etching (RIE). First, a suitable hBN flake (>1000 μm^2, ~50 nm thick) is located, and spin coated with PMMA resist, as schematized in Fig. 4.8 (b) where hBN (teal) lies below PMMA (clear). Next, EBL is used to define a uniform perimeter around the hBN, and an array of 6 holes inside the perimeter. The array consists of 3 sets of duplicate holes, with diameters d_T = 500, 200, 100 nm, respectively. Figure 4.8(c) depicts the sample after developing away exposed resist, where the remaining clear resist has 6 through-holes that expose the underlying teal hBN.

To etch away the exposed hBN, we use a 200 W RIE plasma (50 : 5 sccm SF_6 : O_2 at 100 mTorr). The hBN etching process is shown in Fig. 4.7. Figure 4.7(a) shows optical images of exfoliated, annealed hBN on SiO_2 after different cumulative etch times. In the top left panel, there are flakes of hBN that have various colors, indicating various flake thicknesses. One of the central flakes, marked with a red line, is yellow before any etching. After 10 seconds in the etching process described above, this same flake turns a slightly greener hue. As the cumulative etch time increases, this flake and all of its neighboring flakes turn blue and eventually disappear, indicating that they are etched away. To determine the etch rate, we performed AFM on the central yellow hBN flake after each subsequent etch. Figure 4.7(b) show the results in red and a best fit line in black. The hBN thickness decreases linearly with cumulative etch time, at a rate of ~ 1 nm/ sec.

A cartoon of the etching process is shown in Figs. 4.8(d) and 4.8(e), where the remaining PMMA has masked the hBN underneath, preventing it from being etched away. After the hBN has been etched, the remaining PMMA is removed in an acetone bath for 2 hrs at 50 ˚C. The mask hBN is then treated with a 200 W O_2 plasma (200 sccm O_2, 200 mTorr) for 1 min to increase pickup yield and reduce leftover PMMA contamination. This plasma cleaning is illustrated in Fig. 4.8(f).

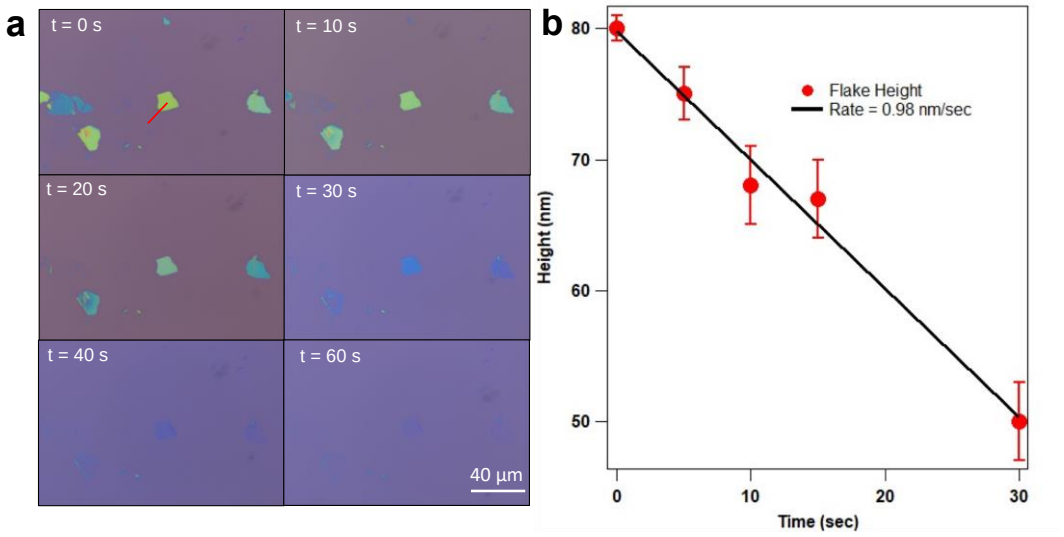

Figure 4.7: Reactive ion etching (RIE) of hBN: (a) Time-lapse of hBN in between sequential etching steps. The top left panel shows an hBN target flake as a yellow polygon on a purple SiO_2 background. Each subsequent panel is an optical microscope image of the same hBN flake after additional 10s of etching. (b) AFM characterization of the etch rate. Topography taken along the red line in (a) is taken after each etch interval. The data show that the etch rate is constant ~0.9nm/s.

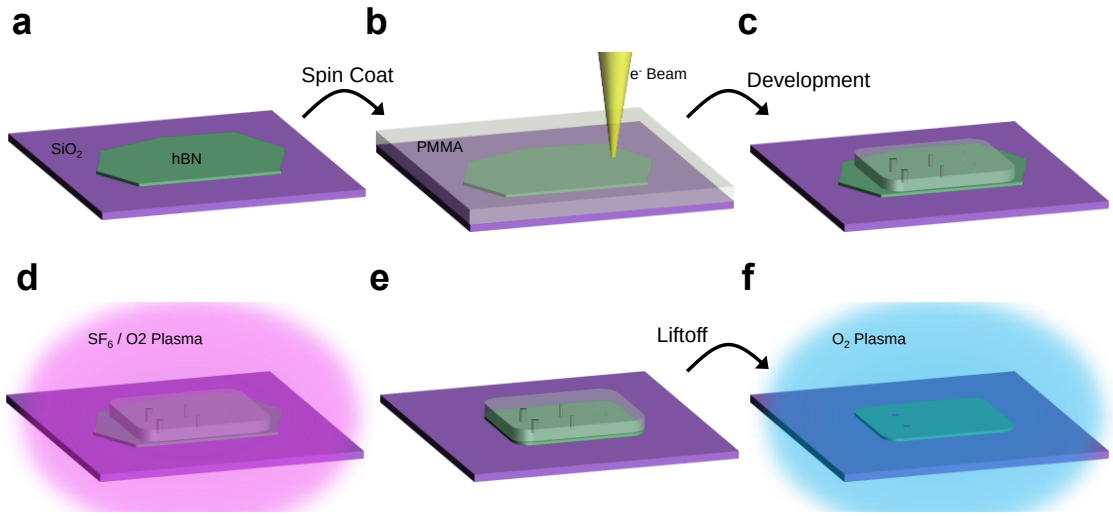

Figure 4.8: Pre-patterning the mask hBN. (a) An exfoliated flake of hBN (teal) rests on an SiO_2 chip (lavender). (b) A layer of PMMA is spin coated over the chip then patterned with an electron beam. (c) The exposed PMMA is removed with MIBK/IPA developer. (d) A reactive ion etcher is used to remove exposed hBN with reactive fluorinated species. (e) The remaining PMMA mask is removed by soaking the chip in acetone. (f) An additional plasma cleaning step removes contaminants atop the patterned hBN mask.

After pre-patterning mask hBN, we characterize the quality and nature of the etch using a combination of optical and atomic force microscopy (AFM). Figure 4.3(b) shows a dark field image of prepatterned hBN on SiO_2. In the image, six bright spots with varying intensities correspond to etched holes of varying sizes. Notably, the

smallest holes on the right are barely visible, indicating that their diameter is approaching the diffraction limit ~100 nm for this objective.

4.7 The Completed PTC Device

The PTC device relies on through-holes in a mask hBN to determine the shape of the top tunneling electrode. It is therefore important to characterize the size and shape of the holes etched in hBN. For a closer look at the morphology of the etched holes, we scanned the underside of the mask hBN with AFM, shown in the inset of Fig. 4.8(f). From the topography of the holes we extract the bottom diameter d_B.

After completing the device with another round of EBL/deposition, the tops of the probes are examined in an SEM. Figure 4.8(c-e) show SEM micrographs of the tops of the printed probes, which are false colored to be yellow-orange. Notably, there is a clear circular depression on the top of each probe, and the diameter of the circular depression is different in each probe. From this image, we extract the top diameter d_T. While the plasma clearly etched completely through the mask hBN, the orifice diameter on the top and underside of the flake (d_T and d_B) are significantly different. Scanning dozens of holes etched in hBN, we find that $d_B = d_T - t*0.5$ where t is the thickness of the hBN flake. Apparently, the etch is semi-anisotropic and forms a circular mesa structure mimicking a countersunk hole. This agrees with previous hBN etching techniques that use the etched mesa to contact the edge of encapsulated 2D materials.[6] Notably, the beveled hole mask can be used to straightforwardly pattern nanometer-sized point contacts which are difficult to make with conventional EBL.[7,8]

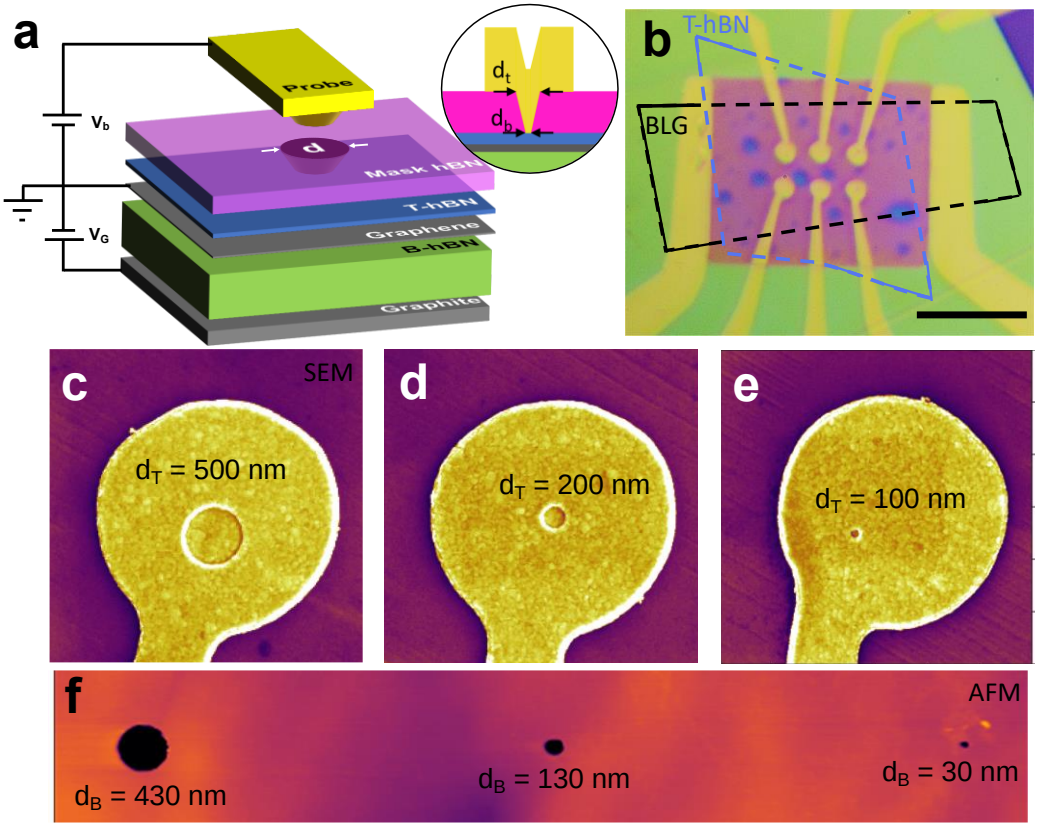

Figure 4.9: The completed PTC device. (a) Schematic of the device layout where a gold probe (yellow) fills a hole drilled in a mask hBN (pink). The gold probe is insulated from graphene (gray) by a few-layer hBN tunneling barrier (blue). The entire stack rests on a substrate hBN (green) which insulates the graphene from a graphite back gate. Inset: zoom-in schematic of the cross section of the filled hole in mask hBN. The diameters of top and bottom opening are labelled d_T and d_B. (b) Optical image of a completed PTC device with six tunneling electrodes overlaying a pink mask hBN. The tunneling hBN and underlying graphene are outlined in blue and black, respectively. (c-e) False color SEM images showing the top of each tunneling probe. Yellow-orange regions show the printed gold pad, and the magenta background is the

mask hBN. There is a circular depression near the center of each tunneling pad. The diameter of the circular depression is d_t.(f) AFM topography image of the underside of mask hBN once it is picked up. There are three noticeable holes, each with a different size.

In this chapter, I provided details on how to fabricate tunneling a nanodevices composed of graphene, bilayer graphene and hBN. These fabrication steps include well established, conventional processes such as electron beam lithography and thermal evaporation (Section 4.4) as well as new, unconventional methods such as anisotropic hBN etching (Section 4.6). All the of the outlined processes were utilized to fabricate two different device geometries, PTS and PTC. The PTS devices are the main experimental focus of the thesis, and PTC devices show promise for future quantum confinement experiments.

References

(1) Zomer, P.; Dash, S.; Tombros, N.; Wees, B. J. *A Transfer Technique for High Mobility Graphene Devices on Commercially Available Hexagonal Boron Nitride*; **2011**; Vol. 99. https://doi.org/10.1063/1.3665405.

(2) Wang, L.; Meric, I.; Huang, P. Y.; Gao, Q.; Gao, Y.; Tran, H.; Taniguchi, T.; Watanabe, K.; Campos, L. M.; Muller, D. A.; et al. One-Dimensional Electrical Contact to a Two-Dimensional Material. *Science (80-.).* **2013**, *342* (6158), 614–617. https://doi.org/10.1126/science.1244358.

(3) Haigh, S. J.; Gholinia, A.; Jalil, R.; Romani, S.; Britnell, L.; Elias, D. C.; Novoselov, K. S.; Ponomarenko, L. A.; Geim, A. K.; Gorbachev, R. Cross-Sectional Imaging of Individual Layers and Buried Interfaces of Graphene-Based Heterostructures and Superlattices. *Nat. Mater.* **2012**, *11* (9), 764–767. https://doi.org/10.1038/nmat3386.

(4) Yankowitz, M.; Ma, Q.; Jarillo-Herrero, P.; LeRoy, B. J. Van Der Waals Heterostructures Combining Graphene and Hexagonal Boron Nitride. *Nat. Rev. Phys.* **2019**, *1* (2), 112–125. https://doi.org/10.1038/s42254-018-0016-0.

(5) Ribeiro-Palau, R.; Chen, S.; Zeng, Y.; Watanabe, K.; Taniguchi, T.; Hone, J.; Dean, C. R. High-Quality Electrostatically Defined Hall Bars in Monolayer Graphene. *Nano Lett.* **2019**, *19* (4), 2583–2587. https://doi.org/10.1021/acs.nanolett.9b00351.

(6) Telford, E. J.; Benyamini, A.; Rhodes, D.; Wang, D.; Jung, Y.; Zangiabadi, A.; Watanabe, K.; Taniguchi, T.; Jia, S.; Barmak, K.; et al. Via Method for

Lithography Free Contact and Preservation of 2D Materials. *Nano Lett.* **2018**, *18* (2), 1416–1420. https://doi.org/10.1021/acs.nanolett.7b05161.

(7) Manfrinato, V. R.; Zhang, L.; Su, D.; Duan, H.; Hobbs, R. G.; Stach, E. A.; Berggren, K. K. Resolution Limits of Electron-Beam Lithography toward the Atomic Scale. *Nano Lett.* **2013**, *13* (4), 1555–1558. https://doi.org/10.1021/nl304715p.

(8) Handschin, C.; Fülöp, B.; Makk, P.; Blanter, S.; Weiss, M.; Watanabe, K.; Taniguchi, T.; Csonka, S.; Schönenberger, C. Point Contacts in Encapsulated Graphene. *Appl. Phys. Lett.* **2015**, *107* (18), 183108. https://doi.org/10.1063/1.4935032.

Chapter 5:

Planar Tunneling Spectroscopy of Graphene

This chapter presents and discusses planar tunneling spectroscopy (PTS) of graphene. While scanning tunneling spectroscopy (STS) has yielded significant insight on the electronic structure of graphene, experimental limitations of STS prevent it from exploring graphene in ultra-high magnetic fields. Recent developments in the assembly of heterostructures composed of graphene and hexagonal boron nitride have enabled a device-based alternative to potentially overcome these roadblocks. In this chapter we report planar tunneling spectroscopy (PTS) of graphene at magnetic fields up to 18 T that establishes a clear benchmark for measurement and analysis of graphene PTS. Our analysis reveals that PTS devices directly probe electronic structure features near and far from the Fermi level. Prior to this work PTS had not been shown to directly measure occupied and unoccupied states in graphene spectroscopically.

In Sections 5.2 and 5.3 the device layout and raw tunneling characteristics are introduced. Motivated by the characteristics of the raw tunneling spectra and prior works, a detailed treatment of the probe-sample coupling is given in Section 5.4, including a correction for probe top-gating effects. Next, the PTS measurement is simulated and compared to the experimental data to support the direct tunneling claim. This can be found in Section 5.5. With the ability to spectroscopically probe graphene away from the Fermi level comes the ability to directly probe graphene's unique Landau levels in the quantum Hall regime. Section 5.6 shows and analyzes tunneling

spectra taken in a perpendicular magnetic field. From the LL spectra, graphene's one fitting parameter, v_F—an analogue of the speed of light—is extracted. Interestingly, we find that this speed changes depending on how full graphene is with charge. The changing Fermi velocity is investigated in Section 5.7. Section 5.8 presents tunneling spectra of graphene at unprecedented magnetic fields, where the LLs are highly degenerate and separated by large (>200 meV) cyclotron gaps. In this regime, we developed a new method to measure the degeneracy factor in graphene—based on tracking LLs as they are pulled to the Fermi level.

5.1 Introduction

As discussed in Chapter 3, STS is a powerful tool used to directly probe the electronic structure of graphene nanodevices.[1,2] Physical phenomena related to electronic correlations are prevalent in these nanodevices in ultra-high magnetic fields and lead to drastic changes in the graphene single particle density of states (DOS). However, STS measurements require extreme mechanical stability and are thus incompatible with experimental setups that incorporate ultra-high magnetic fields ($>$ 15 T).[3] While capacitance spectroscopy and electronic transport do not require the same mechanical stability as STS, they are limited to measure the DOS of a material at its Fermi Level.[4,5] The ability to examine electronic structure features at high magnetic fields both near and far from the Fermi level would enable a more comprehensive comparison with theoretical models including those that account for electron-electron interactions.[6] Previous works have realized device based alternatives for STS *via*

heterostructures composed of graphene and hexagonal boron nitride (hBN). These planar tunneling spectroscopy (PTS) devices have been used to study phonons[7, 8] and Andreev bound states.[9, 10] Landau Levels have also been probed but indirectly and at low magnetic fields.[11] These recent works, however, are inconsistent in treating the probe-sample coupling, a factor that can drastically alter quantitative conclusions drawn from tunneling spectra. A more complete account of the probe-sample coupling in graphene PTS is necessary for understanding graphene planar tunneling spectroscopy.

5.2 Device Layout

In order to develop a tunneling spectra benchmark for graphene PTS, we acquired gate tunable planar tunneling spectra and developed a systematic method for analyzing/interpreting such spectra. Consequently, our study enables the first direct measurement of numerous graphene electronic structure features at B = 18 T as they fill and empty with charge. As schematized in Fig. 5.1(a), the PTS device employed for our study consists of a van der Waals heterostructure with graphene (gray) sandwiched in between a bottom thick hBN flake (blue) and a top few-layer hBN flake (also blue). In this structure, the few-layer hBN flake acts as a tunneling barrier between the graphene sample and a top lying polycrystalline Cr/Au electrode (gold).[12] The thick hBN platform is used to screen graphene from the influence of extrinsic factors such as charge impurities.[13] The entire heterostructure rests on a 300 nm SiO_2 substrate. An optical micrograph of a completed PTS device is shown in Fig. 5.1(b). Numerous probe

electrodes that rest on top of a five-layer hBN flake are outlined in orange. One electrode contacts graphene directly and is outlined in black. The exposed (concealed) region of the graphene is denoted by a solid (dashed) line. Details on the sample fabrication are given in Chapter 4.

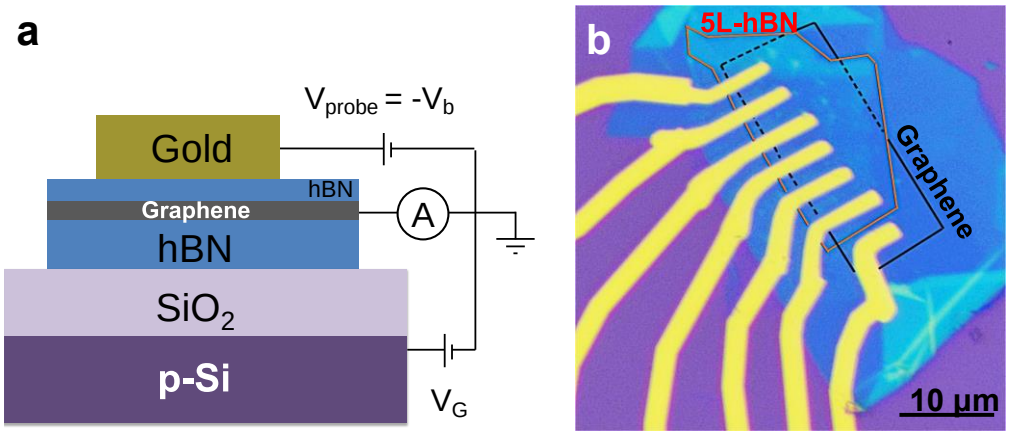

Figure 5.1: Planar tunneling spectroscopy (PTS) device schematic. (a) Graphene (gray) sandwiched between two hexagonal boron nitride (hBN) flakes, both blue. This stack is supported on a SiO_2/Si wafer (lavender/purple), which enables application of a gate voltage (V_G). A gold electrode (yellow) rests on top of the hBN/graphene/hBN stack and enables application of a voltage (V_{probe}) for inducing a tunneling current. (b) Optical micrograph of (a) with graphene (outlined in black) sandwiched between a thin (1.8 nm) hBN tunneling barrier (outlined in red) and a thick (15 nm) hBN supporting substrate. Six Cr / Au electrodes lie atop the thin hBN and V_{probe} is applied to the probes individually to perform tunneling measurements. The seventh electrode on the far-right contacts graphene directly.

5.3 Tunneling Characteristics

When a sample bias V_b (which is equivalent to the negative of a probe bias V_{probe}) is applied between the probe and graphene, charges tunnel through the barrier and into available states in graphene. The resulting tunneling conductance dI/dV_b measured across the junction is proportional to the DOS of graphene at energy eV_b.[14] A gate voltage V_G is applied to the p-doped silicon and is used to capacitively tune graphene's charge density n and enables gate tunable dI/dV_b measurements.[1] We measure dI/dV_b spectra at incremented values of V_G and then compile the spectra into a $dI/dV_b(V_b, V_G)$ map in Fig. 5.2(a). In each of these maps, yellow and purple regions correspond to high and low dI/dV_b, respectively. By examining these maps, we can determine the relative DOS by the color scale, the energy of spectral features by their vertical position, and how electronic states change with charge density by the horizontal position.

Figure 5.2(a) shows a representative $dI/dV_b(V_b, V_G)$ map of a PTS taken at 4.2 K. The data show a prominent, horizontal ~0.130 V dark stripe centered at $V_b = 0$ V. Additional features are present in the data but are obscured by the presence of this horizontal stripe. To access the other features from Fig. 5.1(a) we take the numerical derivative of these data and plot this in Fig. 5.2(b) as dG/dV_G (V_G, V_b). Three additional features that exhibit a dG/dV_G intensity close to zero become immediately apparent: (i) A narrow diagonal white line that moves from the bottom left to the top right of the dG/dV_G (V_G, V_b) map, crossing the horizontal stripe feature from Fig. 5.2(a) (now white) at $V_G = 20$ V and reappearing at $V_G = 40$ V; and (ii) Another narrow white line

that behaves sublinearly with respect to V_G and crosses the horizontal white band at the same points in V_G as (i) but changes concavity upon crossing the horizontal white stripe. Features (i) and (ii) are denoted by a black dotted line and dashed line, respectively.

To gain further insight on the two V_G-dependent features in Fig. 5.2(b) we extract several profiles within Fig. 5.2(a) along diagonal lines that are parallel to feature (i). Each of these line profiles is displayed in Fig. 5.2(c) as a $dI/dV_b(V_b)$ spectrum with a corresponding color from Fig. 5.2(a) and a vertical offset for clarity. The spectra show a strong 0.130 V-wide suppression in tunneling dI/dV_b centered around $V_b = 0$ V that is V_G-independent. This feature corresponds to the dark horizontal stripe in Fig. 5.2(a) and has been seen previously in planar tunneling spectroscopy and STS studies of graphene/SiO_2 devices[1, 15, 16] and graphene/hBN heterostructures.[7, 17] This feature is due to inelastic tunneling in graphene systems, discussed in Chapter 3[7, 17] An additional feature is visible in each of the line profiles presented in Fig. 5.2(c) as a minimum adjacent to the prominent inelastic tunneling feature mentioned above. The position of the minima in Fig. 5.2(c) depends on the location of the respective diagonal lines in Fig. 5.2(a). For example, the red line profile displays the minimum at positive V_b, whereas the purple line profile displays the minimum at negative V_b. For line profiles that are in between (the red and purple profiles) the minimum shifts monotonically from positive to negative V_b.

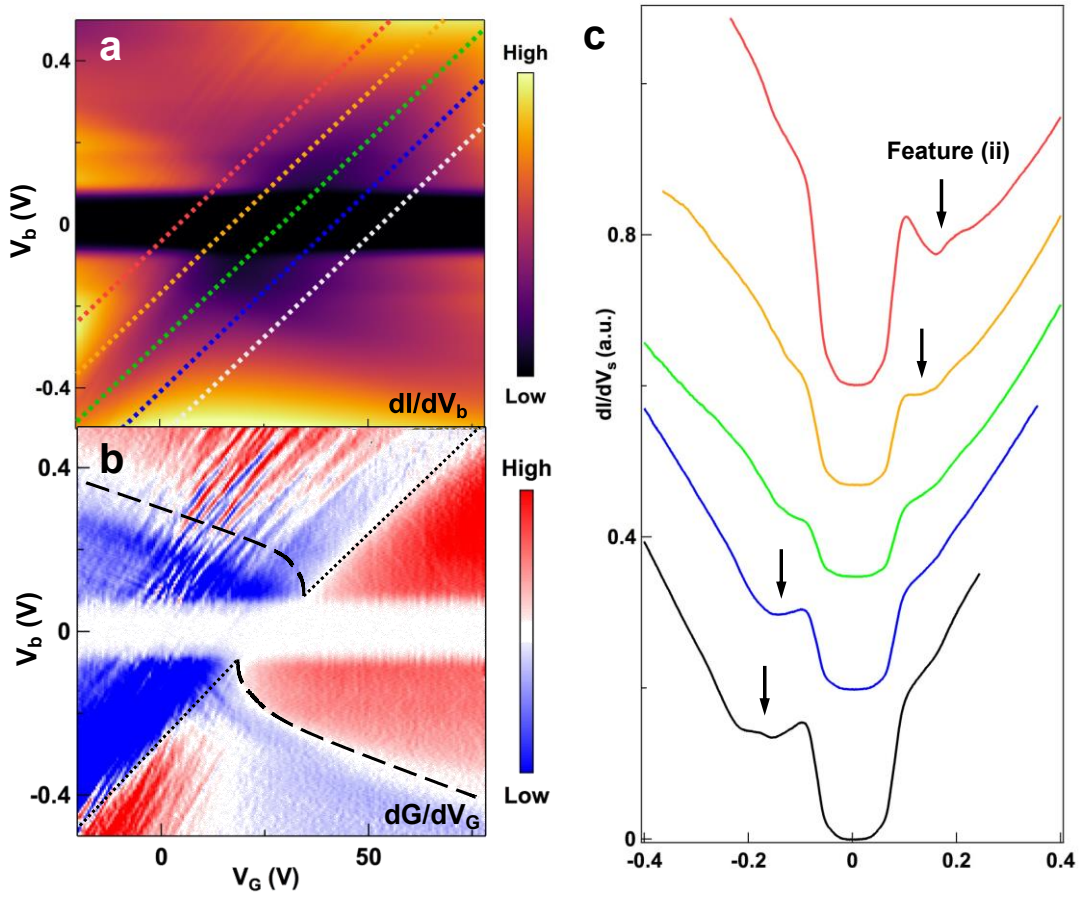

Figure 5.2: Gate tunable tunneling spectroscopy dI/dV$_b$ at zero magnetic field. (a)~$dI/dV_b(V_b, V_G)$ tunneling conductance map of graphene at B = 0 T and T = 4.2 K. (b) Numerical derivative dG/dV_G of (a) taken with respect to V_G with red, blue and white regions marking positive, negative and zero dG/dV_G. Spectral features (i) and (ii) discussed in the main text are marked with black dotted and dashed lines, respectively. (c) $dI/dV_b(V_b)$ spectra taken along the colored diagonal lines in (a). Each line corresponds to different graphene charge densities n, discussed in section 5.4. Line profiles are vertically staggered for clarity. Black arrows indicate the energy of feature (ii), which shifts with different n.

Previous STS and PTS studies have shown features akin to feature (i), feature (ii),[1,2] or both.[3,4] Notably, the work by Zhao, et. al. attributes the two separate features to tunneling channels available at the chemical potential of the probe $E_F + eV_b$, and the chemical potential of graphene E_F, which is modulated by V_b. Importantly, this interpretation implies that spectra taken at constant V_G do not correspond to a constant n.[5] In our experiment a similar systematic consideration of the graphene n with respect to V_b modulation is crucial for understanding the observed spectral features and relating them to prior STS work. This is because the PTS tunneling probe, unlike the STS probe, is a metal plate near graphene, that modulates charge *via* capacitive coupling. As a result, graphene's n (and Fermi level E_F) shift if V_G or V_b is modulated. This effect has two significant consequences: (1) There is an additional contribution to the tunneling dI/dV_b at energy E_F that results in two-channel tunneling; and (2) Applying a V_b shifts spectral features away from their expected energies which complicates the quantitative interpretation of the spectra. The origin of effect (1) was predicted by Malec, et. al.,[3] and noticed in the STS work by Zhao, et. al.[4] A discussion on this two-channel tunneling effect is provided in Section 5.4. Effect (2) has been identified in the literature as band shifting,[18] but is often neglected in graphene STS works,[17,19] including recent works on magic angle twisted bilayer graphene.[20,21] By modeling the PTS system as a parallel plate capacitor, we can *use* two-channel tunneling to *correct* for band shifting. This methodology is outline in Section 5.4.

5.4 Two-Channel Tunneling and Band Shifting in PTS of Graphene

In order to directly examine graphene's electronic structure, we must take a closer look at the invasive nature of the tunneling probe. Here we provide details on the cause of two-channel tunneling and how it is used to correct for band shifting. As discussed in Section 5.2, The PTS device is a three-plate planar capacitor and so changing the tunneling energy (eV_b) modulates charge density (n) of the middle plate. The middle plate in this study is graphene, which has a low DOS in the relevant energy range and is therefore prone to large shifts in E_F (with respect to the monolayer graphene bands) with the addition of charge. Explicitly, there is a strong dependence of E_F on V_b. Revisiting the expression for tunneling current I that flows between the probe and graphene (discussed in Chapter 3) with the dependence of E_F on V_b in mind,

$$I \propto \int_{E_F(V_b)}^{E_F(V_b)+eV_b} |M(\epsilon)|^2 \rho_P(\epsilon + eV_b) g(\epsilon) d\epsilon \tag{5.1}$$

Taking the derivative with respect to V_b and assuming the matrix element $M(\epsilon)$ to be constant,

$$\frac{dI}{dV_b} \propto g(E_F + eV_b)(1-\eta) - g(E_F)\eta \tag{5.2}$$

where $\eta = \frac{\partial E_F}{\partial eV_b}$ is inversely proportional to the quantum capacitance C_q. In conventional STS of semiconductor systems and metals, the DOS is high (>10^{15} cm^{-2}) and η is assumed to be zero.[6,7] In PTS of graphene, however, the tunneling probe acts as a top gate and η cannot be ignored. As a result, the tunneling dI/dV_b measures two channels in parallel: (1) the conventional spectroscopic channel at energy $E_F + eV_b$

which can measure occupied and unoccupied states; and (2) a second thermodynamic channel that is proportional to the density of states in graphene at E_F (given by the far-right term). [3,4] When E_F coincides with the Dirac point, which is a minimum in the DOS, we expect to see a suppression in the dI/dV_b. We attribute feature (i), observed in Section 5.2, to Channel 2 tunneling when E_F is aligned with the Dirac point.

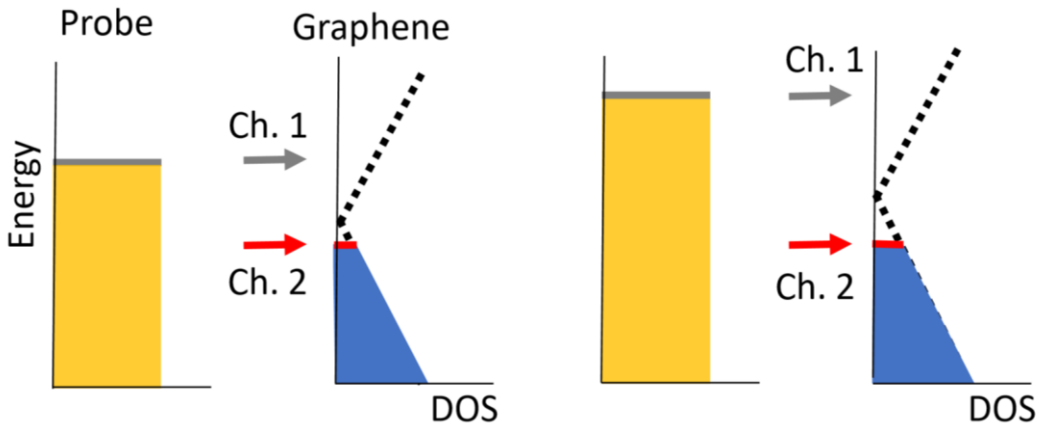

Figure 5.3: Schematic of two-channel tunneling and band shifting. The chemical potentials of the probe and graphene are offset by energy eV_b. When additional bias is applied, more tunneling states are accessible at energy $E_F + eV_b$ and also at energy E_F, leading to parallel contributions to the differential tunneling conductance dI/dV_b. The direct tunneling contribution at energy $E_F + eV_b$ is Channel 1 (Ch.1), shown as a gray arrow, and the tunneling contribution at E_F is Channel 2 (Ch. 2), shown as a red arrow. The relative weights of the two channels is dictated by the lever arm η. Additionally, increasing the sample bias eV_b shifts graphene's electronic structure upwards with

respect to E_F. As a result, measured tunneling energies of states in graphene are lower than their true values.

Following this line of logic, we take a closer look at the trajectory of feature (i) which is followed with black dashed line in Fig. 5.2(b), stretching from the bottom left to the top right of the tunneling map. At each point on the line, E_F is aligned with the Dirac point and graphene is charge-neutral ($n = 0$). Therefore, feature (i) defines the constant n contour along the $dI/dV_b(V_b, V_G)$ map. This agrees with our capacitor description of the PTS devices: In a three-plate planar capacitor, charge density is determined by probe and gate potentials $n = -(C_{tg}V_{probe} + C_{bg}V_G)$ where C_{tg} and C_{bg} are the capacitances between graphene and the probe and back gate, respectively. Each constant-n contour is then expected to be a straight line with slope C_{bg}/C_{tg}, which can be extracted from the well-defined slope of feature (i). It is then appropriate to take profiles along diagonal line cuts parallel to feature (i) as constant-n tunneling spectra. Additionally, the point where a constant n diagonal line crosses $V_b = 0$ V, namely its x-intercept, determines n along the entire line. The x-intercept of feature (i), for example, shows the intrinsic doping n_d of graphene. The value of n at every point on the (V_b, V_G) domain can be determined by following two steps: (1) determining n at every point along the line $V_b = 0$ with relation $n(V_b = 0, V_G) = -\alpha V_G$ and (2) creating constant-n contours along diagonal lines that are parallel to feature (i).

In previous STS studies of gated graphene samples, vertical—not diagonal—lines are assumed to be lines of constant n. Indeed, the $dI/dV_b(V_b)$ line profiles shown

in Fig. 5.2(c) along diagonal line cuts in Fig. 5.2 (a) show strong resemblance to vertical lines from graphene STS spectra previously reported.[1,8] For a more suitable comparison between PTS and STS tunneling maps, we use a linear transformation to map the PTS diagonal constant-n spectra onto vertical lines. To accomplish this we use the relation $n_g = C_{tg}V_b - C_{bg}V_G - n_d$ (where n_d is graphene's extrinsic doping due to the work function mismatch with the probe) from the planar capacitor model to transform each $dI/dV_b(V_b, V_G)$ map into a $dI/dV_b(V_b, n)$ map.[4] The specific linear transformation $T = \begin{bmatrix} C_{bg} & -C_{tg} \\ 0 & 1 \end{bmatrix}$ shears the raw data depending on the ratio $\frac{C_{tg}}{C_{bg}}$ determined from the slope of feature (i). We extract a ratio $\frac{C_{tg}}{C_{bg}} = 96 \pm 3$ from the slope of the feature (i) trajectory in several dozen $dI/dV_b(V_b, V_G)$ maps across 6 devices. For comparison, we also calculate the (area-normalized) capacitances C_{tg} and C_{bg} using the geometry of the device measured with AFM. We measure the thickness of top and substrate hBN to be $t_{hBN1} = 1.8$ nm and, $t_{hBN2} = 15$ nm, respectively. The underlying oxide thickness $t_{SiO_2} = 285$ nm is a specification of the commercially available SiO_2. Using the equations $C_{bg} = \frac{\varepsilon_{hBN2}\varepsilon_{SiO_2}}{t_{hBN2}\varepsilon_{SiO_2} + t_{SiO_2}\varepsilon_{hBN2}}$ and $C_{tg} = \frac{\varepsilon_{hBN1}}{t_{hBN1}}$, with $\varepsilon_{hBN1} = 2.2\varepsilon_0, \varepsilon_{hBN2} = 4.0\varepsilon_0$ and $\varepsilon_{SiO_2} = 3.9\varepsilon_0$,[9] we find a ratio $\frac{C_{tg}}{C_{bg}}$ = 98.4 which agrees with the method discussed above.

[4] In ten devices we find that the x-intercept of spectral feature (i) is consistently ~25 V and so our PTS devices are consistently p-doped to $n_d \approx 2 \times 10^{12}$ cm^{-2}, corresponding to a work function difference of 0.28 eV between graphene and the Cr/Au probe

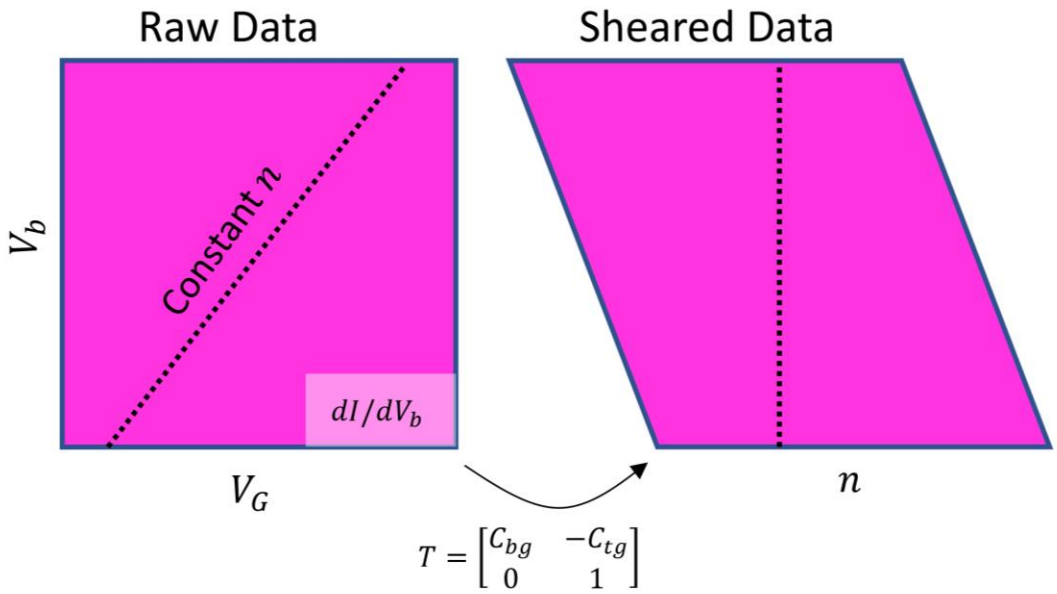

Figure 5.4: Accounting for band-shifting. The square on the left represents a raw tunneling $dI/dV_b(V_b, V_G)$ map. The dotted diagonal line is a constant-n contour, with slope given by the ratio of back gate and probe capacitances C_{bg}/C_{tg}. The raw data is transformed into a sheared $dI/dV_b(V_b, n)$ map with the matrix T, shown under the maps.

After shearing the data so that constant n lines are vertical, it is necessary to assign appropriate values of n to the new horizontal axis. To this end, the matrix T scales the horizontal axis with appropriate n_g values, calculated from $n_g(V_b = 0, V_G) = C_{bg}V_G$. Next, the horizontal axis is shifted by the intrinsic doping n_d, determined by the horizontal position of the Dirac point as it crosses the Fermi level $n_d = C_{bg}V_{G0}$ where V_{G0} is the gate voltage at which features (i) and (ii) cross the inelastic tunneling

feature in the sheared map. Finally, the axes are labelled with $n = -n_g$ for adequate comparison with previously reported STS tunneling $dI/dV_b(V_b, V_G)$ maps, where $V_G = -\alpha n_g$ and α is a positive constant.[5,10,11]

A map resulting from this shearing process is shown in Fig. 5.5. In the map feature (i), discussed above, is a vertical dark band (indicated with a black arrow). Feature (ii) is also visible as a dark region that arcs from the top left to the bottom right of the map. Its path is denoted with a white dashed line. This transformation enables the study of planar tunneling spectroscopy at well-defined n. The trajectory of this suppression is an experimental signature of graphene's Fermi level shifting with n. In Chapter 2, this specific relation was derived for graphene, which has a linear DOS and is two dimensional. Notably, the relation $E_F = \hbar v_F \sqrt{\pi n}$ has only one fitting parameter: the Fermi velocity v_F, which is dictated by the carbon-carbon hopping parameter and bond length. To determine the Fermi velocity, we plot energy of feature (ii) versus n for two different devices in Fig. 5.5(c). Evidently, both devices show good agreement with the theoretical relation that sets $v_F = 1.0 \times 10^6\ m/s$. This validates the shear methodology as adequate for accurately measuring the energies of spectral feature as well as charge densities.

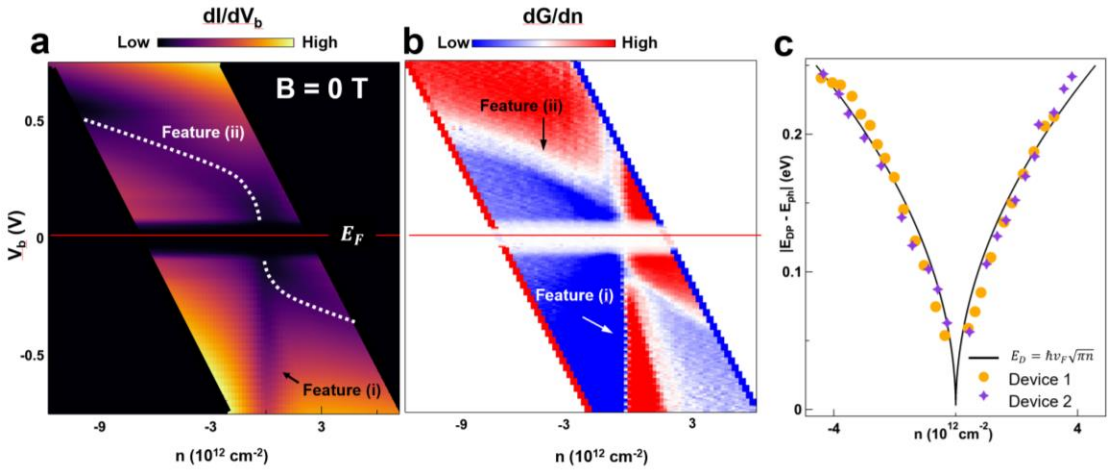

Figure 5.5: Gate tunable tunneling spectroscopy dI/dV_b with well-defined n. (a) Sheared $dI/dV_b(V_b, n)$ map of a graphene PTS, where charge density along the horizontal axis is calculated by $n = C_{tg}V_b + C_{bg}V_G$, and C_{tg}, C_{bg} are the graphene-tunneling probe and graphene-back gate capacitances, respectively. The horizontal red line indicates the Fermi level of graphene (E_F). The shear accounts for the top gating effect of the tunneling probe, as discussed in the main text. Yellow and purple regions correspond to high and low dI/dV_b, respectively. (b) Numerical derivative $dG/dn(V_b, n)$ of the data shown in (a). Red, blue and white regions indicate where dG/dn is positive, negative and zero, respectively. Feature (i), denoted by a white arrow, is a vertical white line used to determine where $n = 0$. Feature (ii), denoted by a black arrow, is a white line that descends nonlinearly from the top left to the bottom right of the map. (c) Energy of the Dirac Point E_D in graphene with changing charge density. The position of spectral feature (ii) in V_b (which is denoted as a dashed line in (b)) is plotted against *n*. The phonon energy, $\hbar\omega = 63$ meV, has been subtracted from the measured position of spectral feature (ii).[8] Such data from two separate devices

(denoted as orange circles and purple diamonds) are compared with the theory $E_D = \hbar v_F \sqrt{n\pi}$, here $v_F = 10^6$ m/s.

5.5 Simulating PTS Tunneling Spectra

Tunneling spectroscopy has the power to probe occupied and unoccupied states. To further demonstrate that the methodology established in the previous section can be used to accurately determine occupied and unoccupied spectral features, we employ a straightforward tunneling model for comparison. Our model is based on a model used previously in planar tunneling spectroscopy as well as scanning tunneling spectroscopy (STS).[3–5,9] This model uses the three-plate capacitor discussed in Section 5.4 to calculate the n in graphene at every (V_b, V_G) pixel point in the relevant domain. Next $E_F(V_b, V_G)$ is determined using the relation $E_F = \hbar v_F \sqrt{\pi n}$. The model calculates the tunneling conductance $\frac{dI}{dV_b}(V_b, V_G)$ based on a total derivative of the tunneling current, expressed in Eq. 5.1.

Additionally, inelastic tunneling is included which shifts the tunneling energy according to the relations outlined by Zhang, et. al.[8] To determine the relevant phonon contributions, we extract peak energies and widths from $dG/dV_b(V_b)$ spectra.[12–14] We include the five most prominent peaks, with energies $E_{ph} = \pm 36, \pm 63, \pm 72, \pm 150, \pm 158$ meV, which agree with phonon energies previously reported in a similar system.[15] More detail on determining phonon energies is given in Chapter 7 on bilayer graphene, where the same phonon energy measuring procedure is used.

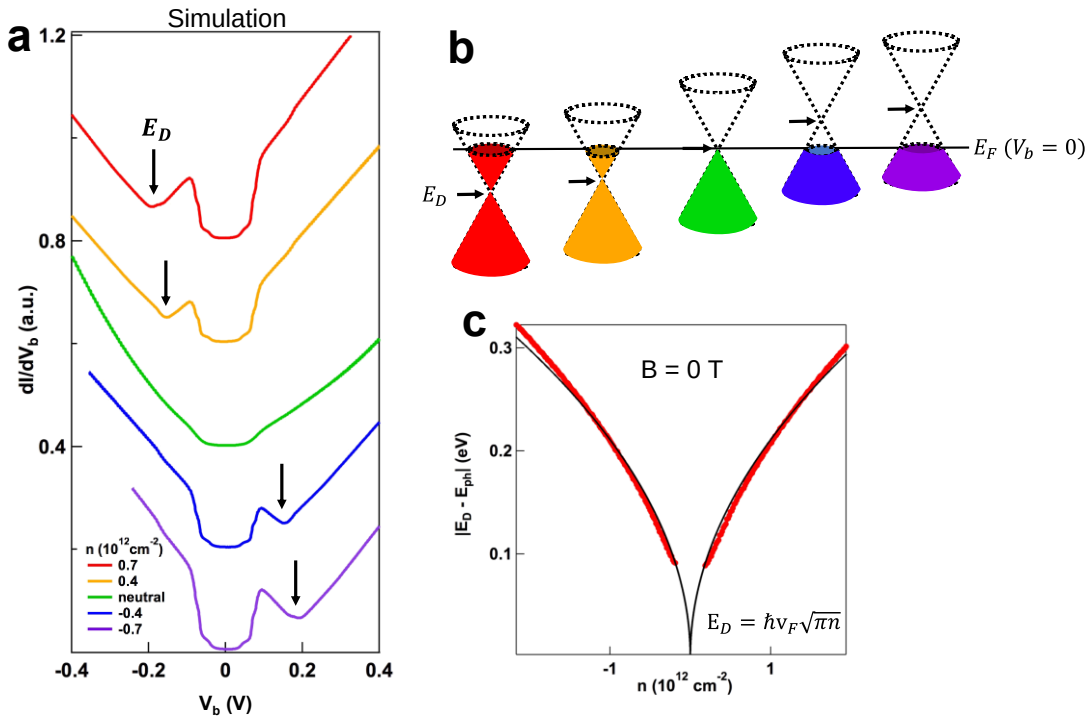

Figure 5.6: Simulated PTS spectra of graphene. (a) Simulated dI/dV_b spectra taken at different charge densities which are indicated in the legend. Red and orange traces are n-doped, the green trace is charge neutral, and blue and purple traces are p-doped. (b) Cartoon of graphene's electronic structure at each trace in (a), with corresponding colors. As the charge density is changed, graphene's bands shift with respect to the Fermi level E_F, changing the relative energy of the Dirac Point E_D with respect to E_F (which is always at $V_b = 0$). (c) Consistency check of the simulation, where the absolute value of E_D is extracted from many traces and plotted against the charge density as a red line. The phonon energy 63 meV has been subtracted to account for the energy offset associated with inelastic tunneling. The theoretical dependence $E_D =$

$\hbar v_F \sqrt{\pi n}$ is plotted for comparison. Strong agreement between theory and simulation indicates that E_D corresponds to the Dirac Point when it is away from E_F.

Figure 5.6 shows five simulated $dI/dV_b(V_b)$ spectra at different n. The simulated spectra display a ~125 meV wide suppression in $dI/dV_b(V_b)$ that is symmetric about $V_b = 0$ and independent of n. This suppression only appears in our model when phonons are considered, and consistently has width $2\hbar\omega_i$ where ω_i is the frequency of the dominant phonon included. The model also reproduces the data's n-dependent dip in dI/dV_b, introduced as feature (ii) in Section 5.2. To further support that feature (ii) represents direct tunneling into the Dirac point when it is away from E_F, we extract its energy at many values of n and plot them next to the expected $\sqrt{n}$ dependence. Figure 5.6(c) shows the resulting plot, where the absolute energy of the simulated Dirac point (E_D), minus the phonon energy 63 meV is plotted in red as a function of n. Notably, the extracted relation shows good agreement with the theoretical behavior (shown as a black line) and returns the value of $v_F = 10^6$ m/s, verifying that the extraction procedure is valid. We have thus verified that feature (ii) in the $dI/dV_b(V_b, V_G)$ maps corresponds to a direct measurement of graphene's Dirac point when it is far from and near to the Fermi level. Furthermore, the PTS measurement can be straightforwardly understood and modelled as a three-plate capacitor, where the tunneling relation is given by Eq. 5.2.

5.6 Tunneling into Quantum Hall States in Graphene

Having established that appropriately sheared PTS data correspond to direct tunneling into occupied and unoccupied states in graphene, we enter the quantum Hall regime. Figure 5.7(a) shows a $dI/dV_b(V_b, n)$ map of the same device in a perpendicular magnetic field $B = 8\,T$. These data reveal features that are present in Fig. 5.5(a) and new features as well. The horizontal dark stripe seen in Fig. 5.5(a) is observed again in Fig. 5.7(a). In addition, new peaks appear that follow the path carved by feature (ii) in Fig. 5.5(a). Interestingly, the trajectory of these new peaks changes significantly as n approaches 0, exhibiting a characteristic step-like behavior with n. The onset of this step-like behavior, denoted by a yellow arrow, is apparent on the bottom-right quadrant of the map. Figure 5.7(b) shows a comparison of constant n tunneling spectra when $B = 0\,T$ (black) and $B = 8\,T$ (blue) at $n = -1.8 \times 10^{12}$ cm^{-2}. Both spectra show the inelastic tunneling feature around $V_b = 0$ V, and the blue spectrum shows a broad peak in the location of the Dirac point in its $B = 0\,T$ counterpart. Several additional peaks are also present in the blue $dI/dV_b(V_b)$ spectrum.

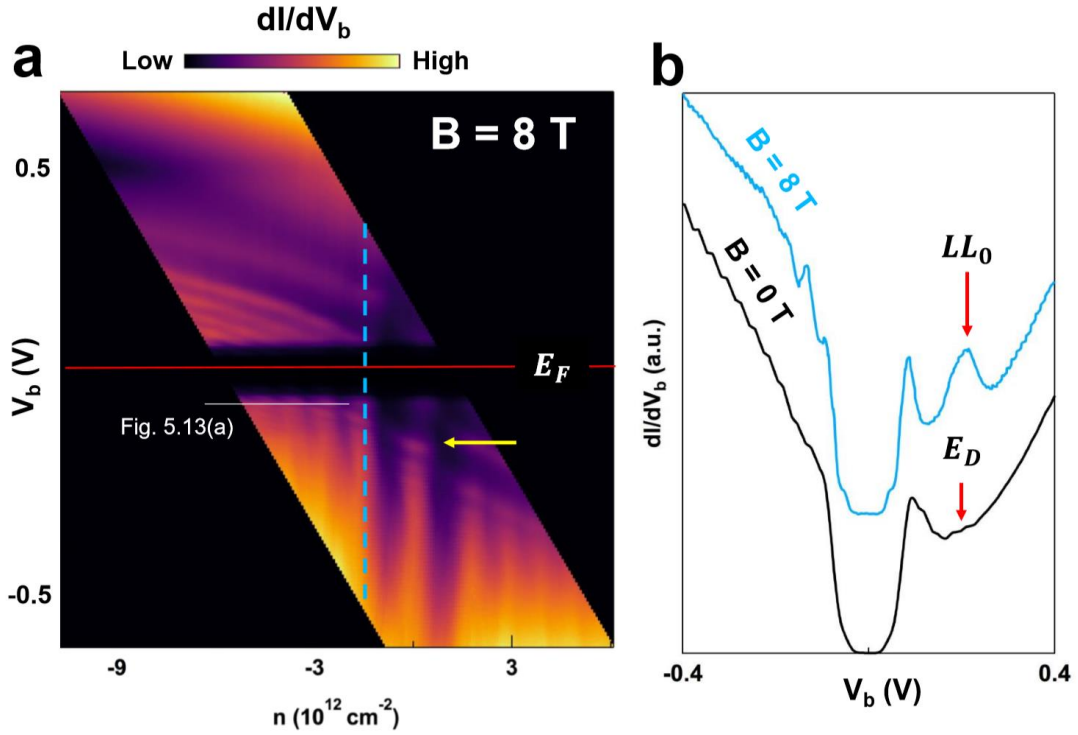

Figure 5.7: PTS Spectroscopy of graphene in a perpendicular magnetic field. (a) Sheared $dI/dV_b(V_b, n)$ map in a perpendicular magnetic field (B = 8 T). The horizontal red line indicates the Fermi level of graphene, and the yellow arrow points to the stair-case like features discussed in the main text. (b) Comparison of the $dI/dV_b(V_b)$ spectra taken at charge density $n = -1.8 \times 10^{12}$ cm^{-2} when $B = 0$ T (blue) and $B = 8$ T (black). The blue spectrum corresponds to the dashed vertical line cut in (a). The spectra are vertically offset for clarity. Red arrows denote E_{LL0} and E_D in the two traces.

In the presence of a large B, charges in a 2D electron gas undergo cyclotron orbits that coalesce to form Landau levels (LLs). As discussed in Chapter 2, graphene's massless Dirac Hamiltonian, endows it with the unique LL spectrum represented by

cyclotron orbit spacings $E_{LLN} - E_{LL0} = sgn(N)v_F\sqrt{2e\hbar|N|B}$, where E_{LLN} is the energy of the N^{th} LL and E_{LL0} is the energy of the zeroth LL. A direct result of graphene's anomalous LL dispersion is the presence of a zeroth LL at the Dirac point. Previous STS works on Landau-quantized graphene have identified a peak in dI/dV_b at the Dirac point energy E_D as a spectroscopic signature of LL_0. Following this interpretation, we attribute the broad peak at $V_b > 0$ in the blue trace to LL_0. Interestingly, LL_0 in our data is much broader than any of its neighboring LLs. To determine the cause of this broadening, we explore its relation to the LL energy.

Figure 5.8(a) shows a tunneling $dI/dV_b(V_b, n)$ map with superimposed vertical lines that represent the FWHM of Lorentzian fits to both LL_0 and LL_{-1}. The two different LLs disperse parallel to one another from the top left to the middle of the map. They also appear in apparently more sporadic regions in the bottom right portion of the map. In the majority of the multiple fit lines, LL_0 appears to have a higher FWHM than LL_{-1}. Figure 5.8(b) shows a histogram of the peak widths. Indeed, the distribution is bimodal, with LL_0 widths clustering around an average value of 41 meV and LL_{-1} values clustering around a mean width of 18 meV. shown in white and cyan, respectively. For more evidence towards the differences in LL width, we next investigate the broadening in occupied and unoccupied LLs. Figure 5.8(c) shows LL broadening as a function of LL energy. The left side of the plot corresponds to occupied states, while the right side corresponds to unoccupied states. White triangles and cyan circles are fits of LL_0 and LL_{-1}, respectively. Best fit lines to the occupied and unoccupied LLs are shown in yellow and red, respectively.

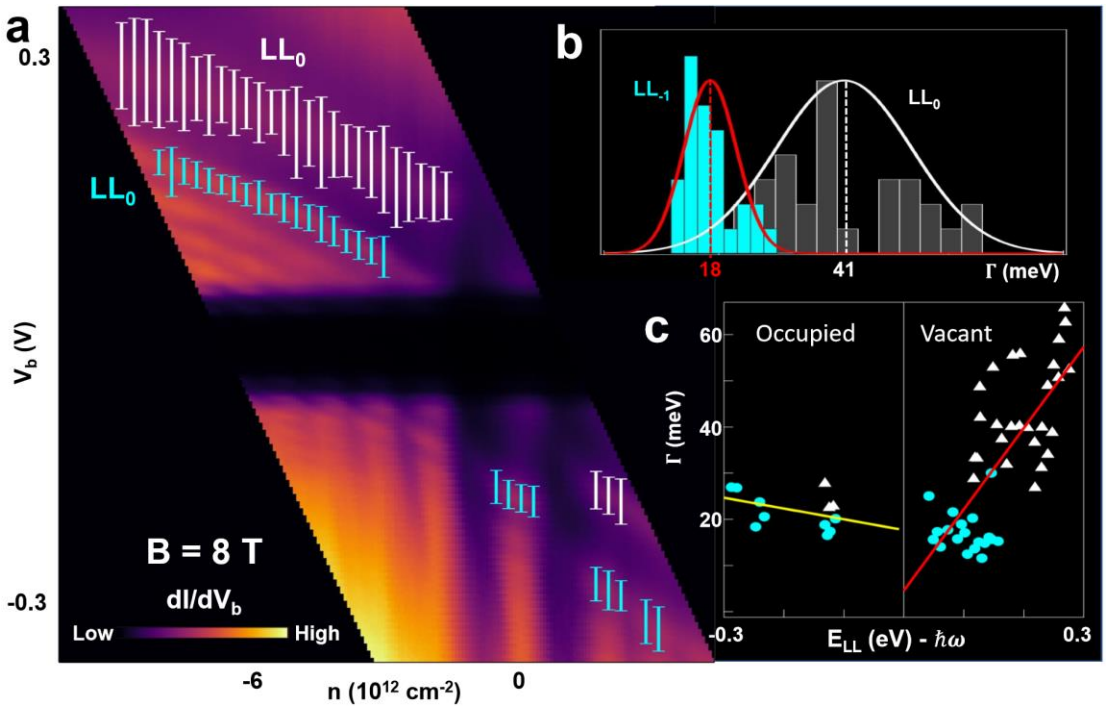

Figure 5.8: Determining the pseudoparticle lifetimes in graphene's Landau levels. (a)~Tunneling $dI/dV_b(V_b, n)$ map taken at $B = 8$ T. Vertical lines represent the FWHM of Lorentzian fits to LL_0 and LL_{-1}, shown in white and cyan, respectively. The fits are taken at different charge densities and energies. (b) Histogram of broadening in LL_0 and LL_{-1}, shown as white and cyan bars, respectively. Gaussian fits of each distribution are shown in red and white, with the mean broadening listed on the horizontal axis. (c) LL broadening as a function of LL energy. The left side of the plot corresponds to occupied states, while the right side corresponds to unoccupied states. White triangles and cyan circles are fits of LL_0 and LL_{-1}, respectively. Best fit lines to the occupied and unoccupied LLs are shown in yellow and red, respectively.

In the single particle picture of Landau quantization outlined in Chapter 2, LLs are expected to collapse the electronic structure into a series of delta functions at energies separated by the cyclotron energy $\hbar\omega_c$. Electrons residing in LLs will remain there, as LLs are eigenstates of the Hamiltonian. While the single particle picture of LLs is an ideal starting place for modeling real systems, a more realistic picture includes perturbations within the sample that arise from disorder or many-particle interactions, for example. Such perturbations cause Lorentzian broadening of the Dirac-delta functions where the resulting linewidths are inversely proportional to the quasiparticle lifetime τ_0. Away from the Fermi level, the inverse of this lifetime—given by the LL broadening—will decrease proportionally with energy.[16] In the LL broadening plot shown in Fig. 5.8(c), yellow and red lines each have different y-intercepts. This result is counterintuitive: we would expect that both occupied and unoccupied LLs broaden symmetrically as their energy away from the Fermi level increases. The fitted data does not show this result, but instead indicates an asymmetry between occupied and unoccupied states. To this point, we so far have several compelling trends: (1) LL lifetimes are not the same in each of the LLs; (2) LL lifetimes depend on whether the states are occupied or unoccupied.

One other, subtler trend is hiding in the $dI/dV_b(V_b, n)$ map shown in Fig. 5.7(a) and 5.8(a). The dark vertical lines that straddle $n = 0$ are suppressions in dI/dV_b corresponding to when Channel 2 (which measures DOS at energy E_F) is aligned with a gap between LLs. Upon closer inspection, we see that the spectra within those dark regions do not get completely suppressed, but instead get dramatically altered. Figure

5.9 demonstrates this behavior. Vertical line cuts along the dark regions bordering $n = 0$ are labelled $\nu = \pm 2$, where $\nu = g_v g_s n/n_\phi$ is the filling factor that indicates the number of full LLs. In graphene, there are two degenerate valleys, so the total degeneracy is $g_s g_v = 4$. However, as derived in Chapter 2, graphene also has a unique zeroth LL, due to its nontrivial Berry phase. As a result, a completely full LL_0 corresponds to $\nu = 2$. The data in Fig. 5.9(b) show $dI/dV_b(V_b)$ profiles along the vertical lines in Fig. 5.9(a). Interestingly, LL peaks in the spectra are prominent in the black traces, where $\nu = \pm 4, 0$ at half filling but they are absent in the blue traces, where $\nu = \pm 1$ when E_F resides in a cyclotron gap.

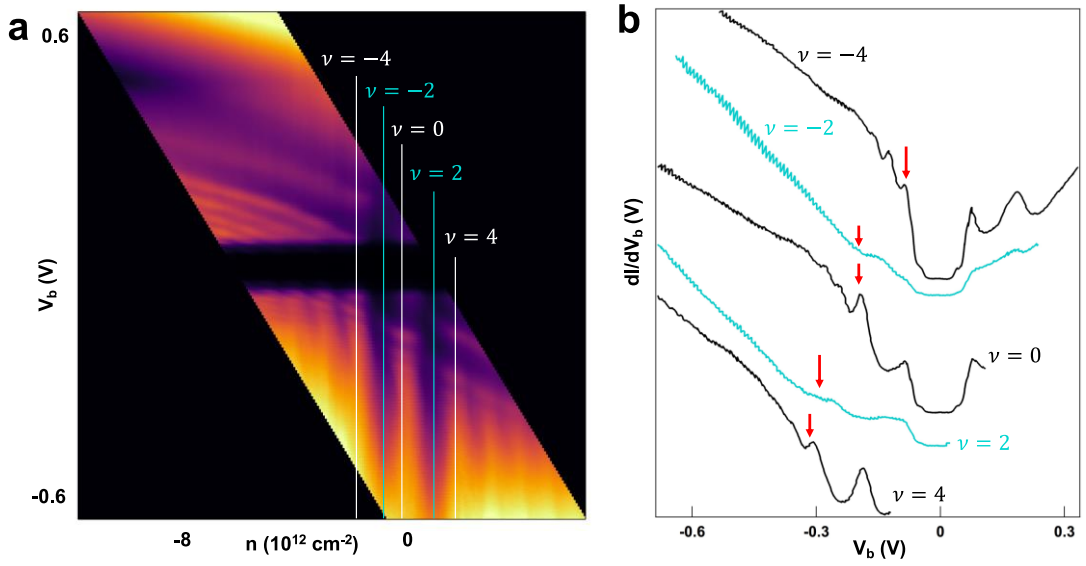

Figure 5.9: Disappearing LLs at full-filling. (a) Tunneling $dI/dV_b(V_b, V_G)$ map with vertical lines marking half filling $\nu = \pm 4,0$ as white lines and full filling $\nu = \pm 2$ as cyan lines. (b) Constant-ν $dI/dV_b(V_b)$ spectra taken along the vertical lines in (a). A red arrow marks the position of LL_{-1}. Notably, LL_{-1} is prominent in all three black spectra, and absent in both cyan spectra.

Previously reported planar tunneling spectroscopy of quantum Hall states in a 2D electron gas observed LL broadening dependence on filling factor.[17] In those works, broadening changes were attributed to disorder in the system, as well as electron-electron interactions. Notably, in those experiments, the LL spacing, linewidths, and temperature were an order of magnitude lower than the ones measured here. Nonetheless, we can follow the line of reasoning from those past works to determine the origin of the peculiar behavior observed in our system.

As the Fermi level is tuned through the range of highly degenerate LLs, the number of available scattering states around the Fermi surface swells at each LL and recedes in the gap. In the Fermi liquid picture, a higher DOS at the Fermi level can lead to increased screening of disorder and, counterintuitively, more electrons in the system results in stronger *single* electron behavior.[18] When the Fermi level is within a LL, then, we should expect to see the single particle Landau level spectrum emerge. Interestingly, when there is a vanishingly small DOS at the Fermi energy, the resultant drop in long-range screening causes the Fermi liquid picture to break down. In ultra clean systems, this can manifest as exotic spectral signatures such as Wigner crystallization.[19] In our devices, we see the augmentation of the spectra. Perhaps this is due to Coulomb scattering sites in the tunneling junction, that are not sufficiently screening in the cyclotron gap, leading to the vanishing of the quantum Hall states

5.7 Fermi Velocity Renormalization

With the ability to directly extract LL energies, we next explore how the Fermi velocity v_F is affected by the amount of charge in graphene. Figure 5.10 shows our methodology for extracting LL energies from constant n line cuts in $dI/dV_b(V_b, V_G)$. We identify the energy position of LLs, marked as black stars in Fig. 5.10(a), based on several criteria: (1) The peaks in dI/dV_b appear as zeros in dG/dV_b indicated by yellow stars in Fig. 5.10(b); (2) The peaks in dI/dV_b appear as zeros in dG/dV_G marked as white stars in Fig. 5.10(c). Figure 5.10(d) shows profiles along diagonal line cuts in $dI/dV_b, dG/dV_b$, and dG/dV_G with corresponding colors. Although we employ

multipeak fitting in the previous section, we find that fitting software introduces ambiguity when extracting peak positions from within the suppressed dI/dV_b regions.

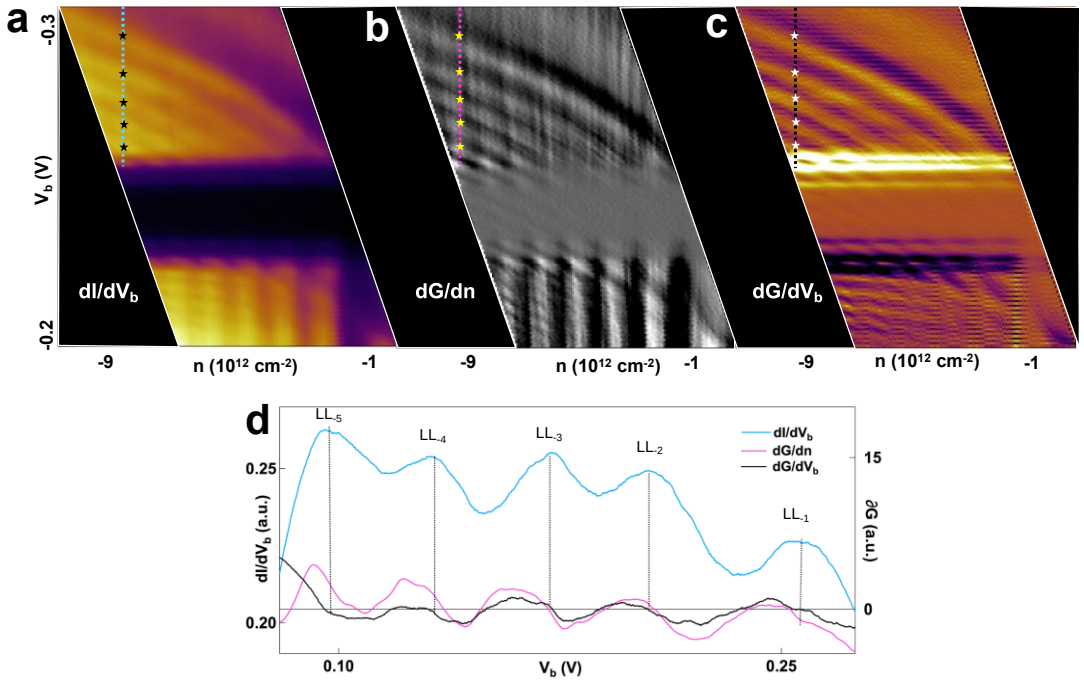

Figure 5.10: Extracting LL energies by hand. (a) $dI/dV_b(V_b, n)$ plot taken at $B = 8$ T. Black stars denote the peaks in dI/dV_b along the diagonal line cut. (b) Numerical derivative $dG/dn(V_b, n)$ taken of the data in (a). Yellow stars indicate the zeros in dG/dn along the diagonal line cut corresponding to the peaks in dI/dV_b. (c) Numerical derivative $dG/dV_b(V_b, n)$ taken of the data in (a). White stars mark the zeros in dG/dV_b along the diagonal line cut corresponding to the peaks in dI/dV_b. (d) Line profiles taken along the diagonal line cuts in (a)-(c) with corresponding colors. Landau level labels mark the positions of peaks in dI/dV_b. Peaks in dI/dV_b (blue) are

designated as Landau levels if they appear as zeros in dG/dn (magenta) and in dG/dV_b (black).

Landau Levels (LL) in graphene have the unique dispersion $|E_{LLN}-E_{LL0}| = sgn(N)v_F\sqrt{2e\hbar|N|B}$ where N is the LL index and B is the magnitude of the perpendicular magnetic field. Using this relation, we plot the relative energy of the LL peaks $|E_{LLN} - E_{LL0}|$ as a function of $\sqrt{|N|B}$, where N is the peak index and $B = 8$ T in Fig. 5.11(a). The data's linearity confirms the expected unique behavior of graphene's LLs and bolsters our analysis procedure. Figure 5.11(a) also includes relative peak energies taken at two additional values of n. While all three datasets are linear, their slopes noticeably increase as $|n|$ approaches zero, suggesting that the v_F is n dependent. Such behavior was reported previously in STS studies of graphene/hBN heterostructures and is described in Chapter 2. This behavior is attributed to electron-electron interaction effects.[24]

In order to determine the relation between v_F and n, it is necessary to determine n to high accuracy. For each spectrum, we calculated the numerical charge density n_q by numerically integrating the graphene LL DOS to mitigate any overestimates due to low compressibility in the gapped regions. Notably, we find that our classical capacitor model for the PTS system must be shifted in the incompressible regions between LL_0 and $LL_{\pm1}$, shown as flat regions on the red line in the inset of Fig. 5.11(b). At higher filling factors $\nu > 4$, underestimates due to quantum capacitance are negligible. This validates the planar capacitor model of the PTS further—in all but the least

compressible systems (Landau quantized graphene) modeling PTS as a planar capacitor is thus a good approximation.

Confident that our n values are accurate in the quantum Hall regime, we next extract v_F from 40 different $dI/dV_b(V_b)$ spectra, each with a different n. Figure 5.11(b) shows the n-dependence of our extracted v_F. Blue dots denote values of v_F fitted to fewer than 4 Landau levels, while orange dots indicate values of v_F taken from four or more Landau levels. Error bars show a single standard deviation in the linear fit. Interestingly, the data show a clear n-dependence of v_F, that is most prominent as $n \rightarrow 0$, indicating that Fermi velocity is renormalized at low carrier densities. A theoretical prediction for velocity renormalization by Das Sarma, et. al. overlays the data in Fig. 5.11(b). This theory, which is outlined in Chapter 2, attributes the low carrier increase in v_F to electron-electron (e-e) interactions. Our spectroscopic observation of renormalized v_F agrees the STS study reported by J. Chae, et. al., but is seen here for the first time with a PTS junction. Surprisingly, it appears that the PTS device is sensitive to e-e interactions even though the probe is a large metal plate which we would naïvely expect to screen a monopole potential to be a dipole potential *via* image charges, for example.[20] Our observation of electron-electron renormalization agrees with which reported recent work by M. Kim, et. al. (Nature Comm. 2339 2020),[21] reported that graphene-metal gate distances could be less than 1 nm before electron-electron interactions are screened away.

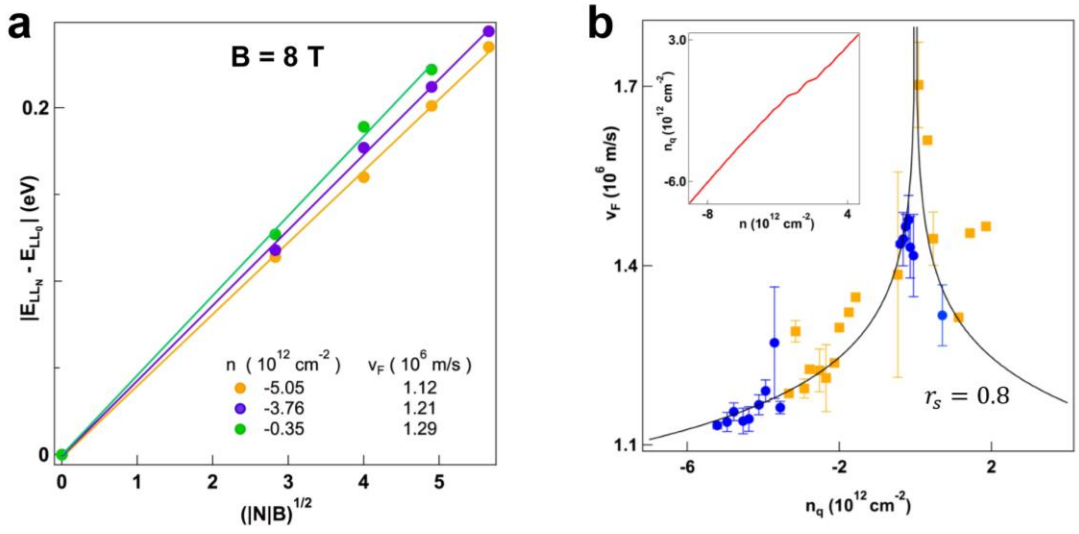

Figure 5.11: Graphene's Fermi velocity (v_F) as a function of n. (a) Determination of the Fermi velocity at different n. Landau level (LL) peak energies are plotted against the square root of the LL index N and magnetic field B, where B = 8 T. Error bars in LL position are smaller than marker sizes. Linear fits are used to extract the Fermi velocity v_F at each of the three different n, shown in the legend. (b) Extracted Fermi velocity from a linear fit of graphene's Landau level energy spacings $|E_{LLN} - E_{LL0}|$. Each point corresponds to the v_f at a specific value of n, which is calculated using a planar capacitor model as well as a numerical integration of the LL DOS, discussed in the text. Blue dots denote values of v_F fitted to fewer than 4 Landau levels. Orange dots indicate values of v_F taken from four or more Landau levels. Error bars show a single standard deviation in the linear fit. The solid black line shows the theoretical dependence $v_F = v^* \left(1 - \frac{r_s}{\pi}\left[\frac{5}{3} + \ln(r_s)\right] + \frac{r_s}{8}\ln\frac{n_C}{n}\right)$ from Das Sarma et al.[22] Here r_s is the Wigner-Seitz radius (0.8), n_C is the charge density corresponding to the ultraviolet cutoff (3 eV), and v^* is the bare dispersion velocity (1.10×10^6 m/s) that are detailed

in Chapter 2. Inset: simulated charge density n_q is plotted as a function of n. This plot shows a modest inequivalence of n_q and n, which is greatest at low charge densities, validating the planar capacitor model for Landau quantized graphene.

5.8 High B Tunneling into Graphene

To further study the spectral features that emerge at $B = 8\,T$, we measured PTS devices at high magnetic fields that are inaccessible to STS. Figures 5.12(a)-(c) show sheared $dI/dV_b(V_b, n)$ maps of a graphene PTS for $B = 8\,T$, $B = 13\,T$ and $B = 18\,T$, respectively. The vertical dashed line cuts in each of these panels is taken along the charge neutrality point and corresponds to a $dI/dV_b(V_b)$ spectrum of matching color in Fig. 5.12(d) with $B = 8\,T$ (orange), $13\,T$ (blue), and $18\,T$ (black). All of the three spectra show the inelastic tunneling feature discussed above and adjacent sharp peaks in dI/dV_b intensity. Additionally, the spectra show a peak indicated by a pink arrow that shifts to the left as B is increased. This peak is visible as a stair-like dispersing band in Fig. 5.12(a), and it appears again in Figs. 5.12(b) and (c) at lower values of V_b. Notably, the length Δn of this step-like feature increases with larger magnetic fields, eventually forming a prominent staircase pattern for $B = 18\,T$ (Fig. 5.12(c)).

Tunneling spectra taken at $B = 18\,T$ presented in Fig. 5.12(c) show a well-defined staircase pattern. Similar patterns have been reported previously in two-dimensional electron systems,[17] and in STS studies of graphene[16,23], though not at $B = 18T$. These staircase patterns arise from highly compressible LLs for which the Fermi level is pinned at a constant energy as they are filled with charge. Once a LL is

completely filled the introduction of additional charge causes the next LL to be pulled to the Fermi level. The resulting tunneling map shows a LL staircase, where the length of each stair (Δn) is equal to the number of degenerate cyclotron orbits in a given LL.

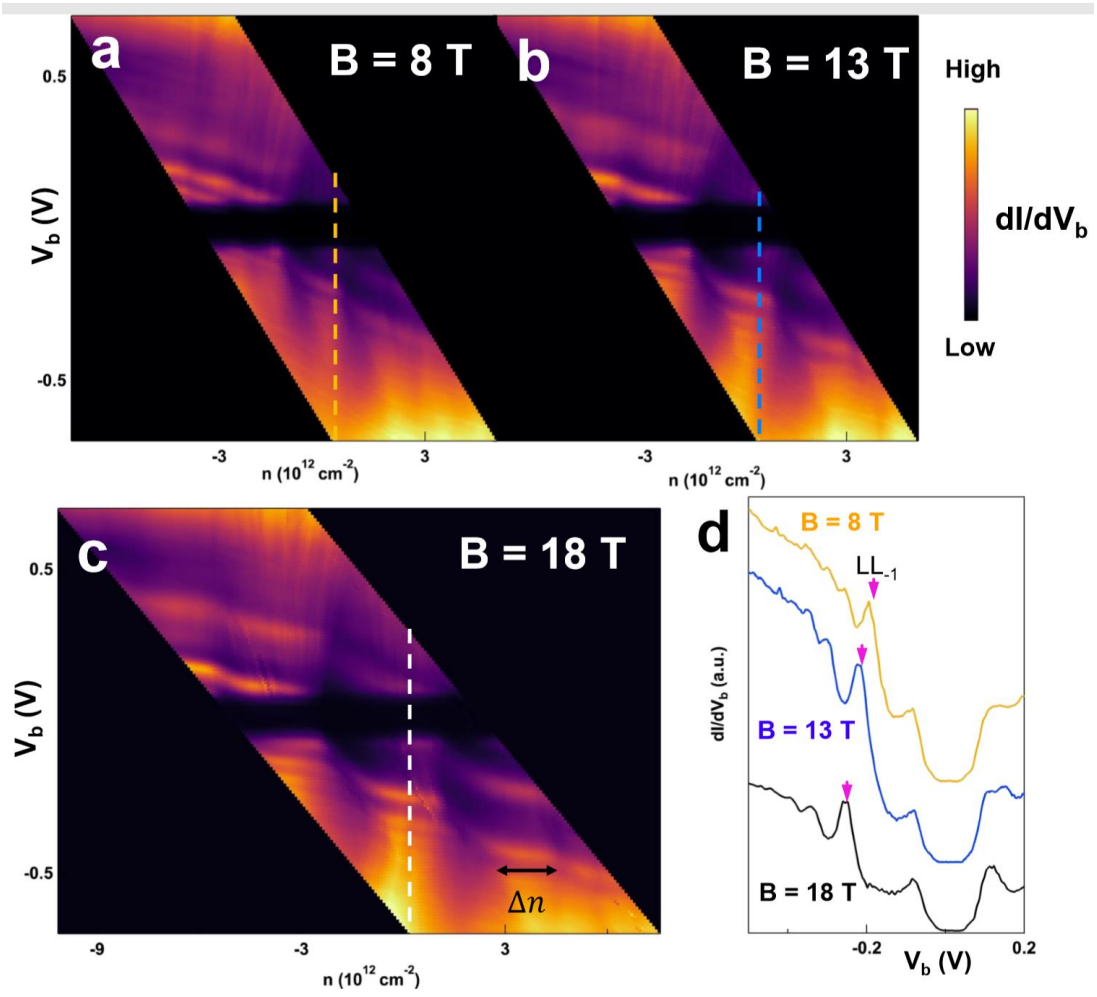

Figure 5.12: Gate tunable tunneling spectroscopy dI/dV_b with well-defined n at high magnetic fields. (a-c) Sheared $dI/dV_b(V_b, n)$ map of a graphene PTS for B = 8 T (a), B = 13 T (b) and B = 18 T (c). The former was performed at T = 4.2 K, while the

latter two were performed at T = 0.5 mK. Landau level degeneracy Δn, indicated in (c) and discussed in the main text. (d) Comparison of the $dI/dV_b(V_b)$ spectra taken along the charge neutral line of $dI/dV_b(V_b, n)$ maps from (a-c), with line colors corresponding to the color of the dashed vertical line in each of the maps. Spectra are vertically offset for clarity with the orange trace taken for B = 8 T, blue trace taken for B = 13 T, and black trace taken for B = 18 T. Pink arrows indicate the prominent LL_{-1}, which shifts away from $V_b = 0$ as B increases.

Based on this interpretation, the LL periodicity Δn can be explained as the filling and emptying of landau levels.[17] When disorder-broadened LLs are half-filled, their density of states is expected to be at its maximum (in the single particle picture). Therefore, the spacing between valleys in $dI/dV_b(n)$ in Fig. 5.13(a) yields the amount of charge necessary to completely fill a LL—namely, its degeneracy. . Figure 5.13(a) shows a constant energy $dI/dV_b(n)$ spectrum taken at $V_b = -0.1$ meV that we use to extract Δn. The data oscillate with a regular periodicity in charge density Δn_i, marked by a black double arrow. This periodicity, which slightly lengthens for the right-most portion of the data, measures the widths of each staircase feature, shown in Fig. 5.12. As expected for graphene, we see a uniform spacing between valleys, corresponding to an LL spectrum with equal degeneracies in each state. We attribute the slightly wider peak at charge neutrality to decreasing quantum capacitance in the prominent gap that separates LL_0 from LL_{-1}, as discussed in Section 5.7. To track the degeneracy as a function of B, we extract Δn for different B and plot the corresponding points in Fig.

5.13(b). Without any fitting parameters, the data show excellent agreement with the theoretical degeneracy $\Delta n = gB/\phi_0$, where $\phi_0 = \frac{h}{e}$ is the flux quantum, and $g = 4$ is the expected single-particle LL degeneracy due to valleys and spins.

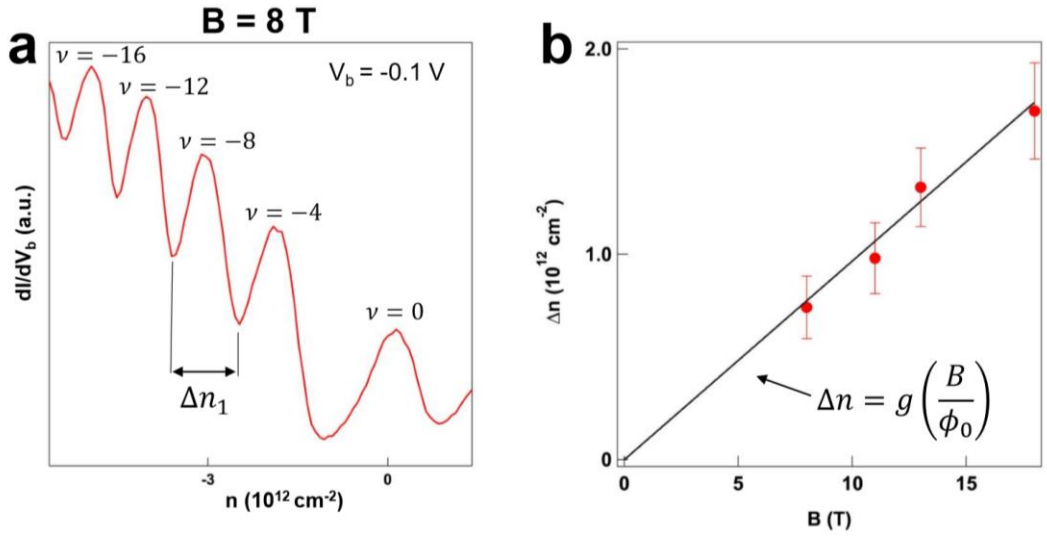

Figure 5.13: Extracting the LL degeneracy (a) Constant $V_b = -0.1$ V horizontal line profile taken from the data in Fig. 5.7(a). The dI/dV_b oscillates with n, with peaks in dI/dV_b corresponding to half-filling of LLs. The period of oscillation corresponds to LL degeneracy Δn. (b) The degeneracy Δn of LL_{-1} at different magnetic fields. The black line shows the expected degeneracy $\Delta n = g\left(\frac{B}{\phi_0}\right)$ where $g = 4$ is the single-particle degeneracy factor for graphene and $\phi_0 = \frac{h}{e}$ is the flux quantum.

5.9 Conclusion and Main Experimental Findings

In conclusion, we developed a systematic method for interpreting and analyzing the gate-tunable tunneling spectra acquired from graphene PTS devices. Our study yields direct identification of graphene's electronic structure features near and far from the Fermi level as they fill and empty with charge. By shearing $dI/dV_b(V_b, V_G)$ to attain $dI/dV_b(V_b, n)$ we resolved the Dirac point For $B = 0$ T and found remarkable agreement between our measurement of the Dirac point and single particle considerations. At finite B we investigated the lifetimes of LLs and determined that they are not equivalent for occupied vs unoccupied states. With full control over the LL filing, we investigated how disorder screening manifests in the LL tunneling spectrum. Interestingly, we observed that the LL spectrum disappears and reemerges as states are pushed through the Fermi level—a phenomenon that we attribute to a tunable screening of disorder. From the LL spectra, we extract graphene's most fundamental parameter, the Fermi velocity, and observe as it renormalizes at low n, a phenomenon predicted to be a result of electron-electron interactions. Surprisingly, the PTS measurement shows signatures of e-e correlations despite the expected screening due to the PTS probe.

Finally, we performed planar tunneling spectroscopy of graphene at unprecedented magnetic fields and observed well-defined LL staircases. From these staircases, we extract a LL degeneracy that shows excellent agreement with single particle theory. We anticipate that the PTS devices presented here will be compatible with yet higher magnetic fields such as 45 T, the highest constant magnetic field

currently available. Thus, our PTS devices and shearing analysis technique will enable direct and thorough characterization of graphene and other 2D materials as their electronic structures are altered by many-body interactions.

References

(1) Decker, R.; Wang, Y.; Brar, V. W.; Regan, W.; Tsai, H.-Z.; Wu, Q.; Gannett, W.; Zettl, A.; Crommie, M. F. Local Electronic Properties of Graphene on a BN Substrate via Scanning Tunneling Microscopy. *Nano Lett.* **2011**, *11* (6), 2291–2295. https://doi.org/10.1021/nl2005115.

(2) Deshpande, A.; Bao, W.; Miao, F.; Lau, C. N.; LeRoy, B. J. Spatially Resolved Spectroscopy of Monolayer Graphene on ${\text{SiO}}_{2}$. *Phys. Rev. B* **2009**, *79* (20), 205411. https://doi.org/10.1103/PhysRevB.79.205411.

(3) Malec, C. E.; Davidović, D. Transport in Graphene Tunnel Junctions. *J. Appl. Phys.* **2011**, *109* (6), 64507. https://doi.org/10.1063/1.3554480.

(4) Zhao, Y.; Wyrick, J.; Natterer, F. D.; Rodriguez-Nieva, J. F.; Lewandowski, C.; Watanabe, K.; Taniguchi, T.; Levitov, L. S.; Zhitenev, N. B.; Stroscio, J. A. Creating and Probing Electron Whispering-Gallery Modes in Graphene. *Science (80-.).* **2015**, *348* (6235), 672–675. https://doi.org/10.1126/science.aaa7469.

(5) Chae, J.; Jung, S.; Young, A. F.; Dean, C. R.; Wang, L.; Gao, Y.; Watanabe, K.; Taniguchi, T.; Hone, J.; Shepard, K. L.; et al. Renormalization of the Graphene Dispersion Velocity Determined from Scanning Tunneling Spectroscopy. *Phys. Rev. Lett.* **2012**, *109* (11), 116802. https://doi.org/10.1103/PhysRevLett.109.116802.

(6) Tersoff, J.; Hamann, D. R. Theory of the Scanning Tunneling Microscope. *Phys. Rev. B* **1985**, *31* (2), 805–813. https://doi.org/10.1103/PhysRevB.31.805.

(7) Chen, C. J. *Introduction to Scanning Tunneling Microscopy*; Oxford Scholarship Online, 2007.

(8) Zhang, Y.; Brar, V. W.; Wang, F.; Girit, C.; Yayon, Y.; Panlasigui, M.; Zettl, A.; Crommie, M. F. Giant Phonon-Induced Conductance in Scanning Tunnelling Spectroscopy of Gate-Tunable Graphene. *Nat. Phys.* **2008**, *4*, 627.

(9) Jung, S.; Myoung, N.; Park, J.; Jeong, T. Y.; Kim, H.; Watanabe, K.; Taniguchi, T.; Ha, D. H.; Hwang, C.; Park, H. C. Direct Probing of the Electronic Structures of Single-Layer and Bilayer Graphene with a Hexagonal Boron Nitride Tunneling Barrier. *Nano Lett.* **2017**, *17* (1), 206–213. https://doi.org/10.1021/acs.nanolett.6b03821.

(10) Velasco, J.; Lee, J.; Wong, D.; Kahn, S.; Tsai, H.-Z.; Costello, J.; Umeda, T.; Taniguchi, T.; Watanabe, K.; Zettl, A.; et al. Visualization and Control of Single-Electron Charging in Bilayer Graphene Quantum Dots. *Nano Lett.* **2018**, *18* (8), 5104–5110. https://doi.org/10.1021/acs.nanolett.8b01972.

(11) Yankowitz, M.; Wang, J. I.-J.; Li, S.; Birdwell, A. G.; Chen, Y.-A.; Watanabe, K.; Taniguchi, T.; Quek, S. Y.; Jarillo-Herrero, P.; LeRoy, B. J. Band Structure Mapping of Bilayer Graphene via Quasiparticle Scattering. *APL Mater.* **2014**, *2* (9), 92503. https://doi.org/10.1063/1.4890543.

(12) Brar, V. W.; Wickenburg, S.; Panlasigui, M.; Park, C.-H.; Wehling, T. O.; Zhang, Y.; Decker, R.; Girit, \ifmmode \mbox\cC\else Ç\fia\ifmmode \breveg\else \ug\filar; Balatsky, A. V; Louie, S. G.; et al. Observation of Carrier-Density-Dependent Many-Body Effects in Graphene via Tunneling

Spectroscopy. *Phys. Rev. Lett.* **2010**, *104* (3), 36805. https://doi.org/10.1103/PhysRevLett.104.036805.

(13) Vdovin, E. E.; Mishchenko, A.; Greenaway, M. T.; Zhu, M. J.; Ghazaryan, D.; Misra, A.; Cao, Y.; Morozov, S. V; Makarovsky, O.; Fromhold, T. M.; et al. Phonon-Assisted Resonant Tunneling of Electrons in Graphene--Boron Nitride Transistors. *Phys. Rev. Lett.* **2016**, *116* (18), 186603. https://doi.org/10.1103/PhysRevLett.116.186603.

(14) Jung, S.; Park, M.; Park, J.; Jeong, T.-Y.; Kim, H.-J.; Watanabe, K.; Taniguchi, T.; Ha, D. H.; Hwang, C.; Kim, Y.-S. Vibrational Properties of H-BN and h-BN-Graphene Heterostructures Probed by Inelastic Electron Tunneling Spectroscopy. *Sci. Rep.* **2015**, *5*, 16642.

(15) Chandni, U.; Watanabe, K.; Taniguchi, T.; Eisenstein, J. P. Signatures of Phonon and Defect-Assisted Tunneling in Planar Metal–Hexagonal Boron Nitride–Graphene Junctions. *Nano Lett.* **2016**, *16* (12), 7982–7987. https://doi.org/10.1021/acs.nanolett.6b04369.

(16) Luican, A.; Li, G.; Andrei, E. Y. Quantized Landau Level Spectrum and Its Density Dependence in Graphene. *Phys. Rev. B* **2011**, *83* (4), 41405. https://doi.org/10.1103/PhysRevB.83.041405.

(17) Dial, O. E.; Ashoori, R. C.; Pfeiffer, L. N.; West, K. W. High-Resolution Spectroscopy of Two-Dimensional Electron Systems. *Nature* **2007**, *448*, 176.

(18) Dial, O. E. Single Particle Spectrum of the Two Dimensional Electron Gas, MIT, 2007.

(19) Jang, J.; Hunt, B. M.; Pfeiffer, L. N.; West, K. W.; Ashoori, R. C. Sharp Tunnelling Resonance from the Vibrations of an Electronic Wigner Crystal. *Nat. Phys.* **2016**, *13*, 340.

(20) Jackson, J. D. *Classical Electrodynamics*; John Wiley & Sons, 1962.

(21) Kim, M.; Xu, S. G.; Berdyugin, A. I.; Principi, A.; Slizovskiy, S.; Xin, N.; Kumaravadivel, P.; Kuang, W.; Hamer, M.; Krishna Kumar, R.; et al. Control of Electron-Electron Interaction in Graphene by Proximity Screenings. *Nat. Commun.* **2020**, *11* (1), 2339. https://doi.org/10.1038/s41467-020-15829-1.

(22) Das Sarma, S.; Hwang, E. H.; Tse, W.-K. Many-Body Interaction Effects in Doped and Undoped Graphene: Fermi Liquid versus Non-Fermi Liquid. *Phys. Rev. B* **2007**, *75* (12), 121406. https://doi.org/10.1103/PhysRevB.75.121406.

(23) Rutter, G. M.; Jung, S.; Klimov, N. N.; Newell, D. B.; Zhitenev, N. B.; Stroscio, J. A. Microscopic Polarization in Bilayer Graphene. *Nat. Phys.* **2011**, *7*, 649.

Chapter 6:

Revealing the Electronic Structure of Bilayer Graphene

Bernal-stacked bilayer graphene (BLG) is the first step towards reconstructing a three-dimensional system out of 2D components. While its constituent graphene sheets can each be characterized by a single parameter, namely γ_0, their coupling in bilayer graphene gives rise to a host of interesting complexity. As a result, up to this point a comprehensive tunneling characterization of BLG is lacking. In this chapter, I apply the planar tunneling spectroscopy (PTS) method to BLG. With the ability to tunnel into occupied and unoccupied states, PTS enables the probing of several important features in the BLG electronic structure that are out of reach for conventional transport and capacitance measurement. These features include the high energy bands and the charge neutrality point as it is pushed away from the Fermi level. Additionally, to explore the crossover between the low and high energy regimes in BLG, we take advantage of the PTS mechanical stability and measure tunneling spectra at unprecedented magnetic fields. In these conditions we observe prominent Landau levels that are spaced on the order of the interlayer coupling. We investigate a large discrepancy in the cyclotron mass extracted at low and high magnetic fields and use it to extract the skew-hopping energy. By conducting tunneling spectroscopy of BLG, we highlight three powerful attributes of PTS: (1) its simple and direct probing of the DOS; (2) its control over the DOS with respect to E_F; and (3) its compatibility with high magnetic fields.

6.1 Device Schematic and Tunneling Characteristics

A schematic of the PTS device is shown in the inset of Fig. 6.1(a) where BLG is sandwiched under a thin hexagonal boron nitride (hBN) tunneling barrier and above a thicker supporting hBN flake. This stack is supported on a SiO_2/Si wafer, which enables application of a gate voltage (V_G). We first perform tunneling spectroscopy at different values of V_G and V_b. Using the methodology established in Section 5.4 we shear the resulting data to produce tunneling maps with charge density n along the horizontal axis. Figure 6.1(a) shows the resulting $dI/dV_b(V_b, n)$ map, with a smooth background subtracted to enhance feature contrast. The data show a dark, ~130 meV horizontal stripe that is independent of n and known to arise from phonon-assisted inelastic tunneling into graphene.[1,2] In addition to the prominent horizontal stripe, there is another suppression in dI/dV_b that descends in energy as BLG is filled with electrons and indicated by a cyan arrow. Additionally, there are enhancements in the tunneling dI/dV_b which descend parallel to the second depression and are indicated by yellow and magenta arrows.

For a closer look at these features, we take vertical line cuts at several values of n from Fig. 6.1(a) (without subtracting a background) and present them as $dI/dV_b(V_b)$ spectra in Fig. 6.1(b). These constant n spectra are shown as black, red, and blue traces which are vertically offset for clarity. Notably, there are several features that the line traces share: (i) a ~130 meV wide suppression in dI/dV_b symmetric about $V_b = 0$; (ii) a dip in dI/dV_b marked by a cyan triangle that appears at $V_b < 0$ in the black trace and moves to $V_b > 0$ in the blue trace; (iii) a kink in dI/dV_b marked by a yellow triangle

that appears ~0.4 eV to the left of feature (ii) in the black trace; and (iv) another kink in dI/dV_b, marked by a magenta arrow that appears ~0.4 eV to the right of feature (ii) in the blue trace. Features (iii) and (iv) are both apparent in the charge neutral trace, symmetric on either side of feature (i). Feature (ii) is absent in the red trace. Spectral features (ii), (iii) and (iv) move to higher energy as BLG becomes more p-doped, but feature (i) remains stationary.

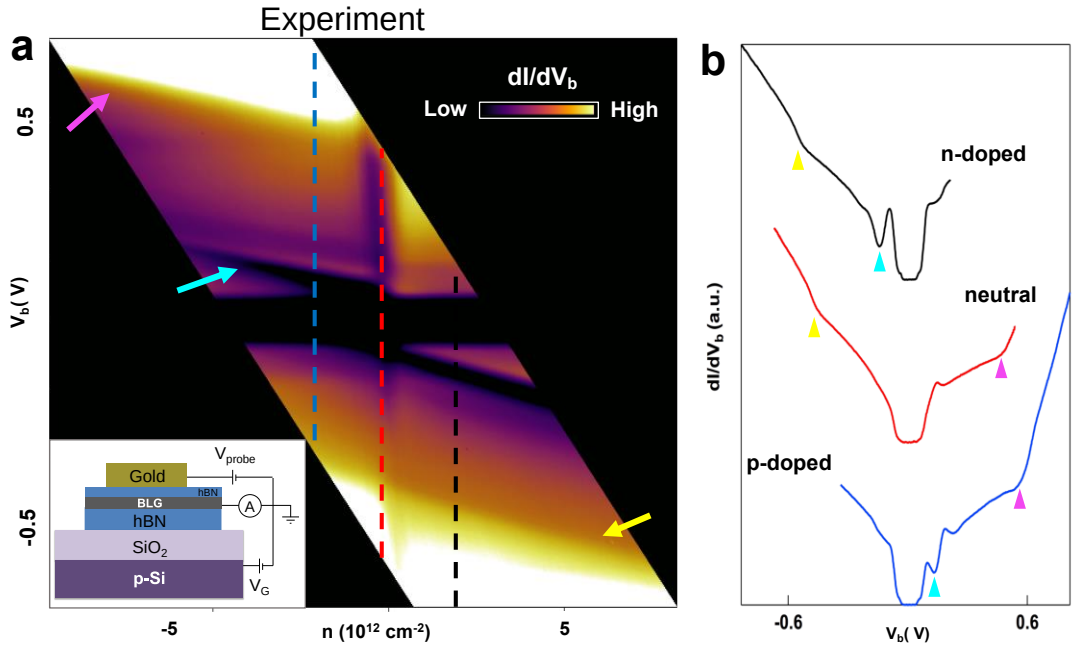

Figure 6.1: Gate-tunable tunneling spectroscopy of bilayer graphene (BLG). (a) Sheared $dI/dV_b(V_b, n)$ map of a BLG planar tunneling spectroscopy (PTS) device where the horizontal axis charge density $n = C_{tg}V_b + C_{bg}V_G$ and C_{tg}, C_{bg} are the top gate and back gate capacitances, respectively. The shear transformation accounts for the charge-inducing effect of the tunneling probe. Inset: schematic of the BLG-PTS device with BLG (gray) sandwiched between two hexagonal boron nitride (hBN) flakes, (both blue). This stack is supported on a SiO_2/Si wafer (lavender/purple), which

enables application of a gate voltage (V_G). A gold electrode (yellow) rests on top of the hBN/BLG/hBN stack and enables application of a voltage (V_{probe}) for inducing a tunneling current. (b) $dI/dV_b(V_b)$ spectra taken along the dashed vertical lines in (a) with corresponding colors. Each line corresponds to a different BLG charge density n, with blue, red and black lines corresponding to p-doped, charge neutral and n-doped BLG, respectively. Line profiles are vertically staggered for clarity. Teal, yellow and magenta triangles denote features (ii), (iii) and (iv), discussed in the text. These features are also marked in Fig. 1(a) with arrows of matching colors.

A feature similar to feature (ii) was also present in the tunneling spectra taken of graphene presented in Section 5.3. The analogous feature was interpreted as the Dirac point, a minimum in graphene's density of states that shifts with respect to the Fermi energy E_F when n is changed. There are several notable differences between the Dirac point suppression in graphene and feature (ii) in BLG. Firstly, feature (ii) is sharper and more pronounced than the suppression in its monolayer counterpart. For instance, at $n = 3 \text{ x } 10^{12} \text{cm}^{-2}$, the width of the Dirac point suppression is ~200 meV, whereas the width of feature (ii) is ~50 meV. Additionally, the trajectory of feature (ii) is markedly distinct from that of the Dirac point in Chapter 5. Feature (ii) appears to draw a straight diagonal line across the map in Fig. 6.1(a), rather than an arc with $\sqrt{n}$ dependence exhibited by the Dirac point. Apparently, both BLG's constant-n tunneling signatures and its filling characteristics are distinct from those of graphene.

Neither feature (iii) nor feature (iv) are present in the tunneling spectra of graphene presented in Chapter 5. These features have several interesting characteristics. At first glance, it appears that feature (iv), marked with a magenta arrow in Fig. 6.1(a), descends parallel to feature (ii), maintaining a constant energy spacing ~0.4 eV. Near charge neutrality, feature (ii) is engulfed by feature (i), and feature (iv) disappears off the map. In the right half of the data, feature (iii) is visible ~0.4 eV below feature (ii). They descend together as n increases. In a short n interval near charge neutrality, coinciding when feature (ii) is near $V_b = 0$, both features (iii) and (iv) are visible and are separated in energy by ~0.9 eV.

6.2. Tunneling Signatures of the BLG High Energy Bands

For a closer look at the behavior of features (i-iv), we take a numerical derivative of the map in Fig. 6.1(a) with respect to V_b. The resulting $|d^2I/dV_b^2(V_b, n)|$ map is shown in Fig. 6.2(a), where purple regions correspond to a low derivative, and yellow regions show large enhancements in dI/dV_b with respect to energy. In the data, feature (ii) now appears as a dark line (denoted with a cyan circle) that has a well-defined, linear trajectory that is bordered above and below by yellow regions. Above feature (ii), feature (iv) is visible as an orange line (denoted by a magenta triangle) that also descends linearly as n increases. The energy spacing between these features is marked with a vertical white double arrow. In the lower half of the map, feature (iii) appears as another orange line, marked with a yellow square. Its separation from feature (ii) is indicated by a double white arrow.

In order to compare feature (iii) to feature (iv), we extract the energy difference between each and feature (ii) at multiple values of n. The histogram of each extracted value is shown in Fig. 6.2(b). Interestingly, the extracted values are bimodal, despite our first impression that they were both ~0.4 eV. Gaussian fits to each of the extracted values are shown as white lines. The precision of shift extraction given by one standard deviation of the fit is ~2 meV. This error value is only slightly higher than the resolution of the measurement, indicating that there is no measurable n-dependence of the feature (ii)—feature (iii) separation or the feature (ii)—feature (iv) separation. In the scope of the measurement, features (i), (ii) and (iii) have parallel trajectories.

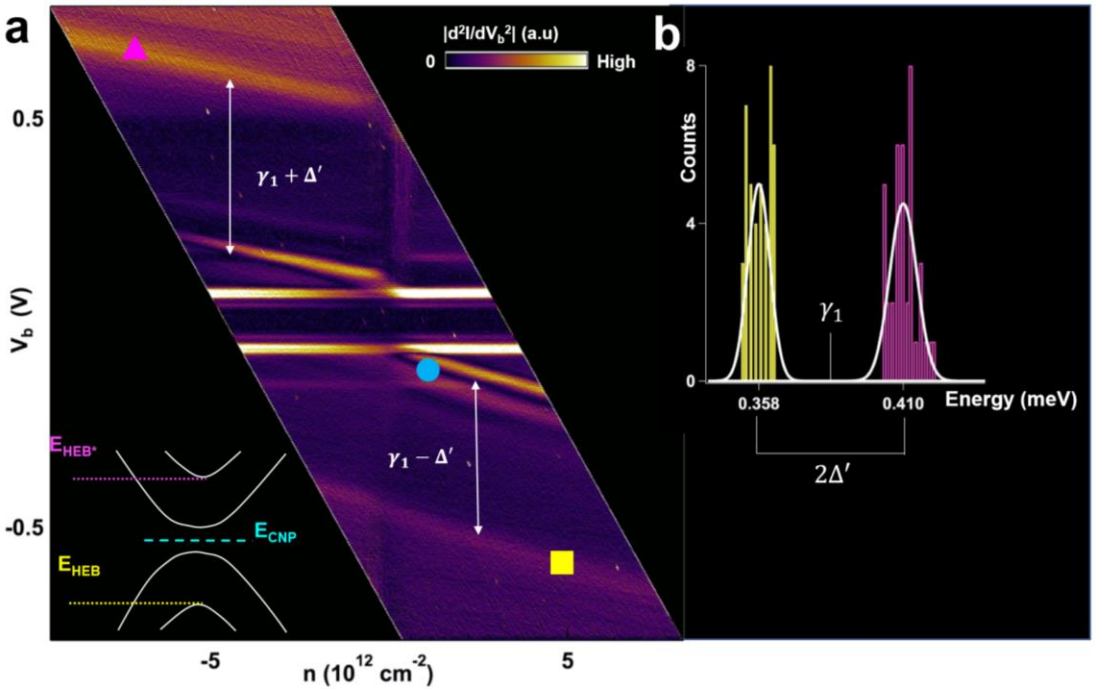

Figure 6.2: Extracting the dimer coupling energy γ_1. (a) Sheared numerical derivative $d^2I/dV_b^2(V_b, n)$ map. Features (ii), (iii) and (iv) are denoted with a cyan circle and yellow square, and magenta triangle, respectively. Lower left inset:

schematic of tunneling into the 4 bands of BLG. Dotted yellow and magenta lines mark the onset of high energy bands (HEB and HEB*). The cyan dashed line indicates the energy of the charge neutrality point (CNP). (b) Histogram showing the extracted CNP to HEB energy difference (yellow) and the HEB* to CNP energy difference (pink). Two white gaussian fits overlay the bimodal data, with mean values of 0.358 and 0.410 eV.

In Chapter 5, a combination of simulations and electrostatic arguments led us to the conclusion that features which shift downward in energy as n increases are states in the electronic structure of graphene (the Dirac point, for example). As electrons are added to the system, the DOS fills, causing states to descend in energy with respect to the Fermi level (E_F, $V_b = 0$). Applying this line of reasoning to the BLG case, we can identify whether tunneling features in Fig 6.2(a) are electronic structure features by their n-dependence. In intrinsic graphene, the density of states is assumed to be linear and thus mostly featureless. Bilayer graphene, however, has a DOS that is textured with several interesting attributes, which were introduced in Chapter 2. We should then expect to see several features shift in energy as n is modulated in Fig. 6.2(a). By examining these features we can uncover the fundamental properties of BLG's electronic structure.

Two prominent features in the BLG electronic structure are high energy bands HEB and HEB*, which arise due to the breaking of mirror plane symmetry by the 4 constituent atoms in the BLG unit cell. These two features are introduced in Chapter 2

but are reintroduced here for continuity. The two layers of Bernal-stacked BLG are arranged such that two carbon atoms are vertically stacked, while the other two are offset (see Fig. 2.7). This arrangement brings each graphene layer one step closer to three dimensions, breaking mirror plane symmetry and causing a dimerization between stacked carbon orbitals. This coupling lifts the degeneracy of the four BLG bands at the K and K' points in reciprocal space, leaving two that remain degenerate, and two that are separated. These two additional high energy bands straddle the CNP but are separated by twice the sheet-coupling energy γ_1.[3,4]

The Bernal configuration causes additional symmetry breaking between atoms in the unit cell, leading to further augmentation of the band structure. The vertically aligned carbon atoms rest in a different electronic environment than carbon atoms which are offset. While not as drastic as carbon-carbon hopping energy γ_0 or dimer-site coupling γ_1, the energy difference between stacked and offset carbon sites Δ' can result in adjustments to the BLG bands, as detailed in Chapter 2. Specifically, HEB and HEB* are shifted up or down in energy by Δ'. While the HEB and HEB* have been probed with optical spectroscopy,[5,6] transport[7] and photoemission,[8] they have yet to be reported with tunneling spectroscopy. In those reports, the energy of HEB and HEB* is in the range of 0.38-0.4 eV.

The n-dependent behavior of features (iii) and (iv) indicates that they are features in the BLG DOS. Furthermore, both of these features cause a ~2-fold enhancement in tunneling dI/dV_b, indicating that they correspond to the onset of a double band degeneracy. Finally, features (iii) and (iv) are separated by 0.768 eV,

which agrees with the previously reported optical excitation energy for transitions between HEB and HEB*.[5,6] Therefore, we identify features (iii) and (iv) as BLG's HEB and HEB*. From their energy separation, we then extract the dimer site coupling energy $\gamma_1 = 0.384 \pm 0.003$ eV. Figure 6.2(b) shows that their energies are offset from the CNP. Halving this offset, we determine the intrinsic energy difference $\Delta' = 0.026 \pm 0.003$ eV. These values agree with those previously reported from reflectivity measurements,[5,6] but are seen here for the first time with tunneling spectroscopy.

6.3. Accounting for Phonon-Assisted Tunneling in BLG

Previous scanning tunneling spectroscopy (STS) and planar tunneling spectroscopy (PTS) studies of graphene have shown strong *n*-independent enhancement in dI/dV_b centered around $V_b = 0$ V that is understood to be associated with phonon-assisted tunneling.[1,2,9–11] As detailed in Section 3.7, the low energy surface state of BLG decays rapidly into the vacuum due to its high in-plane momentum. With STS, it is possible to overcome this decay by reducing the tip-sample distance to several Angstroms. The PTS measurement, however, does not have this freedom. As a result, there is a complete suppression of elastic tunneling between the metal probe and BLG and inelastic tunneling dominates the dI/dV_b signal. In effect, modes with energies $\{\hbar\omega_0, \hbar\omega_1, \hbar\omega_2, \ldots\}$ in either the BLG or tunneling barrier can scatter off tunneling charges, reducing their in-plane momentum and extending their state out of the plane. Notably, phonons can only be excited if the tunneling energy is above a certain quantized threshold. The experimental signature of this inelastic

tunneling is a series of enhancements in dI/dV_b at energies $|eV_b| = \hbar\omega_i$ that are independent of n. Excitation of each additional mode opens another tunneling channel proportional to $g(eV_b - \hbar\omega_i)\Theta(eV_b - \hbar\omega_i)$ if $V_b > 0$, and $g(eV_b - \hbar\omega_i)\Theta(eV_b - \hbar\omega_i)$ if $V_b < 0$, resulting in series tunneling conductance enhancements. The overall tunneling conductance has contributions from each available tunneling channel and can be written (ignoring ch. 2 tunneling discussed in the text):

$$\frac{dI}{dV_b}(eV_b) \propto \sum_i [g(eV_b - \hbar\omega_i)\Theta(eV_b - \hbar\omega_i) + g(eV_b + \hbar\omega_i)(1 - \Theta(eV_b + \hbar\omega_i))] \tag{6.1}$$

where $g(eV_b)$ is the BLG density of states and $\Theta(\epsilon)$ is the Heaviside function. Taking the derivative of Eq. 6.1with respect to eV_b,

$$\frac{d^2I}{dV_b^2}(eV_b) \propto \sum_i [g(eV_b - \hbar\omega_i)\delta(eV_b - \hbar\omega_i) - g(eV_b + \hbar\omega_i)\delta(eV_b + \hbar\omega_i))] \tag{6.2}$$

$$\frac{d^2I}{dV_b^2}(eV_b) \propto \sum_i [\delta(eV_b - \hbar\omega_i) - \delta(eV_b + \hbar\omega_i)] \tag{6.3}$$

Therefore, phonon-assisted tunneling enhancements are associated with sharp peaks in tunneling $\frac{d^2I}{dV_b^2}$ spectra that are antisymmetric about $eV_b = 0$ and the peak energy corresponds to phonon energy $\hbar\omega_i$.

These inelastic tunneling features are readily apparent as bright horizontal lines in the $|d^2I/dV_b^2(V_b, n)|$ map shown in Fig. 6.2(a) and 6.3(a). For a closer look at the n-independent bright lines, we average over n to produce the inelastic tunneling

spectrum shown in the inset as a cyan line. Magenta, white and yellow tick marks in the inset denote the peak positions along this spectrum at energies ± 38, ± 63 and ± 73 meV that are antisymmetric about $V_b = 0$. The peak energies agree well with phonon excitations previously reported.[1,2]

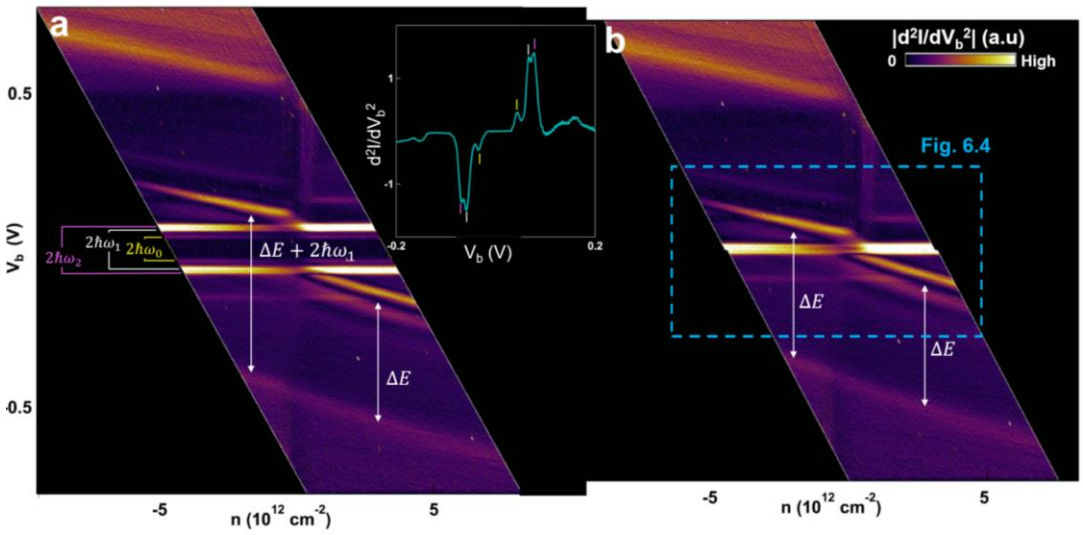

Figure 6.3: Identifying and compensating for phonon-assisted tunneling. (a) Sheared numerical derivative $|d^2I/dV_b^2(V_b, n)|$ map. Here, yellow, white and magenta lines show the energy spacing between horizontal bright streaks in the data. The spacings are labelled $\hbar\omega_0$, $\hbar\omega_1$, and $\hbar\omega_2$, respectively. Vertical, white double arrows denote the charge neutrality point (CNP) to high energy band (HEB) energy shift ΔE in two locations on the map. Notably the difference between ΔE_1 and ΔE_2 is $\hbar\omega_1 = 126$ meV. Inset: averaged $d^2I/dV_b^2(V_b)$ signal showing individual peaks at energies $\hbar\omega_i$ that are antisymmetric about $V_b = 0$. (b) Adjusted tunneling $|d^2I/dV_b^2(V_b, n)|$ map with dominant phonon energy $\hbar\omega_1$ subtracted. Vertical double arrows in (a) and (b) show energy difference between the CNP and HEB when $E_{CNP} > 0$ and $E_{CNP} < 0$.

Subtraction of the correct phonon energy $\hbar\omega_1$ results in vertical double arrows that are equal in length, indicating that the CNP remains a constant energy from the HEB, namely $\gamma_1 - \Delta'$.

Having identified pronounced inelastic tunneling effects, we next account for resulting energy shifts in the BLG tunneling spectrum. Following the methodology established by Zhang, et. al.,[1] we first directly extract the energy eV_b of BLG's tunneling features (the charge neutrality point, for example), then subtract the phonon threshold energy $\hbar\omega$ to determine the energy of that feature.[1] Notably, with several prominent phonon enhancements, it is critical to identify the dominant channel, and subtract its corresponding energy. We unambiguously identify the dominant phonon excitation, and the corresponding energy shift of spectral features, by comparing the two halves of the $|d^2I/dV_b^2(V_b, n)|$ map. Notably, the high energy band HEB in the lower right quadrant of the map in Fig. 6.3(a) is consistently 0.358 V below the CNP. In the lower left quadrant of the same map, the HEB is 0.484 V below the CNP. The dominant phonon energy is identified as (0.484 V– 0.358 V) / 2 = 0.063 V. Therefore, spectral feature shifts due to inelastic tunneling can be compensated for by subtracting 63 mV from each half of the map. The corrected tunneling map is shown in Fig. 6.3(b), where both vertical double arrows indicate the energy difference between HEB and CNP, which is 358 mV everywhere on the map.

6.4 Tracking $E_F(n)$ to Determine in-Plane Hopping γ_0 and Skew Hopping γ_4

Having identified the HEB and HEB* and used their energies to determine two tight binding parameters of BLG—γ_1 and Δ'—we now turn to feature (ii), introduced in Section 6.1. Feature (ii) moves parallel to HEB and HEB* across the tunneling map in Fig. 6.3(b) and can thus be identified as embedded in the BLG DOS. Moreover, feature (ii) is energy $\gamma_1 - \Delta'$ above the HEB and energy $\gamma_1 + \Delta'$ below the HEB*, and positioned where the two lower energy bands should touch in pristine BLG. Therefore, we identify feature (ii) as the charge neutrality point (CNP). With inelastic shifts in the tunneling spectra accounted for, it is now appropriate to compare the top and bottom halves of the data in Fig. 6.3(b). In the top half of the data ($V_b > 0$), states are unoccupied and in the bottom half, they are occupied. Observing the trajectory of the CNP as it shifts in energy from the top to bottom half of the map can thus provide insight on the filling characteristics—and thus the shape—of the BLG DOS.

As discussed in Section 2.1, BLG's bands are nearly parabolic at low energies. As a result, the BLG DOS can be approximated as constant, and as charge is added to BLG, the Fermi energy $E_F(n)$ shifts linearly with respect to the DOS. In tunneling spectroscopy, E_F is pinned to $V_b = 0$, so it is convention to instead treat the DOS as shifting in energy. The trajectory of static features in the DOS (such as the CNP, for example) is related to the fundamental quantity $E_F(n)$ by a minus sign, as discussed in Section 5.5. The dependence $E_F(n)$ in BLG is sensitive to the shape of the DOS, which is in turn sensitive to the BLG Hamiltonian. Therefore, we can determine key

parameters in the Hamiltonian by fitting the resulting filling relation E_F to the trajectory of the CNP.

The full tight binding Hamiltonian for ungapped BLG (introduced in Section 2.13) has five independent intrinsic parameters: γ_0, γ_1, γ_3, γ_4 and Δ'.[3,4] In Section 6.2, we determined γ_1 and Δ'. Two of the remaining parameters, γ_0 and γ_4, the intralayer hopping and skew hopping energies, respectively, influence the shape of the BLG bands, and thus $E_F(n)$. In order to measure these parameters, we calculate the relation $E_F(n)$ for a series of γ_0, γ_4 values and compare to the experimental trajectory of the CNP. Figure 6.4 outlines the sensitivity of $E_F(n)$ to each small variation in either γ_0 or γ_4. In Fig. 6.4(a) there is a zoom in $|dG/dV_G(V_b, V_G)|$ map taken of the region outlined with a blue dashed line in Fig. 6.3(b). The CNP, denoted with a cyan arrow, is a dark region stretching from the top left to bottom right of the data. Three areas used to test the $E_F(n)$ fit are outlined in white. The lower and upper panels in Figs. 6.4(b-e) correspond to the occupied and unoccupied regions of the CNP. The relation $E_F(n)$ is plotted for three different values of γ_0 : 2.7, 2.8, and 2.9 eV, shown as white, pink and red lines, respectively in Figs. 6.4(b) and 6.4(d). Interestingly, as γ_0 increases in the model, $E_F(n)$ decreases for unoccupied states and increases for occupied states. This is not the case for changes in γ_4, shown by white, light blue and dark blue lines in Figs. 6.4(c) and 6.4(e). As shown in the figure, small increases in γ_4 result in an upward shift in $E_F(n)$. Because the two effects are linearly independent, varying γ_0 and γ_4 independently results in an unambiguous fit of the CNP trajectory.

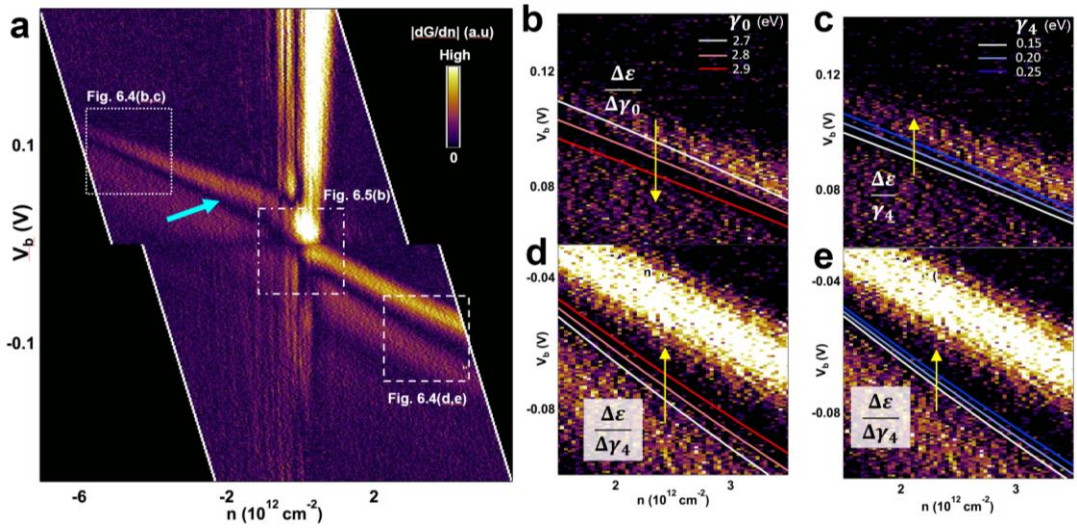

Figure 6.4: Extracting the interlayer coupling γ_0 and electron-hole asymmetry γ_4. (a) Numerical derivative $|dG/dn(V_b, n)|$ tunneling map, showing the charge neutrality point (CNP) as a dark feature denoted with a cyan arrow. (b,c) Zoom in on the trajectory of the CNP in the region outlined with a white dotted square in (a). Red, pink and white lines overlay the data in (b), showing the $E_F(n)$ fit with parameters γ_0 set to 2.9, 3.0 and 3.1 eV, respectively. The dark blue, light blue and white lines in (c) overlay the data indicating the fit values when γ_4 is set to 0.15, 0.2, 0.25 eV, respectively. The yellow arrow indicates the direction of the fit value when each of the parameters is changed. (d,e) Comparison of experimental and fit values of $E_F(n)$ for the region outlined with a white dotted-dashed line in (a). Notably, small increases in γ_4 shift E_F downward in both regions, while small increases in γ_0 decrease $E_F$for holes and decrease E_F for electrons.

Even with the inelastic tunneling shifts accounted for, the data in Fig 6.4(a) shows a discontinuity in the trajectory of the CNP. This "transport gap" is discussed at length in Chapter 7. For our current purposes, it must be accounted for in fitting E_F to the CNP trajectory. In order to compensate for this discontinuity, we include an interlayer potential energy difference U_T in the simulation that breaks the degeneracy between π and π^* bands, causing a jump in E_F at $n = 0$. Figure 6.5(a) demonstrates the effect of including different size U_T. Notably, although U_T in the figure varies by a factor of 2 between the magenta and yellow lines, the asymptotic trajectory of CNP is similar for all three lines. The parameter U_T can then be assumed to not necessarily manipulate the quality of the fit at $|n| \gg 0$, but, interestingly, can be used to characterize the low-n behavior. Methods on measuring and using U_T are detailed in Chapter 7. Figure 6.5(b) shows the best fit relation $E_F(n)$ with parameters $\gamma_0 = 2.65$ eV, $\gamma_4 = 0.12$ eV and $U_T = 0.045$ eV. While the uncertainties in γ_0 and γ_4 are less than 5 %, deviations from the fit at low n have an uncertainty of ~20% for U_T. The cause of this uncertainty poses interesting questions about the BLG electronic structure near charge neutrality. I will discuss the low energy BLG DOS in Chapter 7.

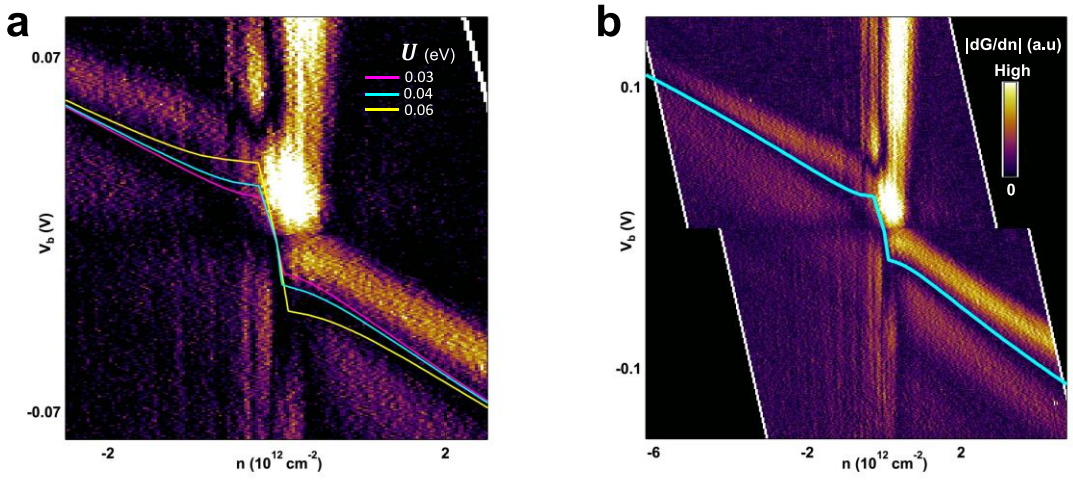

Figure 6.5: Extracting the band shift U_T as the CNP approaches E_F. (a) The charge neutrality point (CNP) trajectory is fit by $\mu(n)$, shown as a cyan line. Parameters $\gamma_0 = 2.65$ eV, $\gamma_4 = 0.12$ eV and $U_T = 0.03 \pm 0.01$ eV are used to calculate $\mu(n)$. The match between experiment and fit is slightly offset at low n, but improves as $|n|$ increases. (b) Zoom in of the low n region in (a), with three different calculated $\mu(n)$ lines overlaying the data. The magenta, cyan and yellow lines are calculated using $U_T = 0.03, 0.04$, and 0.06 eV.

6.5 Extracting the Effective Mass in BLG at Low and High Energy

At low energies ($\varepsilon \ll \gamma_1$), the BLG band structure is nearly parabolic and well characterized by coupling γ_1 between two graphene sheets, that are each described by in-plane hopping γ_0.[4] As shown in the previous section, Δ' and γ_4 are only small adjustments to the overall electronic structure.[5] In this section, we will examine the crossover between the low and high energy regimes in BLG.

In Section 6.4, we extracted two of BLG's tight binding parameters by tracking $E_F(n)$ as it changed with electrostatic gating. While this method is ideal for filling and emptying the low energy DOS, the possibility of gate leakage restricts the energy range where this technique can be employed to roughly <|100 meV| for BLG. On the other hand, while spectroscopy measurements employed in Section 6.2 yielded γ_1 and Δ' by accessing the HEBs ~400 meV away from E_F, they detected no notable electronic structure features between the CNP and the HEBs, where the BLG DOS is featureless. We need a method for examining the DOS between the CNP and the HEBs in order to understand the crossover between the low energy $\varepsilon \ll \gamma_1$ and high energy $\varepsilon \sim \gamma_1$ regimes. In order to add texture to the BLG bands between the CNP and HEBs, we take advantage of the PTS compatibility with high magnetic fields B.

Figure 6.6(a) shows a large-scale numerical derivative $d^2I/dV_b^2(V_b, n)$ map of BLG taken in a perpendicular magnetic field B=11T. Light and dark regions on the map correspond to high and low change in the tunneling dI/dV_b with respect to V_b.

[5] There is one remaining hopping parameter, γ_3, that warps the BLG band structure.[19] Notably, γ_3 does not change the relation $E_F(n)$ away from the CNP and can thus be ignored in this treatment.

Notably, there are numerous features in this data that are not present in Fig. 6.3(a), which was taken of the same device when B=0T. There are two distinct groups of features: (1) equally spaced vertical lines that intensify in the top half of the map and diminish in the bottom half of the map as $|n| \to 0$; and (2) striated features that border the CNP and the HEBs. The vertical features each appear at constant n, similar to feature (i) described in Section 5.3. In our work on graphene in Chapter 5, we attributed constant n-features to an additional tunneling channel that is opened at E_F due to the capacitive coupling between the probe and sample.[12,13] In graphene, feature (i) observed at B=0T became multiple vertical features at B>0T that were identified as Landau levels—quantized cyclotron orbit states with a distinct character in graphene systems. Here, we adopt a similar description of the vertical features as LLs which change the overall dI/dV_b substantially as they are pulled through E_F.

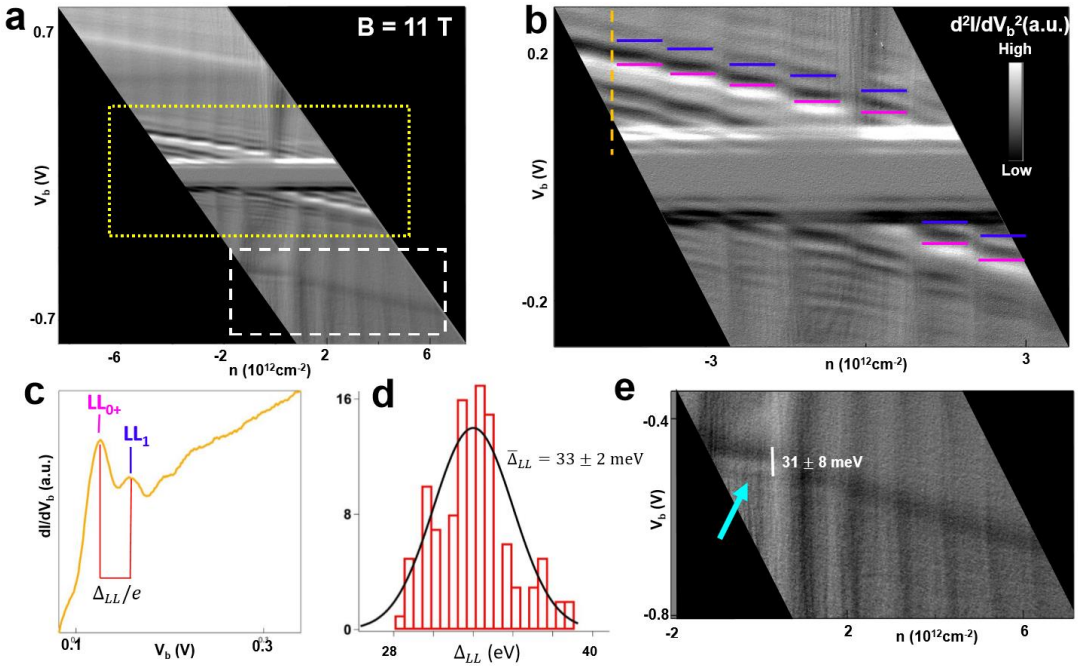

Figure 6.6: Tunneling into BLG Landau levels. (a) Large scale numerical derivative $d^2I/dV_b^2(V_b, n)$ map of BLG taken in a perpendicular magnetic field B=11T. Light and dark regions correspond to high and low change in the tunneling dI/dV_b with respect to V_b. The yellow dashed rectangle outlines staircase features discussed in the text. (b) High resolution zoom-in of the staircase features, outlined by the yellow rectangle in (a) and discussed in the text. Magenta and blue horizontal lines denote regions where dark and bright d^2I/dV_b^2 border each other, corresponding to peaks in the dI/dV_b. (c) Line profile in tunneling conductance dI/dV_b along the same path as the orange line in (b). Peaks in dI/dV_b are labelled LL_{0+} and LL_1 with magenta and blue lines, respectively. The horizontal displacement Δ_{LL}/e between the two peaks is marked with a red line. (d) A histogram of neighboring peak energy difference Δ_{LL} with

a gaussian fit overlaid. The mean value is $\overline{\Delta}_{LL} = 0.033 \pm 0.004$ eV to one standard deviation. (e) Zoom-in tunneling map of the high energy features outlined by a white rectangle in (a). A cyan arrow denotes a parallel set of dark horizontal lines in d^2I/dV_b^2 separated by ~30 meV.

For a closer look at the striated features bordering the CNP, we show a high-resolution zoom-in of the region outlined by a yellow rectangle in Fig. 6.6(a). In the high-resolution map, the striated features have trajectory distinct from the CNP studied in Section 6.4. Specifically, the features, maintain a constant, ladder-like spacing across the map. As n increases, this ladder pattern undergoes a series of jumps in energy. The jumps in the top half of the map occur at regular intervals of $\Delta n \sim 1\text{x}10^{12}\text{cm}^{-2}$. In the bottom half of the map, nearly all jumps are spaced by Δn. Interestingly, there is the absence of a jump near $n = 0$ in the bottom of the map. To track the ladder, we mark two of its most prominent rungs with a magenta and a blue horizontal line in Fig. 6.6(b). Along the map, these two lines maintain a spacing of ~ 0.03 V. Figure 6.6(c) shows a line profile in tunneling conductance dI/dV_b along the same path as the orange line in (b). Peaks in dI/dV_b are labelled LL_{0+} and LL_1 with magenta and blue lines, respectively. The horizontal displacement Δ_{LL}/e between the two peaks is marked with a red line. We track the energy difference between peaks Δ_{LL} at ~100 meV values of n to investigate the uniformity of their spacing. A histogram of the extracted values in Fig. 6.6(d) shows that the average spacing $\overline{\Delta} = 33 \pm 4$ meV is independent of n within the resolution of the experiment.

In the bottom half of the map in Fig. 6.6(a), outlined by a white, dashed rectangle, the HEB shows distinct behavior from its B=0T counterpart in Fig. 6.2(a). Figure 6.6(e) shows a zoom-in of the HEB. The vertical features in this data maintain an even spacing and cross the HEB where it is split into a staircase pattern, indicated by a cyan arrow. Additionally, here is a faint ladder-like structure to the HEB, where the two visible rungs are separated by ~30 meV. Clearly, the presence of a magnetic field can add features to the BLG DOS that are detectable with PTS. Now we turn to determine the origin of these features.

In Chapter 5, we identified striated patterns that bordered the CNP to direct tunneling into graphene's LLs when they were away from E_F. Near $n = 0$, the LLs in graphene were seen undergoing large jumps in energy. This behavior was explained by Fermi level pinning to highly degenerate states at half filling.[14–16] In BLG, the data show many resemblances to graphene. We can therefore apply similar interpretation to BLG. The ladder rungs in Fig. 6.6(b) are LLs when they are away from E_F. After each LL is filled at E_F ($V_b = 0$), the next LL above it is rapidly pulled to E_F. This phenomenon will be discussed further in Chapter 7, where it will be used to explore BLG's DOS near charge neutrality.

The LL spectrum for BLG, derived in Section 2.15, follows the relation $E_{LLN} = \hbar\omega_c\sqrt{n(n-1)}$,where $\omega_c = eB/m$ and m is the carrier effective mass.[17,18] In the presence of a perpendicular displacement field, this relation changes slightly, and the $n = 0, 1$ degeneracy is lifted, shifting all other levels up by the interlayer energy difference. Notably, both the degeneracy-lifted zeroth LL and its adjacent LL_1 are

shifted and the spacing between these two adjacent levels is given by $\Delta_{LL} = \left(\frac{U}{\gamma_1}\right)\hbar\omega_c$.[4,15] Assuming for now that U is approximately constant along the trajectory of mapped by pink lines in Fig. 6.6(b),[6] we can then directly extract a low energy effective mass m_{LE} from the histogram in Fig. 6.6(d) to be $33 \pm 2\text{meV}$, where error is given to one standard deviation of the fit. This approximation gives us a low energy mass $m_{LE} = (4.7 \pm 0.3) \times 10^{-2} m_e$, where m_e is the free electron mass. This effective mass agrees with those previously reported using different methods.[6,15]

Having established the method for extracting the effective mass at low energies, we now examine the case where the LL spacing is on the order of γ_1. Figure 6.7(a) shows a numerical derivative $d^2I/dV_b^2(V_b, n)$ map of BLG taken at B=18T. The data have similar characteristics to the lower B data shown in Fig. 6.6(a), both vertical and ladder-like features. In the higher field data, these features are more pronounced: each vertical feature is spaced from its neighbors by ~2x10^{12} cm^{-2} and the ladder rungs are now more defined due to their separation. Figure 6.7(b) is line profile in tunneling conductance dI/dV_b along the same path as the orange dashed line in Fig. 6.7(a). The peaks in this profile are more prominent, numerous and spread out than those in Fig. 6.6(c).

[6] While the constant U assumption is not necessarily true, in this this experiment we account for the changing U value with experimental error. In Chapter 7, we will address the issue of tunneling into a dynamic band structure.

Following the method established above, we extract the LL spacing between neighboring symmetry-broken LLs. The horizontal displacement Δ_{LL}/e between the two peaks LL_{0+} and LL_1 is marked with a red line in Fig. 6.7(b). We repeat the peak extraction for 50 different spectra, each at a different n and plot the results as a histogram in Fig. 6.7(c). From the mean of the histogram 67 meV, we then calculate the high energy effective mass $m_{HE} = (3.9 \pm 0.1) \times 10^{-2} m_e$. Interestingly m_{LE} and m_{HE} independently agree with previous studies of the effective mass in BLG, but they disagree with each other by ~20%![4,15] One explanation for this discrepancy is the electric field-inducing effect of the probe. The LL spacing depends on interlayer asymmetry U, which is in turn depends on V_b. However, we refute this explanation as incommensurate with the data: within a given tunneling map, either Fig. 6.6(b) or 6.7(a), we do not observe any V_b-dependence of Δ_{LL} beyond the experimental resolution (set by the disorder broadening of LLs). Additionally, the V_b range traversed by LL_{0+} and LL_1 in Fig. 6.6(b) is larger than the difference in V_b between LL_1 at 11 T and at 18 T, indicating that V_b differences cannot account for the discrepancy in m_{LE} and m_{HE}.

An alternative explanation to the change in effective mass at high B is the breakdown of the low-energy approximation for BLG. In order to bolster this claim, we note that there is a third effective mass data point at $B = 0\ T$, that is calculable from the hopping parameters extracted in previous sections. Specifically, the effective mass can be written

$$m = \frac{4\hbar^2}{3a^2}\left(\frac{\gamma_1}{\gamma_0^2}\right) \tag{6.4}$$

Plugging in the values $\gamma_1 = 0.384$ and $\gamma_0 = 2.65$ eV, extracted in Sections 6.2 and 6.4, we calculate $m = (0.049 \pm 0.1)m_e$, which agrees well with m_{LE}. According to our calculations, the low energy approximation becomes an overestimate to the LL spacing. This can be explained by the non-constant curvature of the BLG bands. In future work, we aim to explore a method for extracting the fifth and final parameter, γ_3, from this cyclotron discrepancy.

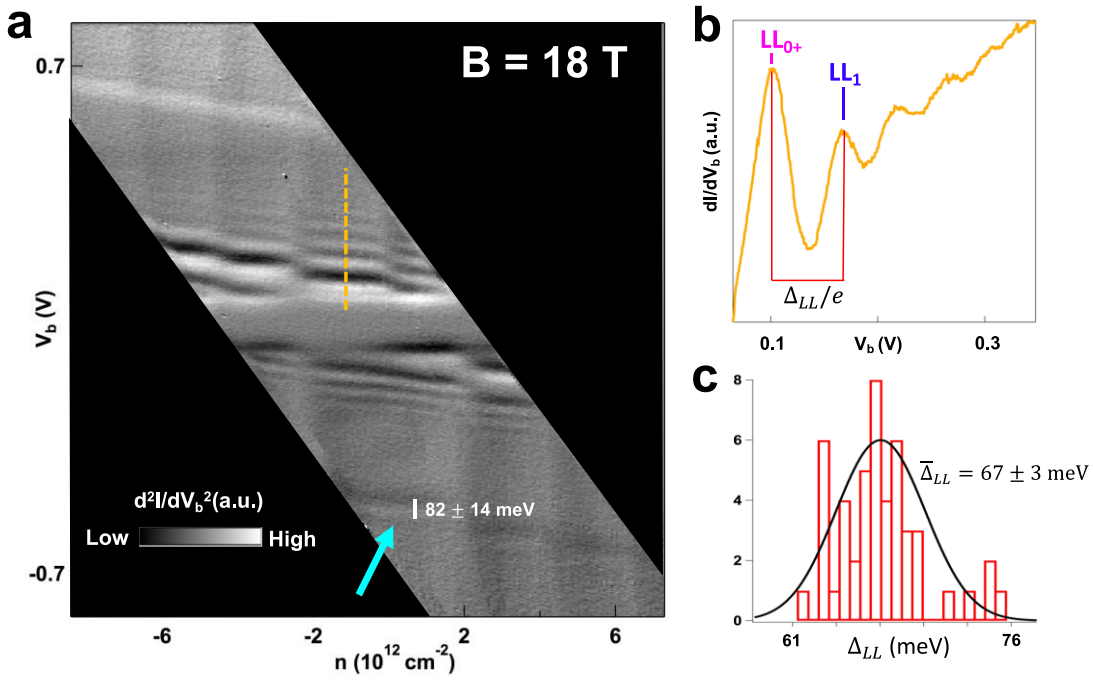

Figure 6.7: Tunneling into BLG at high magnetic field. (a) Numerical derivative $d^2I/dV_b^2(V_b, n)$ map of BLG taken in a perpendicular magnetic field B=18T. Light and dark regions correspond to high and low change in the tunneling dI/dV_b with respect to V_b. A cyan arrow denotes a parallel set of dark horizontal lines in d^2I/dV_b^2, separated by ~80 meV. (b) Line profile in tunneling conductance dI/dV_b along the same path as the orange line in (a). Peaks in dI/dV_b are labelled LL_{0+} and LL_1 with magenta and blue lines, respectively. The horizontal displacement Δ_{LL}/e between the two peaks is marked with a red line. (c) A histogram of neighboring peak energy difference Δ_{LL} with a gaussian fit overlaid. The mean value is $\overline{\Delta}_{LL} = 0.067 \pm 0.003$ eV to one standard deviation.

6.6 Conclusion and Main Experimental Findings

In this chapter, we applied the PTS technique to BLG, a material that is characterized by five independent parameters: $\gamma_0, \gamma_1, \gamma_3, \gamma_4$ and Δ'. With the capability of tunneling into BLG far from E_F, we observed the high energy bands for the first time with tunneling spectroscopy of any kind. We used the high energy bands to extract two of the band structure parameters γ_1 and Δ'. Next, we used the control over n given by the planar capacitor nature of PTS to track E_F as BLG was filled with charge. We used the relation $E_F(n)$ to determine two main components that dictate the shape of the DOS—similar to determining the shape of a water container by adding water and tracking its level. From these measurements we extracted γ_0 and γ_4 for the first time with this technique. Finally, we added texture to the DOS between the CNP and HEBs by inducing Landau quantization with a perpendicular magnetic field. Interestingly, we find that tunneling at unprecedented B allows us to track the crossover between low and high energy regimes in the BLG band structure. From these observations, we determined a non-constant band curvature that manifests in the lowest LL spacing at high magnetic fields.

We have thus used PTS to perform a self-contained and full characterization of BLG's elusive electronic structure. While prior tunneling characterizations of BLG has been reported, no previous measurement has included the number and precision of independent BLG parameters reported here. Our measurements show strong agreement with the literature, indicating that PTS can be used to quantitatively characterize complex 2D materials. This work provides a roadmap for probing the electronic

structure at up to ~0.8 eV from the Fermi level, making it an ideal technique for characterizing gaps and effective masses in monolayer transition metal dichalcogenides and black phosphorus, for example. Many 2D materials have yet to be probed with tunneling spectroscopy at high magnetic fields, and their effective masses remain unknown.

References

(1) Zhang, Y.; Brar, V. W.; Wang, F.; Girit, C.; Yayon, Y.; Panlasigui, M.; Zettl, A.; Crommie, M. F. Giant Phonon-Induced Conductance in Scanning Tunnelling Spectroscopy of Gate-Tunable Graphene. *Nat. Phys.* **2008**, *4*, 627.

(2) Chandni, U.; Watanabe, K.; Taniguchi, T.; Eisenstein, J. P. Signatures of Phonon and Defect-Assisted Tunneling in Planar Metal–Hexagonal Boron Nitride–Graphene Junctions. *Nano Lett.* **2016**, *16* (12), 7982–7987. https://doi.org/10.1021/acs.nanolett.6b04369.

(3) Wallace, P. R. The Band Theory of Graphite. *Phys. Rev.* **1947**, *71* (9), 622–634. https://doi.org/10.1103/PhysRev.71.622.

(4) McCann, E.; Koshino, M. The Electronic Properties of Bilayer Graphene. *Reports Prog. Phys.* **2013**, *76* (5), 56503.

(5) Zhang, L. M.; Li, Z. Q.; Basov, D. N.; Fogler, M. M.; Hao, Z.; Martin, M. C. Determination of the Electronic Structure of Bilayer Graphene from Infrared Spectroscopy. *Phys. Rev. B* **2008**, *78* (23), 235408. https://doi.org/10.1103/PhysRevB.78.235408.

(6) Kuzmenko, A. B.; Crassee, I.; van der Marel, D.; Blake, P.; Novoselov, K. S. Determination of the Gate-Tunable Band Gap and Tight-Binding Parameters in Bilayer Graphene Using Infrared Spectroscopy. *Phys. Rev. B* **2009**, *80* (16), 165406. https://doi.org/10.1103/PhysRevB.80.165406.

(7) Efetov, D. K.; Maher, P.; Glinskis, S.; Kim, P. Multiband Transport in Bilayer Graphene at High Carrier Densities. *Phys. Rev. B* **2011**, *84* (16), 161412.

https://doi.org/10.1103/PhysRevB.84.161412.

(8) Ohta, T.; Bostwick, A.; Seyller, T.; Horn, K.; Rotenberg, E. Controlling the Electronic Structure of Bilayer Graphene. *Science (80-.).* **2006**, *313* (5789), 951–954. https://doi.org/10.1126/science.1130681.

(9) Brar, V. W.; Wickenburg, S.; Panlasigui, M.; Park, C.-H.; Wehling, T. O.; Zhang, Y.; Decker, R.; Girit, \ifmmode \mbox\cC\else Ç\fia\ifmmode \breveg\else \ug\filar; Balatsky, A. V; Louie, S. G.; et al. Observation of Carrier-Density-Dependent Many-Body Effects in Graphene via Tunneling Spectroscopy. *Phys. Rev. Lett.* **2010**, *104* (3), 36805. https://doi.org/10.1103/PhysRevLett.104.036805.

(10) Vdovin, E. E.; Mishchenko, A.; Greenaway, M. T.; Zhu, M. J.; Ghazaryan, D.; Misra, A.; Cao, Y.; Morozov, S. V; Makarovsky, O.; Fromhold, T. M.; et al. Phonon-Assisted Resonant Tunneling of Electrons in Graphene--Boron Nitride Transistors. *Phys. Rev. Lett.* **2016**, *116* (18), 186603. https://doi.org/10.1103/PhysRevLett.116.186603.

(11) Jung, S.; Park, M.; Park, J.; Jeong, T.-Y.; Kim, H.-J.; Watanabe, K.; Taniguchi, T.; Ha, D. H.; Hwang, C.; Kim, Y.-S. Vibrational Properties of H-BN and h-BN-Graphene Heterostructures Probed by Inelastic Electron Tunneling Spectroscopy. *Sci. Rep.* **2015**, *5*, 16642.

(12) Malec, C. E.; Davidović, D. Transport in Graphene Tunnel Junctions. *J. Appl. Phys.* **2011**, *109* (6), 64507. https://doi.org/10.1063/1.3554480.

(13) Zhao, Y.; Wyrick, J.; Natterer, F. D.; Rodriguez-Nieva, J. F.; Lewandowski,

C.; Watanabe, K.; Taniguchi, T.; Levitov, L. S.; Zhitenev, N. B.; Stroscio, J. A. Creating and Probing Electron Whispering-Gallery Modes in Graphene. *Science (80-.).* **2015**, *348* (6235), 672–675. https://doi.org/10.1126/science.aaa7469.

(14) Luican, A.; Li, G.; Andrei, E. Y. Quantized Landau Level Spectrum and Its Density Dependence in Graphene. *Phys. Rev. B* **2011**, *83* (4), 41405. https://doi.org/10.1103/PhysRevB.83.041405.

(15) Rutter, G. M.; Jung, S.; Klimov, N. N.; Newell, D. B.; Zhitenev, N. B.; Stroscio, J. A. Microscopic Polarization in Bilayer Graphene. *Nat. Phys.* **2011**, *7*, 649.

(16) Dial, O. E. Single Particle Spectrum of the Two Dimensional Electron Gas, MIT, 2007.

(17) McClure, J. W. Diamagnetism of Graphite. *Phys. Rev.* **1956**, *104* (3), 666–671. https://doi.org/10.1103/PhysRev.104.666.

(18) McCann, E.; Fal'ko, V. I. Landau-Level Degeneracy and Quantum Hall Effect in a Graphite Bilayer. *Phys. Rev. Lett.* **2006**, *96* (8), 86805. https://doi.org/10.1103/PhysRevLett.96.086805.

(19) Joucken, F.; Ge, Z.; Quezada-López, E. A.; Davenport, J. L.; Watanabe, K.; Taniguchi, T.; Velasco, J. Determination of the Trigonal Warping Orientation in Bernal-Stacked Bilayer Graphene via Scanning Tunneling Microscopy. *Phys. Rev. B* **2020**, *101* (16), 161103. https://doi.org/10.1103/PhysRevB.101.161103.

Chapter 7:

Tuning and Probing Layer Asymmetry in Bilayer Graphene

In this chapter, planar tunneling spectroscopy (PTS) is used to manipulate and directly probe extrinsic symmetry breaking in bilayer graphene (BLG). The low energy electronic structure of multilayer graphene sheets hosts correlated electron phenomena that are tunable by application of a perpendicular electric field. Such tunability is favorable because it can be leveraged to advance fundamental understanding of electronic correlations. Yet, this sensitivity to the electrostatic environment can also be problematic because it is often difficult to model and account for in experimental settings such as in tunneling spectroscopy performed with a scanning tunneling microscope. As a result, the accurate identification and assignment of electronic structure features in the tunneling spectra of multilayer graphene sheets is lacking. To address this issue, in this chapter we employ a planar tunneling spectroscopy (PTS) geometry and apply it to Bernal stacked bilayer graphene (BLG)—the simplest multilayer graphene system that hosts correlations. With the straightforward electrostatics of PTS, we are able to model the electrostatics in our experiment and account for them in our spectroscopic characterization of BLG. We then use these results to extract a value for BLG's electric field induced gap with high precision. Interestingly, we find that our PTS devices enable two different methods to extract values for the electric field induced gap—directly with spectroscopy, and indirectly by following the chemical potential. The work presented in this chapter provides an

extensive methodology for unraveling the tunnel spectrum of BLG. It could also be applied more broadly to numerous multilayer systems including emergent twisted or rhombohedral stacked graphene sheets.

7.1 Introduction

Multilayer graphene systems such as rhombohedral stacked trilayer graphene, twisted bilayer-bilayer graphene, and rhombohedral graphite have recently emerged as platforms for investigating tunable correlated insulating states, magnetism, and unconventional superconductivity.[1–4] Due to their two-dimensionality, these systems are well suited for spectroscopic characterization with a scanning tunneling microscope (STM). Such characterization can provide important insights on electronic correlations because it yields the excitation spectrum near and far from the Fermi level. However, the quality that makes graphene multilayers intriguing—their gate tunability—also leads to their alteration in the presence of a perpendicular electric field. As a result, a sharp STM probe, which induces an unavoidable and complicated electrostatic environment, changes the electronic structure of graphene multilayers as they are measured. Indeed, STM works of Bernal stacked bilayer graphene (BLG), the simplest multilayer graphene system that hosts correlations, have yielded qualitatively different spectra and conflicting electric field induced gap energies ranging over an order of magnitude in the literature.[5–7] In order to extract the intrinsic multilayer graphene electronic structure from tunneling spectra, it is thus necessary to address the complicated electrostatic environment introduced by the STM tunneling probe.

7.2 Device Layout and Tunneling Characteristics

Here we perform similar planar tunneling spectroscopy (PTS) of BLG as was presented in Chapter 6. Notably, while in Chapter 6 this method was used to directly probe high-energy features, here it is employed to circumvent the complex electrostatics inherent to an STM probe. This approach enables a comprehensive understanding of the BLG electronic structure as it fills with charge and changes with electric field. A schematic of the PTS device that is identical to the one presented in Fig. 6.1(a) is shown in the inset of Fig. 7.1(a) where BLG is sandwiched under a thin hexagonal boron nitride (hBN) tunneling barrier and above a thicker supporting hBN flake. This stack is supported on a SiO_2/Si wafer, which enables application of a V_G.We first perform tunneling spectroscopy at different values of V_G and V_b. Using the methodology established in Chapter 5, we then shear the resulting data to produce tunneling maps with charge density n along the horizontal axis. Figure 7.1a shows the resulting $dI/dV_b(V_b, n)$ map, with a smooth background subtracted to enhance feature contrast. The data show a dark, ~130 meV horizontal stripe that is independent of n and known to arise from phonon-assisted inelastic tunneling into graphene.[8,9] In addition to the prominent horizontal stripe at E_F, there is another suppression in dI/dV_b that descends in energy as BLG is filled with electrons and indicated by a cyan arrow.

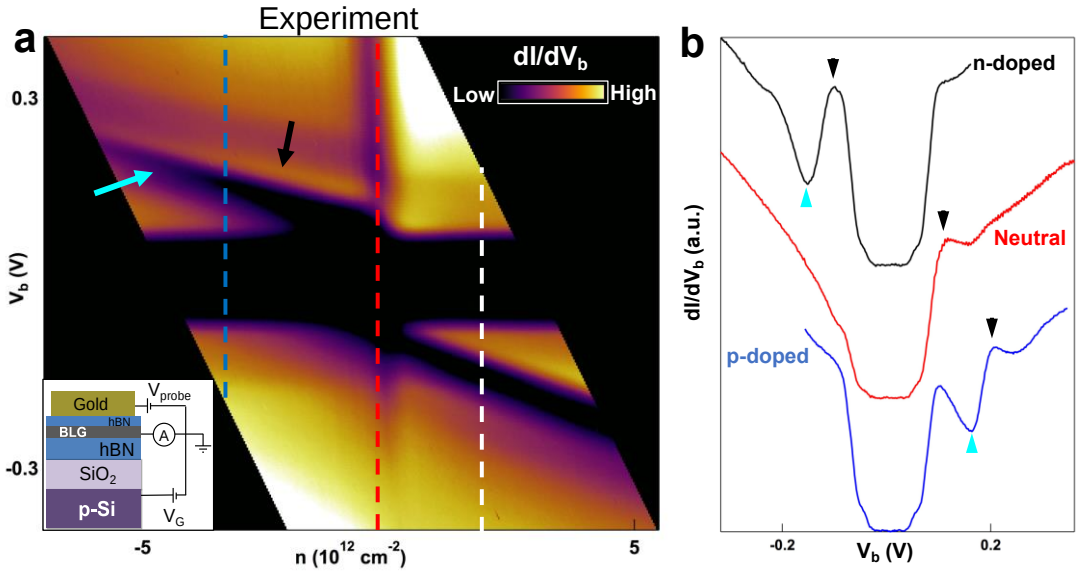

Figure 7.1: Gate-tunable tunneling spectroscopy of bilayer graphene (BLG). (a) Sheared zoom-in $dI/dV_b(V_b, n)$ map of a BLG planar tunneling spectroscopy (PTS) device similar to Fig. 6.1(a), where charge density $n = C_{tg}V_b + C_{bg}V_G$ and C_{tg}, C_{bg} are the top gate and back gate capacitances, respectively. The shear transformation accounts for the charge-inducing effect of the tunneling probe. Inset: schematic of the BLG device with the same layout as in Fig. 6.1(a). (b) $dI/dV_b(V_b)$ spectra taken along the dashed vertical lines in (a) with corresponding colors. Each line corresponds to a different BLG charge density n, with blue, red and black lines corresponding to p-doped, charge neutral and n-doped BLG, respectively. Line profiles are vertically staggered for clarity. Teal, black, yellow and magenta triangles denote features (i) and (ii), discussed in the text. These features are also marked in Fig. 1(a) with arrows of matching colors.

For a closer look at these features, we take vertical line cuts at several values of n from Fig. 7.1(a) (without subtracting a background) and present them as $dI/dV_b(V_b)$ spectra in Fig. 7.1(b). These constant n spectra are shown as black, red, and blue traces, which are vertically offset for clarity. In addition to the central suppression in dI/dV_b, there are two prominent features that the line traces share: (i) a dip in dI/dV_b marked by a cyan triangle that appears at $V_b < 0$ in the black trace and moves to $V_b > 0$ in the blue trace; (ii) a peak in dI/dV_b marked by a gray-black triangle that appears right-adjacent to feature (i). Both spectral features move to higher energy as BLG becomes more p-doped.

7.3 Simulating BLG Tunneling Spectra

In order to assign the spectral features in Fig. 7.1(b) to elements of the BLG electronic structure and identify experimental signatures of the probe-induced gating, we simulated the tunneling $dI/dV_b(V_b, n)$ map for comparison. The full simulation, shown in Fig. 7.2(a), determines the tunneling dI/dV_b from BLG's displacement field (D)-dependent single particle density of states (SPDOS). To acquire the SPDOS, we first calculate values of U which depends on the experimentally tunable parameters V_b and V_G. Next, we construct our Hamiltonian H by incorporating nearest neighbor intralayer γ_o and interlayer γ_1 hopping parameters as well as the calculated U.[7] We

[7] Hopping parameters γ_4 and Δ' determined in Chapter 6 have a negligible effect on our simulated low energy spectrum, and so we exclude them here for simplicity

then diagonalize the resulting H to find the energy spectrum and integrate it to get the DOS.

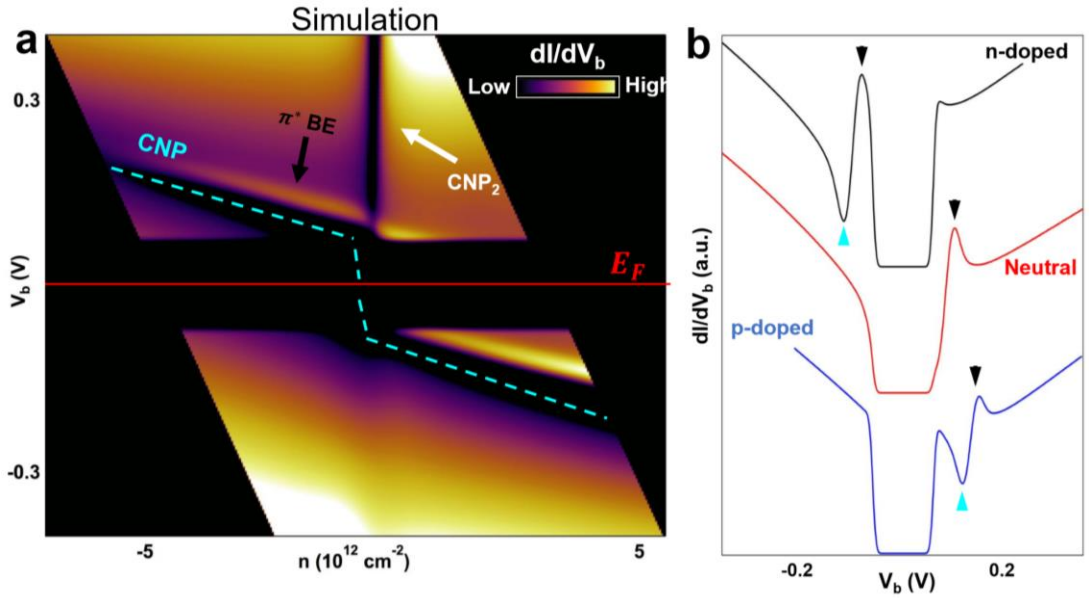

Figure 7.2: Simulation of tunneling $dI/dV_b(V_b, n)$ maps. (a) Simulated $dI/dV_b(V_b, n)$ map of a bilayer graphene TFET. The cyan, magenta and yellow dotted lines follows the trajectory of the BLG charge neutrality point (CNP) and high energy bands (HEB and HEB*). The gray arrow denotes an enhancement in $dI/dV_b(V_b, n)$ at the π^* band edge (π^* BE). (b) Constant-n $dI/dV_b(V_b)$ spectra taken at the n values presented in Fig. 1b. Colored arrows point to spectral features with cyan, gray arrows indicating the energy of the charge neutrality point, layer-polarized π^* band edge.

The simulated PTS spectra in Fig. 7.2(b) strongly resemble the experimental data in Fig. 7.1(b) both qualitatively and quantitatively. As a result, the simulation can offer insight into BLG as it is being measured by PTS. For example, features (i) and

(ii) observed in the experimental data in Fig. 7.1(b) are also evident in the simulation in Fig. 7.2(b), where they are dependent on the inputs to H discussed above. Thus, we identify (i) as BLG's charge neutrality point (CNP, cyan triangle); and (ii) a layer polarized van Hove singularity at the π^* band edge (π^* BE, black triangle). Notably, features (i) and (ii) were previously reported in both STM and PTS of BLG.[7,10–13] In order to gain more nuanced insight into the tunneling measurement, we first outline the separate components of the simulated spectra so that we may later see how they individually reproduce certain attributes of the experiment. In the following three subsections, I will outline the model for tunneling $dI/dV_b(V_b, V_G)$ that incorporates the BLG electronic structure, phonon excitations, two-channel tunneling, and layer polarization.

7.3.1 General Model for Calculating Tunneling dI/dV_b

Based on previously reported simulations of graphene tunneling junctions, we model the tunneling current I as[13–15]

$$I(V_G, V_b) = \sum_i T_i \Big\{ \int d\varepsilon_1 \int d\varepsilon_2 \, f(\varepsilon_1 - eV_b)[1 - f(\varepsilon_2)]\Gamma_i(\varepsilon_1 - \varepsilon_2 - \hbar\omega) g(\varepsilon_1) g_p(\varepsilon_2) - \int d\varepsilon_1 \int d\varepsilon_2 \, [1 - f(\varepsilon_1 - eV_b)] f(\varepsilon_2) \Gamma_i(\varepsilon_2 - \varepsilon_1 - \hbar\omega) g(\varepsilon_1) g_p(\varepsilon_2) \Big\} \quad (7.1)$$

where $g(\varepsilon)$ and $g_p(\varepsilon)$ represent BLG and tunneling probe's DOS, and $f(\varepsilon)$ is the Fermi-Dirac distribution. Inelastic tunneling into BLG, as discussed in Section 3.7, results in multiple phonon-assisted contributions to the overall tunneling dI/dV_b. In eq. (7.1), T_i represents the enhancement ratio of inelastic channel i and $\Gamma_i(\varepsilon) = \frac{1}{\pi}\left(\frac{\gamma_i}{2}\right) / \left(\varepsilon^2 + \frac{\gamma_i^2}{4}\right)$ accounts for inelastic channel broadening.[14,16] In the model, we included two inelastic channels with phonon energies $\hbar\omega_1 = 63\, meV$ and $\hbar\omega_2 = 73\, meV$, enhancement ratios $T_1 = 44.3$ and $T_2 = 38.8$ and broadenings $\gamma_1 = 12.7\, meV$, and $\gamma_1 = 15.8\, meV$. Phonon energies, enhancement ratios and broadenings are extracted directly from multi-peak Lorentzian fit of the experimental $d^2I/dV_b^2(V_b)$ tunneling spectrum shown in the inset of Fig. 6.3 and discussed in Chapter 6.

At $T \approx 0\ K$, assuming constant g_p, the tunneling conductance dI/dV_b can be expressed

$$\frac{dI}{dV_b}(V_G, V_b) = \sum_i T_i \{\int_{E_F}^{\infty}[1+\eta] g(\varepsilon)\Gamma_i(E_F + eV_b - \varepsilon - \hbar\omega)d\varepsilon + \int_{-\infty}^{E_F}[1+ \eta] g(\varepsilon)\Gamma_i(\varepsilon - E_F - eV_b - \hbar\omega)d\varepsilon - \int_{E_F+eV_b}^{\infty} \eta g(E_F)\Gamma_i(E_F + eV_b - \varepsilon - \hbar\omega)d\varepsilon - \int_{-\infty}^{E_F+eV_b} \eta g(E_F)\Gamma_i(\varepsilon - E_F - eV_b - \hbar\omega)d\varepsilon\}, \quad (7.2)$$

where E_F is BLG's Fermi energy at V_G and V_b, $g(\varepsilon)$ is BLG's DOS and $\eta = \frac{\partial E_F}{\partial(eV_b)}$ is the probe-BLG lever arm. Details on calculating $g(\varepsilon)$, $\eta(V_b, V_G)$, and $E_F(V_G, V_b)$ are given in subsections 7.3.2 and 7.3.3. We first calculate gate-dependent parameters at each necessary (V_b, V_G) point, then use Eq. (7.2) to simulate a full $dI/dV_b(V_b, V_G)$ map, as shown in Fig. 7.3(c).

7.3.2 Tight Binding Calculation of BLG's Dynamic DOS

Bilayer graphene's DOS is dependent on the electrostatic environment set by back and top gate voltages V_b and V_G . The gate-dependent tight binding Hamiltonian can be written

$$\begin{aligned} H(V_G,V_b) = &\sum_i \frac{U(V_G,V_b)}{2} {a_{1i}}^\dagger a_{1i} + \sum_i \frac{U(V_G,V_b)}{2} {b_{1i}}^\dagger b_{1i} \\ &- \sum_i \frac{U(V_G,V_b)}{2} {a_{2i}}^\dagger a_{2i} - \sum_i \frac{U(V_G,V_b)}{2} {b_{2i}}^\dagger b_{2i} \\ &- \sum_{<i,j>} \gamma_0 ({a_{1i}}^\dagger b_{1j} + H.c.) - \sum_{<i,j>} \gamma_0 ({a_{2i}}^\dagger b_{2j} + H.c.) \\ &+ \sum_{<i,j>} \gamma_1 ({b_{1i}}^\dagger a_{2j} + H.c.) \end{aligned} \tag{7.3}$$

where the operators ${a_{1i}}^\dagger(a_{1i})$, ${b_{1i}}^\dagger(b_{1i})$, ${a_{2i}}^\dagger(a_{2i})$ and ${b_{2i}}^\dagger(b_{2i})$ create (annihilate) an electron on site R_i of sublattice A_1, B_1, A_2 and B_2, respectively. As in Chapter 2, we define A_1 and B_1 (A_2 and B_2) to be on the top (bottom) layer and we use hopping parameters γ_0 and γ_1 as previously reported.[17] The interlayer potential difference U is calculated with a simple three plate planar capacitor model (discussed in Section 2.13) for each appropriate value of (V_b, V_G). The dependence of U on (V_b, V_G) is shown in Fig. 7.3(a).

We used the package Pybinding,[18,19] which employs the kernel polynomial method to solve each unique Hamiltonian $H(U(V_b, V_G))$ on a circular BLG sheet with radius 70 nm (approximately 5 x 10^5 unit cells). The band structure was first found by diagonalizing $H(V_b, V_G)$, then it was integrated to yield the site-specific DOS $g(\varepsilon)$.

This was done successively for discretized $U(V_b, V_G)$ values in the experimental domain $|V_b| < 0.8\,V \cap -40 < V_G < 80\,V$.

Several layer-resolved $g(\varepsilon)$ simulations are plotted in Fig. 7.3(c) at various V_b values, where the black solid and blue dotted traces represent the top (bottom) layer $g(\varepsilon)$. Notably, $g(\varepsilon)$ around the CNP ($E - E_{CNP} = 0\ eV$) changes significantly as V_b is modulated, with a gap that widens with increasing V_b. There is also a pronounced difference between black and blue line traces around the CNP. Specifically, all black traces have a prominent peak in $g(\varepsilon)$ right-adjacent to the gap, whereas all blue line traces have a peak in $g(\varepsilon)$ left-adjacent to the gap. This peak, which is also apparent in the experimental data, is understood to be a layer-polarized van Hove singularity. For more detail on layer-specific tunneling, see subsection 7.3.4.

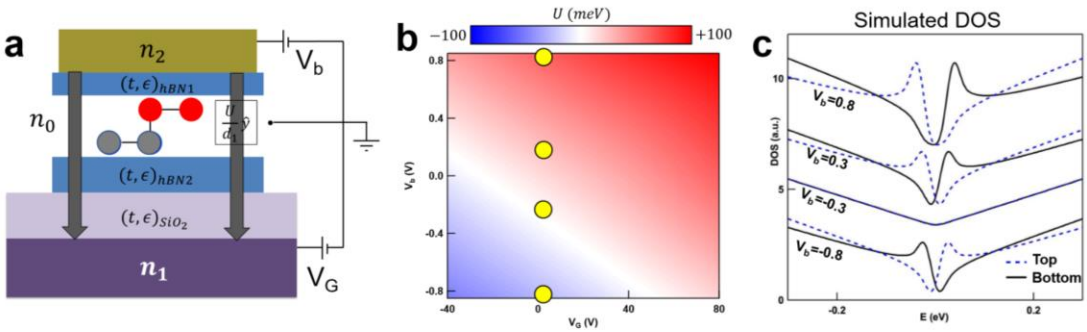

Figure 7.3: Simulating the dynamic BLG DOS. (a) A schematic of the three-plate planar capacitor model. Gray and blue circles represent sites in the BLG top and bottom layers that are sandwiched below an hBN tunneling electrode (blue rectangle) with thickness t_{hBN1} = 1.8 nm and permittivity $\epsilon_{hBN1} = 2.2\epsilon_0$ and atop a substrate hBN (also blue) with thickness t_{hBN2} = 15 nm and permittivity $\epsilon_{hBN2} = 3.8\epsilon_0$. Probe and back gate voltages V_b and V_G induce charge densities n_0, n_1, and n_2 on the BLG, gold

probe and p-doped Si, respectively. Application of V_b and V_G also causes a displacement field between probe and back gate (distance d_1) represented by vertical gray arrows, that changes the potential energy U between BLG layers. (b) Potential energy difference between layers U at different values V_b and V_G that considers the probe-BLG work function mismatch $\Delta W = 0.28\, eV$. (c) Simulated DOS for top (black trace) and bottom (dashed blue line) BLG layers at different values of V_b, marked with yellow circles in (b).

7.3.3 Calculating $E_F(V_G, V_b)$ and $\eta(V_G, V_b)$

A three-plate planar capacitor model adapted from Section 5.5 is used to calculate the BLG Fermi level $E_F(V_G, V_b)$ and tunneling probe gating efficiency $\eta(V_G, V_b)$. A notable difference between this model and the one used for graphene in Section 5.5 is the inclusion of a dynamic DOS. A labelled schematic of the model is shown in Fig. 7.3(a). Taking quantum capacitance into account, from Gauss' law we see that[20]

$$n_0 + n_1 + n_2 = 0 \tag{7.4}$$

$$n_1 = \alpha(E_F - eV_g) \tag{7.5}$$

$$n_2 = \beta(E_F + eV_b + \Delta W) \tag{7.6}$$

Where $\alpha = \frac{1}{e^2}\left(\frac{\epsilon_{hBN_2}\epsilon_{SiO_2}}{t_{hBN_2}\epsilon_{SiO_2} + t_{SiO_2}\epsilon_{hBN_2}}\right)$ and $\beta = \frac{\epsilon_{hBN_1}}{t_{hBN_1}e^2}$. The work function mismatch between BLG and the tunneling electrode $\Delta W = 0.28\, eV$ is

determined by fitting a doping shift that is consistent in three different PTS devices. The top and back-gate capacitance ratios match those listed in Section 5.4.

Combining eq. (7.4-7.6),

$$n_0(E_F) + \alpha\left(\mu - eV_g\right) + \beta(E_F + eV_b + \Delta W) = 0 \qquad (7.7)$$

In order to solve Eq. 7.93 numerically for $E_F(V_G, V_b)$, it is necessary to first determine $n_0(E_F)$. We use the tight binding calculation to determine $g(\varepsilon)$ at each (V_b, V_G) then calculate $n_0(E_F) = \int_{-\infty}^{E_F} g(\varepsilon)d\varepsilon$. After solving Eq. 7.93 for $E_F(V_G, V_b)$, we next compute the tunneling lever arm $\eta(V_G, V_b) = \frac{\partial E_F(V_G, V_b)}{\partial(eV_b)}$. Figure S2b shows the calculated result for $\eta(V_G, V_b)$, and several η profiles as a function of V_b at different V_G are shown in Fig. S2c.

7.3.4 Top Layer Tunneling and the van Hove Singularity

Previously STS studies of BLG have shown that proximity between the tunneling electrode and BLG's top layer causes the top layer DOS to dominate the tunneling spectrum.[12,21,22] To better understand our PTS spectra of BLG with simulation, we take the top layer-probe proximity into account. Figure 7.4 panels b, c and d show different simulated tunneling $dI/dV_b(V_b, V_G)$ maps that include contributions from the top, bottom or both BLG layers, respectively. Each of these simulated maps has different behavior near the CNP, highlighted with a white dashed oval. Notably, the simulated map in Fig. 7.4b shows the strongest resemblance to the experimental data in Fig. 7.1a. Specifically, the experimental data in Fig. 7.1a has a

suppression in dI/dV_b at the CNP with high intensity bordering it above, identified as feature (i). Thus, we conclude that this high intensity region, corresponds to tunneling directly into a van Hove singularity in the top layer, and that the tunneling signal is dominated by contributions from the top layer DOS.

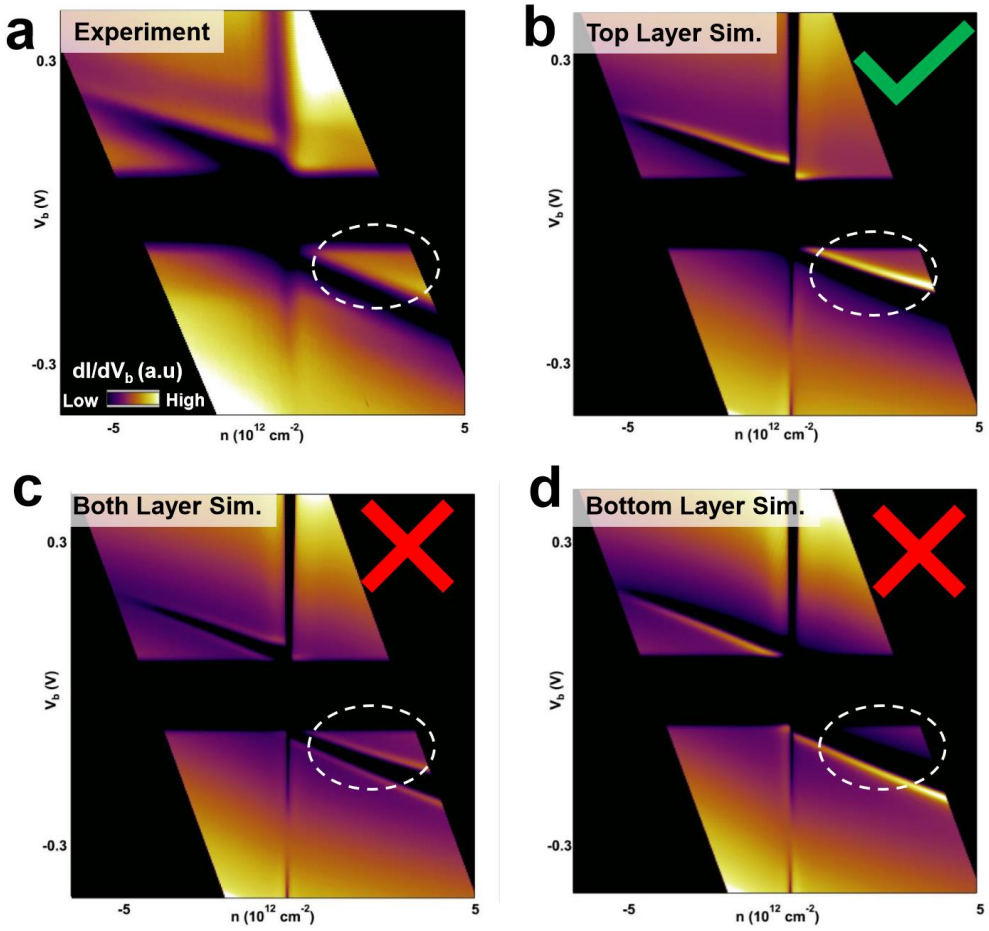

Figure 7.4: Evidence for layer-polarized van Hove singularity and layer-selective tunneling. (a) Experimental tunneling $dI/dV_b(V_b, n)$ map. (b-d) Simulated tunneling $dI/dV_b(V_b, n)$ maps that incorporate only top layer (b), both layers (c) and only bottom layer DOS. Example simulated top and bottom layer DOS curves are shown in

Fig.7.3(c). Each map has a region (outlined with a white dashed line) around the CNP that is used for comparing each simulation to the experiment.

7.4 Two-Channel Tunneling in BLG Serves as an Experimental Probe

The simulated $dI/dV_b(V_b, n)$ map in Fig. 7.1(a) shows a vertical depression in dI/dV_b at $n = 0$, denoted by a white arrow in Fig. 7.2(a) and labeled CNP_2. This feature is also apparent in the experimental data Fig. 7.1(a) as a dark region following the red dashed line. Understanding CNP_2 is the key to observe and account for the electric field induced gap in BLG PTS measurements. In order to investigate the behavior of CNP_2, we take a numerical derivative of the experimental data from Fig. 7.1(a). The resulting $|dG/dV_G(V_b, n)|$ map is shown in Fig. 7.5(a) with yellow (purple) colors indicating high (low) $|dG/dV_G|$. The data show CNP_2 (denoted by an orange arrow) as a dark line running down the center of a vertical yellow stripe. Interestingly, the stripe's intensity decreases as V_b approaches ~ -0.4 V, disappearing in the region indicated by a white arrow. The simulated $|dG/dV_G(V_b, n)|$ is displayed in Fig. 7.5(b) for comparison. Notably, the simulation also has a bright vertical stripe at $n = 0$ that strongly resembles the experimental CNP_2 feature, including its V_b-dependent intensity.

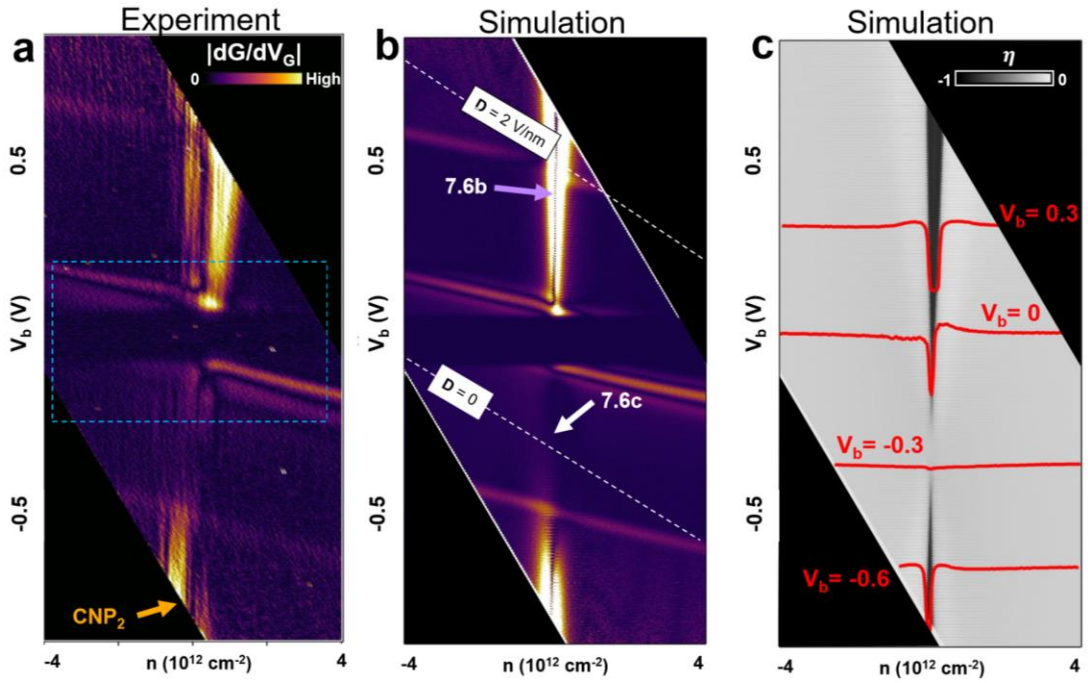

Figure 7.5: Observation of a changing Channel 2 intensity. (a) Measured $|dG/dV_G(V_b, n)|$ map of BLG. The orange arrow points to the vertical tunneling feature that appears as E_F aligns with the CNP, which is labelled CNP_2 and discussed in the main text. (b) Simulated $|dG/dV_G(V_b, n)|$ map. Bright regions correspond to feature edges in the BLG DOS. White dashed lines are constant D contours, calculated using a planar capacitor model. Purple and white arrows denote segments along the vertical Channel 2 features with different intensities, which correspond to differing electronic structure between two points with the same n but different D. (c) Simulated $\eta(V_b, n)$ map. Dark regions on the map correspond to a strong gate coupling between V_b and E_F, due to low quantum capacitance. Red traces are horizontal profiles along the map at constant V_b values of (top to bottom trace) $V_b = 0.3\ V, 0\ V, -3\ V, -0.6\ V$, respectively.

Tunneling features similar to CNP_2 were previously reported in PTS studies of monolayer graphene and were attributed to a dI/dV_b channel at monolayer graphene's Fermi level aligning with the CNP.[13,15,23] Here we apply this understanding to our BLG PTS measurements.

Because of probe-sample gating the tunneling conductance can be expressed as

$$\frac{dI}{dV_b} = g(E_F + eV_B)(1 + \eta) - \eta g(E_F) \tag{7.8}$$

where $\eta = \partial E_F/\partial V_b$ represents the probe-sample capacitive coupling and g is the BLG density of states (DOS).[23,24] In effect, increasing V_b raises the probe energy and lowers E_F, with respect to the BLG bands inducing additional tunneling at $E_F + eV_b$ and E_F. This is a natural attribute of our simulation, which considers the full derivative of tunneling current (discussed in subsection 7.3.1). As a result, dI/dV_b has two parallel contributions shown as horizontal black and orange arrows labelled "Ch. 1" and "Ch. 2" in Fig. 7.6(a). The contribution of each channel varies with V_b. As explained by Malec et. al. for monolayer graphene,[23] these two tunneling channels can be observed as a crisscrossing pattern on a $dI/dV(V_G, V_b)$ map, with features corresponding to Channel 2 following lines of constant n.[15] The CNP_2 in Fig. 7.5a follows the line $n = 0$ and can thus be interpreted as a Channel 2 contribution to dI/dV_b when E_F is aligned with the CNP. Interestingly the intensity of CNP_2 changes as V_b changes, *unlike* its previously reported analog in monolayer graphene.[13,15]

In order to decipher the changing intensity of experimental and simulated CNP_2, we examine the probe-sample gate efficiency $\eta(V_b, n)$ in Fig. 7.5(c). Black regions on the map correspond to higher probe-sample gate efficiency (lower η). Red traces are horizontal line profiles along the map at constant V_b values of (top to bottom trace) $V_b = 0.3\,V, 0\,V, -3\,V, -0.6\,V$, respectively. Clearly, there is a correlation between η and CNP_2: when η is at its lowest on the V_b, n domain, CNP_2 is brightest. Constant electric field contours at D= 2V/nm and D=0 V/nm are superimposed on the simulation diagonal white lines. These contours were calculated using a three-plate planar capacitor model, a natural approximation given the geometry of our PTS device. Comparison of data and simulation indicates that an electric field variation of ~3 V/nm occurs along a constant-n spectrum.

At this point we have determined that both probe-sample coupling η and electric field D vary substantially along a constant-n tunneling spectrum. Moreover, areas of lowest η and highest D correlate with the brightest sections of CNP_2. To find the root cause of this correlation, we take a closer look at the simulated BLG band structure in one of these regions and compare it to the electronic structure where CNP_2 is diminished to a low intensity. Figures 7.6(b) and 7.6(c) show BLG's band structure simulated at two different locations in Fig. 7.5(b), indicated with white and lavender arrows. The calculations in Figs. 7.6(b) and 7.6(c) indicate that BLG has a V_b-dependent gap. The gap is large at the high intensity region in Fig. 7.5(b) (lavender arrow), and small at the low intensity region (white arrow). In both panels the horizontal orange line indicates the Channel 2 tunneling feature at energy E_F, with line

thickness indicating the relative contribution $|\eta|$. The decrease in η in bright sections of CNP_2 is due to the presence of a gap in BLG. With these considerations in mind the question remains why would we expect a gap to lead to an increase in tunneling conductance?

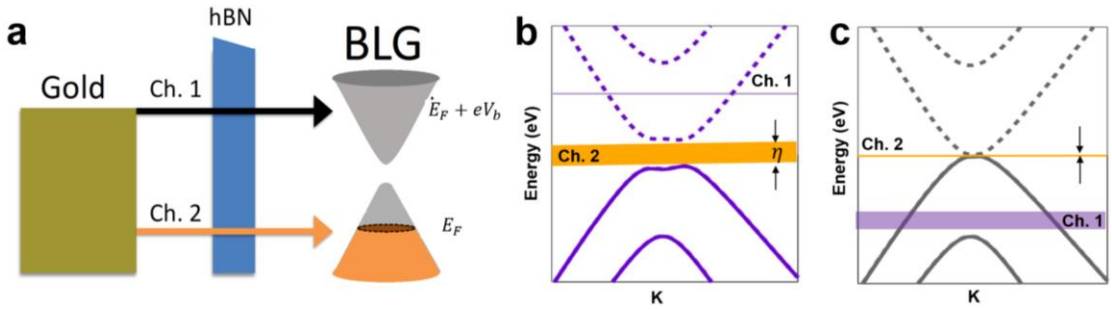

Figure 7.6: Channel 2 tunneling into a dynamic band gap. (a) Illustration two-channel tunneling, introduced in the text. Electrons tunnel between a gold probe (yellow rectangle), through a tunneling barrier (blue), into unoccupied states in bilayer graphene (gray). The black and orange horizontal arrows portray contributions to the measured tunneling dI/dV_b signal from Channel 1, at energy $E_F + eV_b$ and ch. 2, at E_F. As $|\eta|$ increases, Channel 2 tunneling is expected to become more prominent. (b,c) Calculated BLG band structure with (b) inter layer electrostatic energy difference U = 0.14 eV and (c) no interlayer energy difference. In both panels the horizontal orange line indicates the ch.2 tunneling feature at energy E_F, with line thicknesses indicating the relative contribution $|\eta|$. Purple horizontal lines mark the tunneling energy $E_F + eV_b$

To isolate the cause of CNP_2's changing $|dG/dn|$ intensity, we first consider the correspondence between $|dG/dn|$ intensity and Channel 2 tunneling. As discussed above, this tunneling features correspond to $g(E_F)$; hence, $|dG/dn|$ intensity denotes how $g(E_F)$ changes with additional charge dn. If the BLG DOS is smoothly changing at E_F, we expect Channel 2 to have a low $|dG/dn|$ intensity. Conversely, high intensity regions in $|dG/dn|$ correspond to an abrupt onset of additional states at $E_F + \delta E_F$. These behaviors are exemplified by the two regions in Fig. 7.5(b) denoted by lavender and white arrows. At the lavender arrow, the $|dG/dn|$ intensity is high, implying there is an abrupt change in $g(E_F)$ around charge neutrality. The low $|dG/dn|$ intensity at the white arrow suggests that $g(E_F)$ smoothly changes near the CNP. Thus, the different $|dG/dn|$ intensities at two regions of CNP_2 reveal that the BLG band structure is changing as we are examining it. Specifically, the disappearance of CNP_2 at V_b = -0.4 V in Fig. 3a can thus be explained by BLG's gap closing along a vertical $dI/dV_b(V_b)$ spectrum.

Probe-induced gap opening is difficult to account for with STS, typically resulting in overestimated gap values.[7] However, direct observation of Ch. 2 in our PTS measurements enables access to BLG's gap as eV_b is modulated during spectroscopy. With information from both channels, we can compensate for the dynamic band structure of BLG and determine the true gap value via tunneling spectroscopy. In the next section, we use the changing intensity of CNP_2 to directly measure and account for alteration in the BLG DOS along a spectrum that has varying V_b.

7.5 Correcting for BLG's Dynamic Band Structure

As the tunneling energy eV_b is changed in our measurement the probe modulates the BLG charge density n as well as the displacement field D according to the relations $D = \left(C_{tg}V_b + C_{bg}V_G\right)/2 + D_0$ and $n = \left(C_{tg}V_b - C_{bg}V_G\right) + n_0$ where C_{tg} and $C_{bg}$are the probe-BLG and back gate capacitances and D_0 and n_0 result from the BLG-probe work function mismatch.[25,26] The methodology outlined in ref. 15 uses a three plate planar capacitor model to first determine the ratio C_{tg}/C_{bg} directly from the data, then uses the ratio to transform $dI/dV_b(V_b, V_G)$ to $dI/dV_b(V_b, n)$ maps. A similar shear transformation can also produce a $dI/dV_b(V_b, D)$ map. Specifically, by determining the ratio C_{tg}/C_{bg} according to ref. 15, then transforming raw $dI/dV_b(V_b, V_G)$ data with the matrix $\begin{bmatrix} C_{bg} & C_{tg}/2 \\ 0 & 1 \end{bmatrix}$ where $C_{tg} = \epsilon_{hBN1}/t_{hBN1}$ with thicknesses and permittivities of top and back gates determined to be $t_{hBN1} = 1.7$ nm by AFM and previously reported $\varepsilon_{hBN1} = 4.0\varepsilon_0$.[13,15] We can then set D to be constant along the diagonal, thus making BLG's dynamic electronic structure stand still.

Our goal is to directly extract BLG's gap energy U. Following the above procedure, we reorganize the data so that D is held constant when eV_b is changed. Each of the two tunneling channels discussed above provides a point on the tunneling map where BLG has no gap. The first point, discussed above, occurs where CNP_2 vanishes. The second point appears when the CNP and π^*BE, converge, denoting a closing of the band gap. Employing another shear transformation, we align the two points vertically, mapping D onto the horizontal axis. We then scale the horizontal axis using

$D = C_p V_b + C_B V_G - D_0$ where C_p and C_B are the probe-BLG and back gate-BLG capacitances, and D_0 is due to the probe-BLG work function mismatch. Figure 7.7 shows the resulting $dG/dV_G(V_b, D)$ map with the CNP and π^* BE marked with black dotted and dashed lines, respectively. As D decreases along the map, the two features converge in energy. The appropriate shearing aligns their (extrapolated) intersection vertically with the CNP_2 vanishing point at V_b = -0.4 V. As a result, Channels 1 and 2 indicate that BLG's electronic structure is gapless along the vertical gray line in Fig. 4a. Therefore, each vertical line in the sheared $dG/dV_G(V_b, D)$ map is a constant-D contour that and can be used to directly examine BLG's static electronic structure as a function of V_b.

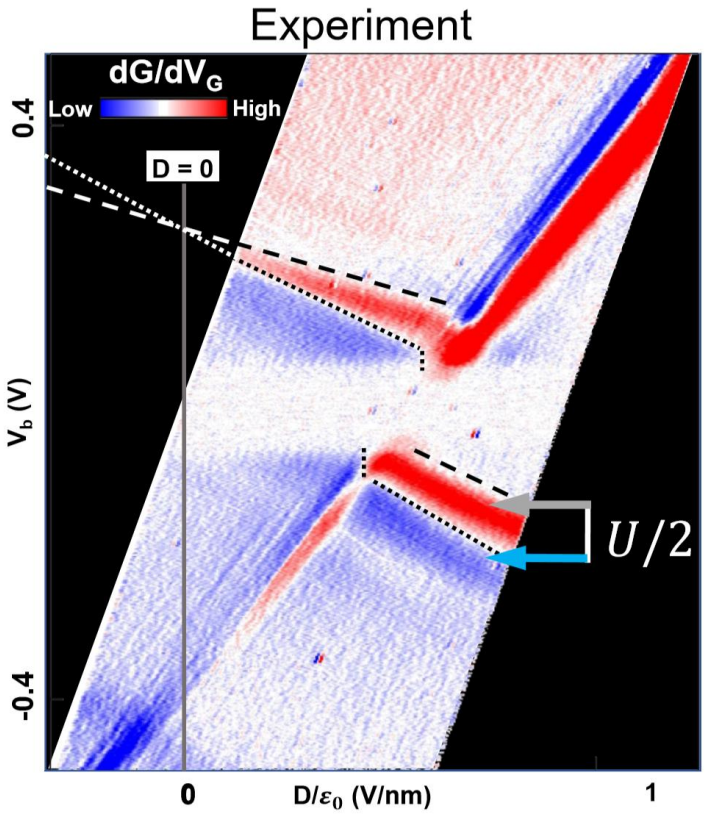

Figure 7.7: Directly measuring BLG's dynamic gap energy. Sheared $dG/dV_G(V_b, D)$ map showing the correction for BLG's dynamic electronic structure. The CNP and π^* BE, marked respectively with black dotted and dashed lines, intersect where $D = 0$. The vertical gray $D = 0$ line intersects the vanishing point of CNP_2, and the convergence of CNP and π^* BE. The spectroscopic gap energy U is found by first extracting the energy difference between E_{CNP} (cyan arrow) and $E_{\pi^* BE}$ (gray arrow), then correcting for changes in E_F (discussed in Section 7.6).

With the dynamic band structure addressed, it is now straightforward to extract U directly from the sheared $dG/dV_G(V_b, D)$ map. Cyan and gray arrows in Fig. 7.7 correspond to the energy of the CNP (E_{CNP}) and π^* BE ($E_{\pi^* BE}$) when $D = 1$ V/nm. Assuming a symmetric gap, we use the relation $U = 2|E_{\pi^* BE} - E_{CNP}| + \Delta E_F(\delta n)$ where $\Delta E_F(\delta n)$ is the band shift that occurs between the two extracted points (marked by gray and cyan arrows). The uncorrected gap value is approximately 110 meV at $D = 1$V/nm. Naïvely, we might assume that band corrections for band shifting may involve an additional data shearing in order to compensate for the compensating for the changing n along each vertical line in Fig. 7.7. This would be unproductive, however, since we underwent a linear transformation to control D along each vertical line. We are thus in need of another way to determine the magnitude of band shifting! The PTS measurement offers a subtle yet convenient way to measure the band-shifting magnitude: by tracking the electronic structure as it is filled with charge and pulled towards the E_F. In the next section we explore this technique then in Section 7.7, we will correct the overestimated spectroscopic gap and compare it to different screening models.

7.6 Spectroscopically Tracking the BLG CNP

From the trajectory of the CNP we can map the nature of the bands as they are pulled through the BLG Fermi level E_F. Figure 7.8(a) shows a zoom-in $|dG/dn(V_b, n)|$ map taken in the region outlined with a blue, dashed perimeter in Fig. 7.5(a). The central inelastic tunneling feature at ($|V_b| < 63$ meV) in the raw data is removed using

the procedure outlined in Chapter 6. The CNP (measured with Channel 1) appears as a dark line running from the top left of the map to bottom right. Beginning at the white marker, the CNP descends linearly towards the yellow marker. Next, the CNP jumps abruptly by energy $U_T = 20$ meV between yellow and magenta markers, where $n \sim 0$. After its jump, the CNP traverses laterally $\sim$0.3 x 10^{12} cm^{-2} to the cyan marker, before resuming its approximately linear descent. We can gain insight on the filling characteristics of BLG by examining the electronic structure at regions denoted by the colored markers.

Figure 7.5(b) shows our interpretation of the CNP trajectory, where each colored line is a simulation of the BLG DOS. The color of each simulation corresponds to the matching location on the experimental map in Fig. 7.5(a) and the red line is the E_F which remains at $V_b = 0$. Beginning with the white trace, BLG is p-doped and the CNP is $\sim$0.1 eV above E_F. The DOS in the white trace is approximately linear around E_F so we then expect that the CNP will descend linearly as n increases. In the yellow trace, the DOS at E_F is no longer constant, and instead decreases rapidly, corresponding to the jump between yellow and magenta markers in Fig. 7.5(a). In the magenta trace, E_F is surrounded by a high DOS, namely the van Hove singularity (VHS) in the top layer. Increasing n then has little effect on E_F, leading to a traverse between magenta and cyan markers in Fig. 7.5(a). Once the VHS has been filled, the DOS around E_F returns to being approximately constant. The CNP energy is then expected to decrease linearly as n is increases between the cyan and orange traces, which agrees with the behavior of the measured CNP in Fig. 7.5(a). Interestingly, regions of approximately

constant DOS correspond to a 2D parabolic band structure, introduced in Chapter 2, can be used to extract the BLG hopping parameters, as discussed in Chapter 6.

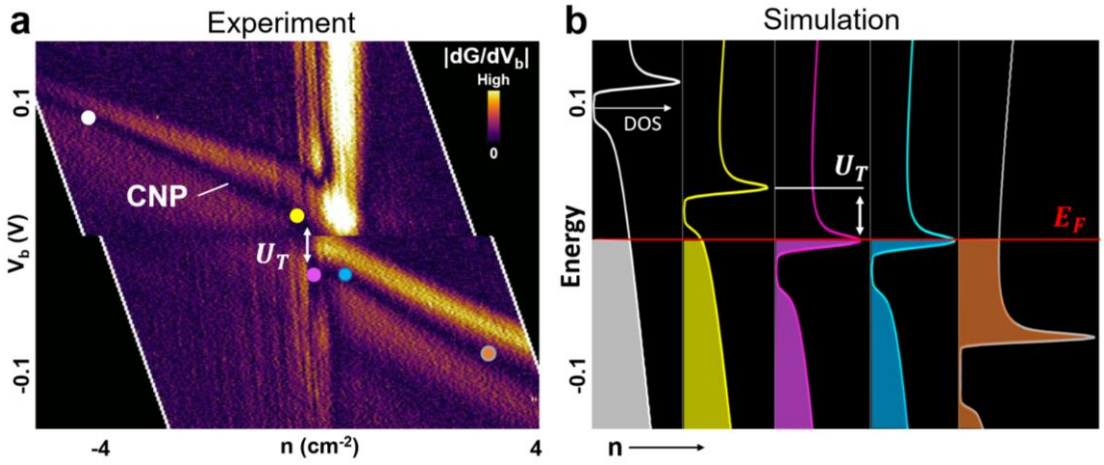

Figure 7.8: Tracking E_F spectroscopically. (a) Zoom-in $dG/dV_G(V_b, n)$ with the central inelastic feature ($|V_b| < 63$ meV) removed. The dark line traversing from top left to bottom right across the map is the charge neutrality point (CNP). The trajectory of the CNP changes abruptly around $n = 0$. (b) Simulation of the BLG DOS filling at different points along the map in (a). The vertical axis is energy and the horizontal axis represents increasing n between the DOS plots. Within each DOS plot, the horizontal axis is DOS. Filled electron states are represented by shaded regions. Colors of each trace correspond to the dotted regions in (a).

Detailed knowledge of the interplay between E_F, n, and CNP energy enable us to unravel the tunneling spectrum of BLG. For example, regions of approximately constant DOS correspond to a 2D parabolic band structure, introduced in Chapter 2,

can be used to extract the BLG hopping parameters, as discussed in Chapter 6. Additionally, regions near the CNP where the DOS undergoes abrupt changes can provide insight on the structure of the BLG gap. Specifically, the energy jump U_T, marked as a white double arrow in Figs. 7.5(a) and (b), is a direct measurement of the effective gap that is leapt by E_F in a transport or capacitance measurement, for example. We extract a value $U_T = 20$ meV, which is consistent with previous transport studies on the electric field induced gap in BLG,[26] which are also Fermi level measurements. In the following section, we will show that our PTS geometry enables measurement of the true spectroscopic gap U near and far from E_F with full control of the electrostatic environment and allows a comparison between Fermi level and spectroscopic measurements within the same system. In Section 7.8, I will compare U_T to the spectroscopic U.

7.7 Compensating for a Shifting DOS

Here we provide details on correcting for the shifting BLG DOS when extracting U spectroscopically. First, it is important to understand the interplay between displacement field D, charge density n, tunneling energy eV_b and the experimental knobs V_b and V_G. With two tunable voltages V_b and V_G, we can control two of the three parameters—D, n or eV_b—independently. In the case of the tunneling measurement, eV_b must be one of the independently controlled parameters. The other independently controlled parameter can be either n or D and each has a corresponding linear (shear) transformation, as discussed in Section 5.4. Holding n constant along a $dI/dV_b(V_b)$

spectrum, we avoid energy *overestimates* that are due to unintentional shifts in the DOS with respect to E_F.[27] Keeping D constant along a $dI/dV_b(V_b)$ spectrum, we avoid *underestimates* in gap energy by maintaining a static BLG band structure during spectroscopy. Each of these methods is beneficial in different scenarios, and accurately measuring U with spectroscopy requires information from both.

To measure U spectroscopically, we first shear the data to keep D constant and hold BLG's dynamic band structure static as eV_b changes. We next account for the band shift ΔE_F associated with changing n between two vertically aligned points V_{b1} and V_{b2}. Specifically,

$$\Delta E_F(V_{b2}, V_{b1}) = \int_{V_{b1}}^{V_{b2}} e \frac{\partial E_F}{\partial n}\left(\frac{\partial n}{\partial V_b}\right) dV_b \tag{7.9}$$

where $\partial n/\partial V_b = C_{tg}$. With detailed knowledge of $E_F(n)$ from observations of the CNP shown in Fig. 7.8, we calculate $\Delta E_F(E_{CNP}/e\,, E_{\pi^* BE}/e)$ then use it to correct the gap energy U. Without this correction, we find a consistent >10% overestimate in U when compared to the corrected data. Conversely, we find the gap is consistently underestimated by > 20 % if n is held constant and D is subject to change along a vertical dI/dV_b spectrum.

7.8 Extracting the Gap Energy

Having corrected for the two major complications with tunneling into BLG: (1) its dynamic band structure; and (2) its shifting DOS; we are able to directly measure the true gap value. We repeat the gap extraction procedure outlined in Section 7.7 for

multiple values of D to explore the role of screening in BLG. Screening is an important consideration for accurately predicting the value of the electric field-induced gap in BLG.[17] Fig. 7.9 shows a plot of U with respect to D as black circles, with U_T discussed in Section 7.6 included as well (black triangle). The plot also shows theoretical predictions for U with two different screening scenarios: in the absence of screening (shown as a black dotted line), and with interlayer screening accounted for by self-consistent tight binding (SCTB, shown as a blue line).[17] Evidently, the data from our work fits well with a tight binding model adapted from McCann and Koshino.[17] This finding agrees with optical spectroscopy and recent transport studies of ultraclean BLG as well.[25,28,29] Notably, strong agreement with SCTB is resolved here for the first time with tunneling spectroscopy that has full and independent control of D and n.

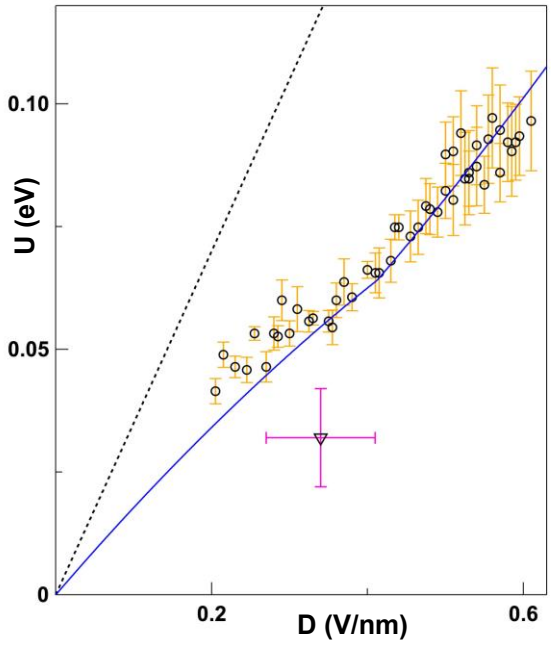

Figure 7.9: Examining the role of screening in BLG. Comparison of gap energies U measured directly from data in Fig. 7.7(a) (open black circles), that have been corrected according to the procedure outlined in Section 7.6. Also plotted is the theoretical U in the unscreened (black dotted line) and self-consistent tight binding (blue solid line) cases from ref. 16 for comparison. The transport gap U_T is plotted as a black triangle.

Following the gap extraction, we note that U_T, shown as a black triangle in Fig. 7.9, is lower than U measured spectroscopically in the same device. This result is consistent with the presence of in-gap states that cause effective gap lowering for measurements occurring at the Fermi level.[29,30]Such in-gap states can be attributed to fabrication-dependent disorder. Our PTS measurements thus enable comparison between measuring DOS features when they are away from the E_F and as they are

pulled through E_F. The former measurement appears to be less sensitive to device fabrication and agrees more readily with recent ultraclean electron transport measurements and comprehensive theory.[29] Moreover, the PTS probe acts as a top gate, shifting the bands with respect to E_F in a relatively large area (~ 4 μm^2) BLG region that is beneath the probe. This region may contain impurities and charge inhomogeneity and as a result, the bands below the tunneling probe may become pinned to disorder states as they shift, resulting in a lower U_T than the expected U for pristine BLG.

7.9 Conclusion and Main Experimental Findings

In conclusion, we performed PTS of BLG and developed a methodology to attain a comprehensive understanding of the BLG tunnel spectra. We achieve unprecedented control of the electrostatic environment and chemical potential and use it to directly probe BLG's elusive band gap. By comparing dI/dV_b maps to a full simulation of BLG-PTS, we identified the CNP and π^* BE as BLG was filled and emptied with charge. To make BLG's dynamic band structure static, we employed a shear transformation which mapped D onto the horizontal axis. With full control of D, n, and $E_F + eV_b$, we comprehensively characterized BLG, yielding its U spectroscopically. The direct observation of $E_F(n)$ and U makes it possible to compare an equilibrium transport gap and a tunneling spectroscopic gap within the same device. The methodology discussed here can be readily applied to other multilayer graphene sheets, potentially enabling finer control of correlated graphene multilayers as they are measured.

References

(1) Chen, G.; Jiang, L.; Wu, S.; Lyu, B.; Li, H.; Chittari, B. L.; Watanabe, K.; Taniguchi, T.; Shi, Z.; Jung, J.; et al. Evidence of a Gate-Tunable Mott Insulator in a Trilayer Graphene Moiré Superlattice. *Nat. Phys.* **2019**, *15* (3), 237–241. https://doi.org/10.1038/s41567-018-0387-2.

(2) Chen, G.; Sharpe, A. L.; Gallagher, P.; Rosen, I. T.; Fox, E. J.; Jiang, L.; Lyu, B.; Li, H.; Watanabe, K.; Taniguchi, T.; et al. Signatures of Tunable Superconductivity in a Trilayer Graphene Moiré Superlattice. *Nature* **2019**, *572* (7768), 215–219. https://doi.org/10.1038/s41586-019-1393-y.

(3) He, M.; Li, Y.; Cai, J.; Liu, Y.; Watanabe, K.; Taniguchi, T.; Xu, X.; Yankowitz, M. Tunable Correlation-Driven Symmetry Breaking in Twisted Double Bilayer Graphene. 2020.

(4) Jarillo-Herrero, Y. C. and D. R.-L. and O. R.-B. and J. M. P. and K. W. and T. T. and P. Electric Field Tunable Correlated States and Magnetic Phase Transitions in Twisted Bilayer-Bilayer Graphene. *ArXiv* **2019**.

(5) Yankowitz, M.; Wang, J. I.-J.; Li, S.; Birdwell, A. G.; Chen, Y.-A.; Watanabe, K.; Taniguchi, T.; Quek, S. Y.; Jarillo-Herrero, P.; LeRoy, B. J. Band Structure Mapping of Bilayer Graphene via Quasiparticle Scattering. *APL Mater.* **2014**, *2* (9), 92503. https://doi.org/10.1063/1.4890543.

(6) Velasco, J.; Lee, J.; Wong, D.; Kahn, S.; Tsai, H.-Z.; Costello, J.; Umeda, T.; Taniguchi, T.; Watanabe, K.; Zettl, A.; et al. Visualization and Control of Single-Electron Charging in Bilayer Graphene Quantum Dots. *Nano Lett.*

2018, *18* (8), 5104–5110. https://doi.org/10.1021/acs.nanolett.8b01972.

(7) Holdman, G. R.; Krebs, Z. J.; Behn, W. A.; Smith, K. J.; Watanabe, K.; Taniguchi, T.; Brar, V. W. Dynamic Band Structure and Capacitance Effects in Scanning Tunneling Spectroscopy of Bilayer Graphene. *Appl. Phys. Lett.* **2019**, *115* (18), 181601. https://doi.org/10.1063/1.5127078.

(8) Zhang, Y.; Brar, V. W.; Wang, F.; Girit, C.; Yayon, Y.; Panlasigui, M.; Zettl, A.; Crommie, M. F. Giant Phonon-Induced Conductance in Scanning Tunnelling Spectroscopy of Gate-Tunable Graphene. *Nat. Phys.* **2008**, *4*, 627.

(9) Chandni, U.; Watanabe, K.; Taniguchi, T.; Eisenstein, J. P. Signatures of Phonon and Defect-Assisted Tunneling in Planar Metal–Hexagonal Boron Nitride–Graphene Junctions. *Nano Lett.* **2016**, *16* (12), 7982–7987. https://doi.org/10.1021/acs.nanolett.6b04369.

(10) Wong, D.; Wang, Y.; Jung, J.; Pezzini, S.; DaSilva, A. M.; Tsai, H.-Z.; Jung, H. S.; Khajeh, R.; Kim, Y.; Lee, J.; et al. Local Spectroscopy of Moiré-Induced Electronic Structure in Gate-Tunable Twisted Bilayer Graphene. *Phys. Rev. B* **2015**, *92* (15), 155409. https://doi.org/10.1103/PhysRevB.92.155409.

(11) Deshpande, A.; Bao, W.; Zhao, Z.; Lau, C. N.; LeRoy, B. J. Mapping the Dirac Point in Gated Bilayer Graphene. *Appl. Phys. Lett.* **2009**, *95* (24), 243502. https://doi.org/10.1063/1.3275755.

(12) Rutter, G. M.; Jung, S.; Klimov, N. N.; Newell, D. B.; Zhitenev, N. B.; Stroscio, J. A. Microscopic Polarization in Bilayer Graphene. *Nat. Phys.* **2011**, *7*, 649.

(13) Jung, S.; Myoung, N.; Park, J.; Jeong, T. Y.; Kim, H.; Watanabe, K.; Taniguchi, T.; Ha, D. H.; Hwang, C.; Park, H. C. Direct Probing of the Electronic Structures of Single-Layer and Bilayer Graphene with a Hexagonal Boron Nitride Tunneling Barrier. *Nano Lett.* **2017**, *17* (1), 206–213. https://doi.org/10.1021/acs.nanolett.6b03821.

(14) Vdovin, E. E.; Mishchenko, A.; Greenaway, M. T.; Zhu, M. J.; Ghazaryan, D.; Misra, A.; Cao, Y.; Morozov, S. V; Makarovsky, O.; Fromhold, T. M.; et al. Phonon-Assisted Resonant Tunneling of Electrons in Graphene--Boron Nitride Transistors. *Phys. Rev. Lett.* **2016**, *116* (18), 186603. https://doi.org/10.1103/PhysRevLett.116.186603.

(15) Davenport, J. L.; Ge, Z.; Liu, J.; Nuñez-Lobato, C.; Moon, S.; Lu, Z.; Quezada-Lopez, E. A.; Hellier, K.; LaBarre, P. G.; Taniguchi, T.; et al. Probing the Electronic Structure of Graphene near and Far from the Fermi Level via Planar Tunneling Spectroscopy. *Appl. Phys. Lett.* **2019**, *115* (16), 163504. https://doi.org/10.1063/1.5118422.

(16) Jung, S.; Park, M.; Park, J.; Jeong, T.-Y.; Kim, H.-J.; Watanabe, K.; Taniguchi, T.; Ha, D. H.; Hwang, C.; Kim, Y.-S. Vibrational Properties of H-BN and h-BN-Graphene Heterostructures Probed by Inelastic Electron Tunneling Spectroscopy. *Sci. Rep.* **2015**, *5*, 16642.

(17) McCann, E.; Koshino, M. The Electronic Properties of Bilayer Graphene. *Reports Prog. Phys.* **2013**, *76* (5), 56503.

(18) Moldovan, D., Anđelković, Miša, & Peeters, F. Pybinding v0.9.4: a Python

Package for Tight-Binding Calculation http://doi.org/10.5281/zenodo.826942.

(19) Wei\sse, A.; Wellein, G.; Alvermann, A.; Fehske, H. The Kernel Polynomial Method. *Rev. Mod. Phys.* **2006**, *78* (1), 275–306. https://doi.org/10.1103/RevModPhys.78.275.

(20) Luryi, S. Quantum Capacitance Devices. *Appl. Phys. Lett.* **1988**, *52* (6), 501–503. https://doi.org/10.1063/1.99649.

(21) Kim, K. S.; Kim, T.-H.; Walter, A. L.; Seyller, T.; Yeom, H. W.; Rotenberg, E.; Bostwick, A. Visualizing Atomic-Scale Negative Differential Resistance in Bilayer Graphene. *Phys. Rev. Lett.* **2013**, *110* (3), 36804. https://doi.org/10.1103/PhysRevLett.110.036804.

(22) Yin, L.-J.; Zhang, Y.; Qiao, J.-B.; Li, S.-Y.; He, L. Experimental Observation of Surface States and Landau Levels Bending in Bilayer Graphene. *Phys. Rev. B* **2016**, *93* (12), 125422. https://doi.org/10.1103/PhysRevB.93.125422.

(23) Malec, C. E.; Davidović, D. Transport in Graphene Tunnel Junctions. *J. Appl. Phys.* **2011**, *109* (6), 64507. https://doi.org/10.1063/1.3554480.

(24) Zhao, Y.; Wyrick, J.; Natterer, F. D.; Rodriguez-Nieva, J. F.; Lewandowski, C.; Watanabe, K.; Taniguchi, T.; Levitov, L. S.; Zhitenev, N. B.; Stroscio, J. A. Creating and Probing Electron Whispering-Gallery Modes in Graphene. *Science (80-.).* **2015**, *348* (6235), 672–675. https://doi.org/10.1126/science.aaa7469.

(25) Zhang, Y.; Tang, T.-T.; Girit, C.; Hao, Z.; Martin, M. C.; Zettl, A.; Crommie, M. F.; Shen, Y. R.; Wang, F. Direct Observation of a Widely Tunable Bandgap

in Bilayer Graphene. *Nature* **2009**, *459*, 820.

(26) Taychatanapat, T.; Jarillo-Herrero, P. Electronic Transport in Dual-Gated Bilayer Graphene at Large Displacement Fields. *Phys. Rev. Lett.* **2010**, *105* (16), 166601. https://doi.org/10.1103/PhysRevLett.105.166601.

(27) Brar, V. W.; Decker, R.; Solowan, H.-M.; Wang, Y.; Maserati, L.; Chan, K. T.; Lee, H.; Girit, Ç. O.; Zettl, A.; Louie, S. G.; et al. Gate-Controlled Ionization and Screening of Cobalt Adatoms on a Graphene Surface. *Nat. Phys.* **2010**, *7*, 43.

(28) Ju, L.; Wang, L.; Cao, T.; Taniguchi, T.; Watanabe, K.; Louie, S. G.; Rana, F.; Park, J.; Hone, J.; Wang, F.; et al. Tunable Excitons in Bilayer Graphene. *Science (80-.).* **2017**, *358* (6365), 907–910. https://doi.org/10.1126/science.aam9175.

(29) Hao, Y.; Wang, L.; Liu, Y.; Chen, H.; Wang, X.; Tan, C.; Nie, S.; Suk, J. W.; Jiang, T.; Liang, T.; et al. Oxygen-Activated Growth and Bandgap Tunability of Large Single-Crystal Bilayer Graphene. *Nat. Nanotechnol.* **2016**, *11* (5), 426–431. https://doi.org/10.1038/nnano.2015.322.

(30) Gava, P.; Lazzeri, M.; Saitta, A. M.; Mauri, F. Ab Initio Study of Gap Opening and Screening Effects in Gated Bilayer Graphene. *Phys. Rev. B* **2009**, *79* (16), 165431. https://doi.org/10.1103/PhysRevB.79.165431.

Chapter 8:

Conclusions and Outlook

In the preceding chapters, PTS was used to explore a variety of electronic structure properties of graphene and bilayer graphene (BLG). The PTS technique, while unconventional, is exceedingly promising for three main reasons, which were demonstrated in experimental Chapters 5,6, and 7. Firstly, the PTS measurement is mechanically stable and can probe graphene in ultra-high magnetic fields. In Chapter 5, we used PTS to observe renormalization and disorder-screening effects in graphene's highly degenerate Landau levels. Secondly, PTS can directly probe states away from the Fermi level. This was important in the study presented in Chapter 6, which accessed low and high energy states in the BLG electronic structure. We extracted the energy of these states as they filled and emptied with charge and used their energies to determine nearly all of BLG's fitting parameters to high precision. Lastly, the PTS device layout has straightforward electrostatics. This attribute makes PTS the ideal tool for characterizing the low energy spectrum of graphene multilayers which are known to modulate in the presence of an electric field.

Ten years after BLG was first characterized with scanning tunneling spectroscopy (STS), there remains a gap in the understanding of how it changes under the STS probe. In Chapter 7 we used PTS to shed light on invasive probe effects and found that tunneling is top-layer specific, that it modulates the Fermi level, and that it

changes the band gap at charge neutrality. Importantly, we presented original methods to correct for the substantial errors associated with each invasive probe effect. With these accomplishments, we believe that PTS can serve as an indispensable tool for spectroscopically characterizing occupied and unoccupied states in two-dimensional (2D) materials with full control of the Fermi level, electrostatic potential and the magnetic vector potential due to an external field.

The methods developed in this thesis can readily be applied to a host of 2D materials. Although the density of states of 2D materials can also be extracted with STS, surface preparation (especially for air sensitive devices) can be painstaking if it is even possible. The PTS method completely circumvents any surface preparation, as it uses atomically sharp interfaces between the tunneling barrier hBN and the underlying sample (graphene or BLG in this thesis). Furthermore, the tunneling hBN has been demonstrated to act as a passivation layer for encapsulated 2D materials.[1] Therefore, we expect PTS to be fully compatible with measuring gap energies and states in 2D semiconductors, yielding important values for physics and technology alike. Corelated and superconducting states, however, may be pushing the limits of even PTS.

The PTS probe, a large metal plate, sits ~2 nm above the electrons in graphene. It is then natural to ask: is this screening the Coulomb repulsion between electrons? Evidence in Chapter 5 suggests that PTS is capable of probing different screening scenarios in graphene, as well as many body renormalization effects. The case of graphene may be special, as electron screening is completely characterized by the Wigner-Seitz radius $r_s \sim 0.8$, and electrons are then closer to one another than to the

probe.[2–4] In correlated multilayers, this is not the case. A simplified Hubbard model of the Moiré lattice formed when two graphene sheets are twisted with respect to each other indicates that Coulomb repulsion must be felt on the order of the Moiré wavelength $\lambda_m \sim 10$ nm. Probing correlated gaps may be unreachable for the PTS measurement as-is. By using lower band gap insulating barriers such as MoS_2, the tunneling probe can be separated farther from the sample without diminishing the tunneling conductance to a point where it is unmeasurable. In this way, new, thicker tunneling barriers may allow access to delicate correlated states with PTS. In the meantime, there is a wealth of knowledge about the dynamic flat bands that make these correlations possible in the first place. The PTS method is an ideal tool for controlling the displacement field and filling factor and can thus be used to validate DFT or tight binding electronic structure predictions in an energy range too small for ARPES and too dynamic for STS.

Fabricating tunneling devices is akin to fabricating transport or capacitance devices. As a result, tunneling devices benefit from the full arsenal of nanofabrication techniques that are continuously being improved. For example, as discussed in Chapter 4, I used a series of etching, ultraclean pickup, lithography and deposition to create nanoscale tunneling probes. For the first time, tunneling probe size and shape are tunable at the nanoscale. Additionally, the final deposition step can be adapted for different metal probe compositions, enabling the exploration of high or low work function mismatch tunneling, 3D to 2D superconductor tunneling, magnetic junctions

or built in quantum dots, to name a few. There are innumerable permutations of the tunneling device that can be straightforwardly accessed by slight fabrication tweaks.

The research presented in this thesis has established PTS as a viable and versatile experimental tool. Validation of PTS on monolayer and bilayer graphene lays the foundation for its use on other interesting 2D solid-state systems. Between its simplicity, stability and experimental control, PTS is well suited to address profound implications of electrons confined to two dimensions.

References

(1) Yankowitz, M.; Ma, Q.; Jarillo-Herrero, P.; LeRoy, B. J. Van Der Waals Heterostructures Combining Graphene and Hexagonal Boron Nitride. *Nat. Rev. Phys.* **2019**, *1* (2), 112–125. https://doi.org/10.1038/s42254-018-0016-0.

(2) McCann, E.; Koshino, M. The Electronic Properties of Bilayer Graphene. *Reports Prog. Phys.* **2013**, *76* (5), 56503.

(3) Jang, C.; Adam, S.; Chen, J.-H.; Williams, E. D.; Das Sarma, S.; Fuhrer, M. S. Tuning the Effective Fine Structure Constant in Graphene: Opposing Effects of Dielectric Screening on Short- and Long-Range Potential Scattering. *Phys. Rev. Lett.* **2008**, *101* (14), 146805. https://doi.org/10.1103/PhysRevLett.101.146805.

(4) Das Sarma, S.; Hwang, E. H. Velocity Renormalization and Anomalous Quasiparticle Dispersion in Extrinsic Graphene. *Phys. Rev. B* **2013**, *87* (4), 45425. https://doi.org/10.1103/PhysRevB.87.045425.

Appendix A:

Exfoliating Graphene onto a SiO_2/Si Wafer

A1 Making silicon chips from wafer

A. Set up a clean prep area by taping four corners of a large Techwipe to the top of the work bench
B. Using tweezers, remove a large circular silicon wafer from its case and place it (reflective side facing up) on the paper Techwipe, shown in Fig. A1.1

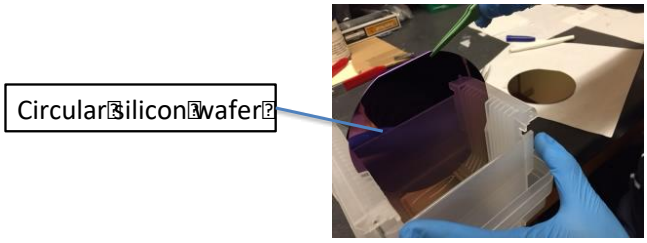

Figure A1.1: Circular silicon wafer being removed from its case

C. Place three glass slides next to each other so they make a 3'' x 3'' square
D. Lay the circular wafer on top of the glass slide platform so that the left half of the circle is on top of the glass slides, shown in Fig. A1.2

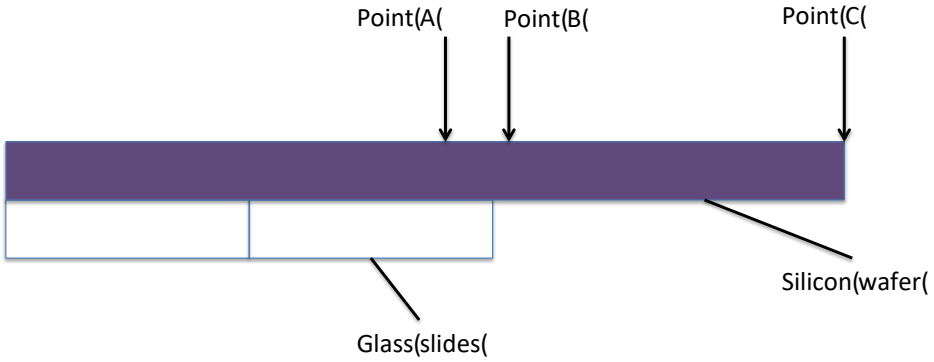

Figure A1.2: Diagram of the silicon wafer hanging over the edge of the glass slides

E. Hold the diamond scribe vertically. Hold the wafer on the glass slide platform with tweezers at point A (Fig. A1.2). Make a single scratch with the diamond scribe at point B (Fig. A1.2). The knick should be roughly 1 mm long and should be where the edge of the right glass slide meets the top of the circle (Fig. A1.3).

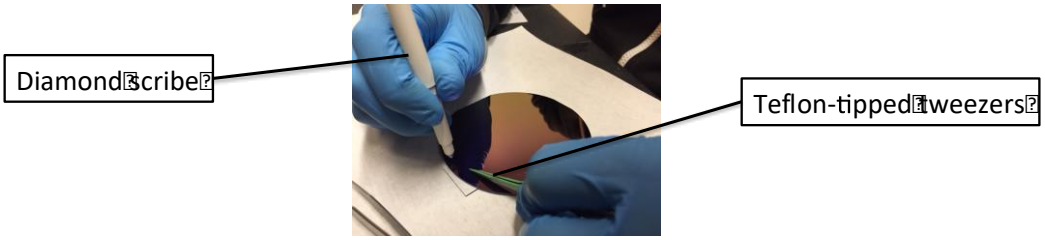

Figure A1.3: Initiating the crack on the silicon wafer with a diamond scribe

F. Hold the wafer at point A (Fig. A1.2) with Teflon tipped tweezers. While holding the wafer in place, take a pair of blunt steel tweezers and tap the wafer at point C (Fig. A1.2). This should break the circle in half along the straight glass edge (Fig. A1.4).

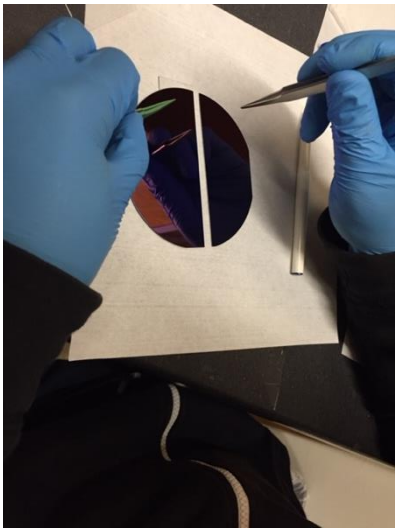

Figure A1.4: After a tap at point C, the silicon wafer should break in half

G. Use tweezers to place one half of the wafer inside of the protective case. Position the other half of the wafer so that straight broken edge is

perpendicular to glass slide edge. Leave roughly 0.8 cm of semicircular wafer hanging over edge of glass slide.

H. Hold the wafer with tweezers at point A (Fig. A1.2). Scratch the wafer at point B (Fig. A1.2) with the diamond scribe. This should break off a 0.8 cm wide strip of wafer.
I. Set the wafer strip aside, and with a similar technique break the remaining semicircle into 0.8 cm wide strips. Set each strip aside on the Techwipe to avoid contaminating them with debris.
J. Using the same technique, break each strip into 0.8 cm x 0.8 cm squares, placing each square aside (Fig. A1.5). (**Note: reduce contact between tweezers and surface of square by holding squares with Teflon tweezers at corner)

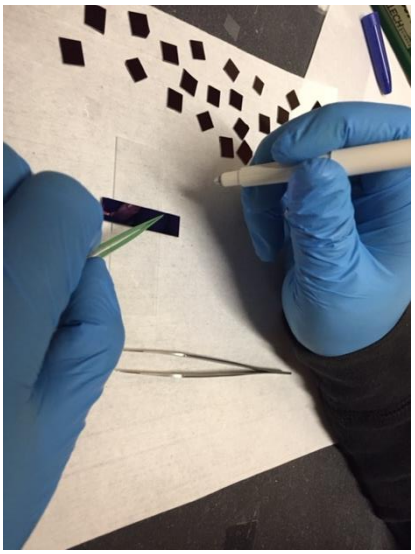

Figure A1.5: continue to break the silicon into smaller square pieces

A2 Cleaning Silicon Chips by Sonication

A. Fill a 100 mL halfway beaker with acetone (Fig. A2.1).

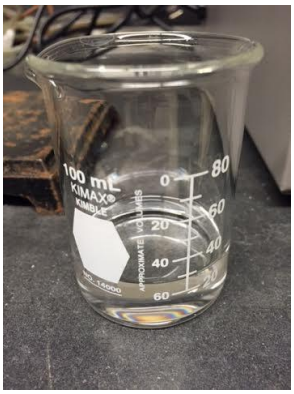

Figure A2.1: A beaker half empty with acetone

B. Place 5-10 chips in beaker with their reflective sides facing up (Fig. A2.2).

Figure A2.2: Silicon chips sit at the bottom of the beaker and do not overlay one another

C. Attach the beaker to the ring stand and adjust the ring level so that the bottom half of the beaker is submerged in the sonicator water bath (Fig. A2.3).

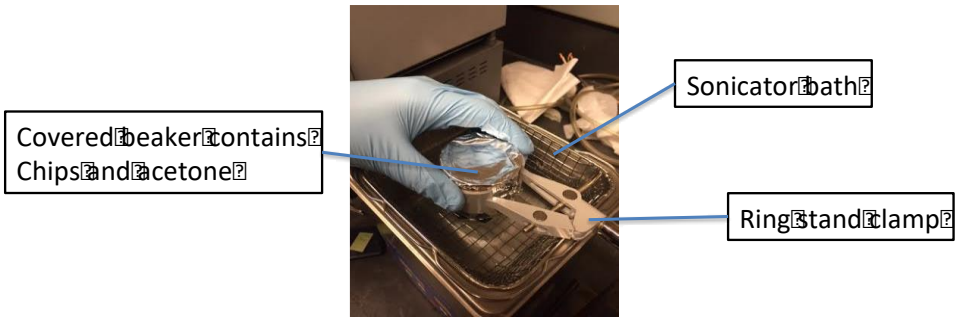

Figure A2.3: Attach the beaker to a ring stand clamp and lower it into the sonicator bath

D. Run the sonicator for 10 minutes (Fig. A2.4)

Figure A2.4: The sonicator time setting it the right display

E. Lift the beaker from the water bath, then remove it from the ring stand. Next, carefully use tweezers to lift each chip out of the acetone. Rinse each chip with isopropyl alcohol (IPA) then blow dry them with ultra-high-purity nitrogen gas (Airgas UHP-40)
F. Pour the waste acetone out of the beaker then rinse the beaker with acetone. Refill the beaker halfway with new acetone
G. Place the chips back into beaker
H. Repeat the 10 minute sonication process (steps 2C-2D)
I. Repeat the IPA rinse (step 2E)
J. Place each chip on a hot plate (pre-heated to 150 °C) for at least 10 minutes to boil off some of the remaining impurities

A3 Prepping for Graphite Exfoliation

A. Choose a flat bulk graphite flake and carefully pick it up out of the bag with tweezers. Place it flat side up on the sticky side of a 3 inch strip of tape.
B. Place this strip of tape on a glass slide with the graphite facing up
C. Use two more strips of tape to fasten the first strip to the glass slide at both ends
D. Use tape to anchor the slide to the table with the graphite facing up

Figure A3.1: Two slides anchored to the table with graphite facing up

A4 Graphite Exfoliation (The Scotch Tape Method)

A. Pull tape 1 inch past sharp edge on dispenser. Fold the overhanging tape on itself to create handle for gripping.
B. Pull 6 inches of tape off of the dispenser, and fold another handle on the opposite side (**4a**).

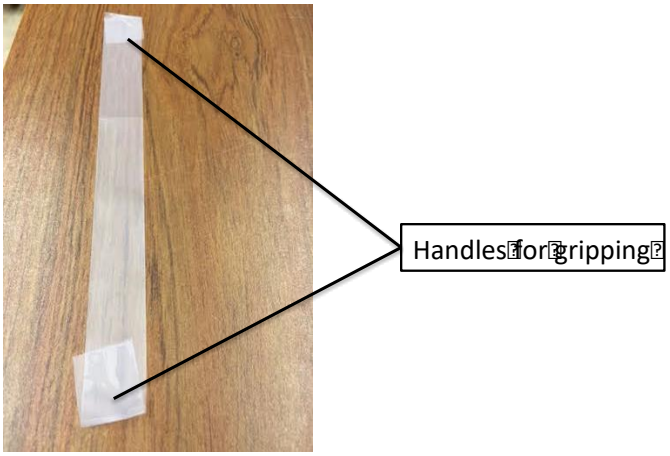

Figure A4.1: Setup of the tape strip

C. Use your dominant thumb to gently roll sticky side of tape over bulk graphite from section 3. (See figure Fig. A4.2)

Figure A4.2 (i) bring tape above graphite on table (ii) lightly apply thumb pressure to bring tape into contact with graphite

D. Apply light pressure between the tape and graphite without excessive exertion, then slowly peel off the tape at 90 degrees to the normal of the table

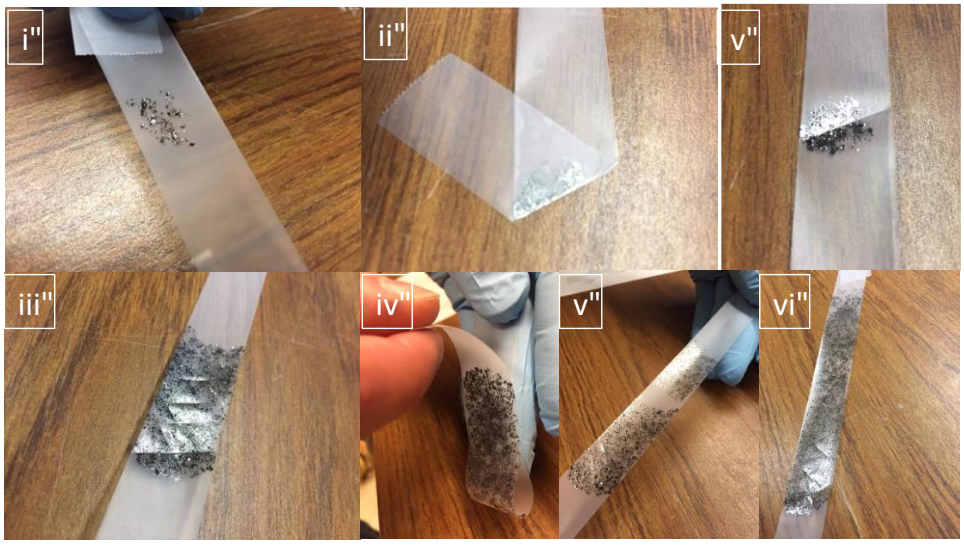

Figure A4.3 (i) graphite chunks taken from table graphite (ii) 45 degree fold of the tape (iii) first region of the tape covered after multiple 45 degree folds (iv) lightly touch first region of the tape with adjacent region (v) pull the tape apart (vi) continue this until the entire tape is covered

E. In the region where graphite transferred (Fig. A4.3(i)), make repeated 45 degree folds (Fig. A4.3(ii)) in the tape until nearly whole width of tape is covered (Fig. A4.3(iii))
F. Bring the covered region of the tape in contact with the region directly adjacent on the tape (Fig. A4.3(iv)). Apply light pressure with finger to contacted region. Swiftly pull tape apart (Fig. A4.3(v)).
G. Repeat this process with adjacent, clean sections of tape until the entire strip is covered (Fig. A4.3(vi)).
H. Hold tape up to the light with the graphite side facing towards you. Look for transfer regions that have transparent, intact flakes of graphite. Theseregions are ideal for transferring graphene in the next section.

A5 Transfer Graphene onto SiO2

A. Clean the workbench with isopropyl alcohol and a Kimwipe
B. Place a clean silicon chip (see section 2) (reflective side facing up) on a glass slide on the workbench (Fig. A5.1)

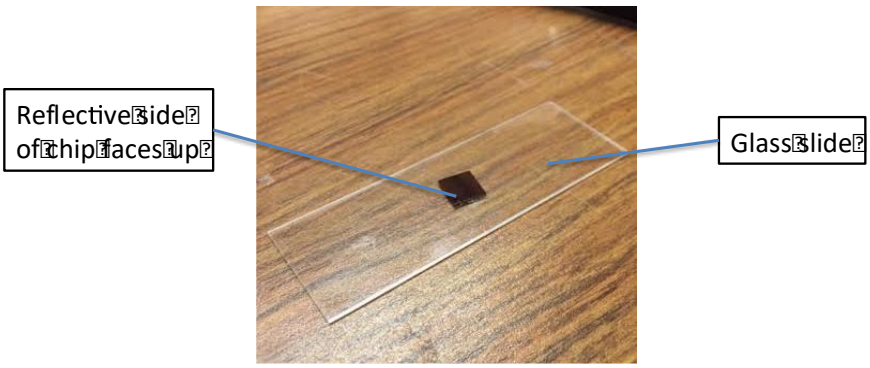

Figure A5.1: Silicon chip on a glass slide

C. Hold the exfoliated tape (see section 4) tape so that your dominant thumb is in contact with the non-sticky side of the tape, over the ideal transfer region (Fig. A5.2(i)).
D. Slowly use your thumb to roll the tape on top of the chip (Fig. A5.2(ii)). Take care to roll out any possible bubbles in tape. Press the remaining tape onto surrounding glass slide.

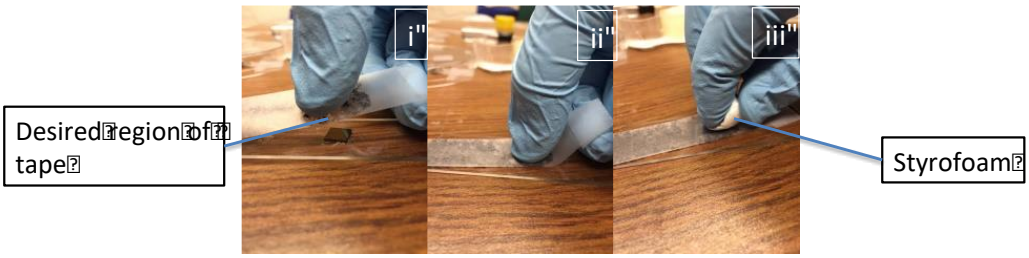

Figure A5.2 (a) Bring the desired region of the tape over the chip (b) firmly press with your thumb so there are no bubbles between the tape and the chip (c) lightly rub the top of the tape covered chip with styrofoam

E. Lightly rub top of chip with chunk of Styrofoam for 10 seconds (Fig. A5.2(iii)).
F. Cut off overhanging tape with a razor blade and place slide on hot plate at 100 degrees C for 2 minutes
G. Remove the slide from the hotplate and place it back on the clean workbench. Allow the slide to cool for 1 min, then pull back the tape until one corner of the chip is exposed (Fig. A5.3(i)).
H. Hold down the exposed corner with Teflon tweezers and pull the tape slowly off of chip at 45 degrees to the normal of the table and 135 degrees from remaining tape on the glass slide (Fig. A5.3(ii)**,** Fig. A5.3(iii)).

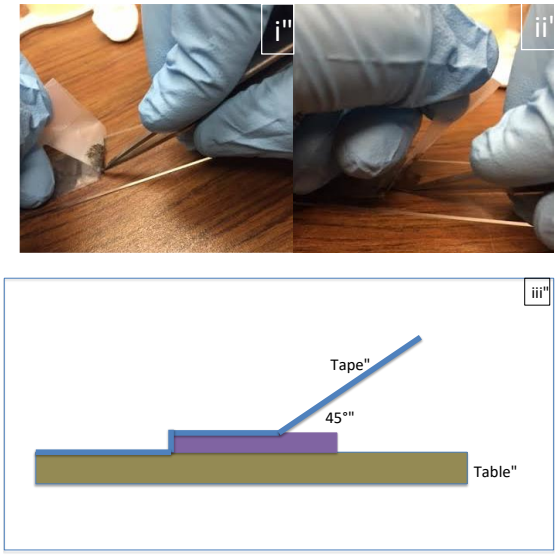

Figure A5.3 (i) grip the corner of the chip with tweezers (ii) lift the tape off of the chip
(iii) diagram of the angle at which the tape should be lifted

Appendix B:

Cooling the Janis Cryostat from Room Temp. to ~4 K

System Schematic:

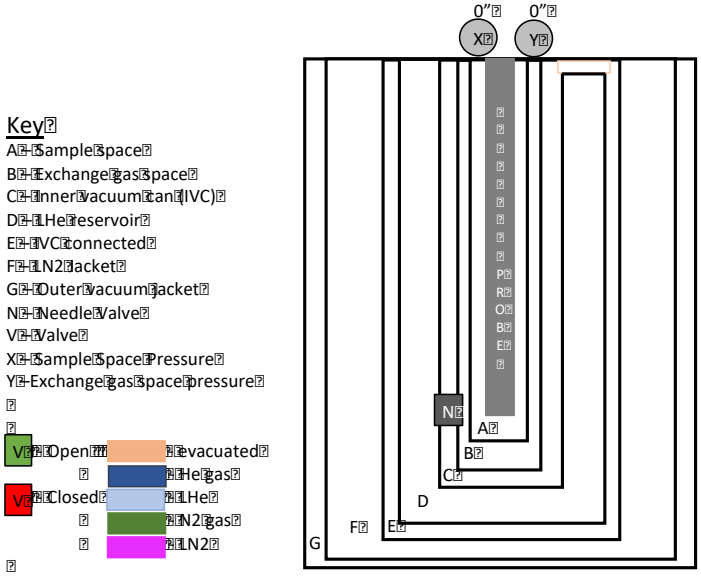

B1 Attaching the proper fittings

A. Remove the quench valve / reservoir recovery assembly from the outlet of the LHe reservoir.
B. Replace this assembly with a cross that has
    a. A +/- pressure gauge
    b. A valve with a 1/8" hose barb for He gas back filling
    c. A valve attached to a line to house vacuum

    This cross will be referred to as the "backfilling assembly (BA)"

B2 Preparing vacuum spaces and reservoirs

A. Attach a turbo pump and ion gauge to the inner vacuum can (IVC) inlet flange.
B. Evacuate the line to a pressure of 5 x 10^{-5} Torr or lower.
C. Open the valve to connect the IVC space to the turbo pump line.
D. Wait until the pressure reaches lower than 5 x 10^{-5} Torr (this should take approximately 1 day), then close the valve tightly.
E. Vent the pump and remove the line, then blank off the flange.

Frequency: every 6 months or if LHe consumption is abnormally high

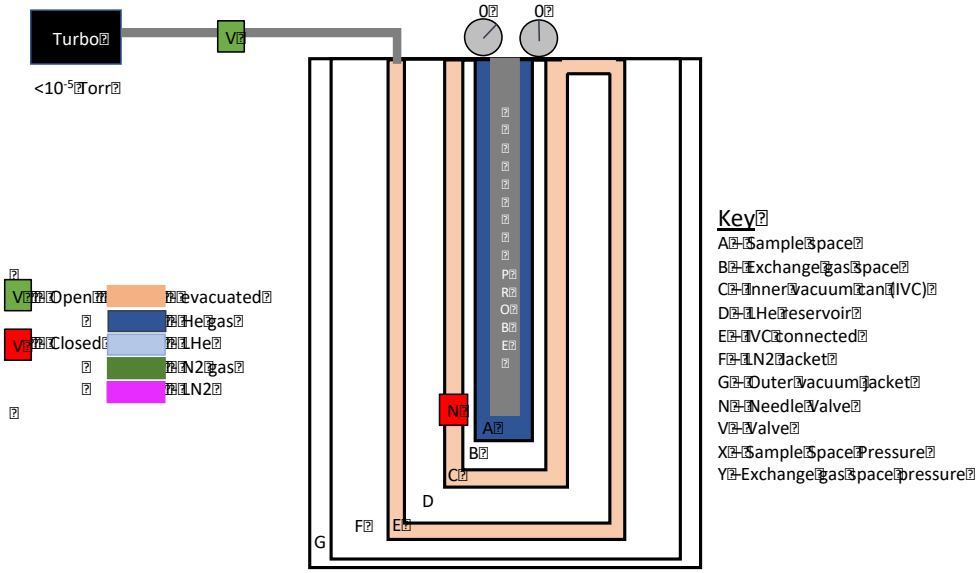

Follow steps 1A-E for the outer vacuum jacket

Frequency: every 2 years or if LHe consumption is abnormally high

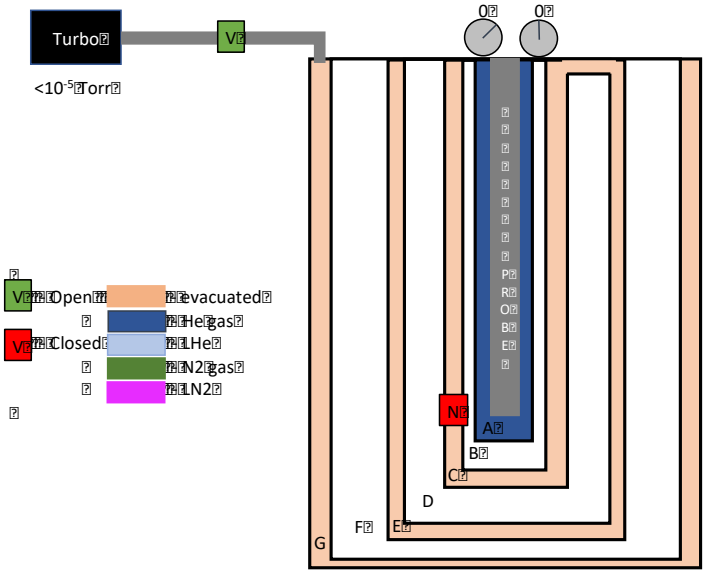

F. With all BA valves closed, evacuate the attached vacuum line
G. Purge the He gas line and attach it to the BA gas inlet with a hose clamp
H. Open the BA vacuum valve to evacuate the LHe reservoir
   Note: if the system has been warm or left open to air, pump on this space over a weekend to remove any residual water
I. Close the BA vacuum valve. Open the BA He gas valve to backfill the LHe reservoir with He gas to a pressure of 2 psi.
J. Repeat steps 1F-I three times, then close all BA valves and turn off the He gas. The LHe reservoir should now be filled with clean, dry He gas.

B3 Evacuating and Backfilling the Exchange Gas Space

A. To a T, attach the turbo, a valve to helium gas supply at 10 psig, and a valve to the exchange gas space flange

B. Close the needle valve tightly and pump the exchange gas space to a pressure < 10^{-4} Torr

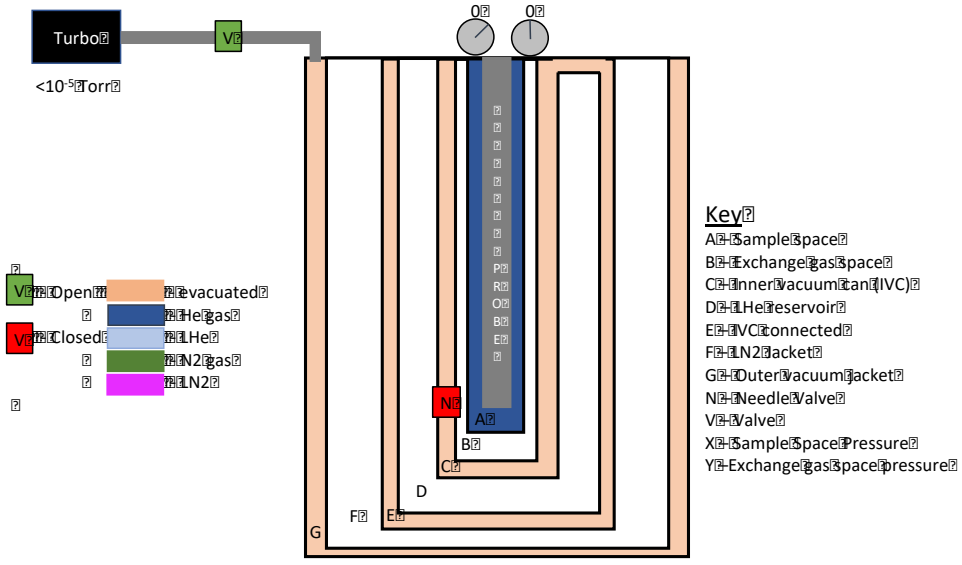

C. Close the valve to the turbo and backfill the exchange gas space with helium gas to positive pressure

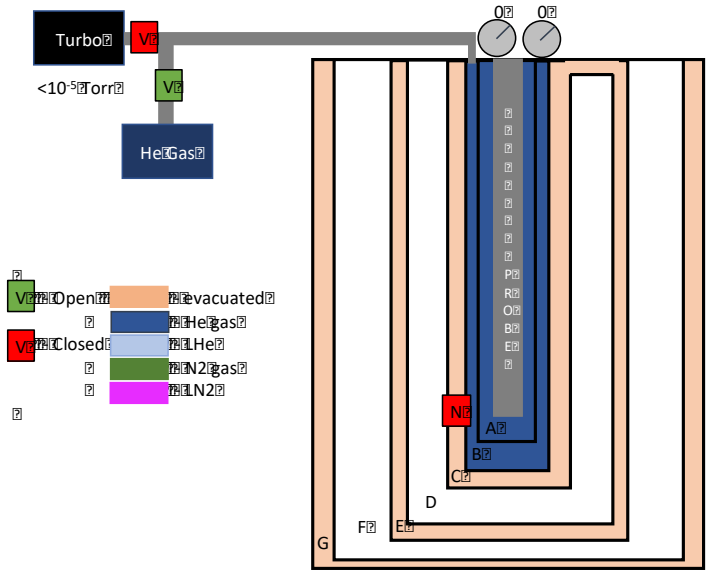

B4 Prepping and filling the liquid nitrogen (LN2) jacket

D. Position a low pressure (22 psi) LN2 tank within 4 feet of the inlet to the LN2 jacket
E. Use hose clamps to attach one end of a thick cryogenic rubber hose to the liquid outlet of the tank and the other end to the inlet hose barb on the cryostat LN2 jacket
F. Remove the check valve flange from the LN2 jacket.
G. Open the inlet valve on the cryostat completely and the valve on the tank ½ turn – liquid should begin to pulse through the rubber hose and fog should begin to blow out of the LN2 jacket outlet
H. Once the fog flow rate subsides, open the outlet on the tank all the way.
I. Wait until liquid begins to spew out of the LN2 jacket—roughly 25 minutes—to close the outlet of the tank. **Note: to avoid dangerous pressure buildup in the hose always close the tank outlet first, then the LN2 jacket inlet.**

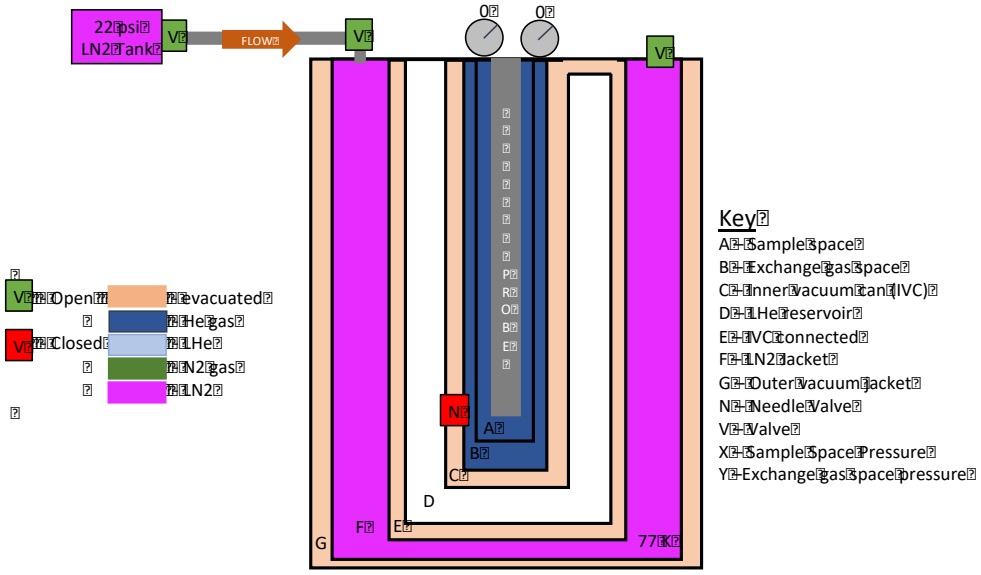

J. Replace the check valve flange on the opening to the LN2 jacket
K. Allow the hose to thaw or heat it up with a heat gun.

B5 Cooling the (LHe) reservoir to 77 K

A. Attach the Backfill Assembly (BA) to the exhaust flange of the LHe reservoir
B. Pump the LHe reservoir and backfill with He gas 3 times. Fill the LHe reservoir with He gas to positive pressure.

Note: Do not pump on the LHe reservoir at this stage.

Pump Configuration

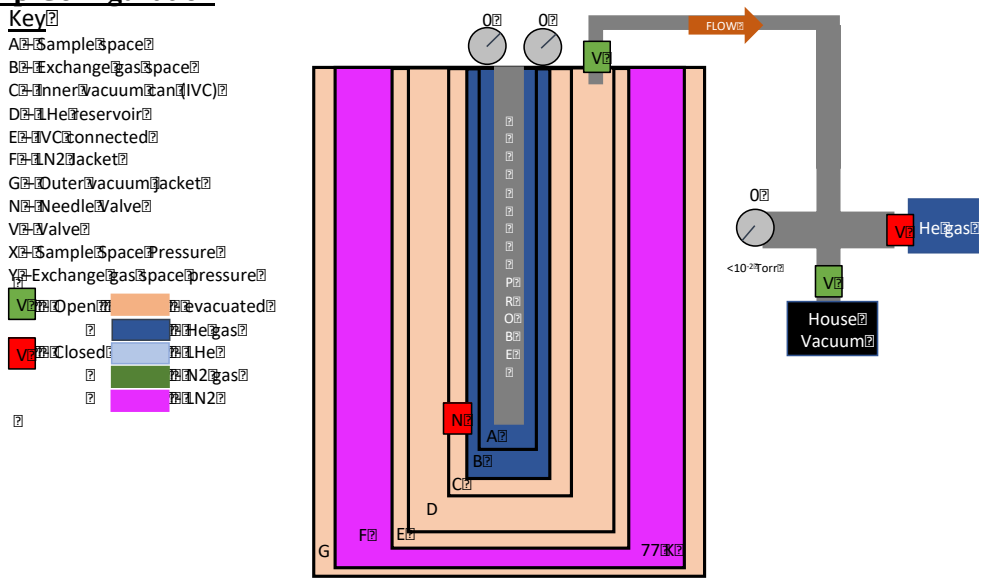

Purge Configuration:

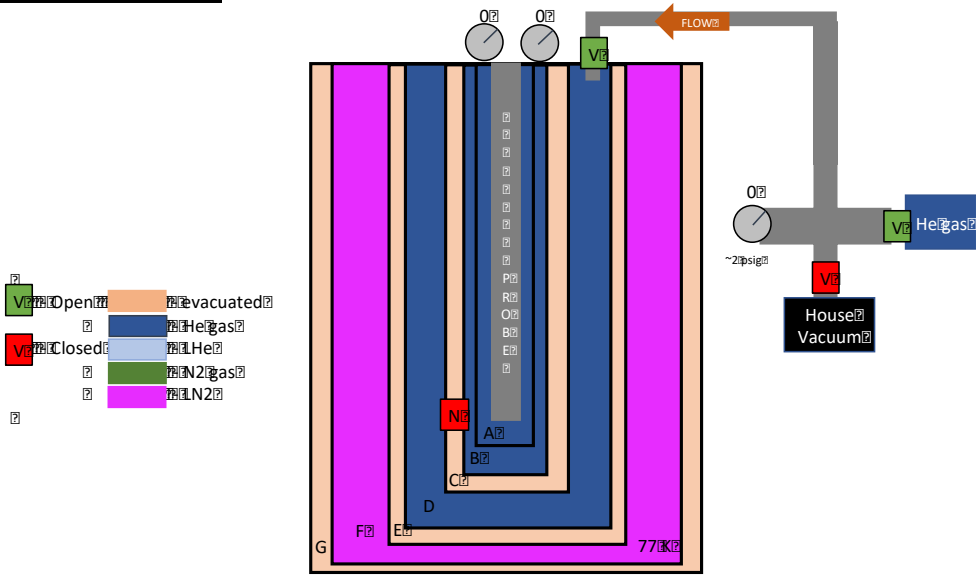

C. Attach a 3/8” diameter stainless steel straw to one end of thick cryogenic rubber hose with a hose clamp.
D. Attach the other end of the hose to the liquid outlet of the LN2 tank
E. Slide a male Goddard fitting onto the stainless steel straw
F. Remove the bunt (stopper) from the LHe reservoir Goddard fitting inlet.
G. Slide the straw at the end of the rubber hose into the open inlet and tighten the fitting around the straw
H. Open the exhaust valve on the LHe reservoir and open the valve on the LN2 tank 1 turn. Gas should rush out of the open exhaust flange.

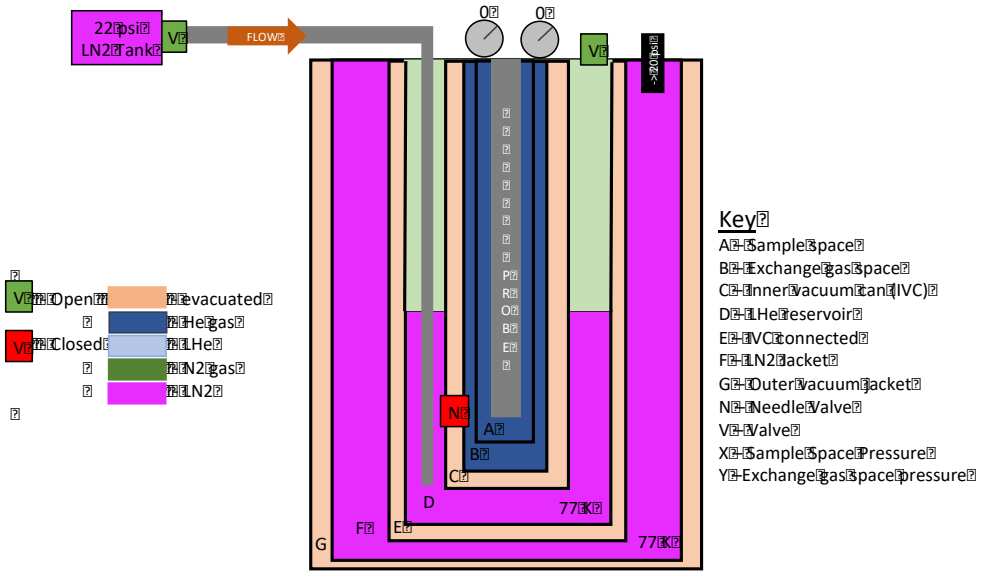

I. Turn on the carbon resistor ohmmeter. The resistance of the carbon resistor should begin to increase after several minutes from 413 ohms to 513 ohms.
J. After the carbon resistor R begins to increase, open the valve on the LN2 tank 3 more turns.
K. Continue filling the LHe reservoir with LN2 for 15 minutes after the carbon resistor stabilizes at 513 ohms.
L. Place a 1/3 psi quench safety valve on the exhaust flange
M. Remove the straw from the LHe inlet. Replace the bunt to seal the reservoir.
N. Wait 2 days. Monitor the carbon resistor. If the resistance falls below 512 ohms, repeat steps 5A-M

B6 Pushing out the LN2

A. Remove the 1/3 psi quench safety valve from the LHe reservoir exhaust flange and replace it with a K50 – ¼ hose barb. To the hose barb, attach a helium gas line.
B. Remove the bunt from the LHe reservoir inlet.
C. Attach an extension to the LHe transfer line on the long, straight leg.
D. Insert the extended end of the transfer line into the LHe reservoir and slide it until it touches the bottom of the reservoir.
E. Insert the other end of the transfer line into a LN2 dewar
F. Apply 10 psi of He gas pressure through the exhaust barb and push out all LN2 from the LHe reservoir into the dewar
G. After there is no remaining LN2, continue pushing with He gas for 15 minutes.

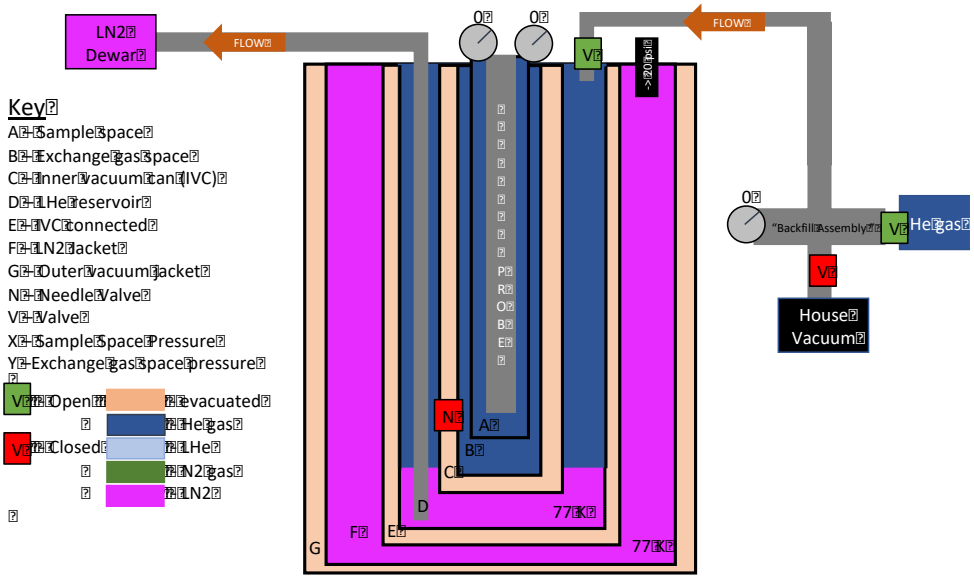

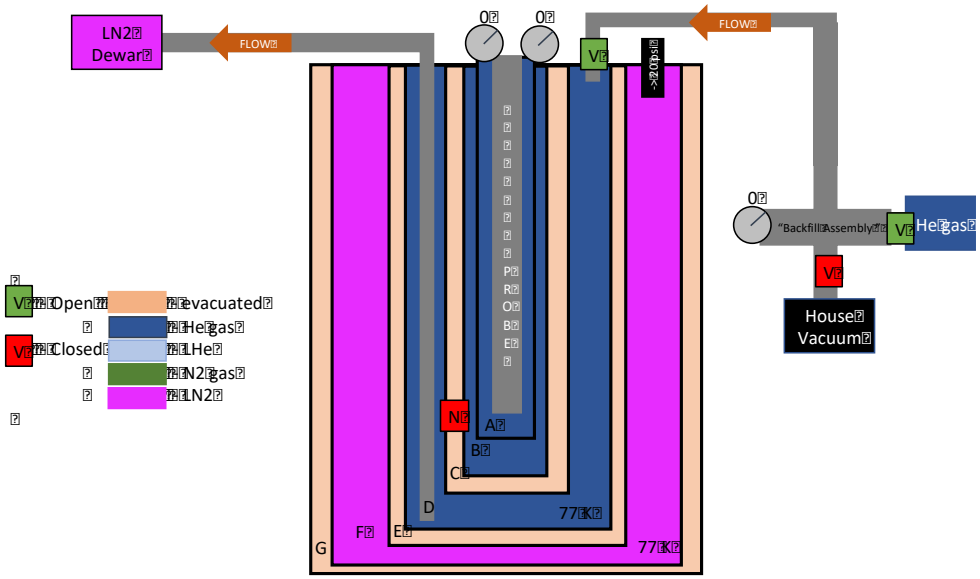

H. Use the BA to pump on the LHe reservoir and backfill with He gas 3 times, each time pumping for 3 minutes and filling for 3 minutes

Pump Configuration

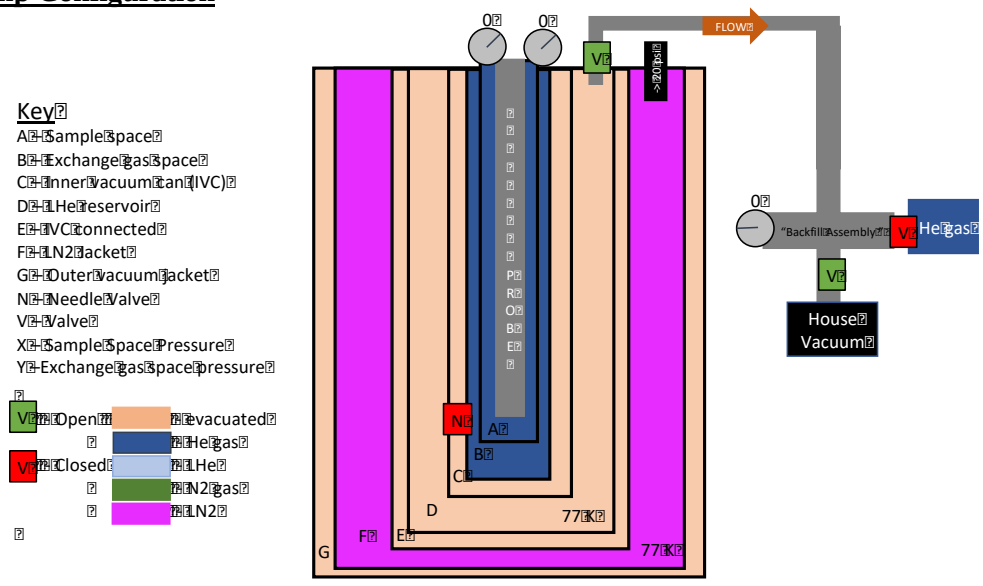

Purge Configuration

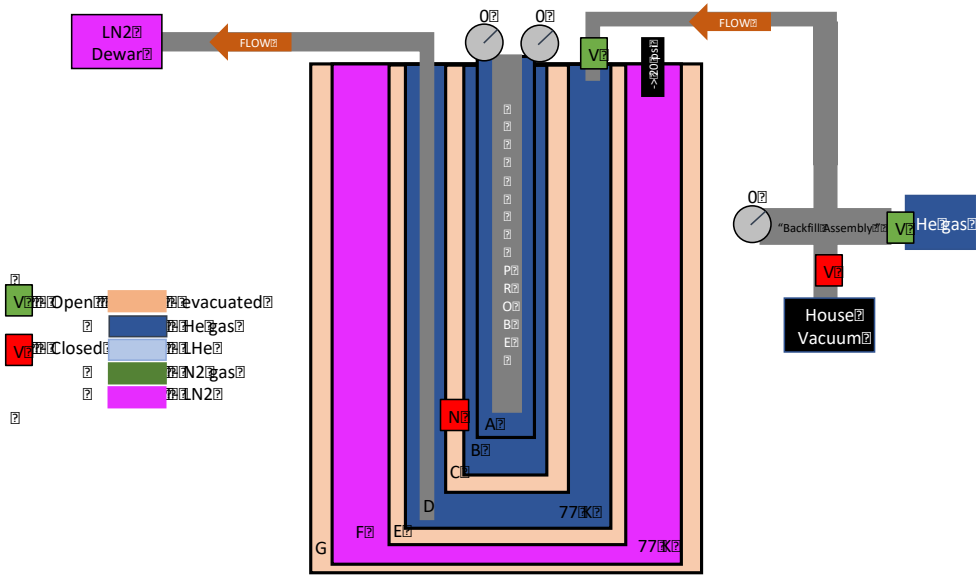

I. Monitor the resistance of the carbon resistor. If it falls below 500 ohms, repeat steps 5A-M

B7 Cooling the (LHe) reservoir to 4 K

A. Remove the BA from the LHe reservoir exhaust valve flange
B. Follow the LHe transfer SOP to cool the system to 4 K

Outline:

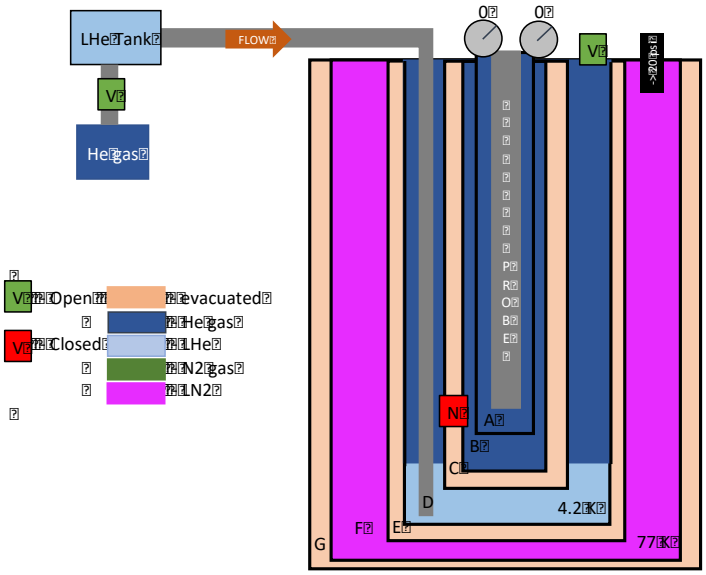

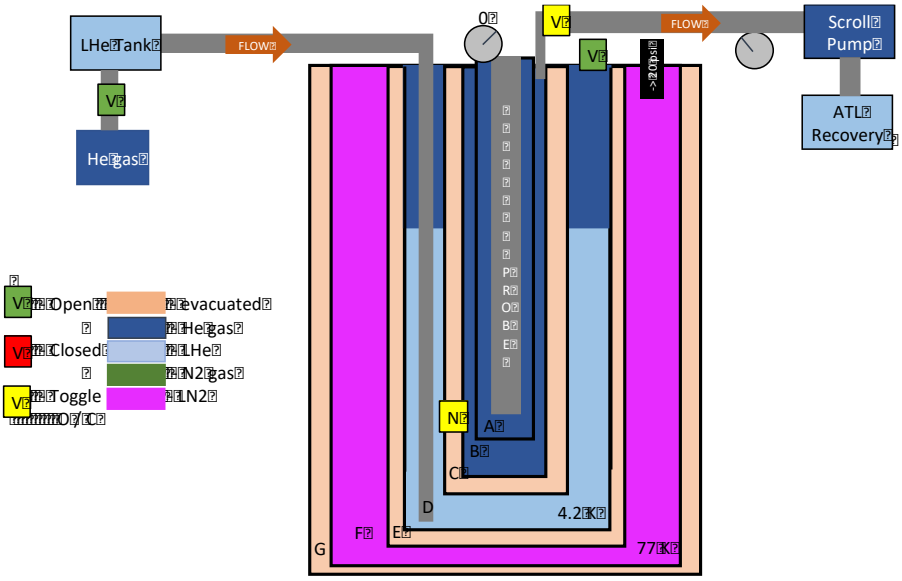

Final Configuration:

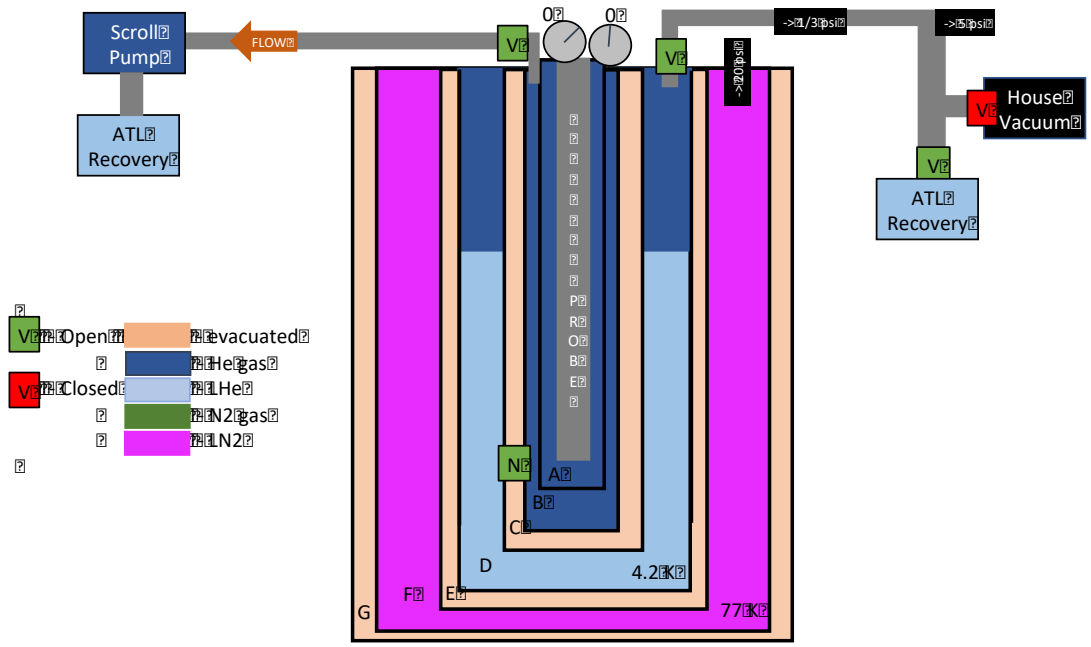

Appendix C:

Janis Cryostat Sample Exchange Instructions

Equipment that will be used for sample exchange:

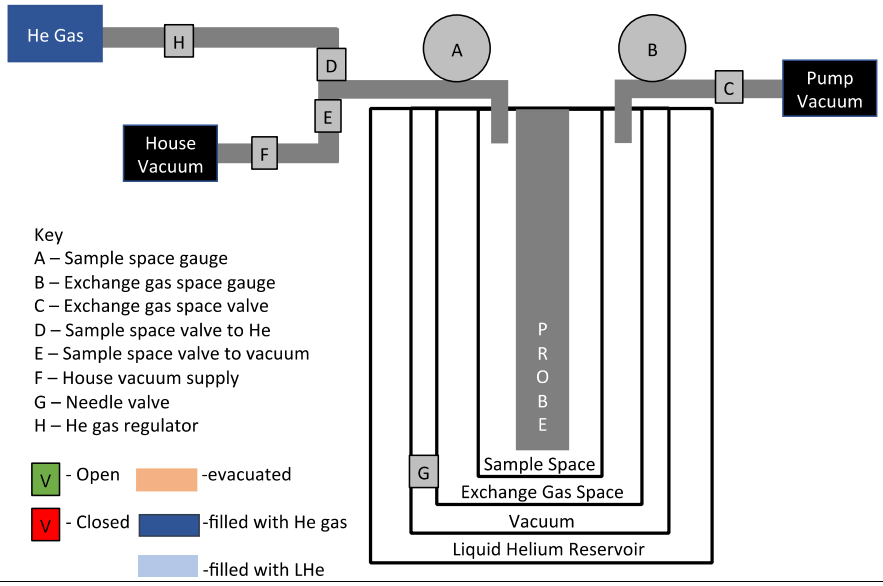

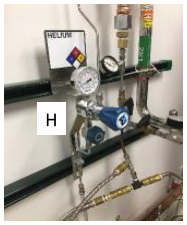

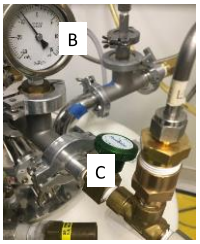

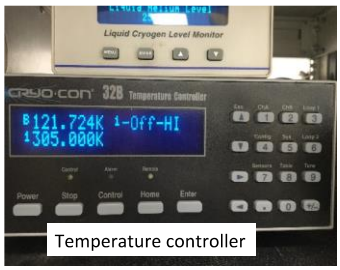

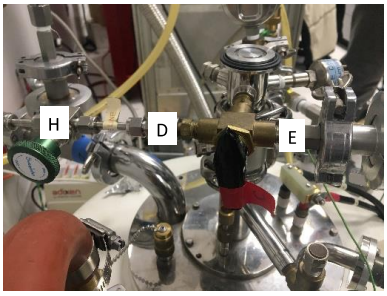

In order to protect the device from ESD device, always wear a grounding while touching anything on the cryostat. Also, the device should always be grounded while it is not being measured.

----------Remove the sample----------

1. Close the needle valve. This ensures the helium gas flow from the exchange gas space to the ATL is not excessive. **If the flow is too high, the ATL will warm up.** Continue to pump out the exchange gas space for roughly 20 minutes until the gauge reads -30" Hg. To check that the space has been evacuated completely, close the exchange gas space valve for 5 minutes. The pressure should remain at -30" Hg. If this is not the case, you must continue pumping on the exchange gas space.

Exchange Gas Space Purged:

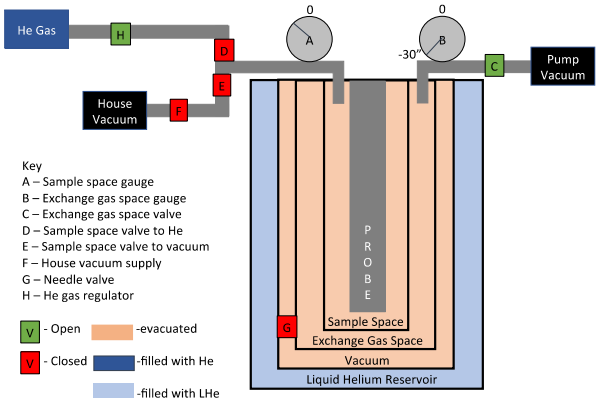

Exchange gas space sealed:

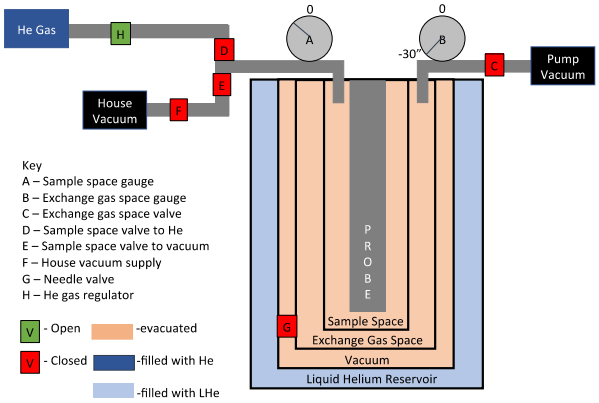

Now, both the sample space and the exchange gas space have been evacuated. Open the exchange gas valve ½ turn.

2. Make sure there is helium gas supply from the corridor and that the helium regulator is set to 10 psi. Open the sample space valve to He gas until the safety valve triggers. Close the sample space valve.

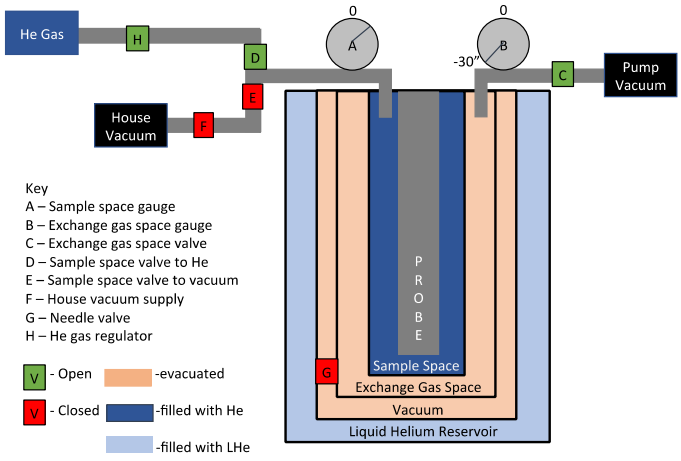

3. Set the temperature controller to PID mode with the heater on HI and the setpoint at 305 K. Press “control” to start heating the sample. The sample temperature should rise to around 50 K in 30 seconds. **If the sample temperature does not rise monotonically or acts irregular in any way press “stop” on the heater. There could be a very dangerous ice blockage! Refer to the Ice removal SOP.** The sample should reach 305 K in roughly 5 minutes.

4. Once the sample temperature is 305 K, open the sample space valve to helium gas until the safety valve is triggered. At this point, the He gas into the sample space should be turned off. To avoid overshooting 305 K, monitor the temperature during the period when the sample temperature goes up to 305 K and press “stop” if heating continues past 320 K. **Large temperature fluctuations are suggestive of ice blockage. Immediately turn off the heater and refer to the ice removal SOP.** Finally, this step requires supervision at all times, it will take 30 minutes.

5. Make sure the He gas regulator reads positive pressure. If this is the case, then switch the sample space valve to the He gas side and fill with gas until the safety valve triggers. Otherwise replace the He gas tank in the corridor. Flow He gas continuously while removing the probe. Once the probe has been taken out, close the exchange gas valve.

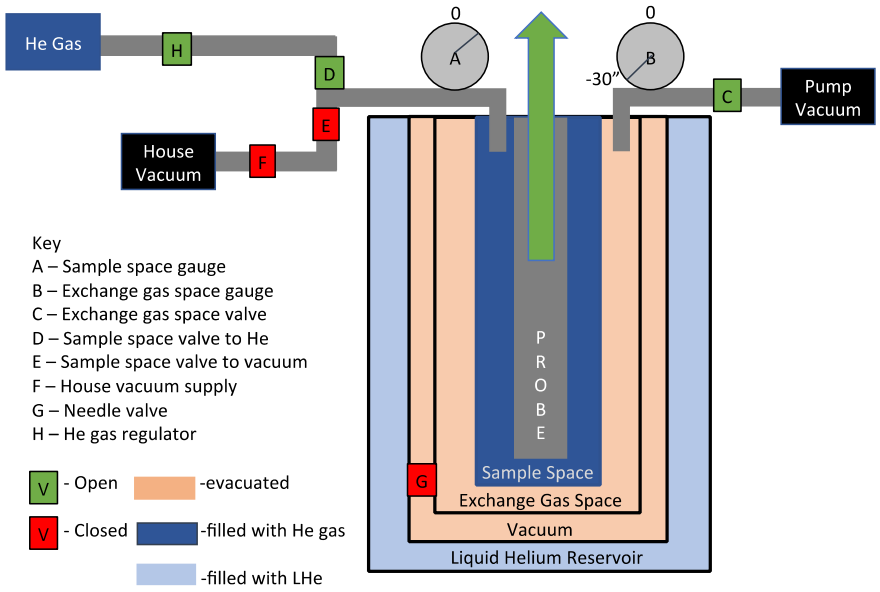

6. Clamp the metal cap onto the sample space and change the sample space valve from He gas flow configuration to the pumping configuration. Make sure that the cap is securely fastened during this step to avoid the chance that air getting into the sample space. Close the exchange gas space valve. Pump and purge with He gas three times to remove any air in the sample space. Leave the sample space filled with He gas and then switch the sample space valve to the neutral configuration.

PUMP:

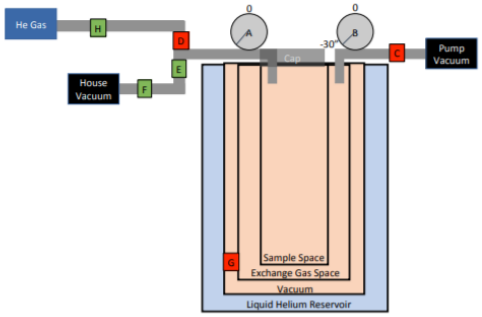

X 3

PURGE:

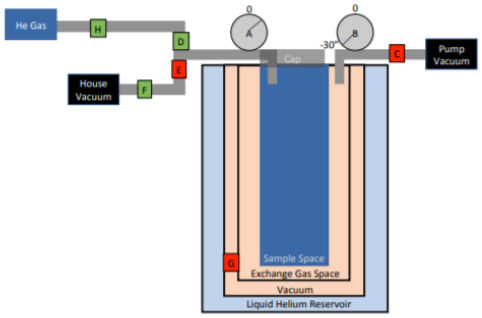

X 3

SEAL:

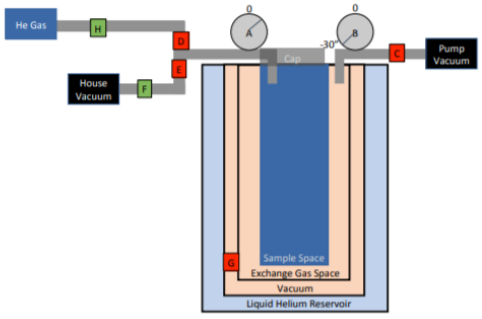

7. Turn off the heater by pressing the “Stop” button.

8. Remove the device from the sample holder and wait for a while (e.g. 20min) to let the probe de-ice and thaw.

----------Load in the sample----------

9. Put the new device into the sample holder and perform an initial test. (i.e. Line profile and gate effect check.). If the device is sufficient, then prepare to load the device into the cryostat.

10. Switch the sample space valve to Helium gas side to over pressurize the sample space, watch for the safety valve to trigger and then remove the metal cap. Load the sample into the cryostat carefully to avoid hitting the device against the cryostat walls. This step must be done while continuously flowing He.

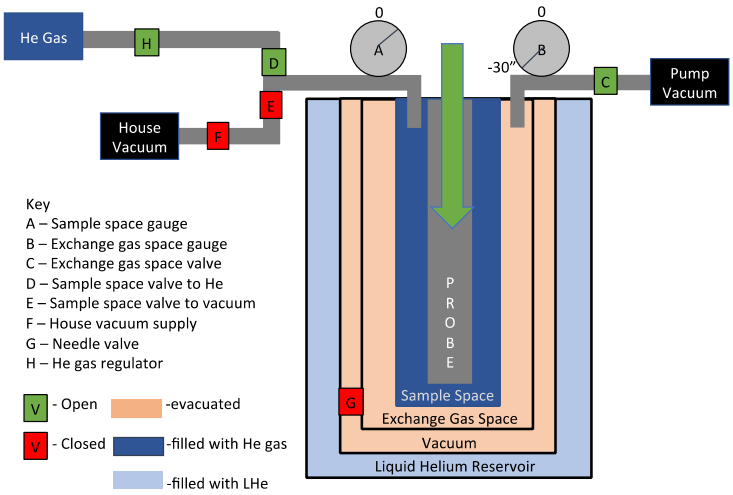

11. Clamp the probe. Pump and purge the He sample space 3 times. Finally leave the sample space full of He gas.

12. Confirm that the exchange gas space valve is open ½ turn. Then open the needle valve slightly (1/16 of a turn) and monitor the pressure of the exchange gas space. This pressure should be adjusted until it reaches 0” Hg. The thermometer reading should begin to drop from 305 K. As the sample cools, periodically feed in He gas to keep the sample space pressure at ~5 psi. To cool down the temperature faster, decrease the pressure in the exchange gas space by opening the exchange gas valve a little bit more. (Cool down to 4.2K can take between 2.5~4 hours depending on the pressure in exchange gas space.)

COOLING CONFIGURATION:

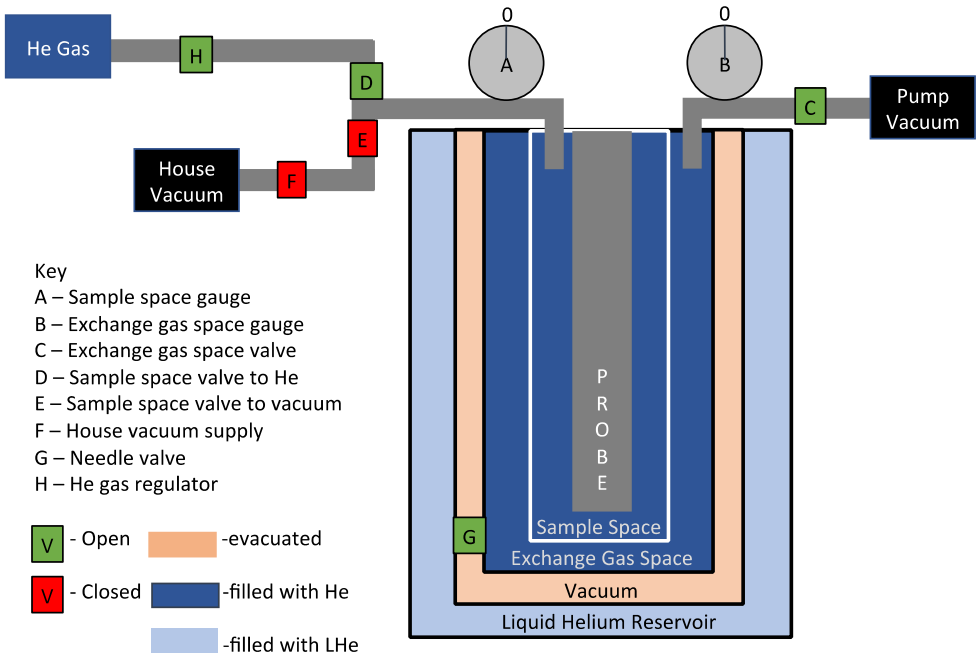

13. Close the Helium gas tank and regulator.

Appendix D:

Igor Data Analysis Functions

This Appendix includes the Igor procedure scripts used to plot, scale, shear and enhance the contrast of data displayed in chapters 5,6 and 7. The following scripts are straightforward to implement in Igor by opening a new procedure file and copy-pasting the desired block of code into that procedure. More detail as well as figures corresponding to the functions are presented in the final section of Chapter 3.

```
// import the appropriate libraries

#pragma rtGlobals=1
#include <all ip procedures>
#include <wave loading>

// The following function will create a 2D colormap or “megasweep” with Gwave as
// the colorscale, Vwave as the vertical axis and Gate as the horizontal axis
Function Megasweep(Gwave, Vwave, Gate) //  data, Backgate, Topgate
	Wave Gwave, Vwave, Gate
	variable i=0
	variable j=0
	variable counter=0
	variable totlen=numpnts(Gwave)
	do
		if (counter>=totlen)
			break
		endif
		counter+=1
	 while (gate[counter]==gate[counter-1])
	string namebase="test"
		String newname
		WaveStats/Q Vwave
		variable vstart=V_min
		Variable  vend = V_max
		wavestats/Q/R=[0, 20] Vwave
		Variable vstep=(V_max-V_min)/20
		WaveStats /Q Gate
		Variable gatestart=V_min
		Variable gateend=V_max
		Variable gatestep=gate[counter]-gate[counter-1]
```

```
        Variable Vnow
        Variable newplot
        Prompt namebase, "enter the name of the 2D plot"
        Prompt vstart, "bias minimum"
        Prompt vstep, "bias step"
        prompt vend, "bias maximum"
        Prompt gatestart, "gate minimum"
        Prompt gatestep, "gate step"
        prompt gateend, "gate maximum"
        Prompt Newplot, "newplot", popup, "yes;no"
        Doprompt "Configure", namebase, vstart, vstep, vend, gatestart, gateend,
gatestep, newplot
        print "x range is from", gatestart, "to", gateend,  "in steps of ", gatestep
        print "y range is from", vstart, "to", vend, "in steps of", vstep
        print "the output filename is", namebase
        variable rowno=(abs(vend-vstart)/vstep)+1
        variable colno=abs((gateend-gatestart)/gatestep)+1
        //variable rowno=4000
        //variable colno=324
      make/N=((rowno-0), colno)/O $namebase, tempwave
      wave twoDplot=$namebase
      //setscale/P x vstart, vstep, "", twoDplot
      //setscale/P y gatestart, gatestep, "", twoDplot
      counter=0
      do
            j=0
            make /N=2e6 /O tempV=0, tempG=0, tempG_L=0
            if (mod(i,20)==0)
                  print i
            endif
            if (i==5)
                  print i
            endif
            do
                  if (counter>=totlen)
                        break
                  endif
                 tempV[j]=Vwave[counter]
                 tempG[j]=Gwave[counter]
                 j+=1
                 counter+=1
            while (abs(gate[counter]-gate[counter-1])<1e-5)
            Redimension /N=(j) tempV, tempG
          //  sort tempV, tempV, tempG
```

```
            Interpolate2/X=tempV_L /T=1/I=0 /N=(rowno-0) /Y=tempG_L tempV,
tempG
            tempwave[][i]=tempG_L[p]
            i=i+1
       while (counter<totlen)
      MatrixOp/O twoDplot=(tempwave)^t
       //twoDplot=tempwave
      setscale/I x gatestart, gateend, "", twoDplot
      setscale/I y vstart, Vend, "V", twoDplot
       If (newplot==1)
          Display; appendimage TwoDplot
          ModifyImage " ctab= {*,*,Gold,0}
          ModifyGraph tick=2,fStyle=1,fSize=18,tickUnit=1,standoff=0;DelayUpdate
                  Label left "Sample Bias (V)";DelayUpdate
                  Label bottom "V\BG\M (V)"
       endif
End

// The following function will find the ratio between top and back gate capacitances in
// a tunneling devices. First place Igor graph cursors on the megasweep (produced by
// the above // function). The cursors should be placed at two points on “feature (i),”
// discussed in Chapter 5.

Function get_C_ratio(sweep_wave)
          Wave sweep_wave
          Variable /G C_ratio
          C_ratio = (hcsr(b)-hcsr(a))/(vcsr(b)-vcsr(a))*1000
          Return C_ratio
End

Function n_prof(sweep_wave,MaxGate)
          Wave sweep_wave
          Variable MaxGate
          Wave xwave1, ywave1
          Variable NextVb, nrel, Gate_Rat
          Variable /G ZeroVg, n_actual
          Nvar C_ratio
          Gate_Rat = C_ratio
          NextVb = (vcsr(a)*0.001+(1/Gate_Rat)*(MaxGate-hcsr(a)))*1000
          nrel = -Gate_Rat*vcsr(a)/1000+hcsr(a)
          Make/N=2/O xwave1
          Make/N=2/O ywave1
          xwave1[0] = xcsr(a)
          xwave1[1] = MaxGate
```

```
        ywave1[0] = vcsr(a)
        ywave1[1] = NextVb
        appendtograph ywave1 vs xwave1
        ImageLineProfile xWave=xwave1, yWave=ywave1, srcwave=sweep_wave
        SetScale/I x vcsr(a) ,NextVb,"", W_ImageLineProfile
        Duplicate /O W_ImageLineProfile profile1
        ZeroVg = -vcsr(a)*Gate_Rat*0.001 + hcsr(a)
        n_actual = ZeroVg*6.7e10   //  assuming bottom BN and SiO2 are same eps =
3.9, d = 320 nm
        Display profile1
        ModifyGraph tick=2,mirror=2,fStyle=1,fSize=10,font="Arial";DelayUpdate
        Label left "G (au)";DelayUpdate
        Label bottom "Vb (mV)"
        Print NextVb
        Print nrel
        Print n_actual
End

// The following function will shear a megasweep (produced by the megasweep
// function above) // so that two cursors placed on the map with a diagonal offset will
// be aligned vertically. This was used to map constant charge density features onto
// the horizontal axis. Note that the horizontal axis will be scaled by a factor rel;ated
// to the back gate capacitance, which is determined geometrically with AFM. This is
// subject to change and must be determined for each device. To use this function,
// first place Igor graph cursors on the megasweep. The cursors should be placed at
// two points on “feature (i),” discussed in Chapter 5.

Function shear(old)
        wave old
        variable/g nrow, ncol, n, j, d, m, dx, w, nmax, nmin, vbmx, vbmn, vgmx,
vgmn, xyslope
        string new_name
        Prompt new_name, "shear wave name"
        Doprompt "Configure", new_name
        nrow = dimsize(old,0)
        ncol = dimsize(old,1)
        m = (qcsr(b)-qcsr(a)) / (pcsr(b)-pcsr(a))
        w=abs(ceil(m))
        print w
        dx = 1
        d=nrow+ncol/w
        make /o/n = (d,ncol) new = 0
        print "w is negative"
    print w
```

```
        if (m>0)
                print "m is positive"
                for(n=0; n<ncol/w; n+=1)
                        make/o/n=(d-n*dx-nrow,w) block1 = 0
                        make/o/n=(nrow,w) block2 = old[p][q+n*w]
                        make/o/n=(n*dx,w) block3 = 0
                        Concatenate/o/NP=0 {block1,block2,block3}, block
                        new[][n*w,(n+1)*w]=block[p][q-n*w]
                endfor
    else
        print "m is negative"
                for(n=0; n<ncol/w; n+=1)
                        make/o/n=(n*dx,w) block1 = 0
                        make/o/n=(nrow,w) block2 = old[p][q+n*w]
                        make/o/n=(d-n*dx-nrow,w) block3 = 0
                        Concatenate/o/NP=0 {block1,block2,block3}, block
                        new[][n*w,(n+1)*w]=block[p][q-n*w]
                endfor
        endif
        vgmn = dimoffset(old,0)
        vbmn = dimoffset(old,1)
        vgmx = vgmn + dimdelta(old,0)*dimsize(old,0)
        vbmx = vbmn + dimdelta(old,1)*dimsize(old,1)
        xyslope = (vcsr(b)-vcsr(a))/(hcsr(b)-hcsr(a))
        SetScale/I x (vgmn-abs(vbmx/xyslope))*0.067,
(vgmx+abs(vbmn/xyslope))*0.067, "cm^-2", new //absolute value is to compensate
for flipped vbmx and vbmn
        SetScale/I y vbmn,vbmx,"V", new
        display; appendimage new
        ModifyGraph tick=2,fStyle=1,fSize=18,tickUnit=1,standoff=0;DelayUpdate
        ModifyGraph manTick(left)={0,0.3,0,1},manMinor(left)={0,0};DelayUpdate
        ModifyGraph manTick(bottom)={-
1,2,0,0},manMinor(bottom)={1,0},font="Arial";DelayUpdate
        Label left "Sample Bias (V)";DelayUpdate
        Label bottom "n (10\\S12 \\Mcm\\S-2\\M)"
        rename new $new_name
end
```

```
// The following function is used to account for the central phonon feature, discussed
// in chapter 6. Specifically, the function will shift the top and bottom portions of the
// 2D color  map down and up, respectively to close the gap between cursors placed
// on the input graph. In order to use this function, first use the “shear” function above
// to produce a dI/dV(Vb,n) map. Then place the Igor graph cursors on this map so
// that they are horizontally aligned, and their vertical positions are at the edge of the
// central phonon feature. Finding the exact edges of the phonon feature is discussed
// in Chapter 6. The resulting output map from this function will have shifted the map
// energies accordingly.
function squishfast(old)
        wave old
        variable/g nrow, ncol, dx, dy, gapE
        wave new_s
        dx = abs(pcsr(a)-pcsr(b))
        dy = abs(qcsr(a)-qcsr(b))
        gapE = abs(dy*dimdelta(old,1))
        nrow = dimsize(old,0)
        ncol = dimsize(old,1)
        make /o/n = (dx+nrow,ncol-dy) new_s = 0
        make/o/n=(nrow,ncol-qcsr(b)) block1 = old[p][q+qcsr(b)]
        make/o/n=(dx,ncol-qcsr(b)) block2 = 0
        print(dimsize(block2,0))
        print(dimsize(block2,1))
        Concatenate/o/NP=0 {block1,block2}, block12
        make/o/n=(dx,qcsr(a)) block3 = 0
        make/o/n=(nrow,qcsr(a)) block4 = old[p][q]
        Concatenate/o/NP=0 {block3,block4}, block34
        new_s[][,dimsize(block34,1)]=block34[p][q]
        new_s[][dimsize(block34,1),dimsize(new_s,1)]=block12[p][q-
dimsize(block34,1)]
        display; appendimage new_s
        SetScale/I x
dimoffset(old,0),dimoffset(old,0)+dimdelta(old,0)*dimsize(old,0),"cm^-2", new_s
        SetScale/I y dimoffset(old,1)-
gapE,dimoffset(old,1)+gapE+dimdelta(old,1)*dimsize(old,1),"V", new_s
        ModifyGraph tick=2,fStyle=1,fSize=18,tickUnit=1,standoff=0;DelayUpdate
        ModifyGraph manTick(left)={0,0.2,0,1},manMinor(left)={0,0};DelayUpdate
        ModifyGraph manTick(bottom)={-
1,2,0,0},manMinor(bottom)={1,0},font="Arial";DelayUpdate
        Label left "Sample Bias (V)";DelayUpdate
        Label bottom "n (10\\S12 \\Mcm\\S-2\\M)"
        ModifyGraph width=504,height={Aspect,1}
        ModifyImage new_s ctab= {-0.1,0.1,RedWhiteBlue,0}
end
```

```
// The following function sets the n=0 point on a sheared dI/dVb(Vb,n) tunneling
// map. To use this function, begin with the output wave of the “shear” function
// introduced above. Place Igor cursor A on the map at the location where n=0 (this is
// the location of the central dark feature in graphene and bilayer graphene tunneling
// maps when B=0 T, and the center of the zeroth landau level when B!=0T). This
// function will shift the scale of the horizontal n axis without dilating values.

function nscale(old)
        wave old
        setscale x dimoffset(old,0)-hcsr(a),
dimoffset(old,0)+dimdelta(old,0)*dimsize(old,0)-hcsr(a),"cm^-2" old
end

function quantum_n(old,relation) //relation is dependent on the density of states, not
the capacitance
        wave old, relation
        wave new
        duplicate/o old new
        new[]=relation(old[p])
end

// The following function is used to enhance color contrast in tunneling dI/dV color
// maps by subtracting a background function from each vertical line along a color
// map. To use this function, begin by taking a vertical line trace of width “0” from
// the target color map (this could be either a raw megasweep or a sheared
// megasweep, both introduced above). Next, “checkpoint” the vertical line profile to
// save it in the buffer. Finally, call the below function with the starting colormap as
// “old,” the line profile as “smth,” and a “1” for “column.” Note that you can alter the
// procedure to instead subtract a horizontal line trace by first taking a  horizontal line
// trace, than calling “0” for row in the below function.

function bknd_sbt(old,smth,row_or_col)
        wave old, smth
        variable row_or_col
        wave new
        string newname
        variable /g n=0
        Prompt newname, "processed wave name"
        Doprompt "Configure", newname
        duplicate/o old new
        if (row_or_col==0)
                print "row"
                for(n=1; n<dimsize(old,0); n+=1)
```

```
                new[][n]=old[p][n]-smth[p]
            endfor
        else
            print "column"
            for(n=1; n<dimsize(old,1); n+=1)
                new[n][]=old[n][q]-smth[q]
            endfor
        endif
        rename new $newname
        print newname
        display; appendimage $newname
end
```

Appendix E:

MBraun Glovebox Operation and Maintenance

In this Appendix, I outline the key operation and maintenance procedures for the MBraun glovebox in the shared cleanroom space. Additional details can be found in the glovebox manual, or by calling MBraun USA customer support. The support number for this glovebox unit is 37-273.

E1 Supply Gas (N_2 or Ar) Cylinder Exchange—Every 2 weeks

1. In the gas corridor to the west of the cleanroom, close valve attaching the (empty) glovebox supply gas cylinder to the glove box supply line. This valve is directly upstream of the first regulator stage.
2. Close the gas cylinder valve, located on the top of the cylinder
3. Open the lab vent valve (to the left of the supply valve) to depressurize the line. Once depressurized, close the gas vent line.
4. Close the vent valve
5. Using a large adjustable wrench, disconnect the old gas cylinder and connect the line to the new gas cylinder.
6. Open the new tank all the way via the valve on top of the cylinder.
7. Open the vent valve slightly until it hisses for 3 seconds, then close the vent valve
8. Open the supply valve, and record the pressure of the new cylinder (displayed on the regulator) in the notebook with the date and your initials
9. Check the levels on the glovebox to ensure that no O_2 was introduced when cylinders were switched

Note: Make sure that the new gas cylinder has a yellow tag that says “In Service” while it is in use.

E2 Loading Samples with the small Ante-Chambers—Very frequent

- MAKE SURE inside door to glove box is closed and latched
- Open outside door, load sample, close door, *pump and purge to ~1/2 ATM 3 times* on the third purge, fill to 1 atm
- Open the ante chamber to the inside of the box to load the sample
- Close the inside door to the ante chamber and leave it at 1 atm to indicate that it is cleaned and can be opened to the inside of the glovebox without further cleaning

E3 Unloading Samples with the small Ante-Chambers—Very frequent

- Check antechamber pressure: if pressure is low, antechamber was left "dirty" and SHOULD NOT be opened to the inside of the box without cleaning first
- If the chamber must be cleaned follow this procedure:
    - Make sure both antechamber doors are closed and latched
    - Pump and purge to ~1/2 atm three times and on the third time, purge to 1 atm
    - Open the inside door to the glove box and load the sample
    - Close and latch the inside door of the antechamber
    - Open the outside door and unload the sample
    - Close and latch the outside door and PUMP BUT DO NOT PURGE the empty, dirty ante chamber to notify that the chamber must be cleaned again before opening to the inside of the glove box
- If the chamber is at 1 atm, it is clean and the above procedure must be altered:
    - MAKE SURE outside door of the antechamber is closed and latched
    - Open the ante chamber to the inside of the box to load the sample
    - Close and latch the inside door of the antechamber
    - Open the outside door and unload the sample
    - Close and latch the outside door and PUMP BUT DO NOT PURGE the empty, dirty ante chamber to notify that the chamber must be cleaned again before opening to the inside of the glove box

E4 Loading and Unloading Large Objects in the Large Ante-Chamber—Need-based

- Follow the same policy for pumping and purging outlined in the small antechamber procedures above with several exceptions:
    - Rather than pumping and purging the large antechamber 3 times to clean it, pump it once overnight, then purge once.
- All pump and purge controls for the large antechamber can be found in the main control screen of the glovebox System -> Antechamber

E5 Replacing Gloves—Every 2 years or when a glove is compromised

- Inside the glove box, place and tighten the porthole cover over the port where the compromised glove is connected
- Remove the compromised glove
- Select a replacement glove with the same dexterity (right, left or neutral-handed) in the correct rotational orientation as the compromised glove
- Roll up the replacement glove starting at the fingertips to press out any air in the glove arm
- Attach the end of the rolled up glove arm to the exterior of the covered porthole
- Attach 2 rubber gaskets to seal the interface between glove arm and porthole exterior
- Remove the porthole cover from the interior of the porthole

- Put glove box in "quick purge" mode to lower the O_2 level which will probably rise rapidly from the introduced air
- Monitor the O_2 level until it is below 50 ppm, then return to recirculation mode

E6 Initiating Quick Purge Mode—Need based when either O_2 or H_2O level is > 100 ppm

- If for any reason the glovebox O_2 or H_2O levels rise above 100 ppm, you should set the glove box in recirculation mode until BOTH levels have decreased below 100 ppm
- On the front control panel of the glove box select the following options
    - Functions → recirculation OFF → quick purge ON
    - Once the levels are lower than 100 ppm, select Functions → quick purge OFF → recirculation ON

E7 Regeneration Process—Quarterly

- NOTE: If O_2 or H_2O levels are higher than 0.1 ppm during normal operation, a regeneration is needed
- Three things to check before regeneration begins:
    - Ante-chambers are NOT open to the vacuum pump
    - O_2 level is not > 50 ppm (if O_2 levels are >50 ppm, then enter "quick purge", described above)
    - Regeneration gas tank level is at least 800 psi
- Before starting the regeneration process, the regeneration tank must be connected to the glove box. Use a hydrogen-specific regulator/valve assembly to connect the regeneration gas to the glove box via a hose.
- Open the regeneration gas cylinder via the valve on top, and upen the secondary valve connected to the regulator.
- Adjust the regulator until the secondary gauge reads ~ 4 psi.
- On the output of the recirculation reactor, attach a water bottle to a hose. This water bottle will collect ~50 mL of water during regeneration
- Stop recirculation mode via the main control screen of the glove box
- Enter the regeneration cycle by pressing the "regeneration" push button on the main control screen. This will prompt you to check the flow of regeneration gas
- Press "check flow" and wait 2 min. The rotometer on the bottom of the recircvulation reactor will measure the flow of regeneration gas. Adjust the regulator on the regeneration gas cylinder until the flow through the rotometer is in the acceptable range (marked by double arrows on the rotometer)
- Once the flow is adequate, on the main glovebox control panel, press "begin regeneration"
- Note the "time remaining" should be 960 minutes (16 hours). Wait until this is decremented to 959 minutes before leaving the glovebox

- Notify all users that the glovebox cannot be touched until the regeneration cycle is complete. The glovebox can then be left regenerating overnight.
- Once the cycle is complete, the glovebox will AUTOMATICALLY return to normal recirculation mode.
- Note the amount of water that was excreted into the water bottle. If there is ~50 mL of water, and the O_2 and H_2O levels in the glovebox are <0.1 ppm, the regeneration was successful. If anything abnormal occurs during the regeneration cycle, contact MBraun USA.

All other (less frequent) Maintenance to the Glovebox is outlined in the manual, available on the Velasco Lab Google Drive

This Space is Allocated for Handwritten Notes and Calculations